January 17, 2002

Fractured Reservoir E&P in Rocky Mountain Basins: A 3-D RTM Modeling Approach

U.S. DOE Contract #DE-FG26-99FT40264

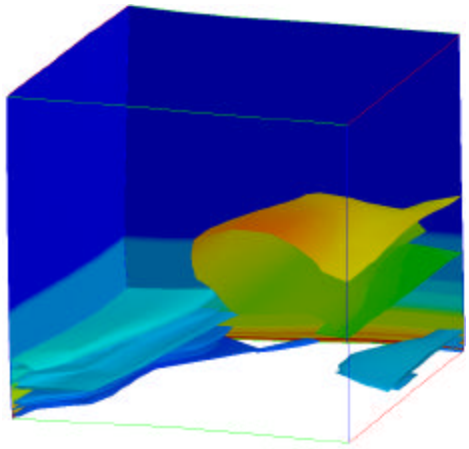

Principal Investigator: P. Ortoleva

Report Authors: J. Comer, P. Ortoleva, A. Park, D. Payne, W. Sibo and K. Tuncay

Laboratory for Computational Geodynamics
Department of Chemistry
Indiana University
Bloomington, IN 47405
Phone (812) 855-2717, Fax (812) 855-8300
ortoleva@indiana.edu

ABSTRACT

Key natural gas reserves in Rocky Mountain and other U.S. basins are in reservoirs with economic producibility due to natural fractures. In this project, we evaluate a unique technology for predicting fractured reservoir location and characteristics ahead of drilling based on a 3-D basin/field simulator, Basin RTM. Recommendations are made for making Basin RTM a key element of a practical E&P strategy.

A myriad of reaction, transport, and mechanical (RTM) processes underlie the creation, cementation and preservation of fractured reservoirs. These processes are often so strongly coupled that they cannot be understood individually. Furthermore, sedimentary nonuniformity, overall tectonics and basement heat flux histories make a basin a fundamentally 3-D object. Basin RTM is the only 3-D, comprehensive, fully coupled RTM basin simulator available for the exploration of fractured reservoirs. Results of Basin RTM simulations are presented, that demonstrate its capabilities and limitations. Furthermore, it is shown how Basin RTM is a basis for a revolutionary automated methodology for simultaneously using a range of remote and other basin datasets to locate reservoirs and to assess risk.

Characteristics predicted by our model include reserves and composition, matrix and fracture permeability, reservoir rock strength, porosity, *in situ* stress and the statistics of fracture aperture, length and orientation. Our model integrates its input data (overall sedimentation, tectonic and basement heat flux histories) via the laws of physics and chemistry that describe the RTM processes to predict reservoir location and characteristics. Basin RTM uses 3-D, finite element solutions of the equations of rock mechanics, organic and inorganic diagenesis and multi-phase hydrology to make its predictions. As our model predicts reservoir characteristics, it can be used to optimize production approaches (e.g., assess the stability of horizontal wells or vulnerability of fractures to production-induced formation pressure drawdown).

The Piceance Basin (Colorado) was chosen for this study because of the extensive set of data provided to us by federal agencies and industry partners, its remaining reserves, and its similarities with other Rocky Mountain basins. We focused on the Rulison Field to test our ability to capture details in a well-characterized area.

In this study, we developed a number of general principles including (1) the importance of even subtle flexure in creating fractures; (2) the tendency to preserve fractures due to the compressibility of gases; (3) the importance of oscillatory fracture/flow cycles in the expulsion of natural gas from source rock; and (4) that predicting fractures requires a basin model that is comprehensive, all processes are coupled, and is fully 3-D. A major difficulty in using Basin RTM or other basin simulator has been overcome in this project; we have set forth an information theory technology for automatically integrating basin modeling with classical database analysis; this technology also provides an assessment of risk. We have created a relational database for the Piceance Basin. We have developed a formulation of devolatilization shrinkage that integrates organic geochemical kinetics into incremental stress theory, allowing for the prediction of coal cleating and associated enhancement of natural gas expulsion from coal. An estimation of the potential economic benefits of the technologies developed or recommended here is set forth. All of the above findings are documented in this report.

LIST OF ABBREVIATIONS

1-D	one spatial dimensional
2-D	two spatial dimensional
3-D	three spatial dimensional
Basin RTM	basin simulator developed by LCG
IU	Indiana University
LCG	Laboratory for Computational Geodynamics (at Indiana University)
RTM	reaction, transport, mechanical processes operating on a basin or reservoir
MWX	Multiwell Experiment
GIS	Geographic Information System

CONTENTS

I. PROJECT SUMMARY

A. Overview

Much of the available natural gas in Rocky Mountain basins resides in reservoirs whose producibility is due to natural fractures. Locating, evaluating, and predicting the characteristics of such reservoirs requires an approach that yields reliable information ahead of drilling. Unfortunately, there is no technology available to date. For example, a lithology can have curvature but be unfractured, or can be flat-lying and be fractured, thereby frustrating a simple flexure analysis. Considering our increasing reliance on natural gas, such a technology should be an important asset in our stable, long-term energy policy.

The lack of a strong relationship between major producing fields in the Piceance Basin and the basin shape, coal formation thickness, vitrinite reflectance, and basin scale structural features is shown in Appendix A. The purpose of this report is to present a technology for remote fracture detection based on a comprehensive basin simulator, and to evaluate this technology and identify improvements and strategies for making it a practical technology for locating, characterizing and optimizing production from U.S. natural gas fields.

Many benefits could accrue from a remote detection technology for natural gas-bearing reservoirs. A horizontal drilling program, which can be a successful strategy for significantly increasing production in fractured reservoirs, requires finding lithologies with sufficient mechanical stability to support the borehole; in addition, fracture orientation and aperture must be estimated to arrive at an optimal direction for the well so as to intersect the greatest number of open fractures. Also, estimates of *in situ* formation stresses and fluid pressures are required to predict how the fracture network will respond to production-induced pressure drawdown, while gas composition and the overall geometry of the fractured zone are needed to determine the economics of a reserve. In summary, a technology is required that will yield many details on reservoir location and characteristics ahead of drilling so as to maximize the use of our natural gas reserves.

This report is based on the simulator Basin RTM developed by us at the Laboratory for Computational Geodynamics at Indiana University. Basin RTM is the most comprehensive basin/field simulator available at present. It accounts for most of the processes believed to be key to fracturing (mechanics, multi-phase flow, diagenesis) and thereby serves as a natural starting point for a fracture-prediction technology. In this project, we have built on our earlier DOE project (Contract DE-AC21-93MC30086), for which we were a subcontractor to Advanced Resources International, Inc. We have evaluated the capability of Basin RTM for applications in Rocky Mountain and other natural gas-bearing basins. Our evaluation was carried out using data from the Piceance Basin, although our approach is viable in similar natural gas, fracture production regimes worldwide.

In this report we address the following central issues:

- What reservoir attributes can Basin RTM predict (see Chapters II and III)?
- What are the shortcomings of Basin RTM (see Section I.C) ?
- What new features and technologies can be added to Basin RTM and to the way that it is implemented/used to attain results that are more accurate (see Section I.C and Chapter IV)?
- How can the labor-intensive task of developing Basin RTM input data be automated, and thereby, be made more efficient and free of biased interpretation of the geological record (see Subsection I.C3 and Chapter V)?
- How can we predict uncertainties/risk in Basin RTM predictions (see Chapter V)?

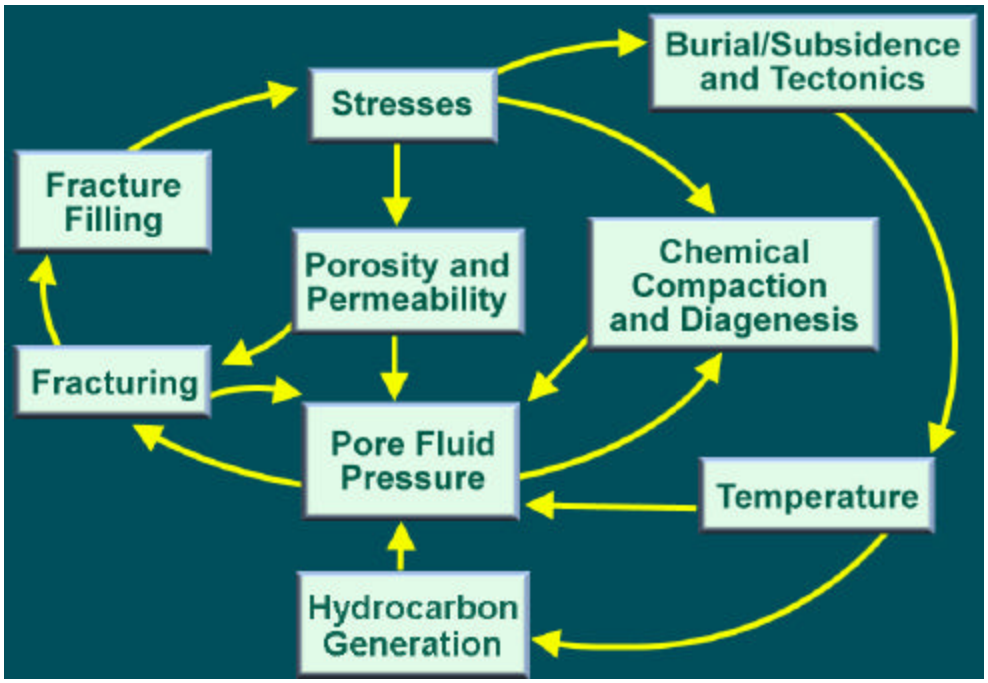

Fig. I-1 Complex network of coupled processes underlying the dynamics of a sedimentary basin or evolving reservoir. These factors and their coupling are accounted for in our unique basin simulator, Basin RTM.

- What general conclusions can be drawn from the Piceance Basin study that can be applied to exploration and development in the Piceance and other basins (see Subsection I.C2)?

These questions are addressed in summary remarks in this chapter and in greater detail in the following chapters.

The difficulty of fractured reservoir prediction stems from the complexity of sedimentological, overall basin tectonic and thermal histories, and the myriad of interacting reaction, transport, and mechanical (RTM) processes that transform the internal state of a basin to create petroleum reservoirs and other related geological features (Fig. I-1). While remote, downhole logging and surface observations are used with partial success to predict reservoir location and characteristics, a technology is needed to extract more information from this data and to automate the use of the large databases of seismic, well log, and other data available to the industry in mature basins and which are often available in frontier areas. Until now, no comprehensive 3-D RTM model has been available to assist the petroleum industry in making predictions which account for the full suite of coupled RTM processes that create petroleum reservoirs in general, and notably in fracture regimes in particular. The integration of such a comprehensive model, together with the field data analysis approaches already in use, would provide a major advance in petroleum E&P technology as applied to fractured regimes.

In this project, we have combined the 3-D, multi-RTM process basin modeling capabilities of Indiana University's Laboratory for Computational Geodynamics (LCG) with the practical E&P experience of our industry and institutional partners. This team brought an extensive data set to this effort. Contributors to this Piceance Basin database and expertise pool include:

- Amoco
- Barrett Resources International

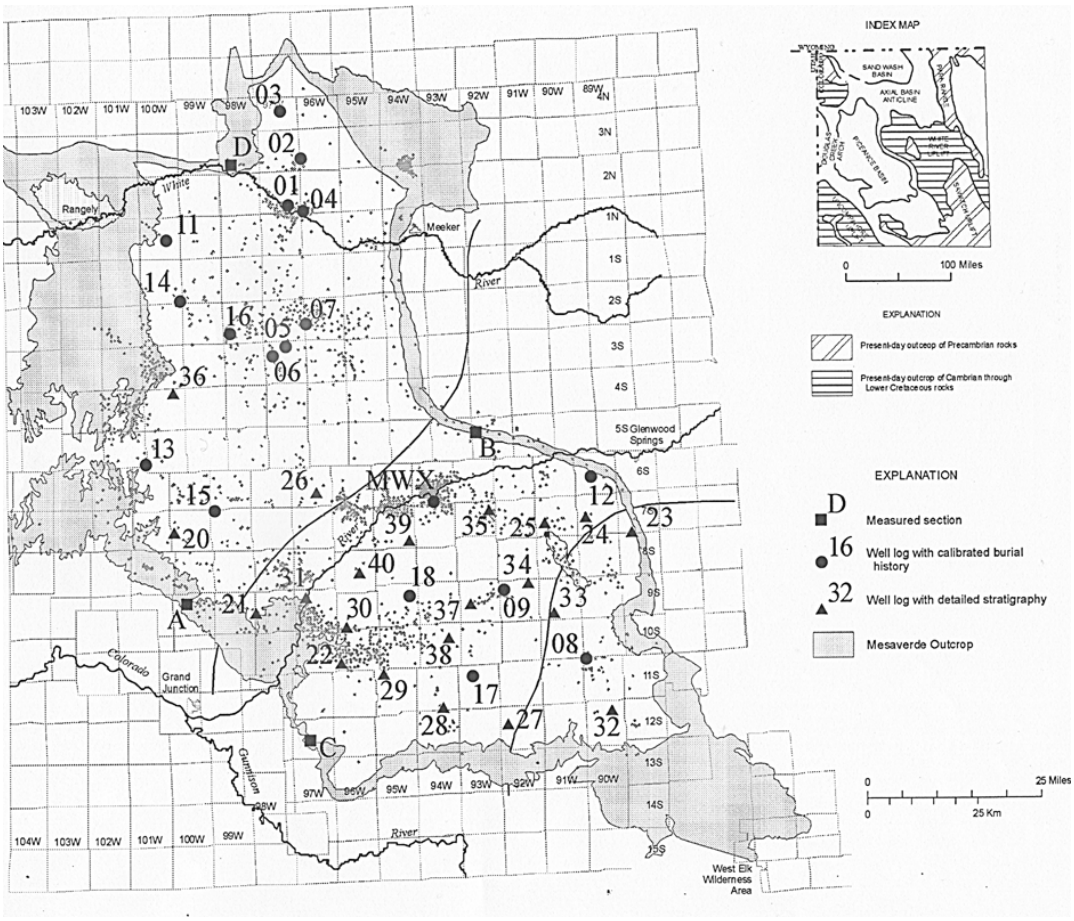

Fig. I-2 Map of Piceance Basin showing locations of wells and measured sections used to develop the database for RTM modeling.

- Chevron
- Geochemical Research Associates
- Kestrel Geoscience, LLC
- Koch Exploration
- Mobil Technology Center
- Phillips Petroleum Company
- Texas Bureau of Economic Geology
- Tom Brown Inc.
- Geochemical Research Associates
- U.S. Naval Oil Shale Reserve
- Unocal.

The required data for this project was archived in our (LCG's) database and is delivered to DOE as a part of this project in CD-ROM format.

B. The Piceance Basin Test Site

The Piceance Basin (Fig. I-2) is ideally suited for this study due to a number of factors:

- the natural gas in Mesaverde reservoirs is believed to be thermogenic and mostly derived from Cretaceous coal so that the organic geochemical kinetics model for lignin implemented in Basin RTM (see Appendix D) provides an accurate description;
- production from Cretaceous reservoirs in many Piceance Basin gas fields is known to be from fractures;
- other methods for locating and characterizing the fracture networks has only met with partial success;
- sufficient data from DOE's MWX and industry databases is available;
- there is a pre-existing culture of industry/DOE/academic cooperation in research on the Piceance Basin;
- the tectonic and thermal history of the Piceance Basin is sufficiently rich to test many of the features of Basin RTM; and
- there are still prospective areas for future natural gas production in the Piceance Basin.

In addition to the above, the geological context of the Piceance Basin makes it ideal for this study because many lessons can be learned and applied to finding and producing natural gas in other Rocky Mountain basins and because basic geologic principles can be derived that provide deeper insights into the dynamic evolution of fractured/natural gas reservoirs in sedimentary basins; the geological information available for this study is summarized in Appendices A, B, and C. A central focus of this study is technology evaluation and suggestions for future commercialization. Thus we ran simulations on the Piceance Basin to use a realistic set of input data.

C. Conclusions and Recommendations

1. Overall Conclusions

A number of general conclusions regarding basin processes and basin simulation were drawn in the course of this project. Our findings are derived from an extensive set of Basin RTM simulations, such as the 3-D example of Fig. I-3. A more complete discussion of our simulation results is found in Chapter III.

(a) Overpressuring persists during cooling (uplift and erosion) periods in a gas and gas/liquid saturated system due to the high compressibility of natural gas.

(b) Even very minor flexure can greatly affect the pattern of fracturing, and thus effective fractures may be missed by classical flexure analysis.

(c) Basin RTM's numerical approach is sufficiently robust that relatively low spatial resolution simulations can be used to gain a semi-quantitative understanding of the system's dynamics. However, lower dimensionality (1- or 2- vs. 3-D) simulations must be used with great care as stresses and fluid flows may strongly differ from full, 3-D simulations (see Fig. I-4).

(e) While predicting the migration of natural gas from source rock to the present-day reservoir is highly sensitive to correctly predicting the timing and spatial pattern of fracturing, Basin RTM appears to be sufficiently comprehensive to make such predictions (see Fig. I-5).

(f) Expulsion of natural gas from source rock can be highly dynamic, displaying autonomous oscillatory flow and fracturing arising from the coupling of fracturing and fluid flow (see also Ortoleva 1990, 1994a, 1998 and Chapt. III below).

(g) Extensional stresses induced by variations in the local uplift/subsidence history cause large variations in fracture density and permeability within a given lithology.

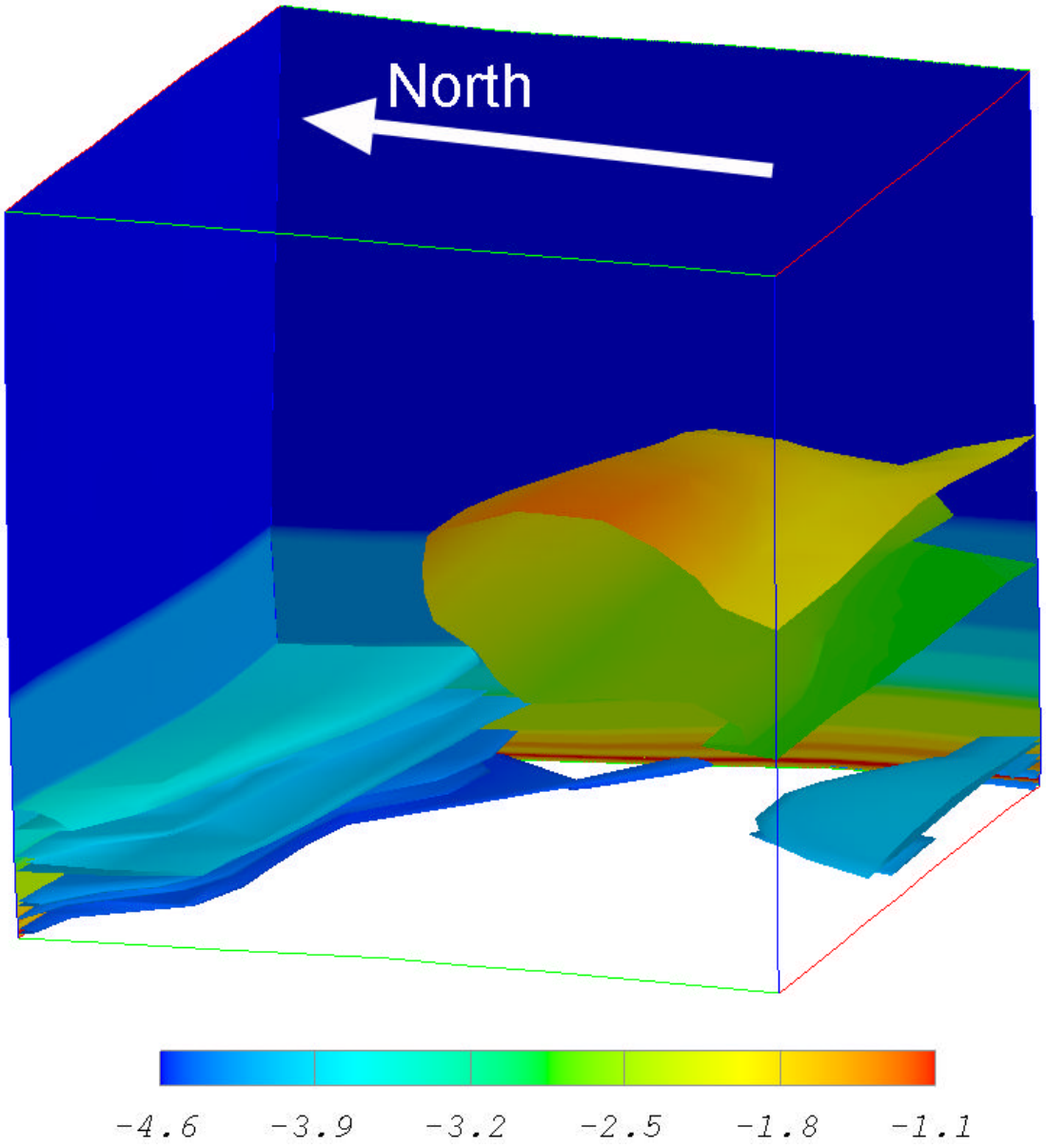

Fig. I-3 Isosurface of 100 Nano Darcy fracture permeability colored with depth (km). This isosurface indicates 3-D image of fracture sweetspots in the Rulison Field predicted using the Basin RTM simulator. The location and morphology of the fracture zones results from the interplay of sedimentology, overall tectonics and basement heat flux histories with the myriad of RTM processes. Fracturing was thus shown in this study to not be reliably predicted by less comprehensive, uncoupled, 1-D or 2-D models.

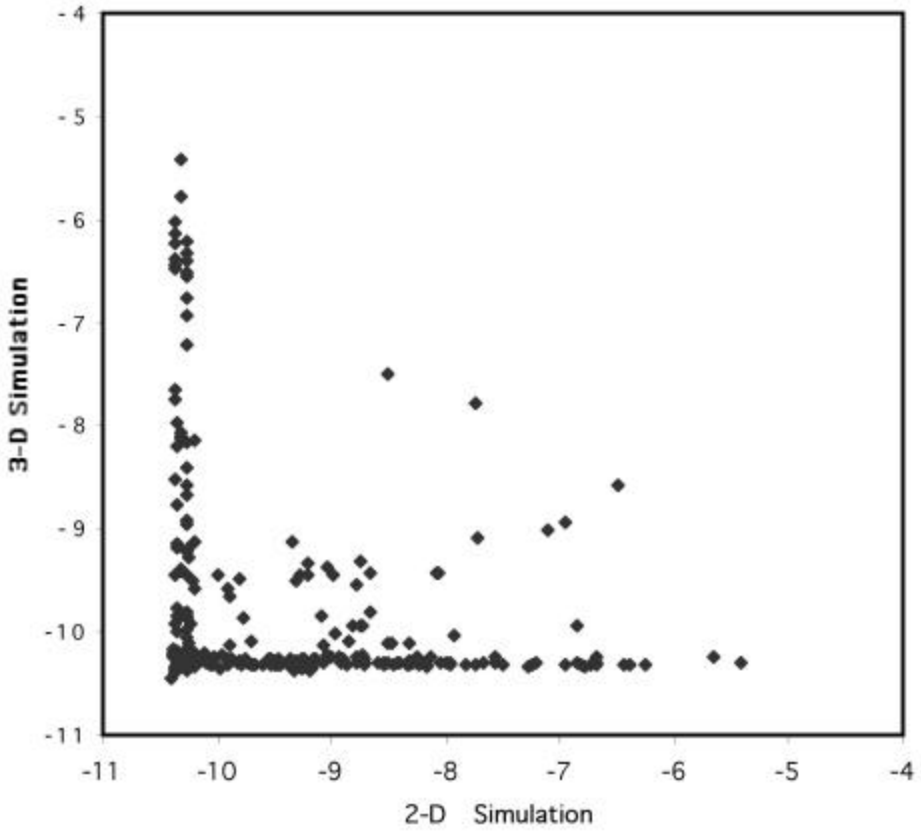

Fig. I-4 Correlation of the prediction of fracture permeability using a 3-D vs. 2-D simulation. Horizontal and vertical trends show that fracture zones do not always coincide in 2-D and 3-D results.

(h) The present-day state of a fractured reservoir results from the very complex interplay among RTM processes and the influence of overall tectonics, basement heat flux, and sediment input history. During the geological history of a reservoir, fractures may form and heal at widely different times due to changing sets of controlling processes.

(i) Erosion and the magnitude of relief created by unloading is a key factor in determining the location and characteristics of present-day fractures and the changing relative importance of processes that led to them. The extent and timing of erosion are often difficult to estimate and errors in these factors can introduce a significant degree of uncertainty into a Basin RTM (or other) simulation-based fracture prediction.

(j) Basin simulations carried out without an accurate methanogenesis or multi-phase flow model cannot reliably predict present-day fractures.

(k) Basin RTM has the potential to predict the location of fracture sweetspots, as suggested in Fig. I-6.

(l) The full benefit of the use of a comprehensive model such as Basin RTM will be realized when the collateral technologies as outlined below are integrated with it.

A more complete discussion of our simulation results is found in Chapter III.

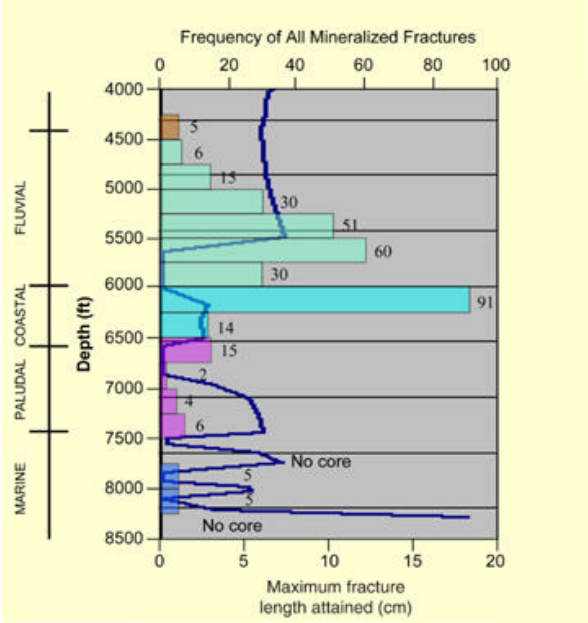

Fig. I-5 Comparison of observed (histogram) and predicted (curve) fractures in the Mesaverde Group at the MWX site. The upper scale applies to the histogram and refers to the number of mineralized fractures counted in MWX cores and the lower scale applies to the curve and refers to the predicted maximum fracture length which is related to fracture density (from Finley and Lorenz 1988).

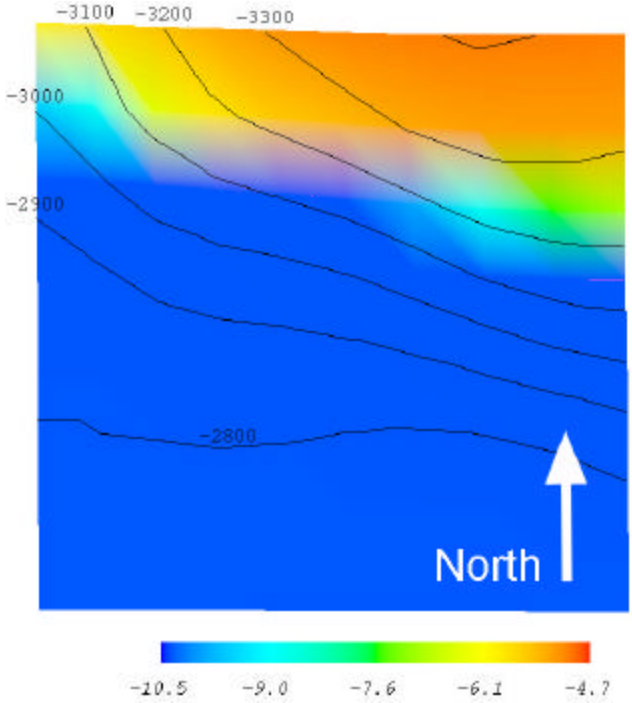

Fig. I-6 Predicted fracture permeability (log Darcy) in the Coastal Sandstone contoured with depth (m). The simulation domain is shown in Fig. III-D1. As seen in Fig. III-C1, the zone of production widens northward. Basin RTM predicts that fracture-mediated permeability in the Coastal Sandstone is greatest

in the north, suggesting a qualitative agreement with production trends. Agreement with production trends will be improved with the implementation of the data/simulation integration as outlined in Sect. I.C2.

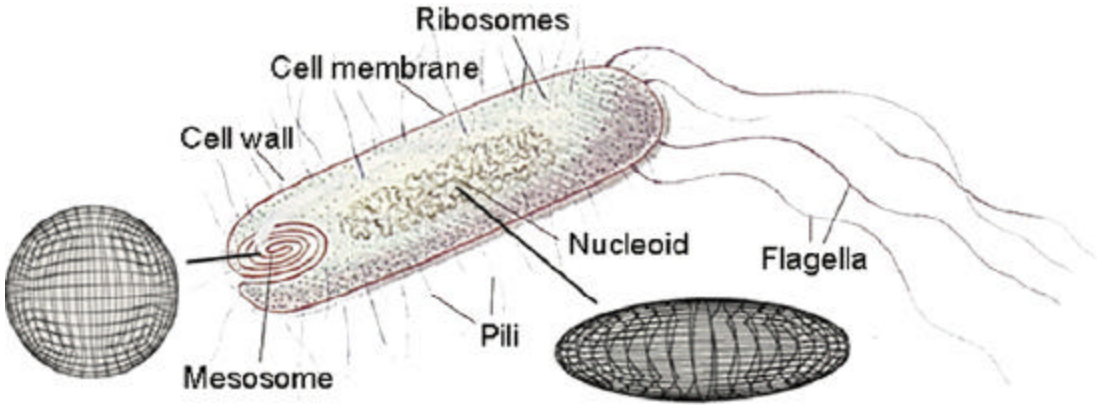

Fig. I-7 Schematic prokaryote model showing compartments within which special reactions occur; such a model is needed to obtain estimates of microbial degradation of subsurface organic matter and recalcitrant natural gas generation (Weitzke and Ortoleva 2001; Navid and Ortoleva 2001a,b).

2. Automated Generation of Basin Model/Data Integration

As outlined in Chapter V, an information theory methodology can be developed whereby the input data (basement heat flux, overall tectonic, and sedimentation history) parameters can be determined from the observed seismic, well log, and other data in an automated fashion. This approach requires the comprehensiveness of the set of processes presently only implemented in Basin RTM in order to carry it out. We are presently engaged in a follow-on project (DOE contract # DE-AC26-00NT40689) to attain this goal. This strategy evolved from our experience with the present project.

An analysis of the types of data that can be used and the types of boundary data that can be determined from them are found at the end of Chapter V.

3. Improved RTM Phenomenologies and Calibration

While Basin RTM is the most comprehensive basin simulator available, several RTM phenomenologies should be added to improve predictability. These are as follows:

(a) A contribution to the net rate of strain due to coal devolatilization (to account for cleating and resulting natural gas expulsion—see Chapter IV).

(b) A more comprehensive mechanistic model of organic reactions similar to the lignin model developed for Basin RTM (see Appendix D) for more accurate estimates of the rate, composition and timing of natural gas released from source rocks having a range and mixture of organic matter types.

(c) Rock rheology, notably the dependency of the rates of continuous deformation and fracturing on mineralogy, grain size, porosity and fracture network statistics (for better calculations of stresses needed to evolve the fracture network over geological time).

(d) Three phase compositional flow accounting for wetting dynamics and the changing geometry of the fluid phases within the pore space (natural gas expulsion, migration and trapping) (see Ortoleva 1998, 2001).

(e) Dual porosity multi-phase flow.

(f) Microbial degradation of kerogen starting with a model of the prokaryote cell that accounts for the many metabolic and genomic reactions taking place in specialized zones

Spatial Dimension	Minimum CPU (days)	Maximum CPU (days)
1-D	0.5	1
2-D	3	7
3-D	30	90

Table I-1 CPU time required by Basin RTM for comprehensive simulation/prediction of fractured reservoirs based on the status of Basin RTM at the end of this project and the use of a single processor on an IBM SP (RS/6000).

(compartments) within the cell (see Fig. I-7 and Weitzke, Navid and Ortoleva 2001 and Ortoleva 2001) (for computing the rate and composition of methane generated by bacteria from coal, as is believed to be a central process in many Rocky Mountain reservoirs).

4. Computer Hardware Issues

A serious limitation to the successful use of Basin RTM is the large amount of CPU time presently required for each simulation. The CPU time required during a run depends on the spatial dimensionality, spatial resolution and the number of processes considered (all of which can be chosen in Basin RTM). The typical number of CPU days required are seen in Table I-1.

With improvements in the algorithms and approximations we are making (contract # DE-AC26-00NT40689), these numbers could be reduced by factors ranging from 3 to 10. Also, IBM is expected to increase CPU speed in the next one to two years by a factor of 3. The information theory method of Chapter V for data/model integration will require many simulations for a given prediction and risk assessment. These computations can be done in a purely parallel fashion so that the IBM SP and anticipated parallel architecture will be ideal for these computations. We thus believe that the Basin RTM efficiencies we are developing and the advance of fast, parallel hardware will make the use of this technology a practical and valuable facet of a modern E&P effort.

D. Piceance Basin Database/CD-ROM

Through this project we have developed a relational database for the Piceance Basin (See Appendix C for details). We believe this database will be a valuable asset to exploration and production groups. In a follow-on project, we hope to advance this database and interface software so that it can be directly used for input into Basin RTM or into the information theory shell program incorporating Basin RTM as discussed in Chapter V.

The relational database contained in the accompanying CD-ROM will be completed in follow-on projects by adding missing information, proofing data entries, normalizing the structure of the data tables, and creating user-friendly data entry forms. The database will be designed so that new data can easily be added as exploration and development of natural gas reservoirs progress.

GIS coverage will be made for the Mesaverde Group in the Piceance Basin. GIS coverage will be made available so that operators in the basin can optimize their E&P programs and efficiently explore for and recover natural gas from unconventional tight Upper Cretaceous

reservoirs. GIS product development requires access to a comprehensive basin-wide dataset, which would be available in the new relational database described above. Although GIS coverage based on significant datasets exist in some companies, they are proprietary and thus generally not available to competitors or academic research groups. A combination of GIS with a comprehensive relational database that is openly accessible would reduce E&P costs by reducing the time and money each operator must spend to gather and evaluate data. The information generated by availability of this data to academic and other non-profit research groups will facilitate the discovery of U.S. resources and the development of new E&P technologies.

E. Economic Benefits

Establishing a steady, long-term, clean natural gas supply is key to the energy economy of the United States. This project provides three approaches to achieving this goal through exploration and production technologies based on the computer automated use of well log, seismic, geochemical and other data. These approaches are:

- Improve the prediction of reservoir location and characteristics so as to lower the cost of exploration for deep gas reserves.
- Identify compartments and, thereby, locate by-passed resources; and
- Make use of the billions of dollars of well log, seismic and geochemical data on U.S. basins which are presently under-used due to the cost of labor-intensive and often unreliable methods for interpreting well logs and geochemical data.

The economic value of these advances can be estimated as follows:

(a) The amount of natural gas remaining to be discovered is estimated to be 2,366 TCF in the U.S. and 25,790 TCF worldwide (AAPG 2000). These figures represent 72% of estimated ultimate recovery for gas in the U.S. and 93% of estimated ultimate gas recovery worldwide. If this project reduces the cost of finding and producing these reserves and thereby increases the producible fraction of this reserve by 10%, this yields a value of 710 billion dollars for the U.S and 8 trillion dollars worldwide assuming a price of $3.00 per MCF.

(b) A typical well log costs $1 per foot for a conventional suite of logs. Assuming there are about 6 million logs averaging 5,000 feet available today on U.S. basins and that this project ultimately makes use of 20% of these logs which would have otherwise gone unused or would have to be taken anew, implies a savings of 6 billion dollars.

(c) Our method could save investment dollars by more judicious choice of exploration well siting. To meet projected demands for natural gas, 420,000 exploration wells will need to be drilled in the next 15 years (NPC 1999). Assuming 1/4 will be deep wells (>16,000 ft) drilled at an average cost of 1 million dollars and 1/2 of these will be completed at an additional cost of 1 million dollars, a 10% improvement in well citing efficiency and log costs would net a savings of 16 billion dollars for that period.

(d) It is estimated that exploration in the next 15 years could cost 658 billion dollars in the U.S. (NPC 1999) and much more outside the U.S. If the methods developed here could save 10% of this, and we believe it easily could, this is a savings of 65 billion dollars in the U.S. over the next 15 years.

In summary, the total estimated savings for gas exploration in the U.S. would be 65 billion dollars and the total increased value from new reserves would be 710 billion dollars in the next 15 years. Also, the new production expected is 235 TCF; at the projected rate of

consumption of 31 TCF/year by 2015, this additional U.S. reserve alone could support domestic gas consumption for 7.5 years, adding stability to our economy.

II. THE BASIN RTM SIMULATOR

A. Overview and Comparison With Other Approaches

An overview of Basin RTM's capabilities is as follows. A complex network of geochemical reactions, fluid and energy transport and rock mechanical (RTM) processes underlies the genesis, dynamics and characteristics of petroleum reservoirs in Basin RTM (see Fig. I-1). Prediction of reservoir location and producibility lies outside the realm of simple approaches as noted in Sections I.B and C above. In order to develop a predictive capability for exploration and field development projects, LCG developed the quantitative simulator, Basin RTM. This simulator allows an E&P team to integrate all the relevant geological factors and RTM processes into an analysis (see Fig. II-1). As reservoirs are fundamentally three-dimensional in nature, Basin RTM is fully 3-D.

Basin RTM represents over 120 person-years of research and software development at LCG and its industry partners. It has resulted from collaborations developed with the petroleum industry, the Gas Research Institute and the U.S. Department of Energy as well as Oklahoma State University, Institut Français du Pétrole and the Indiana Geological Survey.

The RTM processes and geological factors accounted for in Basin RTM are outlined in Figs. I-1 and II-1. External influences such as sediment input, sea level, basement heat flux and tectonic effects are allowed to influence the internal RTM processes through conditions they impose at the boundaries of the sediment package as boundary conditions on the partial differential equations describing the RTM process. Within the basin, these RTM processes modify the sediment chemically and mechanically to arrive at petroleum and mineral reserves, fluid compartments and other internal features.

Basin RTM is based on our novel basin RTM model and sophisticated computer simulation algorithms. Basin RTM provides a platform for integrating all available geological data as suggested in Fig. II-1 using the framework provided by the laws of physics and chemistry in order to perform a case study or facilitate the choice of exploration/field development targets.

Available information on a basin can be divided into geological data and the physico-chemical laws and associated rate law parameters. The former make a simulation tailored to a specific basin. The physico-chemical information gives Basin RTM the power to predict the affect of RTM processes on reservoirs and other features of the evolving basin.

Basin RTM can be used to identify windows of time during which formations along a proposed migration pathway were open to migration, and not closed due to compaction, fracture closure or diagenetic cementation. Basin RTM can predict if and when a seal was breached due to natural fracturing or permeability-enhancing diagenetic reactions allowing some of hydrocarbons to escape (see Fig. II-1). In summary, as Basin RTM evolves a study area from the geological past to the present, it allows the E&P team to test conjectured scenarios on basin histories leading to the present-day location and characteristics of reservoirs. Basin RTM is so rich with detail of rock and fluid properties, that it predicts key reservoir producibility parameters in addition to reservoir location and overall geometry.

Because of its importance to both petroleum and geological sciences, fracturing has been studied by many researchers (see Pollard and Aydin 1988 and Lorenz and Finley 1991 for reviews). Fractures in areas subjected to bending are usually explained by associated extensional stresses (Friedman 1976). The existence of fractures in near-horizontal layers has been attributed to unloading (Currie and Nwachukwu 1974; Engelder 1987), high fluid pressure (Pollard and

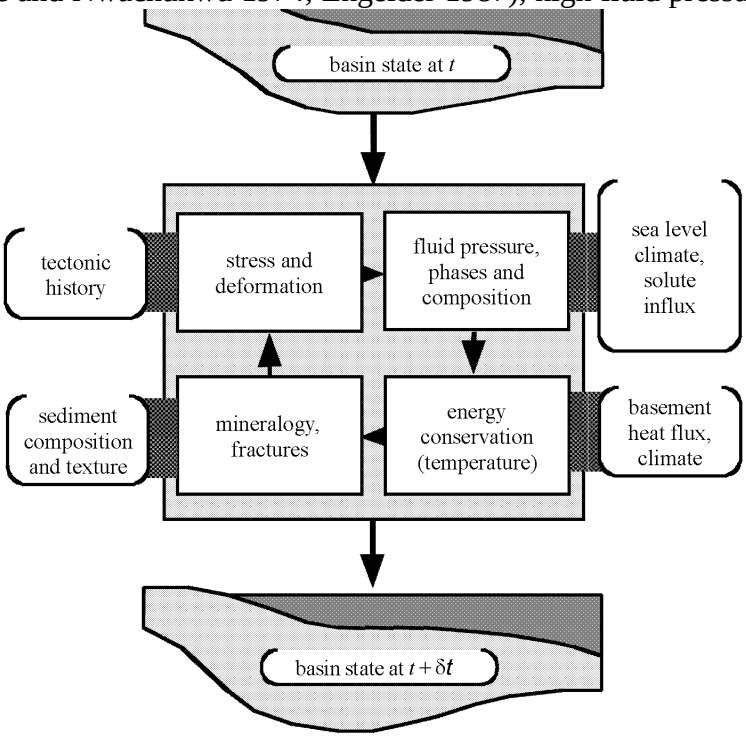

Fig. II-1 Schematic Basin RTM flow chart showing the interplay of geological data and the internal RTM processes in evolving a basin over one computational time step.

Aydin 1988; Ortoleva 1998) and anisotropic stress influenced by nearby geologic structures (Segall and Pollard 1983; Currie and Nwachukwu 1974). We believe that fracturing in near-horizontal or folded areas is due to a combination of the effects listed above. If the local fracture kinetics is well described by fracture growth/healing laws, a multi-process deformation model coupled to fluid flow and fracturing can be used to quantify the relative importance of these effects.

It is well documented that fracturing strongly depends on lithology (Segall and Pollard 1983; Lorenz et al. 1991; Fischer et al. 1995; Gross 1993; Wu and Pollard 1995; Hancock et al. 1984; Kulander et al. 1979). Although fracturing can occur in almost any type of rock, they are more common in brittle rocks (Mallory 1977). Furthermore, fractures in a brittle lithology commonly discontinue at the interface of more ductile lithologies (Engelder and Geiser 1980). Another observation is that fracture spacing is strongly dependent on bed thickness and lithology (Fisher et al. 1995; Wu and Pollard 1995; Gross 1993; Nickelsen and Hough 1967; Harris et al. 1960). However, a simple correlation between fracturing and bed thickness does not seem feasible because of the many factors operating such as fluid pressure, state of stress, neighboring lithology properties and tectonics.

Other basin models do exist and have been used to gain valuable insights into the petroleum system. However, the many strongly coupled basin RTM processes as suggested in

Fig. I-1 require a comprehensiveness and 3-D approach that goes far beyond these two- or three-process, typically 2-D, models (Maubeuge and Lerche 1993, 1994; Roberts and Nunn 1995; Wang and Xie 1998; Ungerer et al. 1990; Schneider et al. 1996; Luo and Vasseur 1996; Larson et al. 1993; Luo et al. 1998). To be effective, models must be fully 3-D to capture basin sedimentological geometry, fracture orientation, changing compression/extensional tectonic regimes, and other factors not included in these models. Nor are they comprehensive or fully coupled as in Fig. I-1.

By fixing the parameters of the mechanical laws and the basement subsidence/upheaval history, one can "fit" the state of fracturing in a given field. However, in another field such a single process model is likely to fail. The two fields likely had different histories of methanogenic overpressuring, original grain size and mineralogy, and the suite of other factors in Fig. I-1 that affect fluid pressure.

Purely mechanical models suffer from the same oversimplified approach. Several well-publicized mechanical models ignore the irreversible strain processes. Our studies show that these carry most of the effect of the lithologic control on fracturing. Furthermore, the various rheological parameters continuously change over the basin's history. These are also ignored in these models. Thus, they cannot distinguish between the behavior of seals and brittle reservoir rocks or distinguish whether fractures allow natural gas to be housed or led to its escape through what is now (and not during reservoir formation) a seal. Adherence to such models when a comprehensive, predictive model is available does not service the petroleum industry.

Fracture-mediated petroleum expulsion, migration, and escape from reservoirs are key aspects of the dynamic petroleum system. In most of the existing basin evolution models, it is assumed that rocks fracture when the fluid pressure exceeds a specified fraction of lithostatic stress (Maubeuge and Lerche 1993, 1994; Roberts and Nunn 1995; Wang and Xie 1998). This assumption essentially eliminates the dependence of fracturing on lithologic properties. In our studies, we find that fracturing strongly depends on the rock texture, i.e., mineral composition, grain size, porosity, etc. Another limiting assumption made in other studies is that there exists a simple dependence of porosity on effective stress (Maubeuge and Lerche 1993, 1994; Roberts and Nunn 1995; Wang and Xie 1998; Ungerer et al. 1990; Schneider et al. 1996; Luo and Vasseur 1996). This results in a very smooth porosity profile and once again, eliminates the importance of lithologic dependence of rock properties. In our approach, porosity is obtained by solving the mass balance equation for solids for rock deformation velocity computed using a multi-process, incremental stress rheology (see Section II.D below). Since, in our approach, the elastic and viscous parameters are functions of texture, porosity and stress evolution are strongly coupled and thereby computed self-consistently. As a result, shales usually have lower porosity, and higher least compressive stress than sandstones. The small grain size combined with low porosity results in very low permeability and thus these layers can form efficient seals. Furthermore, our results show that low shear viscosity/bulk viscosity ratio makes fracturing very unlikely in the absence of flexure or extreme overpressuring mechanisms like petroleum generation or fluid thermal expansion. Fracturing can occur in the absence of these factors when this ratio is high (as such rocks can sustain very low least compressive stress).

In other basin evolution simulators, fracture permeability is assumed to be isotropic. This can be attributed to the fact that, for an accurate description of fracture orientations, the full stress tensor must be known nor can irreversible (e.g., viscous-like and not purely elastic) behavior be ignored. Sufficiently accurate predictions of the characteristics of fracture networks were achieved with our unique 3-D, multiple deformation process basin mechanics model.

Another effect that is always disregarded is the interaction between the deformation/stress computation, and fracturing. It is true that rocks fracture due to the difference between the fluid pressure and the least compressive stress. But as fractures open, overall rock volume increases and fluid pressure in the fractures compresses the rock, increasing the compressive stress normal to the fracture plane. Thus, fracturing is a self-limiting process: firstly, as fractures open, they provide a pathway for fluid escape, and secondly, the volumetric strain caused by fractures increase the confining stress that reduces the rate of fracture growth.

Although one and two dimensional studies give hints about the dynamics of basin evolution, a three-dimensional basin simulator is necessary to take three-dimensional geometric effects into account. This becomes extremely important when fracturing is due mainly to flexure and the direction of tectonic compression/extension is changing over the basin's history. Fracture networks provide a pathway for fluid flow and, especially in a layered basin, fluids can move laterally. This can only be taken into account by a three-dimensional basin simulator with stress/deformation solver that can capture the nonplanar layers (notably, anticlines) and the strong variations in rheology from layer to layer (e.g., sandstones vs. shales or salt). To our knowledge, existing basin evolution simulators are mostly one or two dimensional (Maubeuge and Lerche 1993, 1994; Roberts and Nunn 1995; Wang and Xie 1998; Ungerer et al. 1990; Schneider et al. 1996; Luo and Vasseur 1996; Larson et al. 1993; Luo et al. 1998).

Although the history of temperature, sedimentation rate, and subsidence rate are among the most important parameters that effect the evolution of a basin, some basin evolution simulators start with a predefined grid (Schneider et al. 1996). In other words, two basins with the same final thickness and sediments but different time history are assumed to behave similarly. It is well known that overpressuring, a key factor in fracturing as well as deformation, correlates with sedimentation rate (Wang and Xie 1998; Ortoleva 1999). Also, in the classical flexure analysis the history of deformation and its relation to the lithologic properties is ignored although, present day flexure is often a poor indication of fracturing. If the rate of fracture development was very slow, then rock could deform slowly, and depending on viscosities there would be no fracturing. Flexure early in a sediment's continuous evolution, i.e., when it is poorly lithified or has inherent ductile behavior (organic rich shales, rock salt or anhydrates) can occur without fracturing. Therefore, the next generation of basin evolution simulators should not only be three-dimensional, but should also consider the history of sedimentation, tectonics and thermal influence on evolution.

Another limitation of previous models is the absence of shear failure. Only a few models consider the contribution of mechanical shear to rock failure (Luo et al. 1998; Larson et al. 1993). However, these models are limited to two dimensions. In our model, a Drucker-Prager-type failure function is used to build in a shear failure via a transition in rock viscosity. As the rock approaches failure, shear viscosity decreases. This feature extends the applicability of our basin simulator to fault formation problems.

Our model uniquely accounts for the changing rock rheological parameters that accompany the changing texture (e.g., grain size, mineralogy and porosity) and fracture properties. The bulk, shear and effective stress coefficients of the (assumed) isotropic rocks are computed using Berryman's composite medium theory (Berryman 1980, 1986). The shear and bulk viscosities are assumed in our approach to depend on grain contact areas and mineralogy, fitting specific formulas to geologic data from our laboratory basins. Thus, the mechanical and diagenetic modification of texture directly affects rheology which then is used to compute basin stress/deformation history using our extended incremental stress rheology (Bathe, Ramm, and

Wilson 1975; Snyder and Bathe 1981). This strongly coupled texture $\Leftrightarrow$ stress coevolution is unique to our approach. Our 3-D geomechanics integrates poroelasticity, nonlinear viscosity, pressure solution, gouge and fracturing in a self-consistently unified model.

In summary, our comprehensive, fully 3-D basin simulator is unique. Its inclusion of many RTM processes and full 3-D implementation underscores its role as a first of new generation of basin simulators.

Our Basin RTM model derives its predictive power from its firm basis in physical and chemical laws that govern the behavior of geological materials. This is in sharp contrast to purely correlative approaches such as porosity/depth curves or curvature analysis. These approaches derive their predictions from statistics that are weighted by available data. The data sampling is dictated from wells cited using classical exploration concepts. Fig. II-2a shows a correlation of permeability with curvature. With this data taken across the Piceance Basin, there is seen to be great uncertainty in this relation or with the rate of change of curvature (see Fig. II-2b) as computed with a reconstructed deformation history. This is because fracturing is a dynamic process, involving the competition between fracture opening and extension with the continuous deformation and cementation induced by the surrounding rocks. Thus, fracturing and the permeability/producibility derived from it are the result of the basin's detailed RTM process history. Fig. II-2c shows two typical paths of evolution of a material point in the permeability-curvature plane. As today's rock state is one point on such a trajectory, it is clear that there is little hope of finding a simple correlation for such properties.

Another classic exploration methodology is to map various properties across a study area by interpolation and extrapolation of data taken at selected points. The problem is that the available well data is usually sparsely distributed in ways which reflect drilling strategies. With our Basin RTM approach, such extrapolations are constrained with the laws of physics and chemistry and are not simple mathematical interpolations as in Fig. II-2.

In contrast to these and other classical exploration methods, our Basin RTM approach predicts over 100 properties at all points within the basin and shows how they change over the basin's history. These parameters include:

- stress tensor and rock deformation velocity (Tuncay, Park, and Ortoleva 2000a);
- fracture length, aperture and orientation statistics (Tuncay, Park, and Ortoleva 2000b);
- grain size, shape and mineralogy (Ortoleva 1994a, 1998; Meshri and Ortoleva 1990);
- pressure, saturation and composition of all fluid phases (Ortoleva 1994a, 1998);
- gouge (Ozkan and Ortoleva 2000; Ozkan, Tuncay, and Ortoleva 1998);
- rock mechanical and transport properties;
- temperature; and
- remaining amount and composition of kerogen (Payne 1998; Payne et al. 2000; Payne and Ortoleva 2001).

These parameters allow one to understand key aspects of the dynamic petroleum system including:

- the geometry and timing of seal formation and breaching;
- the geometry of migration pathways and the periods during which they were open;
- the location of compartments and their inner fluid phases and composition;
- directed petroleum migration and its time variations due to the changing directionality of dominant fracture sets;
- petroleum quality vs. CO_2, H_2S and other components;
- rock strength and *in situ* stress and their implied horizontal wellbore stability;

- rock lithification vs. friability; and
- extreme overpressure and underpressure.

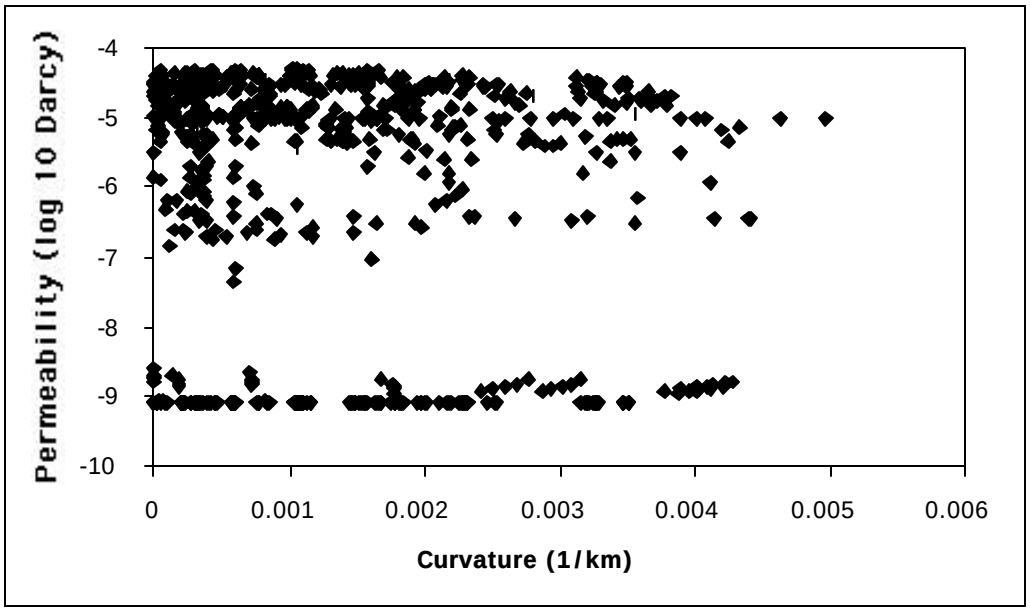

a)

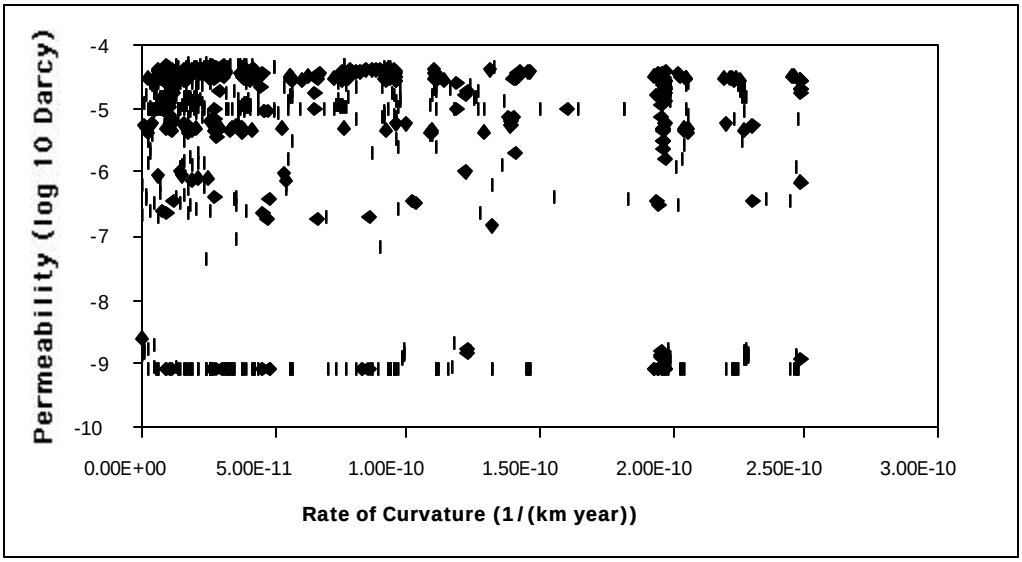

b)

Fig. II-2a,b Correlation of a) curvature and b) curvature rate with permeability shows little relation. Data here generated from a Basin RTM simulation of the Piceance Basin. Due to data shortage and selectivity of drilling sites associate with classical exploration strategies, such an unbiased correlation has never been done using observations.

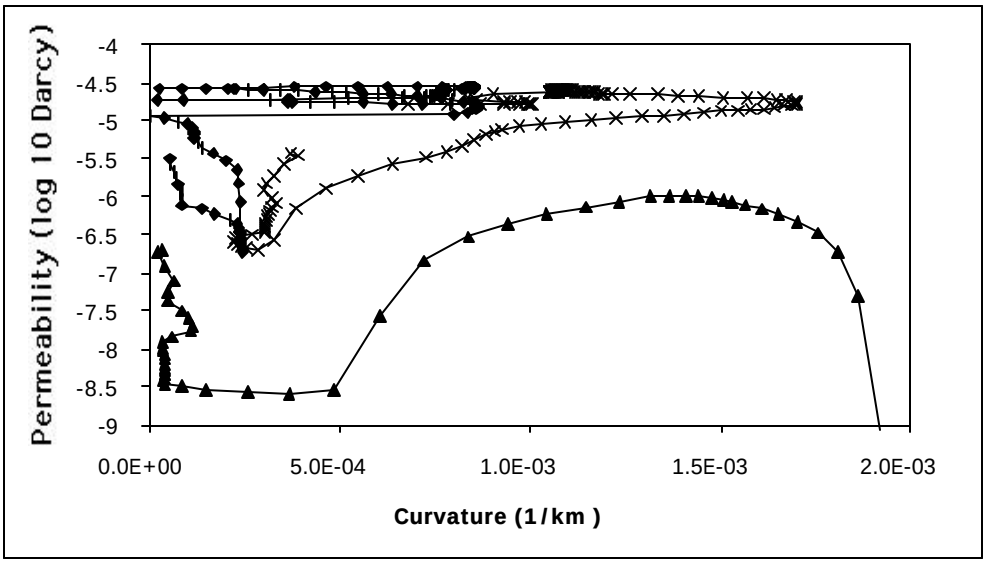

Fig. II-2c Shown is the typical trajectory of two material points in the permeability/curvature plane—it is little wonder why the producibility-curvature relation is poorly defined.

Having the power to predict these factors and reservoir characteristics will greatly assist in the development of economic exploration and field extension/infill drilling strategies. Our Basin RTM simulator is uniquely capable of predicting them at this time.

B. How Basin RTM Works

Basin RTM can predict reservoir producibility by estimating the effects on permeability and other reservoir parameters due to diagenetic reactions and fracture network statistics. The computations are made in a self-consistent way through a set of multi-phase, organic and inorganic, reaction-transport and rock rheological modules. Calculations of all effects are done self-consistently to preserve all couplings between processes (see Figs. I-1 and II-1). For example, the determination of temperature is affected by fluid transport, which, in turn, is affected by the changes of fluid pressure that arises due to temperature-dependent organic and mineral reaction rates. All such coupling relations between the full set of RTM processes as in Fig. I-1 are accounted for in Basin RTM.

Predictive power is diminished for less rigorous approaches that use statistical correlations. For example, in such methods, porosity history is often based on a formula relating it to mineralogy and depth of burial. However, porosity evolves due to the detailed stress, fluid composition and pressure, and thermal histories. These histories are different for every basin. Thus a simple correlation of porosity with depth and lithologic type does not exist in principle. Basin RTM avoids such problems by solving the fully coupled rock deformation, fluid and mineral reactions, fluid transport and temperature problems.

The interplay of geological and physico-chemical information in Basin RTM is suggested in Fig. II-3. Basin RTM evolves the system via a sequence of discrete time steps. In each incremental evolution step, Basin RTM advances the state of the system from a time t to a later time $t + dt$, a time dt closer to the present. In this forward modeling scheme, the system is evolved from an initial state (tens or hundreds of millions of years ago) to the present.

Two distinct operations take place simultaneously during each time interval dt. The geological information is used to 1) fix the input/output of energy and mass at the basin

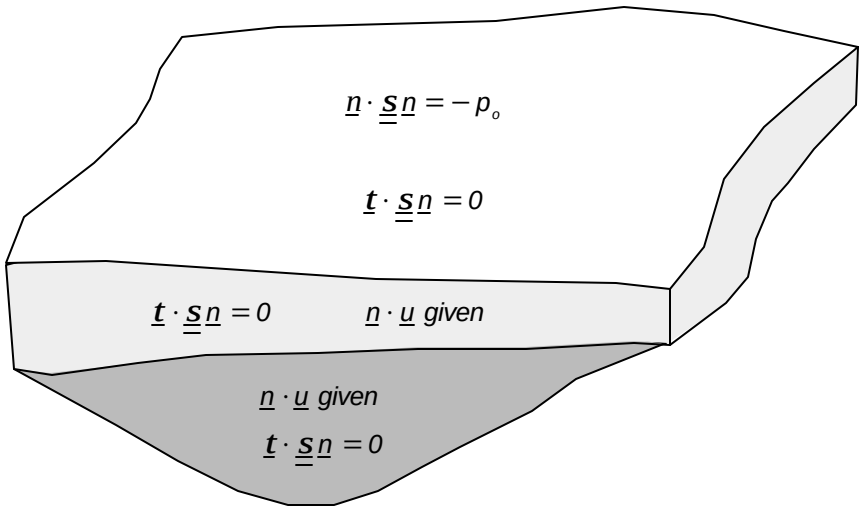

Fig. II-3 Conditions at boundary of basin simulation domain allow for imposition of ocean bottom or atmosphere pressure p_O and no tangential shear at the top ($\underline{t}$ being a unit tangent vector and $\underline{n}$ being an outward pointing unit normal vector with respect to the basin boundary). At the bottom the tectonic history fixes the evolution of the normal component of the deformation velocity $\underline{u}$ with a slip condition (and similarly for the sides—lightly shaded).

boundaries and 2) impose the tectonic history (i.e., the overall basin deformation) at the basin boundary. On the other hand, the physico-chemical processes are used to determine the evolution in *dt* of the spatial distribution of the local state. The latter describes stress, fluid properties, mineral content, rock texture, permeability, fracture characteristics and temperature. Finally, the size of *dt* is automatically chosen to maximize accuracy and computational speed.

Basin RTM geological input data is divided into four categories as shown in Fig. I-1 and II-1. The tectonic data gives the change in the lateral extent and the shape of the basement-sediment interface during *dt*. As suggested in Figs. II-1 and II-3, this data provides the conditions at the basin boundaries needed to calculate the change in the spatial distribution of stress and rock deformation within the basin. This latter physico-chemical calculation is carried out by a stress module that solves equations for incremental stress rock rheology and force balance (see Subsection II.D below).

The next type of Basin RTM geological data is that affecting the fluid transport, pressure and composition. This fluid data includes sea level changes, basin recharge conditions and the composition of fluids injected from the ocean, meteoric and basement sources. This history of boundary input data is then used by the hydrologic and chemical modules to calculate the evolution of the spatial distribution of fluid pressure, fluid composition and fluid phases within the basin. These physico-chemical calculations are based on single or multi-phase flow in a porous medium and on fluid phase molecular species conservation of mass (i.e., the reaction-transport equations). The physico-chemical equations draw on internal data banks for permeability-rock texture relations, relative permeability formulae, chemical reaction rate laws and reaction and phase-equilibrium thermodynamics.

The spatial distribution of heat flux imposed at the bottom of the basin is another geological input/control. This data as well as the temperature imposed at the top of the sediment pile (i.e., climate and ocean-bottom temperature) is used to evolve the spatial distribution of temperature within the basin during the time interval *dt*. This evolution is computed using the

equations of energy conservation formulae and data for mineral and rock thermal properties (conductivities and specific heats).

The sedimentation data provide the detailed textural characteristics such as grain size, shape, mineralogy, mode and organic texture of the sediment being deposited during *dt*. This history is automatically computed by Basin RTM using well log, seismic core and surface data. The physico-chemical laws and data are used to calculate the change of the spatial distribution of mineral and organic texture within the basin during *dt*. These physico-chemical calculations involve the rate laws for free face grain chemical kinetics, pressure solution and grain rotation or breakage, grain nucleation and the laws of kerogen chemical kinetic transformation. Also used are the laws of fracture nucleation, extension, aperture dynamics and the kinetics of cement infilling.

All this geological input data and the physico-chemical calculations are integrated in Basin RTM over many time steps *dt* to arrive at a prediction of the evolution history and the present-day internal state of the basin or field. In this way, the physico-chemical laws are used to translate the geological input data into a prediction of the changes of internal basin state and its evolution over the basin's history from its inception (or other chosen initial state) to the present.

C. Practicality and Uncertainty

The Basin RTM forward modeling approach is cost effective because the required geological input data is the same or less than that presently required in petroleum resource exploration and production approaches. In fact, all the geological data noted above is in common usage in the petroleum industry. It is derived from well logs, seismic data, general basin tectonic history reconstruction studies, vitrinite reflectance and other temperature history measurements, stress and strain indicators, core analysis and production data. As stress, strain, and the other data are predicted and captured as Basin RTM output, such data serve to test the accuracy of the Basin RTM predictions and, furthermore, to test some of the less well-constrained assumptions about thermal and tectonic history.

Most of the physico-chemical data was in our Basin RTM data base. Additional data for further calibrating our rheology, permeability and other laws was made available from the literature, industry reports and sensitivity analysis by comparing our predictions with observations

The physico-chemical computations provided a new way of integrating the presently-used geological data. These calculations put constraints on the interpretation of the geological data. For example, an interpretation of the geological data without the benefit of Basin RTM is subject to assumptions on the relative timing of events; estimates of the times of these events could be made more reliably when they are predicted based on the known rates of the underlying physico-chemical processes. As these rates are changing during basin history and as they are strongly coupled, they can only be computed via a comprehensive simulator. The only one which is presently available is Basin RTM.

Like any analysis of the geological data (including those presently used in other approaches), data integration and predictions using Basin RTM are subject to uncertainties. These are of four types:

- inaccuracy and spatial sparseness of the raw geological data;
- variations in interpretations of the geological data;
- inaccuracies in the physico-chemical data; and
- errors from the numerical simulation algorithms.

These discrepancies must be addressed in evaluating any predictions. First, Basin RTM itself serves as a tool for error analysis; by carrying out sensitivity studies, one can determine the contributions of uncertainties in the various input data on the predictions. This is accomplished by varying the less well-constrained geological and physico-chemical data and observing the consequences on the predictions of reservoir location and characteristics. The effect of the parameters controlling the numerical accuracy (time and space step, convergence criteria for iterative algorithms, etc.) can be similarly evaluated.

The enormity of the physico-chemical computations has historically made a Basin RTM approach seem unfeasible. However, the rapid improvements in processor speed, memory size and speed, combined with improved algorithms allow us to surmount this difficulty. Advances in modeling approaches also are bringing in great reductions in computational time. These include homogenization techniques whereby small spatial scale features can be embedded into large (basin or field) scale simulations. The latter is done in such a way that the particularities of the small scale features are not lost in a crude averaging (see Qin and Ortoleva 1994; Ortoleva 1998).

D. Stress and Deformation

Key elements of the dynamic petroleum system are compaction, fracturing and ductile deformation. These processes are strongly affected by basin stress history. Thus, good estimates of the evolution of stress distribution are required to predict these reservoir characteristics. As rocks fracture when fluid pressure exceeds least compressive stress, estimates of the time of fracture creation, growth, healing or closure, and orientation rely on estimates of the stress tensor distribution and its history. Simple estimates of least compressive stress are not sufficient for accurate predictions of fracturing and other properties. For example, least compressive stress can vary greatly between adjacent lithologies—a notable example being sandstones versus shale.

In Basin RTM, stress evolution is tightly coupled to other effects. For example, fracture permeability can affect fluid pressure through the escape of fluids from overpressured zones; in turn, fluid pressure strongly affects stress in porous media. For these reasons, the estimation of the history of the distribution and history of stress must be carried out within a basin model that accounts for the coupling among stress and processes as in Fig. I-1.

The strong coupling of deformation with the diagenetic, hydrologic and thermal processes is captured in Basin RTM using an incremental stress rheology. The specific rheology used in Basin RTM integrates all the strain mechanisms believed to operate in a basin. It has the form (Tuncay, Park, and Ortoleva 2000a; Ortoleva 1994a, 1998)

$$\underline{\underline{\dot{\varepsilon}}} = \underline{\underline{\dot{\varepsilon}}}^{el} + \underline{\underline{\dot{\varepsilon}}}^{vp} + \underline{\underline{\dot{\varepsilon}}}^{ps} + \underline{\underline{\dot{\varepsilon}}}^{fr} + \underline{\underline{\dot{\varepsilon}}}^{go} . \qquad \text{(II-1)}$$

Here, $\underline{\underline{\dot{\varepsilon}}}$ is the net rate of strain while the terms on the right give the specifics of four processes: poroelasticity (el), continuous viscoplastic (vp), pressure solution (ps), fracturing (fr) and gouge (go). Specific expressions for each term have been taken from the literature or newly developed for our RTM simulator (see III-A1 for the development of the rate of strain tensor due to fracturing).

Let us make some of the coupling more explicit. The poroelasticity rate of strain $\underline{\underline{\dot{\varepsilon}}}^{el}$ may be expressed in terms of stress $\underline{\underline{\sigma}}$, pressure p of the wetting fluid phase, and rock texture Q via

$$\underline{\underline{\dot{\varepsilon}}}^{el} = \underline{\underline{\underline{\underline{C}}}}^{-1}(Q)\frac{D}{Dt}\left(\underline{\underline{\sigma}} + \alpha(Q)p\underline{\underline{1}}\right) \qquad \text{(II.2)}$$

for fourth rank matrix of poroelastic coefficients $\underline{\underline{\underline{\underline{C}}}}$ and effective stress coefficient a; D/Dt represents a material time derivative measuring the rate of change of a tensor in time with respect to a local reference frame fixed to a translating, rotating material volume element. The texture Q represents a set of variables characterizing the mineralogy, shape, size, orientation and packing of the grains. In summary

$$\dot{\underline{\underline{\varepsilon}}}^{el} = \dot{\underline{\underline{\varepsilon}}}^{el}(Q, p, \underline{\underline{\sigma}}), \qquad \text{(II.3)}$$

illustrating the strong coupling between deformation, fluid properties and texture.

A direct coupling of mechanics and chemistry arises through pressure solution. Grain dissolution at stressed grain-grain contacts induces compaction and, thereby, contributes to $\dot{\underline{\underline{\varepsilon}}}^{v}$. The rate of this pressure solution contribution, $\dot{\underline{\underline{\varepsilon}}}^{(v,ps)}$, depends on the stress at grain-grain contacts and, hence, on the macro-stress $\underline{\underline{\sigma}}$, fluid pressure and texture. However, $\dot{\underline{\underline{\varepsilon}}}^{(v,ps)}$ should also depend on the composition of the (assumed single-phase) pore fluid. The latter may be characterized by the set of concentrations $c = \{c_1, c_2, \cdots c_N\}$ for the N pore fluid species system; hence, $\dot{\underline{\underline{\varepsilon}}}^{(v,ps)}$ depends on $\underline{\underline{\sigma}}$, Q, p and c.

As the present theory is macroscopic, the variables describing fractures are considered to be part of the texture Q. This assumes that the length scale on which the phenomena of interest vary is much greater than the fracture length or inter-fracture spacing. Otherwise one must treat fractures individually, an approach that is not viable for basin-scale modeling. With our macro-textural description, one must allow for the potential influence of the fracture variables on rock mechanical and other properties.

One expects that $\dot{\underline{\underline{\varepsilon}}}^{(v,j)}$, j=poroelasticity, viscosity, pressure solution, fracturing, gouge, etc., should, in general, depend on all the aforementioned variables $(\underline{\underline{\sigma}}, Q, p, c)$, as well as absolute temperature T. With this,

$$\dot{\underline{\underline{\varepsilon}}}^{v} = \sum_{j=1}^{N_d} \dot{\underline{\underline{\varepsilon}}}^{(v,j)}(Q, \underline{\underline{\sigma}}, p, c, T). \qquad \text{(II.4)}$$

The dependency of the $\dot{\underline{\underline{\varepsilon}}}^{(v,j)}$ on the indicated state variables may be nonlocal in time. For example, in the case of poroelasticity, $\dot{\underline{\underline{\varepsilon}}}^{(v,pe)}$ depends on the time-derivative of effective stress. Therefore, the $\dot{\underline{\underline{\varepsilon}}}^{(v,j)}$ may be functionals of their arguments that can, in principle, sample the state variables in some finite volume of space-time. The dependence of the strain rates on state clarifies the central role of incremental stress theory (Ortoleva 1994a, 1998; Tuncay et al. 1998, 2000a; Tuncay and Ortoleva 2001a; Rice 1975, 1992; Sakrani 1996; Zienkiewicz et al. 1974) in integrating all the RTM basin processes into a unified model. It is the coupling allowed by this integration that underlies many key basin phenomena from fault dynamics to episodic fluid flow, seal formation and overpressure.

To complete the incremental stress formulation, explicit expressions for the rate functions $\dot{\underline{\underline{\varepsilon}}}^{(v,j)}(Q, \underline{\underline{\sigma}}, p, c, T)$ are required. For $\dot{\underline{\underline{\varepsilon}}}^{(v,ps)}$, for example, these can be obtained through geometric considerations of the texture variables and the rate of grain shortening from pressure solution (see Dewers and Ortoleva 1994a, and Ortoleva 1994a, 1998).

The total rate of strain $\dot{\underline{\underline{\varepsilon}}}^{v}$ is defined via

$$\dot{\varepsilon}_{ii'} = \frac{1}{2}\left(\frac{\partial u_i}{\partial x_{i'}} + \frac{\partial u_{i'}}{\partial x_i} \right). \qquad \text{(II.5)}$$

The six independent components of the symmetric second rank tensor equation (A.3) must be supplemented with three additional equations so that the three deformation velocity components $\left(\underline{u} = u_1, u_2, u_3\right)$ can be determined. The required condition arises from force balance:

$$\sum_{i'=1}^{3} \frac{\partial \sigma_{ii'}}{\partial x_{i'}} + f_i = 0 \qquad \text{(II.6)}$$

for body force f_i which, for gravity, is given by

$$f_i = g \rho_m \delta_{i3}. \qquad \text{(II.7)}$$

Here g is the gravitational acceleration, ρ_m is the mass density, and the 3-direction is upward.

The above formulation must be augmented with equations of texture dynamics and fluid mass and energy conservation (the latter to fix T). With this, our model provides a complete theory of basin dynamics when the equations are solved subject to the boundary conditions imposed by the overall tectonics and by the surfacial fluids (i.e., ocean bottom and atmospheric pressure).

Effects such as strain hardening or weakening are accounted for in the present model via the coupled dynamics of texture and stress. The differential equations of texture evolution introduce the time delays (memory) that make our rheology capture hardening or softening. The latter properties are reflections of texture, i.e., hardness/weakness is a unique function of texture but not of stress. Thus, rock rheology depends on texture which, via the evolution equations of the latter, depends on the history of deformation. In addition to the coupling of deformation to other phenomena through the incremental stress formulation, there are numerous indirect couplings. For example, rock properties such as permeability, multi-phase flow parameters, reactive grain surface area and thermal conductivity depend strongly on texture. As the latter is affected by stress and deformation, a complex network of coupling relations is thereby expressed. For further discussion of the consequence of this network, see Ortoleva 1994a,b, 1998; Tuncay, Park and Ortoleva 2000a,b; Ozkan, Tuncay and Ortoleva 1998; and Dewers and Ortoleva 1994b.

The boundary conditions implemented in the Basin RTM stress module are indicated in Fig. II-3. They allow for a prescribed tectonic history at the bottom and sides of the basin. This data is input as a history of rock velocity at these boundaries. This type of geological input data is obtained through the sedimentary history input data by Basin RTM and directly input by the user from an analysis of the overall tectonics of the basin. At the simulation domain sides and bottom the tangential shear are set to zero. This avoids artificial interference with the natural dynamics there. Normal stress at the top of the basin is set to ocean bottom or atmospheric pressure. Tangential shear on the top is also set to zero under the assumption that the shears imposed by ocean currents may be neglected. As with any simulation of this type, care must be taken not to introduce artifacts by choosing system boundaries and boundary conditions carefully.

The boundary conditions in the Basin RTM stress module allow for the full range of tectonic scenarios to which a basin is subjected. These include complex histories of subsidence and uplift, compression or extension, and their variation along the basin periphery and basement-

sediment interface. These features make the Basin RTM 3-D stress and deformation module a powerful tool uniquely able to capture the interplay between rock deformation, hydrology diagenesis and heat flow.

E. Dynamic Fracture Network Statistics Module

A key to the reservoirs of interest in this project is the statistics of the fracture network. We have developed a model of the probability for fracture length, aperture and orientation (Tuncay, Park, and Ortoleva 2000a,b). The model predicts the evolution of this probability in response to the changing stress, fluid pressure and rock properties as the basin changes. The fracture probability is used to compute the permeability tensor. The latter affects the direction of petroleum migration, information key to finding new resources. It is central to planning infill drilling spacing and likely directions for field extension. It is key to the design of horizontal wells and the optimum rate of production in stress-sensitive reservoirs. Finally, the predicted distribution of fracture network statistics across a field is a necessary input to reservoir simulators used to optimize production.

The dynamics of the fracture network in our model is based on a statistical representation. For example, consider a set of fractures of length L with normal $\underline{n}$ for a 3-D spectrum of normal orientations. Then the rate of change for L in the rock-fixed frame takes the form

$$\frac{dL}{dt} = R(L, a, p, Q, \underline{\underline{s}}) \tag{II.8}$$

where the fracture extension rate R depends on the normal stress s, the wetting phase fluid pressure p and the texture Q of the surrounding rock, and a is the aperture of the $\underline{n}$-fracture. A similar equation for the fracture aperture is developed (see Tuncay, Park and Ortoleva 2000b for further details).

Let h' be the number density of sites at which fractures may nucleate. By definition of the undeformed rock $h' = h$ (h being the original, depositional value of h') but h' can differ from h due to changes in rock texture from diagenesis or mechanical processes. In the simplest case where fracture nucleation sites are not created or destroyed, h' obeys the conservation equation $\partial h'/\partial t + \nabla \cdot (h' \underline{u}) = 0$. In a macrovolume element of volume V there are Vh' fractures and hence a fracture void space $Vh'\pi L^2 a$ where a and L are the aperture and length(radius) of the assumed penny-shaped fractures, respectively. To compute the dilatation, we focus on a fixed volume V_m of solids and follow its change in a time dt. The volume of the unfractured rock V_{unfr} is related to V_m and the porosity ϕ_m of the unfractured rock via $V_{unfr} = V_m + \phi_m V_{unfr}$. Hence, $V_{unfr} = V_m / (1 - \phi_m)$. The total volume V of the sample of rock containing V_m is then

$$V = (1 - \phi_m)^{-1} V_m + V\Delta \tag{II.9}$$

where $\Delta = h'\pi L^2 a$. With this, the volume of rock $V(t)$ at time t for fixed volume of solids V_m (considered incompressible and not to expand thermally or react) is given by

$$V(t) = V_m (1 - \phi_m)^{-1} (1 - \Delta). \tag{II.10}$$

Noting that

$$tr\underline{\underline{d}}^{(fr)} = \lim_{dt \to 0} \frac{V(t + dt) - V(t)}{V(t)\, dt} \tag{II.11}$$

one obtains

$$tr\underline{\dot{\varepsilon}}^{(fr)} = [1-\Delta]^{-1}\frac{D\Delta}{Dt} \tag{II.12}$$

where *D/Dt* is the material derivative, i.e., the derivative in the reference frame fixed to the solids.

The tensor character of the fracture mediated deformation is related to the directions of each fracture through its normal $\underline{n}$ to the fracture plane. Consider the expression

$$\dot{\varepsilon}_{kl}^{(fr)} = [1-\Delta]^{-1}\frac{D}{Dt}(\Delta n_k n_l). \tag{II.13}$$

Here *D/Dt* represents a material time derivative; however, now, it also must account for the rotation of the fracture normals as they change direction with flexure, shearing or other deformation. Note that the trace of this expression agrees with the earlier result for the dilatation. Finally, this expression agrees with simple cases wherein all fractures are parallel.

In our model, a finite (but representative) number of fracture orientations is accounted for. We use the fracture kinetics formulation of Ortoleva (1994a), and Sonnenthal and Ortoleva (1994). However, here we replace the least compressive stress in the formulation by the stress component normal to each fracture plane. This allows calculation of fracture length and aperture for each fracture orientation. For example, if we assume that only vertical fractures can occur as for a one dimensional problem, since the stress component normal to any vertical plane is the same because of the symmetry, an isotropic fracture network develops. In three dimensional problems, our proposed algorithm has the power to predict a complex fracture network with preferential orientations dictated by the structure of the stress tensor.

Since the fracture network is well defined, the anisotropic fracture permeability can be calculated approximately. The anisotropic fracture permeability of a fracture network consisting of a single fracture orientation is given by

$$\kappa_{ij}^{fr} = \lambda(\delta_{ij} - n_i n_j) \tag{II.14}$$

where $\underline{n}$ is the unit normal to the fracture plane and $\underline{\underline{K}}^{fr}$ is the fracture permeability. The parameter λ can be approximated by

$$\lambda = \beta\phi_{fr}\frac{a^2}{12}. \tag{II.15}$$

Here β is a factor accounting for the connectivity of fractures. For large fracture lengths and dense networks β approaches unity whereas for small fracture lengths and low fracture densities it vanishes (Oda 1986). Oda (1985, 1986) proposed that this coefficient should be a function of a dimensionless second order tensor of fracture geometry. He called this tensor the fabric tensor (Oda 1982). A discussion of this factor can be found in the papers of Oda (1985, 1986). In this study β is taken as unity. We assume that the total fracture permeability is obtained by summation of fracture permeabilities for all orientations and statistical classes multiplied by the fracture porosity which has been proposed previously by Chen et al. (1999). It is assumed that fluid flow is slow and the disturbance at fracture intersections is negligible. Summation is inadequate when the fracture density is lower than the percolation threshold (Berkowitz 1995; Odling 1992; Bour and Davy 1998). Another limitation is due to the surface roughness of fractures. In this study fracture aperture is assumed to be constant in a particular fracture. The spatial distribution of fracture aperture alters the fracture permeability. Waite et al. (1998) measured water flow through a sinusoidal fracture to compare sinusoidal flow with parallel plate flow. Their experimental and numerical results showed that a sinusoidal fracture has a significantly lower permeability and for the sinusoidal geometry the effective aperture is very

close to the minimum value of the normal aperture. Thomson and Brown (1991) showed that the directional nonuniformities in the fracture surface are more important than the degree of surface roughness. Therefore equation (II.15) should be viewed as a simple fracture permeability tensor to approximate dense fracture networks with relatively smooth fracture surface. Note that the fracture permeability tensor is obtained by post processing the fracture network characteristics. We refer to Tuncay, Park and Ortoleva (2000b) for further details.

Figs. II-4, 5, and 6 show the capabilities of our dynamics statistical fracture network module. Episodic fracturing of a seal due to volume increasing oil generation is shown in Fig. II-4. Oscillatory behavior is a result of cyclic fracturing of the seal driven by petroleum generation. After 470 My the cyclic petroleum expulsion ceases and the pressure, oil saturation fracturing and other variables show a more steady behavior. Fracture permeability profile sequence illustrating the fracture front moving through the seal (between 2450 and 2700 meters). Overpressuring of oil and water phases primarily due to oil generation creates a fracture front moving upward through the seal. Once the overpressure is released, the fractures close, which in turn results in descent of the fracture front and overpressuring restarts. This cycle continues until the oil generation rate slows down, or the seal remains fractured due to tectonic effects (not included here) (Tuncay, Park and Ortoleva 2000a).

Fig. II-5 shows the relationship between porosity, fluid flow, and fracture network. Higher porosity regions (in the lower-right and upper-left corners) and the fracture length (contour lines) arose due to the deformation created by differential subsidence. Both stress field and fracturing are strongly affected by rock composition and texture. The arrows indicate fluid flow toward the region of increasing porosity (lower-right) and through the most extensively fractured shale (Tuncay, Park and Ortoleva 2000b).

Fig. II-6 illustrates the lithologic dependence of fracturing. Changing sediment properties, stress and fluid pressure during the evolution of the basin result in dynamic fracture patterns, which in turn significantly affect the anisotropy of fracture permeability. If the enhanced permeability from fracturing is significant, it can direct the flow of petroleum; understanding such occurrences in the past, therefore, can be important for identifying reservoirs in presently unlikely structural and stratigraphic locations.

In Fig. II-7, Basin RTM results show fault generated fractures and their relationship to the creation of fracture-mediated compartments and flow. This system shows the interplay of stress, fracturing and hydrology with overall tectonism—features which give Basin RTM its unique power.

F. Other Process Modules

We have created modules each of which computes the effects of a given class of processes as suggested in Figs. I-1 and II-1 The sedimentation/erosion history recreation module takes data at user-selected well sites on the age and present-day depth, thickness and lithology and creates the history of sedimentation or erosion rate and texture (grain size, shape and mineralogy) at all times over the basin history. An example of erosion is shown in Fig. II-8. The multi-phase and kerogen decomposition modules add the important component of petroleum generation, expulsion and migration to Basin RTM simulations (Figs. III-4). Other modules calculate grain growth/dissolution at free faces and grain-grain contacts (e.g., pressure solution). Finally, the evolution of temperature is determined from energy balance. All physico-chemical modules are based on full 3-D, finite element implementation. As with the stress/deformation module, each

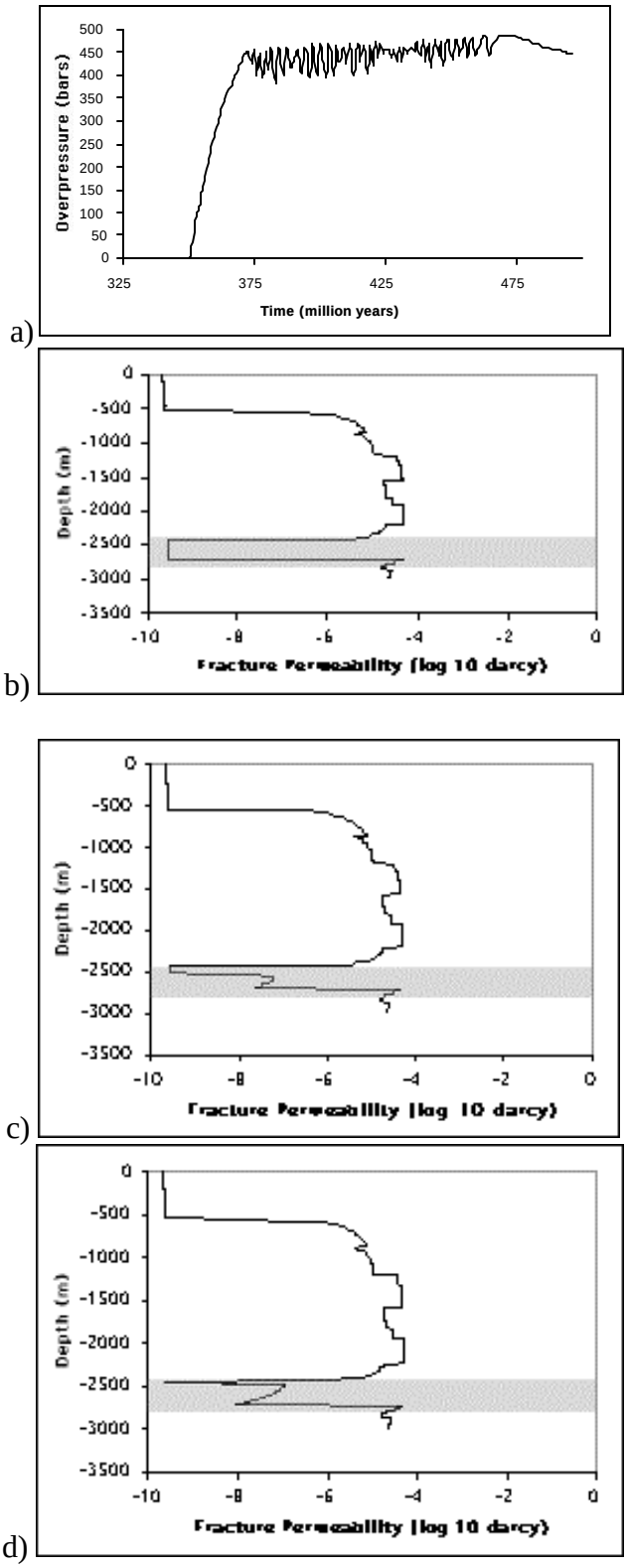

Fig. II-4a,b,c,d a) Evolution of overpressure at the bottom of the Ellenburger Formation. Overpressuring starts around 350 million years into the simulation, when fractures in the layer above the source rock disappear.

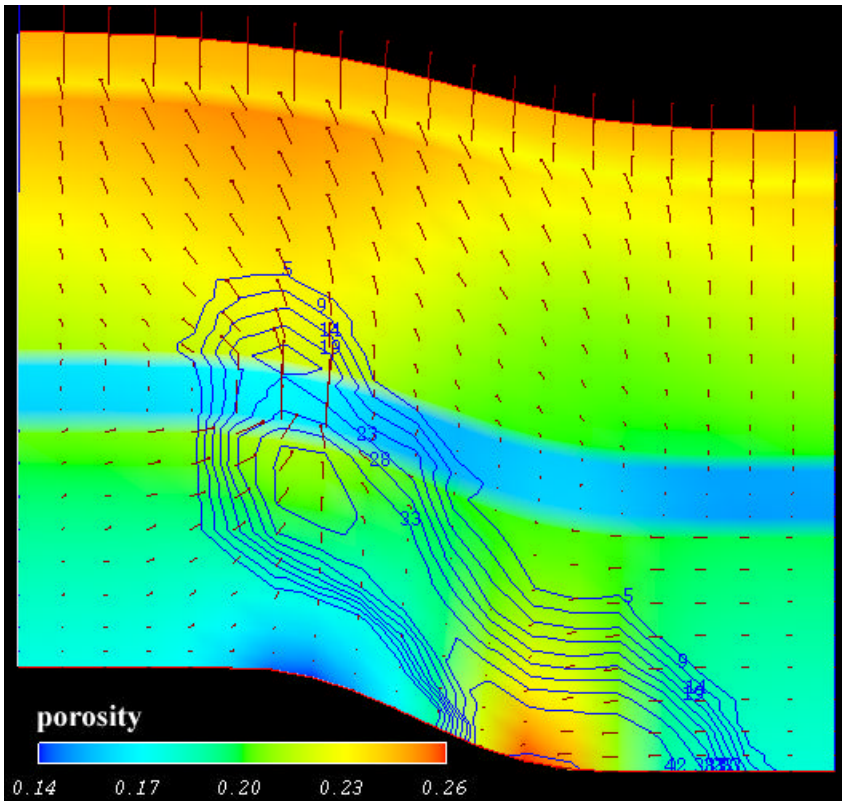

Fig. II-5 Cross-section of a 2-D, 5x2.5 km system subjected to differential subsidence after 5 My of simulation. The coloring indicates porosity and shows differences between the four lithologies; the shales (low porosity) are at the middle and top of the domain. Higher porosity regions (in the lower-right and upper-left corners) and the fracture length (contour lines) arose due to the deformation created by differential subsidence. Both stress field and fracturing are strongly affected by rock composition and texture. The arrows indicate fluid flow toward the region of increasing porosity (lower-right) and through the most extensively fractured shale (Tuncay, Park and Ortoleva 2000b).

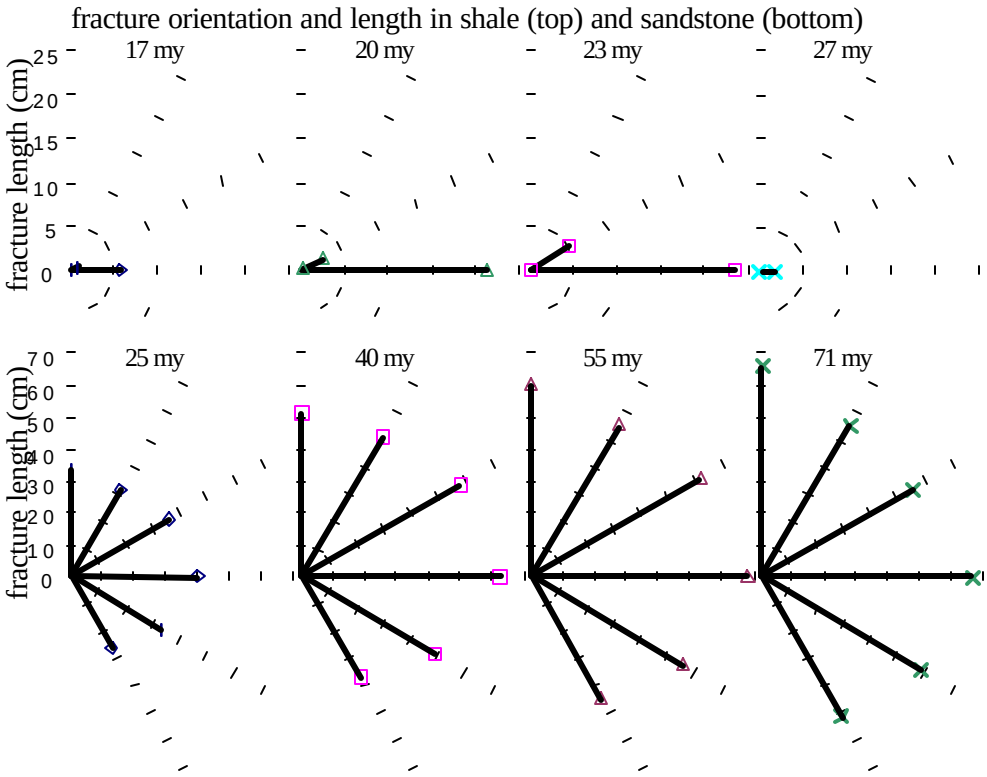

Fig. II.6 Predicted fracture orientations and lengths in a shale (top) and a sandstone (bottom) showing the lithologic dependence of fractures .

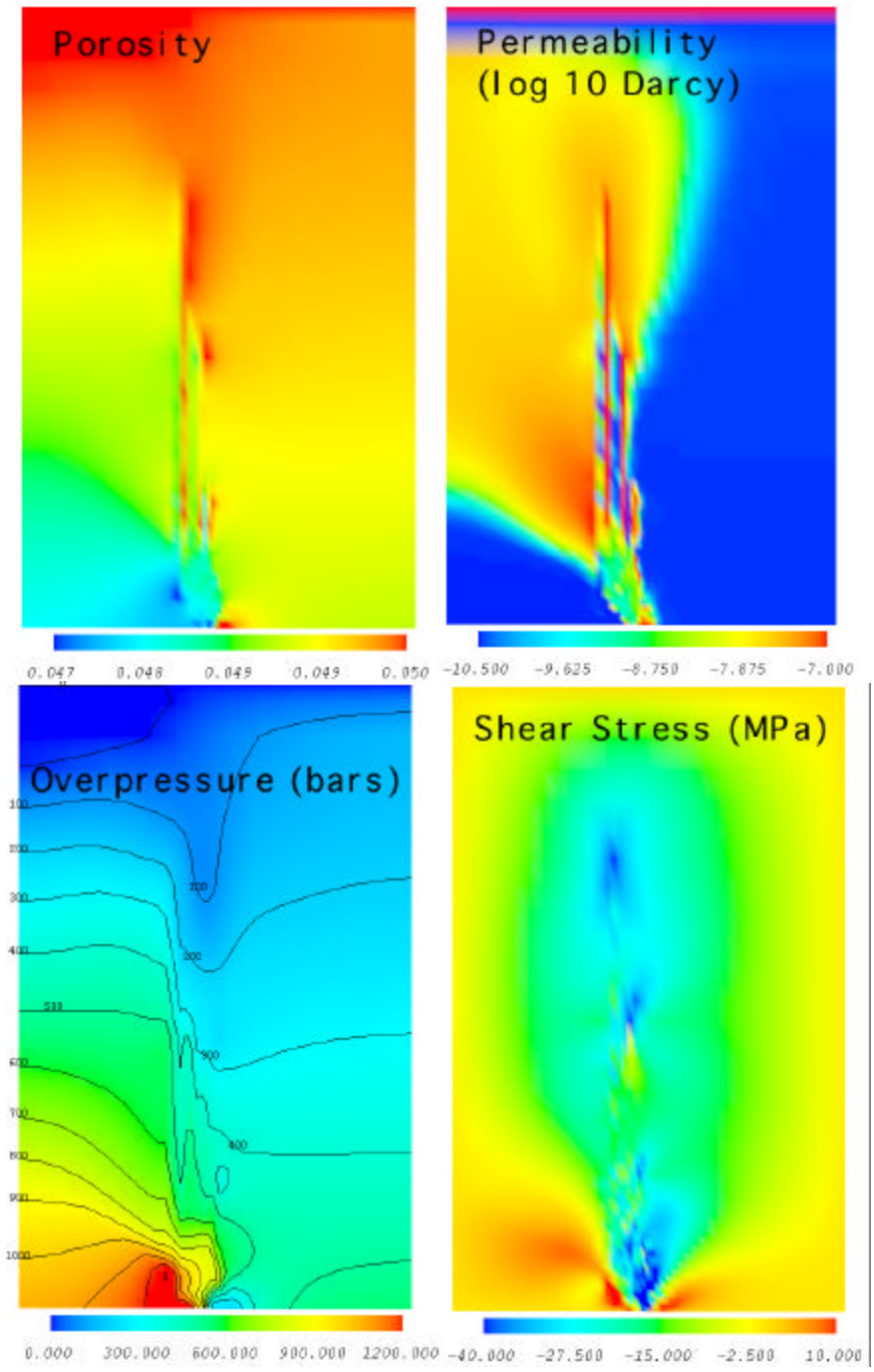

Fig.II.7 The computational domain (initially consisted of homogeneous intact granite) is 6 km by 9 km in cross section. The velocity of vertical movement on the right side is 1 km / million years. Note the stress concentration that develops at the fault tips in association with upward growth. Broken grain-grain contacts increase permeability and significantly alter fluid pressure and fluid flow which in turn affects the rock behavior through the effective stress principle. The branching and stress heterogeneity are self-organized, arising through the coupling of RTM processes accounted for in Basin RTM.

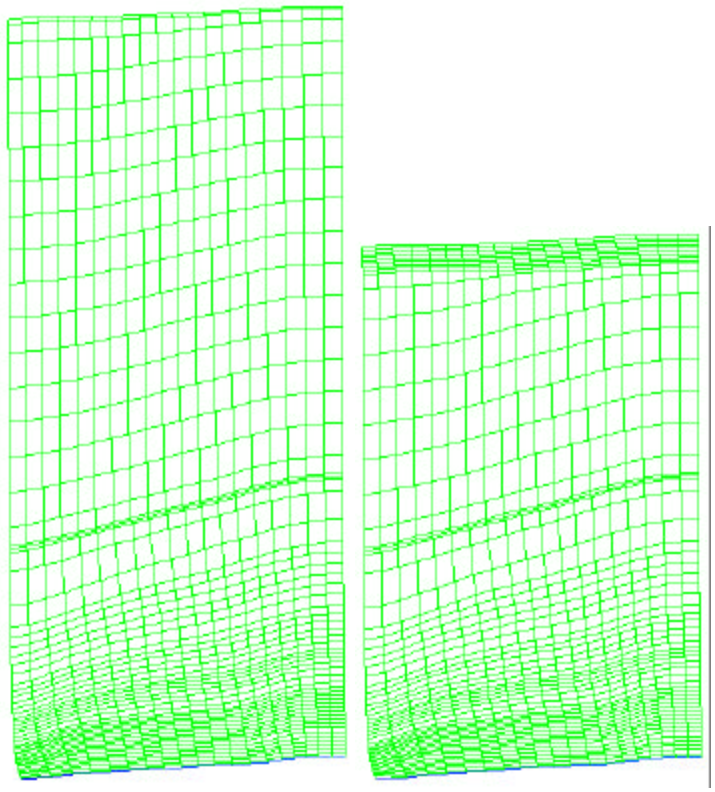

Fig. II-8 Finite element grid at a) 9 Ma and b) 7. Note the grid is adapted to lithologic layers. The fine mesh at the middle is because of the first erosion period between 63.5 and 60.5 Ma. Erosion is a first order factor that should be taken into account in Rocky Mountain Basins (see Section III-D for details on this simulation).

III. EVALUATION OF BASIN RTM VIA PICEANCE BASIN STUDY

A. Overview

The Rulison Field, located near the center of the Piceance Basin, is the focus of our modeling study. The data used for these Piceance Basin tests is summarized in Appendices A-C and a preliminary basin scale database is contained in an accompanying CD-ROM. Basin scale data has been collected from published reports and our industry and institutional contacts; data on the Rulison Field has come from Barrett Resources and DOE reports on the MWX site.

There were a number of overall objectives for the Basin RTM simulations. We wanted to show that Basin RTM could predict features such as location, geometry and characteristics of fracture zones and compartments, over- and under-pressuring, permeability distribution, in situ stress and controls on fracture zone existence and character. The latter controls include overpressuring, flexure and proximity to source rock. A second general motivation was to determine how the use of Basin RTM could be made more practical for the industry; e.g. how we could make the preprocessing of input data more efficient and how the output of Basin RTM could be made easier to interpret and yield practical E&P guidance. This issue is addressed in Chapter V. The importance of the spatial dimensionality of the simulations was also investigated. The question addressed was to what degree can one carry out one (vertical) dimensional simulation to avoid the computer time expenditure required for 2-D and 3-D Basin RTM runs.

B. Piceance Basin and Rulison Field Overview

Rulison Field is located near the center of the Piceance Basin (Figs. III-B1 and B2), mostly in T.6S. and R.94W. The production trend parallels a low-relief NW striking anticline (indicated by the closed 1900 ft. elevation contour in Fig. III-B1) and crosses the depositional trend of fluvial meander belt reservoir sands at right angles (Hoak et al. 1995). Subtle structural curvature of Upper Cretaceous strata in the Rulison Field is cited as causing sufficient permeability enhancement to allow commercial gas production from tight gas sands in the Mesaverde Group. Natural fractures, which trend EW and WNW at an oblique angle to the anticline (Hoak et al. 1995), presumably dilated with flexure and provided the improved permeability necessary for commercial gas production (Lorenz and Finley 1991).

C. 1-D Rulison Field Study

1-D simulations are significantly faster than 2-D and 3-D simulations, which greatly facilitates troubleshooting, and they provide useful preliminary predictions. We sought to determine if 1-D simulations themselves could be useful in the E&P context despite the expected difficulties due to errors in lateral stress associated with flexure and other structural effects. 1-D simulations were run to check for problems with vertical grid resolution, convergence, calibration, and input data that might cause the computations to be unacceptably slow or incomplete and to assure that this data was free of transcription or other errors. The location of wells used for 1-D simulations is shown in Fig. III-C1.

Fig. III-C2 shows gas saturation, overpressure (bars), maximum fracture length attained (cm), time of maximum fracture attained (75 million years is the present day), and permeability (log Darcy) for 6 well locations indicated in Fig. III-C1. The maximum fracture length attained is an indication of whether or not fractures had occurred at any time during the past. This result appears to correlate well with the observations of Finley and Lorenz (1988) shown in Fig. III-C3 for the frequency of mineralized fractures in cores from the MWX site. Agreement is seen in that both show intense fracturing in coastal interval sandstone and less in the immediately overlying

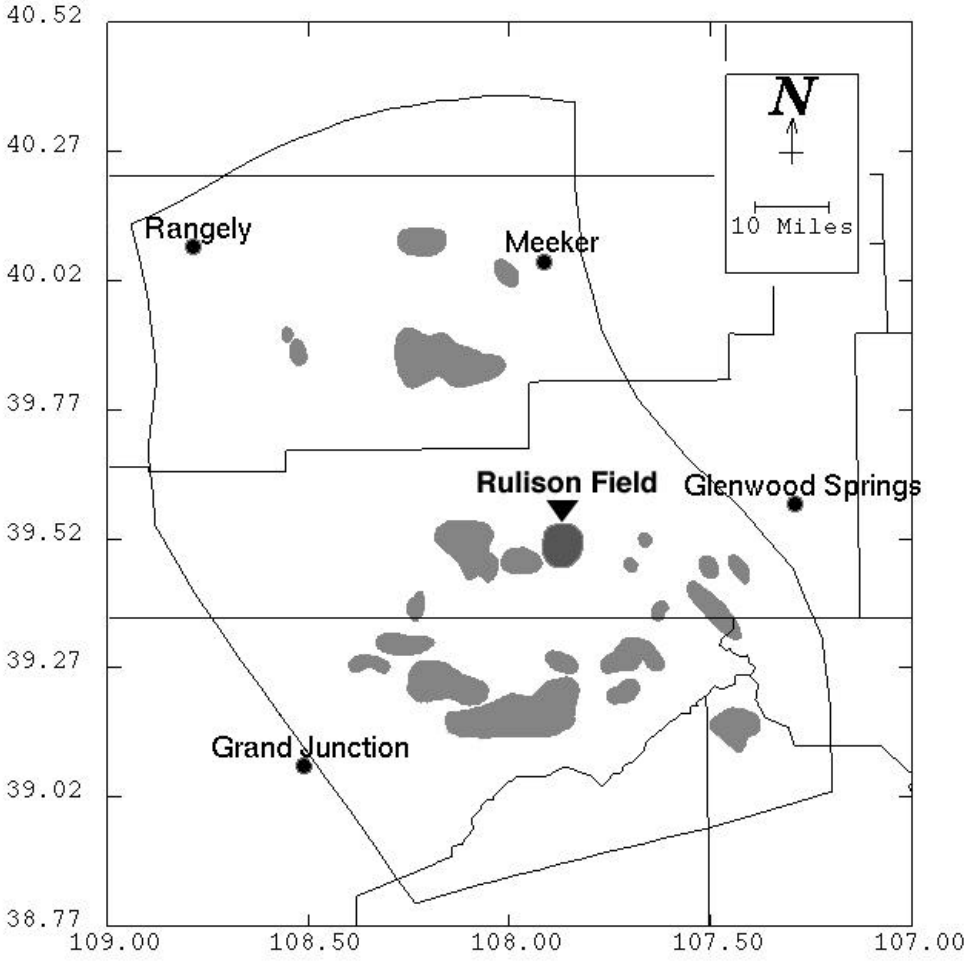

Fig. III-A1 Domain for our Piceance Basin simulation study. Shaded areas are gas fields. Rulison Field, located near the center of the domain, was the site chosen for field scale simulation.

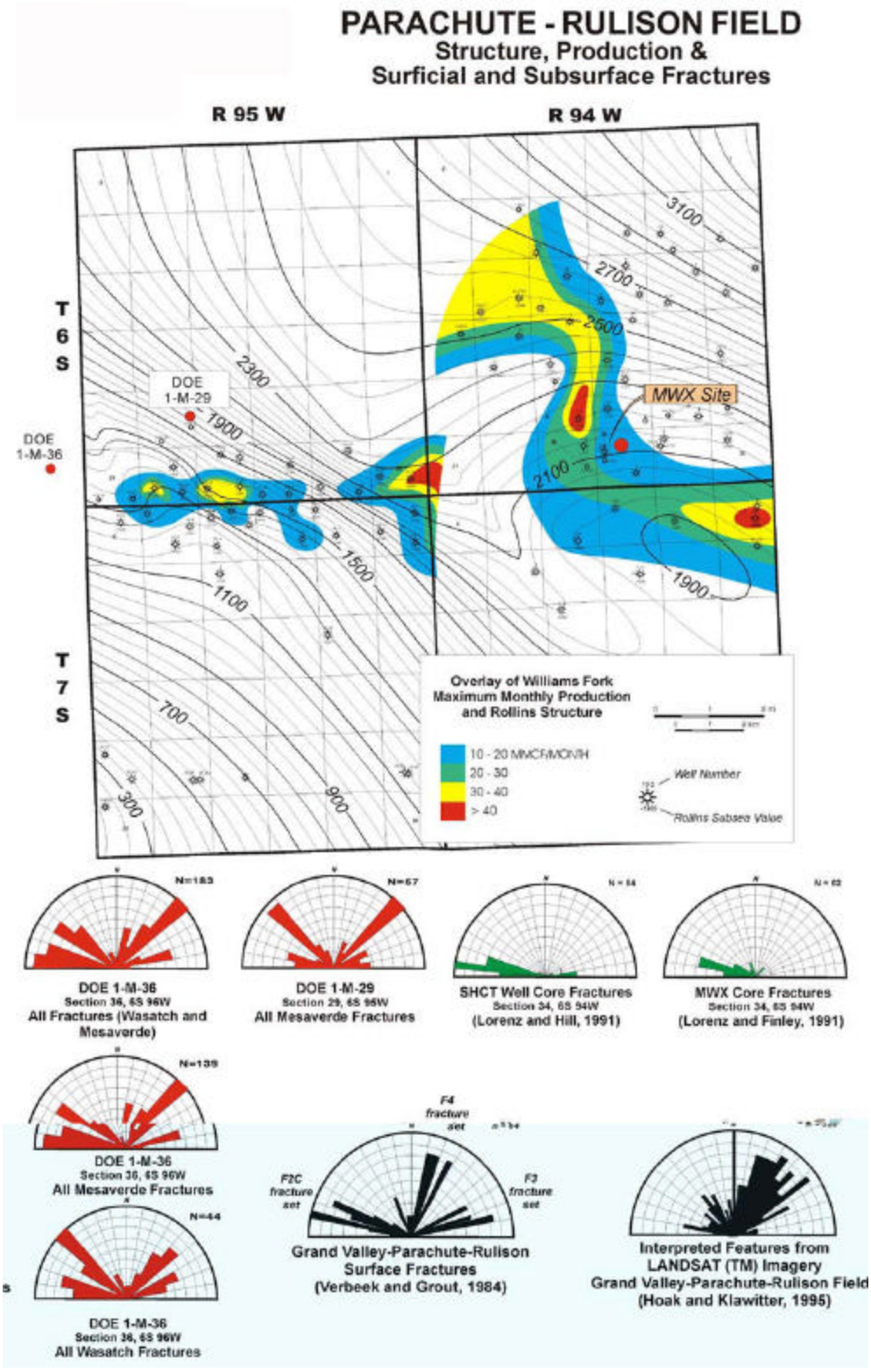

Fig. III-B1 Map showing structure and production trend for the Rulison Field (R.94W.). Production in R.95W. is from the Parachute Field. Rose diagrams show fracture trends in the mapped area (from Kestrel Geosciences, LLC).

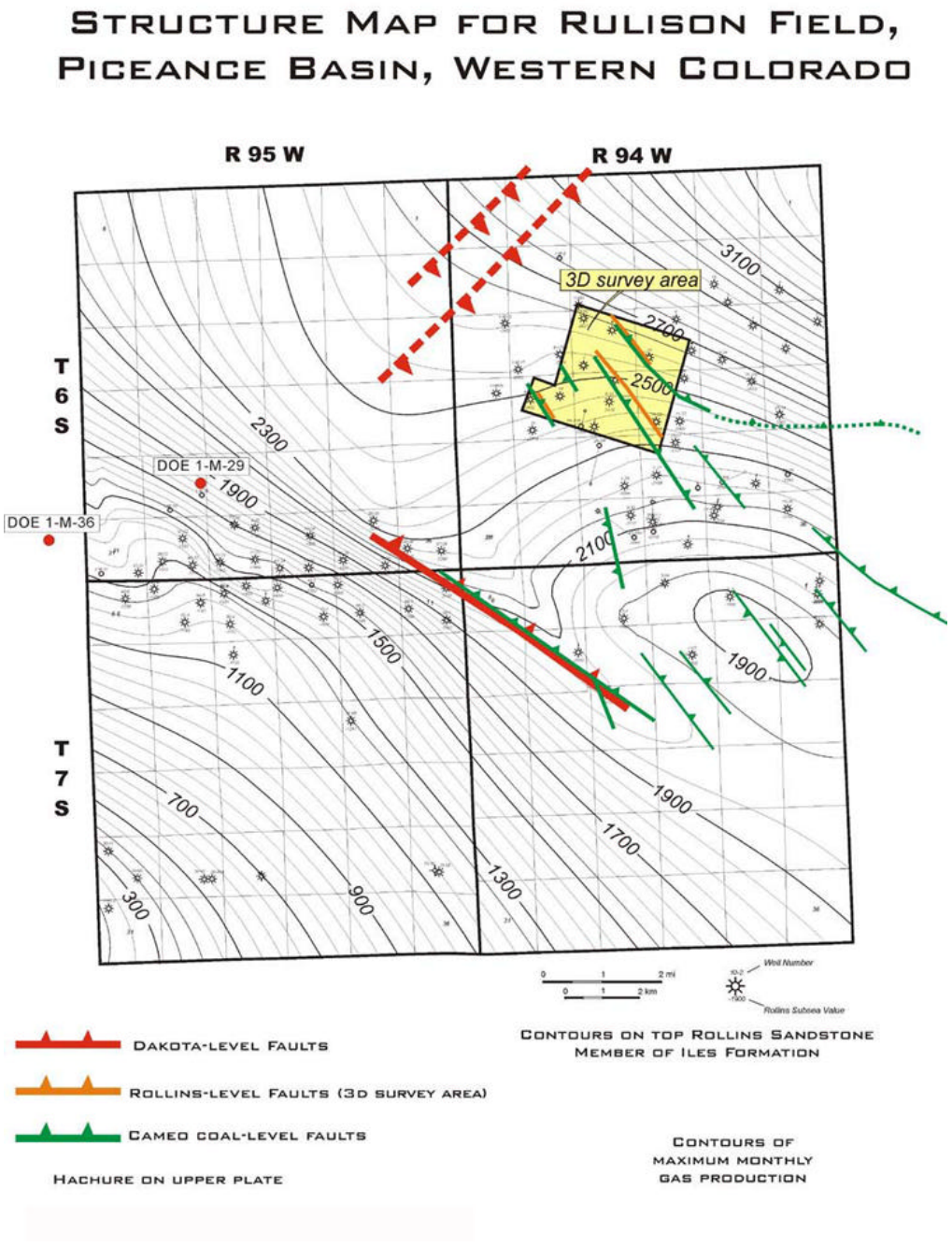

Fig. III-B2 Structure map of Rulison Field (R.94W.) showing fault locations and characteristics (from Kestrel Geosciences, LLC).

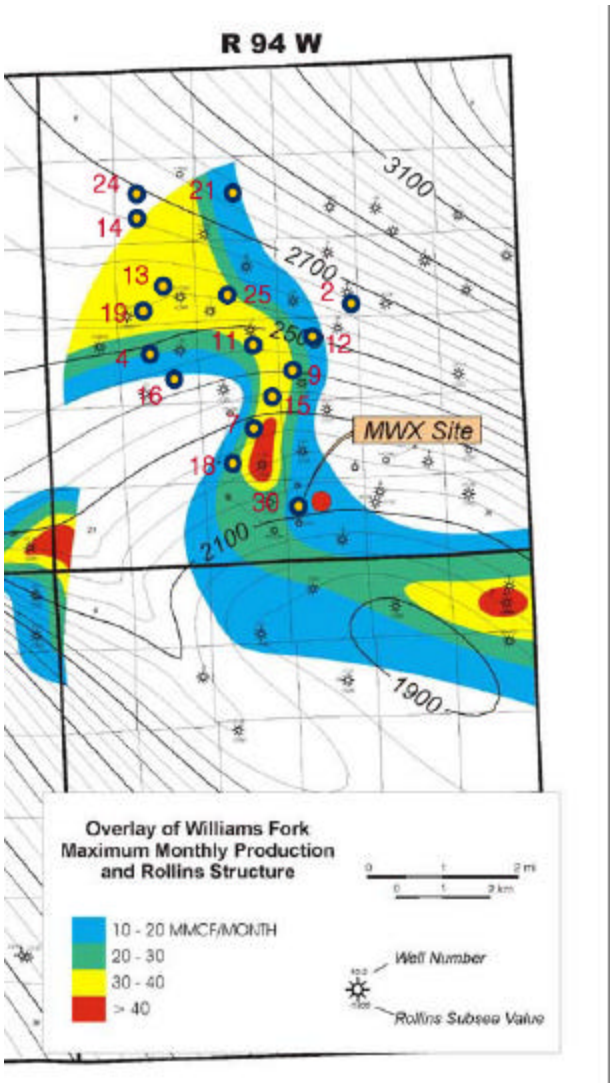

Fig. III-C1 Regional map of Rulison Field, modified from Hoak (1999), showing the approximate locations (open circles) where 1-dimensional simulations were conducted. Figures III-B2 - III-B6 compile results from wells 30 (MWX), 9,2,4,21, and 25. Not all simulation results are included in this report for brevity.

and underlying sediments. Predicted fractures having the greatest lengths and apertures and yielding the highest permeabilities occur in the lower Fluvial and upper Coastal intervals of the Williams Fork Formation. Fractures mostly having relatively shorter lengths, smaller apertures, and lower permeabilities are predicted for the regressive marine sandstones of the Iles Formation.

The maximum overpressure across the field is between 380 and 440 bars and occurs beneath a seal around 1800 m from the surface. This seal is located in the upper Paludal sandstone. Most rocks below 800 m fractured and maximum fracturing occurred between 15 and 35 Ma. Also in this interval porosity ranges between 0.05 and 0.15 and porosity profiles are found to be very similar at all locations. Below the main seal at 1800 m, there are three additional seals across the study area as seen in the permeability profiles.

Fig. III-C4 shows the overpressure (bars), permeability (log Darcy), and gas saturation profiles at 56 Ma, 36 Ma, 16 Ma, and present day. Compaction induced loss of porosity and

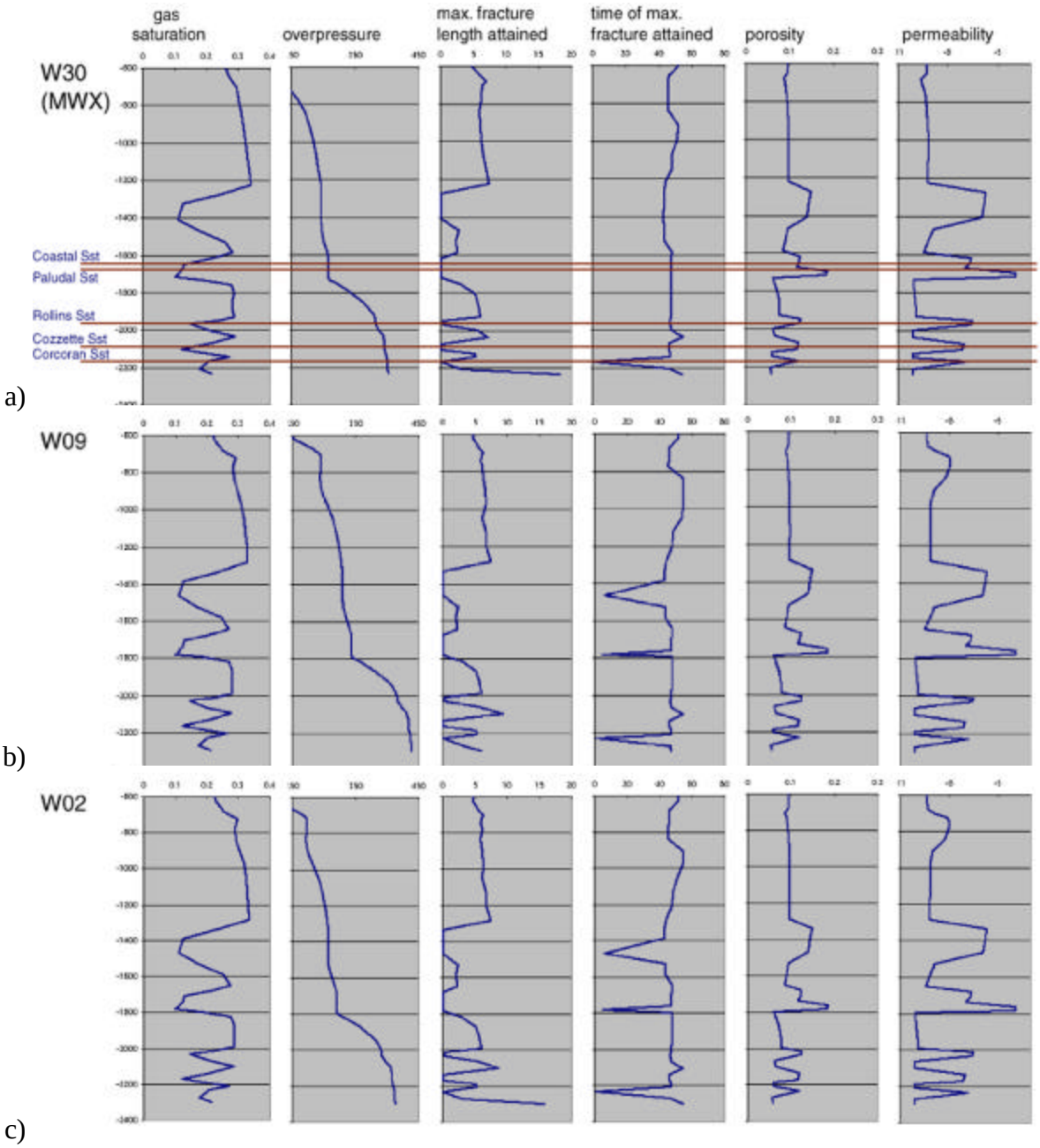
gas saturation
overpressure
max. fracture length attained
time of max. fracture attained
porosity
permeability
W30 (MWX)
Coastal Sst
Paludal Sst
Rollins Sst
Cozzette Sst
Corcoran Sst
a)
W09
b)
W02
c)

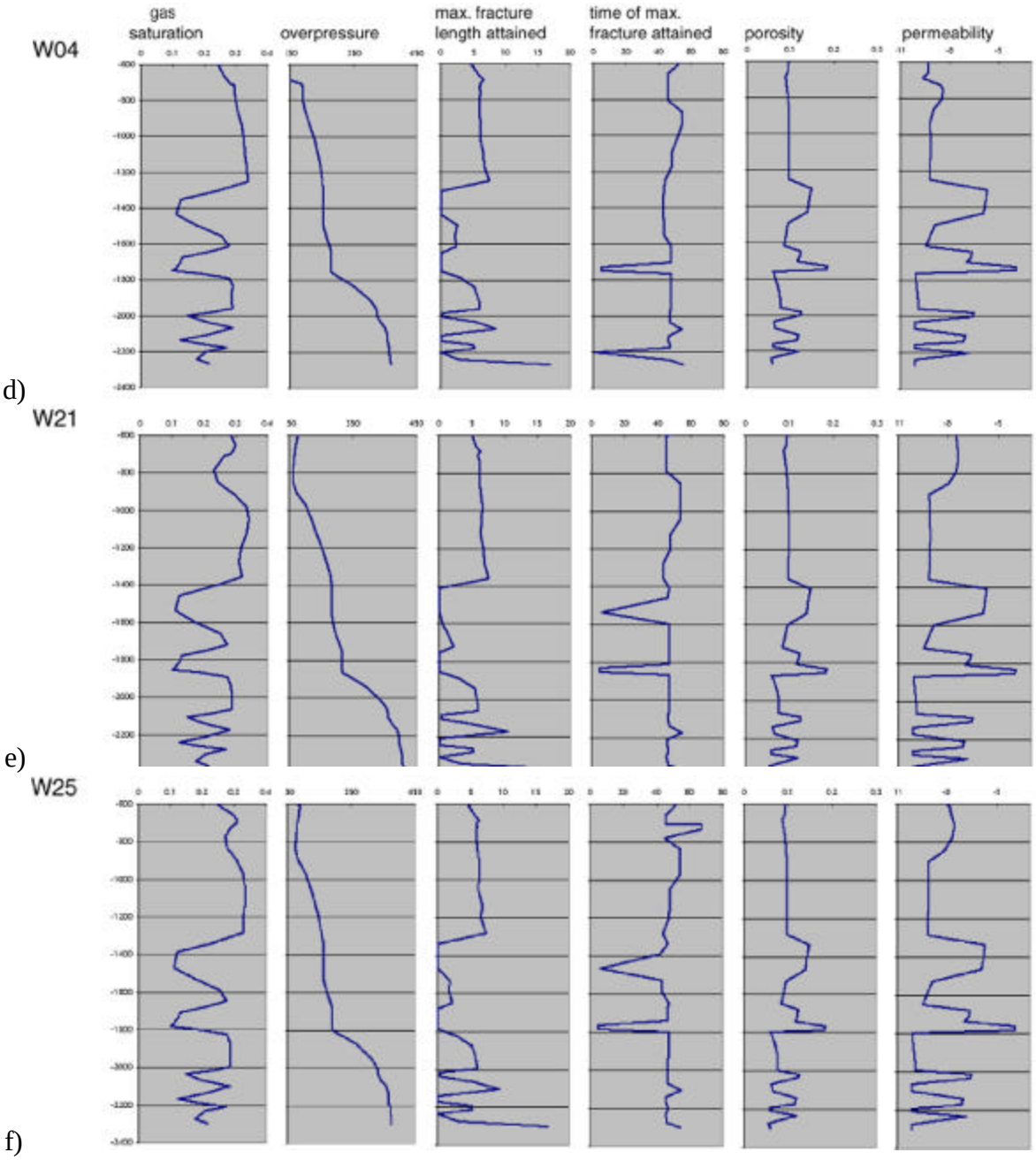

Fig. III-C2 Results of 1-D Basin RTM simulations from 6 wells, identified by their numbers on Fig. III-B1. Shown are predicted gas saturation, overpressure (bars), maximum fracture length attained during basin history (cm), time when maximum fracture was attained (76 represents present day), porosity, and permeability (log Darcy) at present day for the depth interval from 600 to 2,400 m. Several sandstones are identified on Fig. III-C2a; their locations in other wells can be identified by their similar permeability and porosity trends. Because of the similarities in the sedimentologic and subsidence and erosion histories of all wells, little differences appear in the porosity and permeability profiles. Slight differences are evident in the saturation and overpressure profiles in the interval from 600 to 1,200 m, however most important differences are when maximum fracturing was attained.

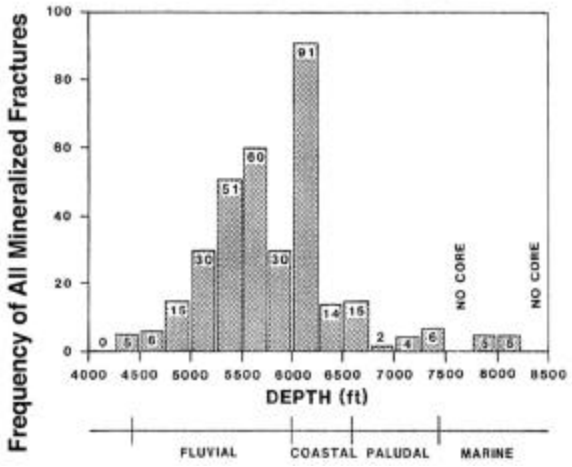

Fig. III-C3 Histogram showing distribution of mineralized fractures in cores from the MWX site. Compare this figure to the plots of maximum fracture length in Fig. III-C2. Basin RTM predicted correctly that most fractures are in the Paludal interval, and that the lower-lying sediments experienced less intense fracturing (Finley and Lorenz 1988).

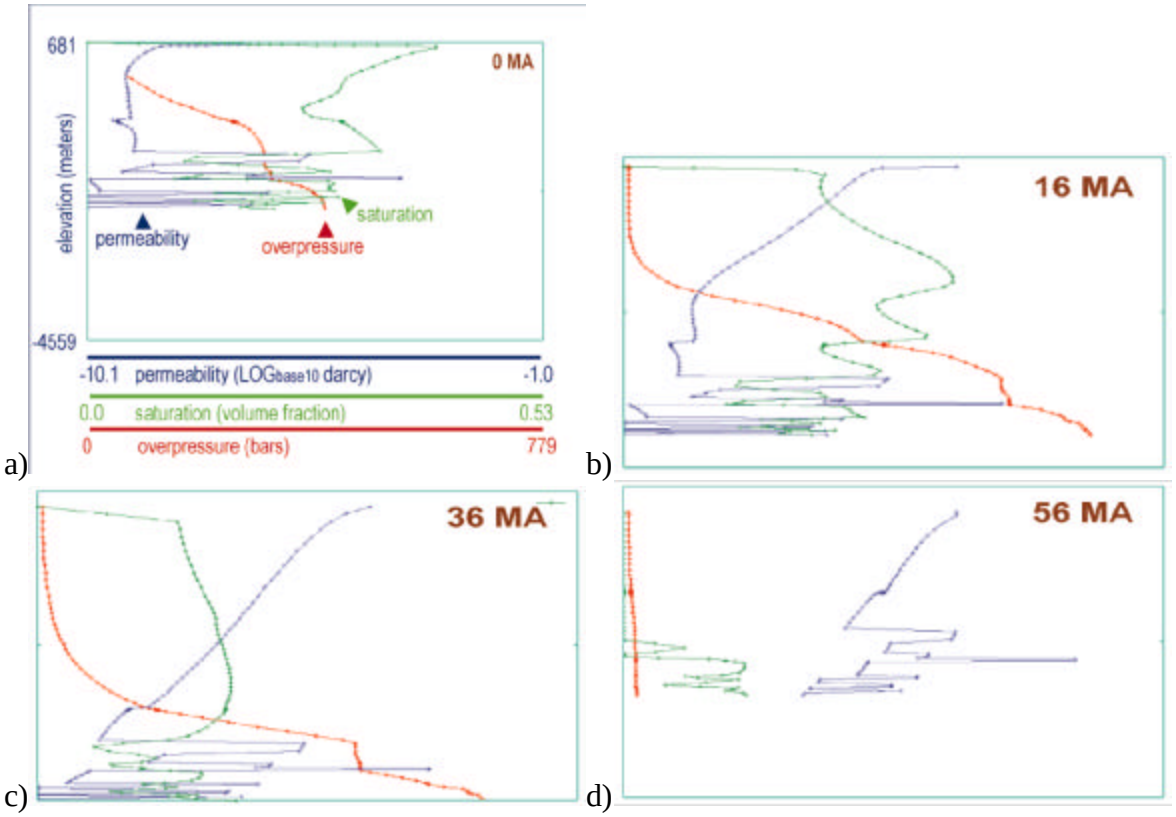

Fig. III-C4 Time sequence in vertical profiles of fracture permeability (log Darcy), overpressure (bars), and gas saturation, from MWX site 1-D simulation. Fig. a indicates the ranges of the maximum and minimum values, while Figs. b, c and d represent the state of the three variables at 16, 36, and 56 Ma.

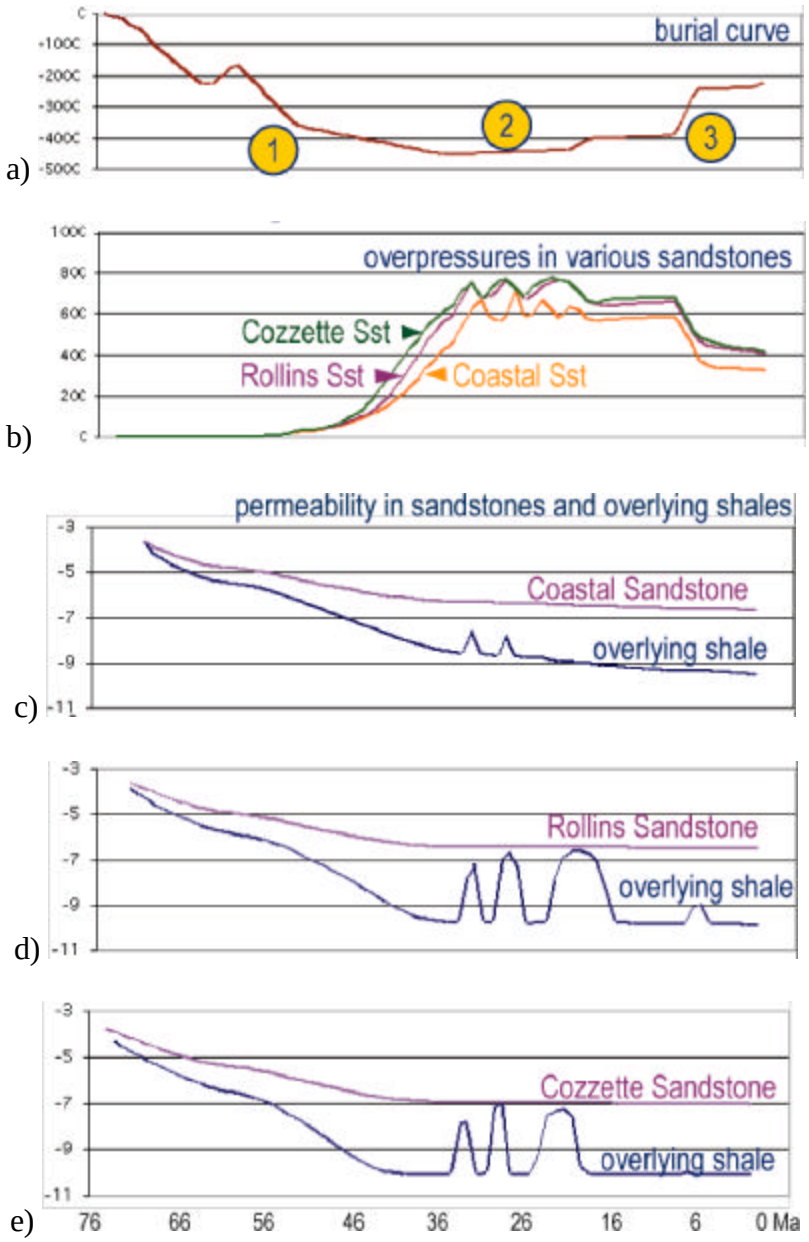

Fig. III-C5 Temporal evolutions a) burial curve, b) overpressure, and c) - e) permeabilities in various sandstones and shales in the MWX site. Overpressure in the sandstones correlates with the compaction and related seal formation in the shales (stage 1, Fig. a). Episodic release of fluid from the sandstones, as evidenced by oscillations during stage 2 is accomplished through the fracturing of overlying shales, as indicated by increases in overlying shale permeabilities. With rebounding and the removal of overburden, fracturing activity in the shales ceases (stage 3).

therefore matrix permeability is evident in Fig. III-C4b,c, and d. Fig. III-C5 shows a complex scenario of correlated fracturing, overpressure, and fluid release. Fracturing in the shales occurred in three distinct periods (35-34 Ma, 30-28 Ma, and 26-20 Ma). Overpressure reaches a maximum at the end of stage 1 (35 Ma). This period of monotonic pressure increase is followed by a dynamic period where overpressure oscillates in association with episodes of fracturing. The fracturing in a given shale is correlated with overpressure decrease in the underlying sandstone.

These coupled overpressuring, fracturing oscillations are autonomous (are due to the nonlinear dynamics of the fracture flow system) and are not driven by erosion or other external factors (see Ortoleva 1994a, 1998, and Tuncay, Park and Ortoleva 2000a for a more detailed discussion of this type of episodic fracturing). This dynamic period is terminated at 25 Ma due to fast uplift and erosion as see in the burial curve. Overpressure during the later period of stage 2 is essentially constant. Stage 3, starting at 8 Ma to the present is characterized by a fast period of erosion that lasted for 2 million years followed by slow erosion to the present. During the fast erosion period, overburden was decreased by 1500 m which resulted in 200 bars decrease in overpressure.

D. 2-D Rulison Field Simulations and Comparisons with 1-D Results

The 2-D Rulison simulations show that fracturing is closely related to the development of compartments, which are confined zones of fluid overpressure, and is influenced by rock rheology, depth of burial, temperature, and gas generation. Multiple episodes of fracturing and compartmentation caused by pressure build-up and release characterize the simulations beginning around 50 Ma (closely related to the dynamical behavior seen in the early part of stage 2 in the 1-D simulations of Fig. III-C5). Appreciable development of a gas phase began around 40 Ma from coal in the Paludal Interval of the Williams Fork Formation. Maximum development of gas charged compartments coincided mostly with the period of deepest burial during the Eocene and Obligocene between 40 and 25 Ma.

The modeling results indicate that the development and dissipation of fractured, gas charged compartments in the Rulison Field was complex but arose locally in the regressive marine sandstones of the Iles Formation, fluvial and coastal sandstones of the Williams Fork Formation, and parts of the Wasatch Formation. Large pressure contrasts between compartments and surrounding strata that existed before 20 Ma in the Wasatch and Williams Fork Formations mostly have dissipated during subsequent uplift and erosion. Our results suggest that current producing reservoirs are the remnants of more extensive and highly charged compartments that formed during mid-Tertiary deep burial. The 2-D modeling results show that even subtle flexure in the strata affects internal stress distribution, and thus exercise an important control on the location and evolution of compartments through time.

1. Cross Section L1

As seen in Fig. III-D2, the fracture permeability significantly changes across lithologic contacts. The number of compartments and their locations change as a result of the interplay between erosion and tectonics of the basin bottom. At 30 Ma, there seems to be several fractured layers in the deeper parts of the basin. The large compartment in the shallow region moves upwards and changes its shape at 20 Ma. This trend continues until the fast erosion between 9 and 7 Ma. As a result of cooling and the very small compressibility of water (only water flow was considered in this simulation), fluid pressure decreases significantly during this erosion period, resulting in closure of most fractures.

To make sure that our numerical approach is consistent, the simulation of Fig. III-D2 is repeated with twice as many finite elements in the horizontal direction. A comparison of Fig. III-D2 and Fig. III-D3 shows that results are consistent, a remarkable fact considering the large number of RTM processes taken into account in the simulations. Thus we believe that this is a confirmation of the robustness and accuracy of our numerical scheme. It also shows that relatively crude simulations can justifiably be used to determine the general status of a system.

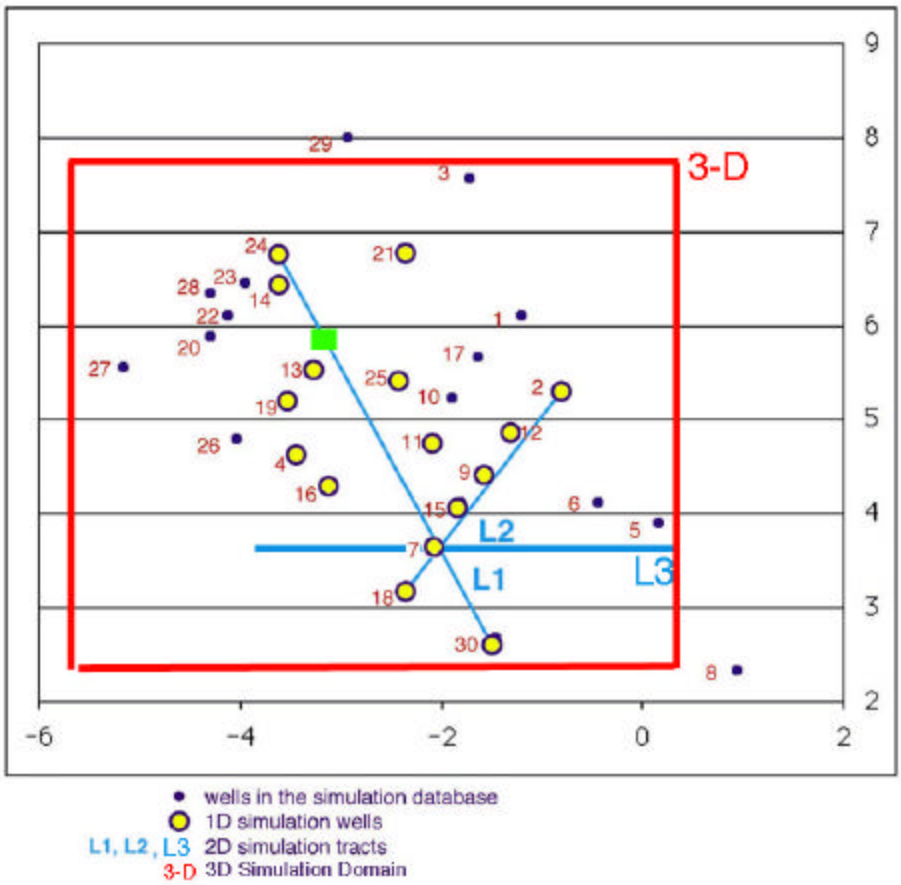

Fig. III-D1 Distribution of wells used in 1-D and 2-D Rulison Field simulations. Well #30 is at the MWX site. Lines L1, L2, and L3 indicate the 2-D simulation tracts. The green square is the location where we compared 2-D and 3-D simulation results (Fig. III-E8).

Although Figs. III-D2 and III-D3 show consistency of our numerical approach, addition of important RTM processes such as multi-phase flow and methanogenesis might change the results significantly (Fig. III-D4). A comparison of Fig. III-D3 and Fig. III-D4 shows that fracturing is strongly affected by the multi-phase (gas/water) flow and methanogenesis. The most significant difference is the survival of fractures to the present day as seen in Fig. III-D4. A decrease in temperature results in a large decrease in water pressure if pore volume is kept constant. However, the presence of a gas phase in the pores and its high compressibility allow the water phase to change its volume more freely, resulting in higher pressure after a drop in temperature. Therefore, fractures are expected to remain open longer in a gas-liquid saturated medium. Matrix permeability is similarly preserved in a gas/water saturated system. Note this effect is in addition to the more conventional concept that methanogenesis and capillary sealing can promote overpressuring and, thereby preserve fractures and matrix porosity. This might be one of the important reasons for the large number of compartments in Rocky Mountain Basins.

The patterns of fluid flow are shown in Fig. III-D5. Migration of gas towards the right and upward is fostered by the pattern of fracture permeability. This illustrates the principle that fracture-mediated puncturing of seals tends to occur at the highest point in the seal (Ortoleva 1998).

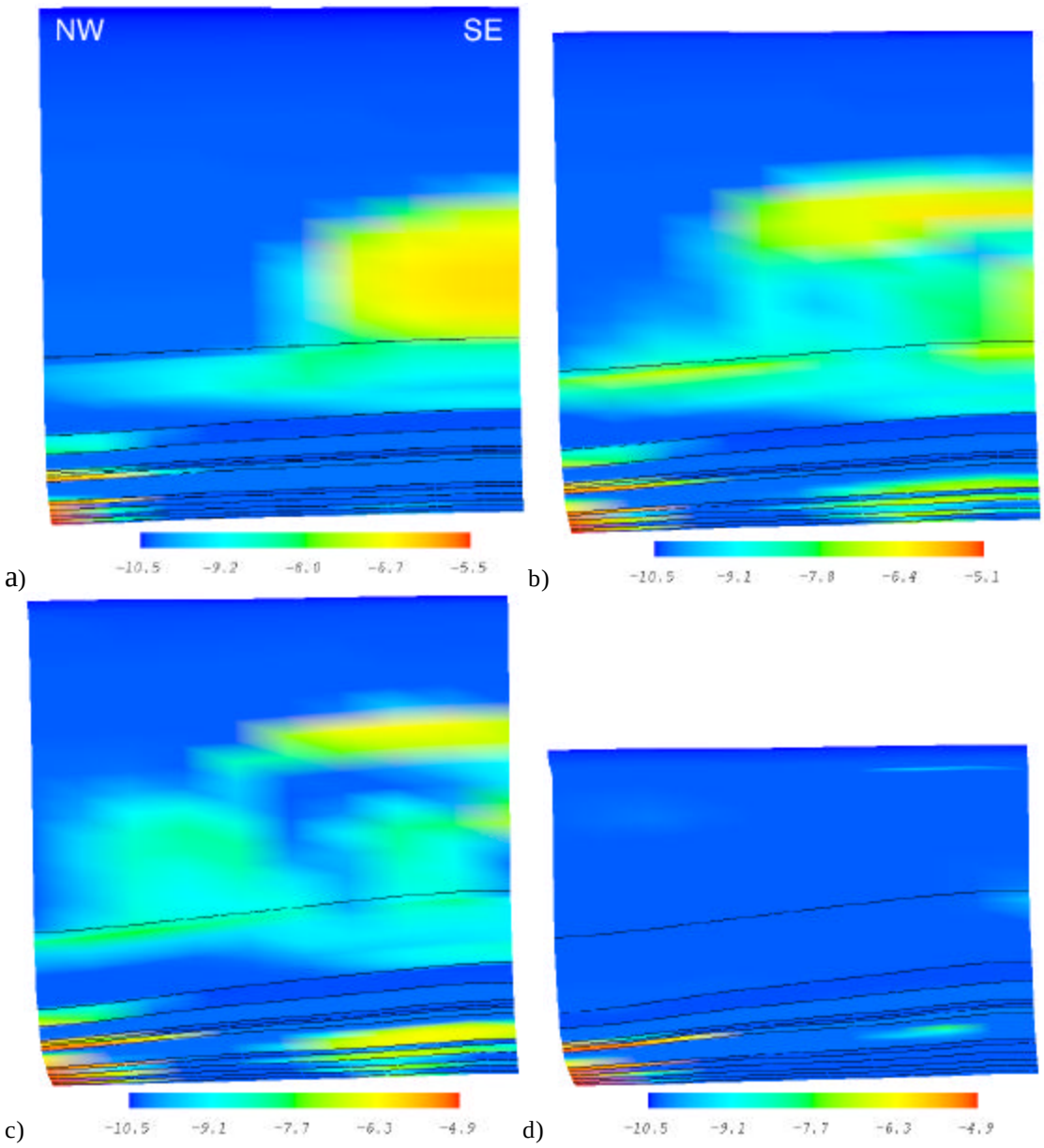

Fig III-D2 Basin RTM predicted fracture permeability (log Darcy) at a) 30 Ma, b) 20 Ma, c) 10 Ma and d) present day for cross-section L1 of Fig. III-D1. Black lines indicate lithologic contacts. The slope of the bottom at present day is 0.0273. The vertical and horizontal extents of the system are 3,000 m and 4,600 m, respectively. Only single phase (water) flow is considered in this simulation.

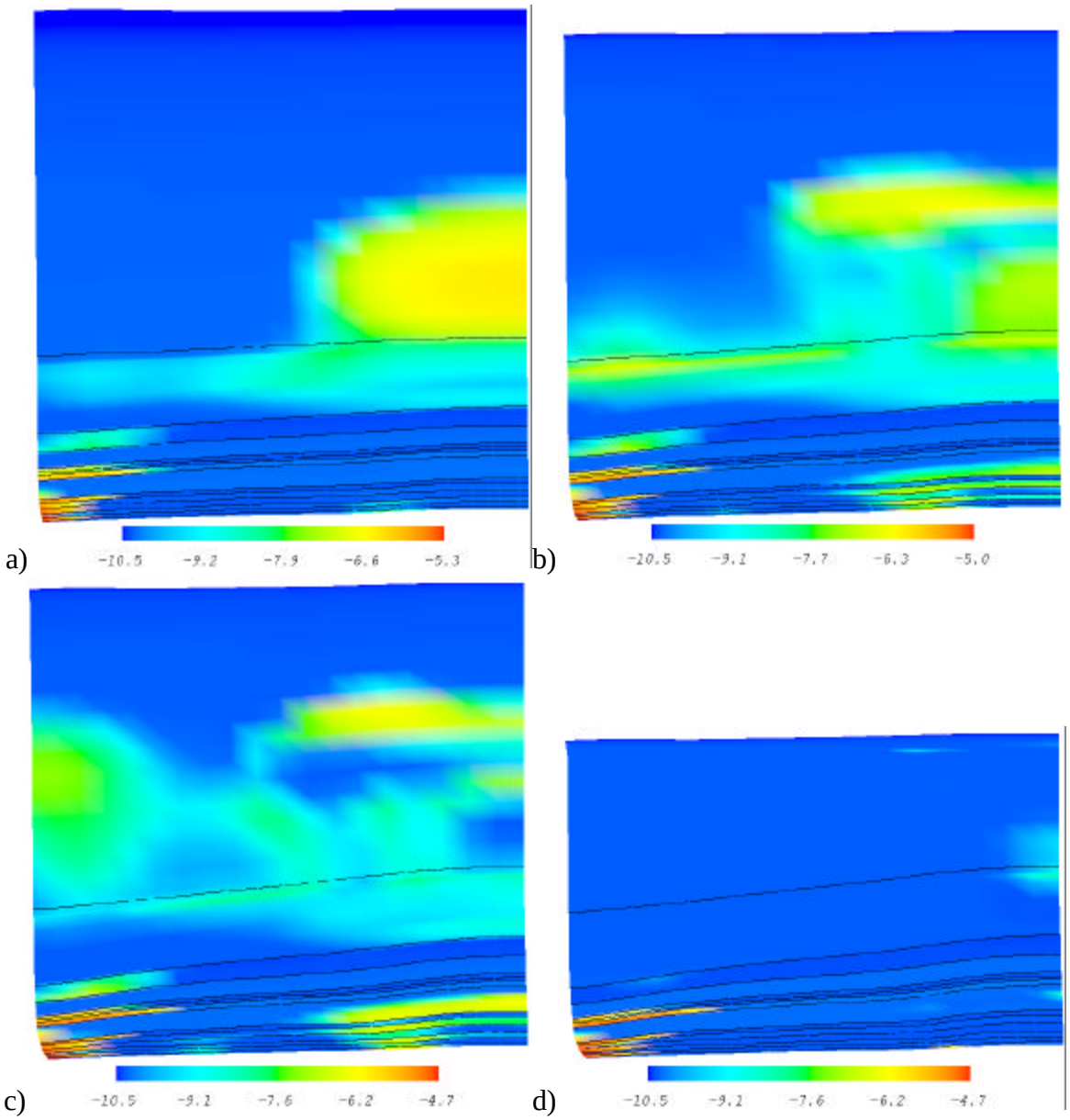

Fig. III-D3 Basin RTM predicted fracture permeability (log Darcy) at a) 30 Ma, b) 20 Ma, c) 10 Ma and d) present day for cross-section L1 of Fig. III-D1. To make sure that our numerical approach is consistent, the simulation of Fig. III-D2 is repeated here with twice as many finite elements in the horizontal direction.

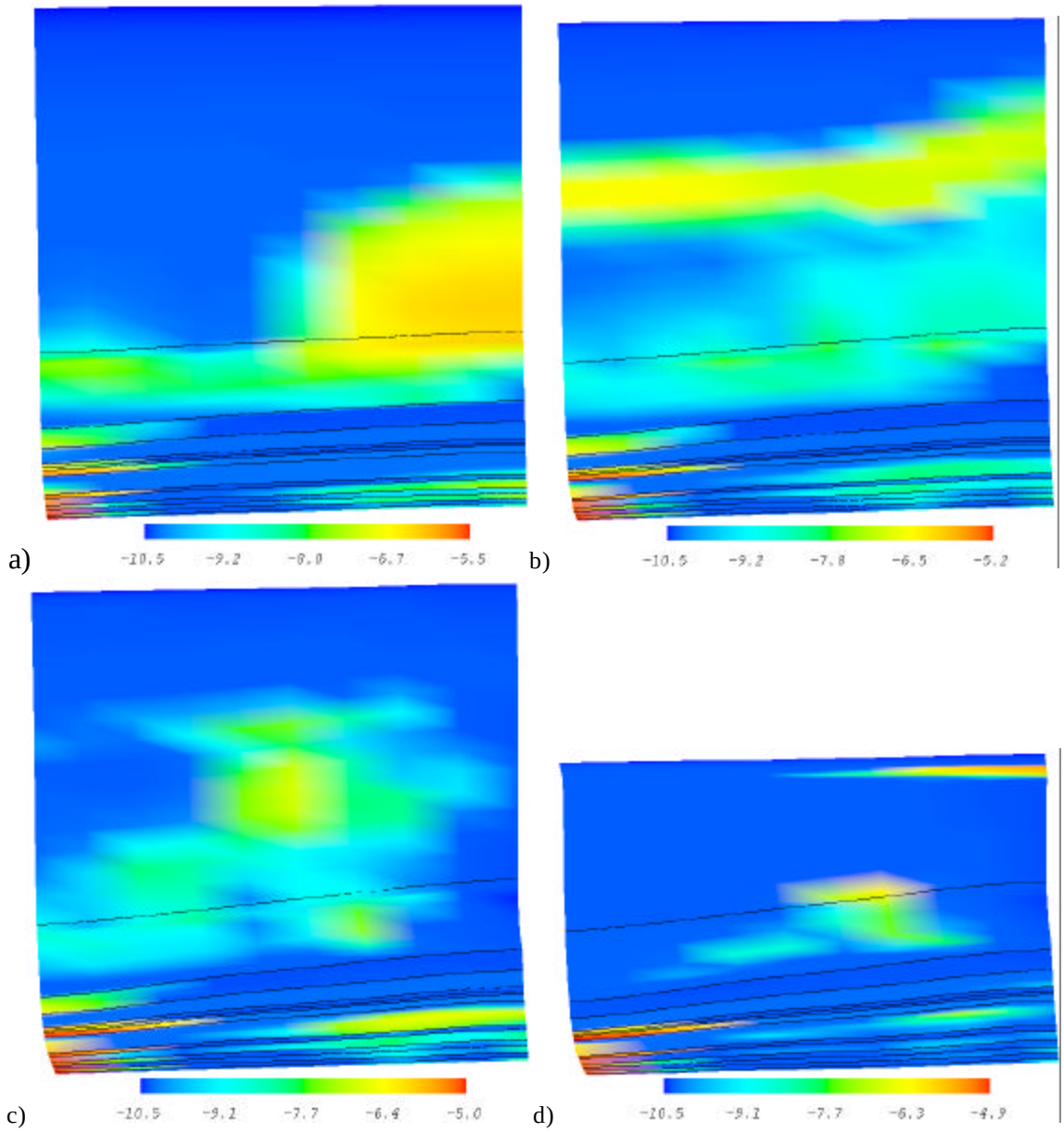

Fig. III-D4 Basin RTM predicted fracture permeability (log Darcy) at a) 30 Ma, b) 20 Ma, c) 10 Ma and d) present day for cross-section L1 of Fig. III-D1. Multi-phase (gas/water) flow and methanogenesis are accounted for in this simulation (in contrast to Figs. III-D2 and III-D3).

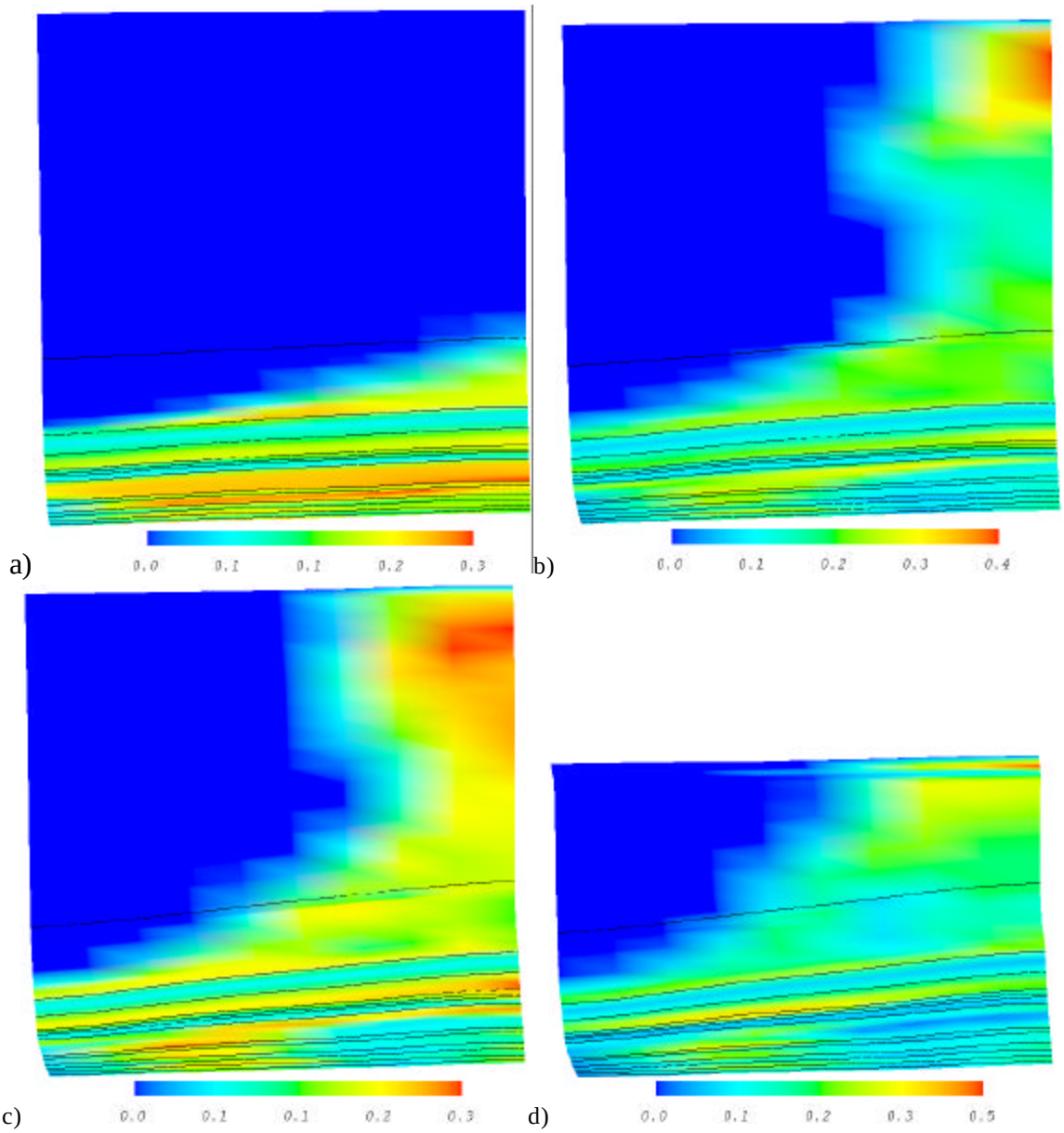

Fig. III-D5 Basin RTM predicted gas saturation at a) 30 Ma, b) 20 Ma, c) 10 Ma and d) present day for the case of Fig. III-D3 for cross-section L1 of Fig. III-D1. Migration of gas towards the right and upward is fostered by the pattern of fracture permeability.

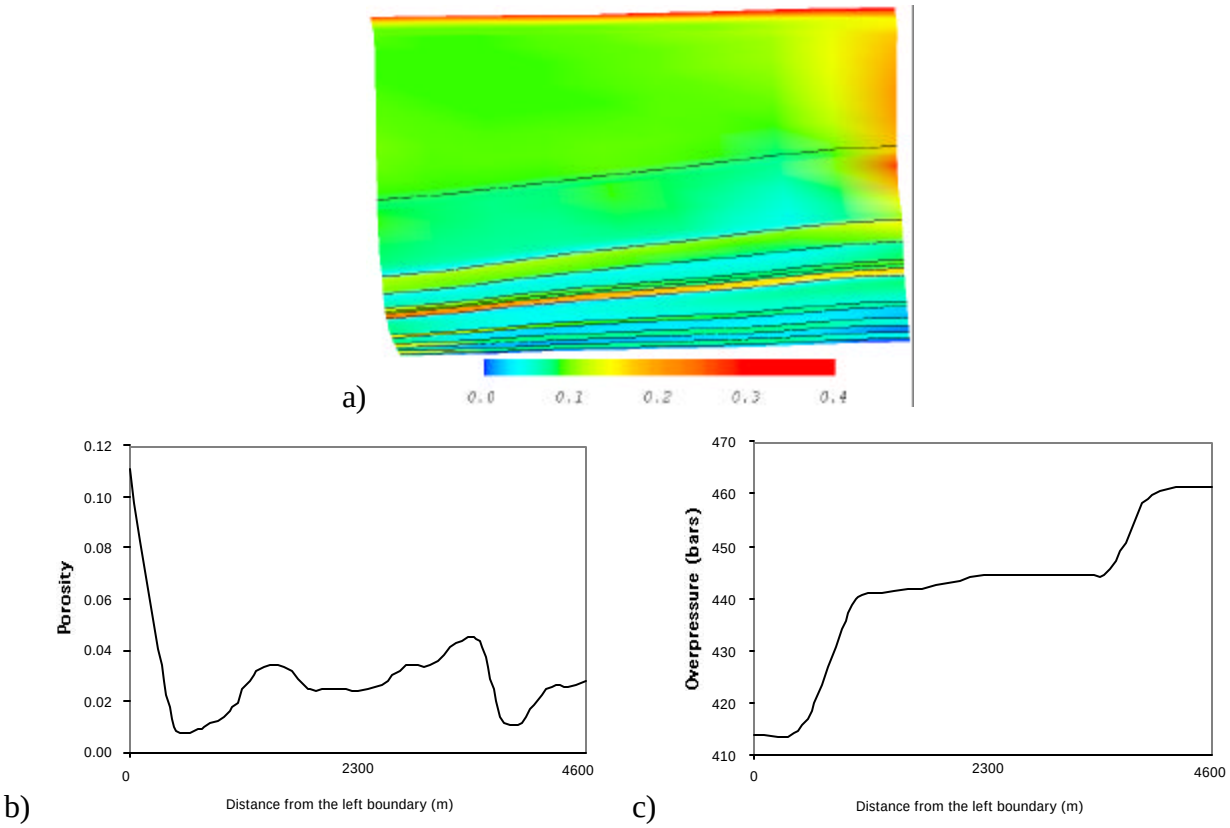

Fig. III-D6 a) Basin RTM predicted present day porosity for cross-section L1 for the simulation of Fig. III-D4. Note the relatively high porosity where gas flows upwards. The porosity is associated with both fracturing and overpressure-preserved matrix porosity. b) Porosity at the bottom of the domain of frame (a). The large lateral variation is due to structural tilt and curvature as the initial sediment deposited was the same across the domain. c) Overpressure at the bottom of the domain.

Present day porosity, and the lateral variation of porosity and overpressure (bars) are shown in Fig. III-D6. The relatively high porosity where gas moves upwards is associated with both fracturing and overpressure-preserved matrix porosity.

2. Cross Section L2

2-D simulations were carried out for cross section L2 (Fig. III-D1) to identify factors that influence 2-D simulations. The vertical and horizontal extents of the system are 2,800 m and 2,600 m, respectively. Due to the uplift, the elevation at the high point (one-third distance from the left) is 40 m than the far right and 10 m greater than the far left. This topographic relief has induced great lateral variations in fracturing along a given lithology arising from the variation in local stresses as seen in Fig. III-D7. When single phase flow is considered, most fractures closed during the fast erosion period and remained closed to the present day.

When multi-phase flow and methanogenesis are operating, as for the simulation in Fig. III-D8, the location, intensity, and pattern of fracturing are greatly altered due to the greater compressibility of gas and volume-increasing methanogenesis reactions which allow for longer lived overpressuring compared with the single phase flow system Fig. III-D7. The strong relationship between multi-phase flow and fracturing is observed in Fig. III-D9. Figs. III-D10

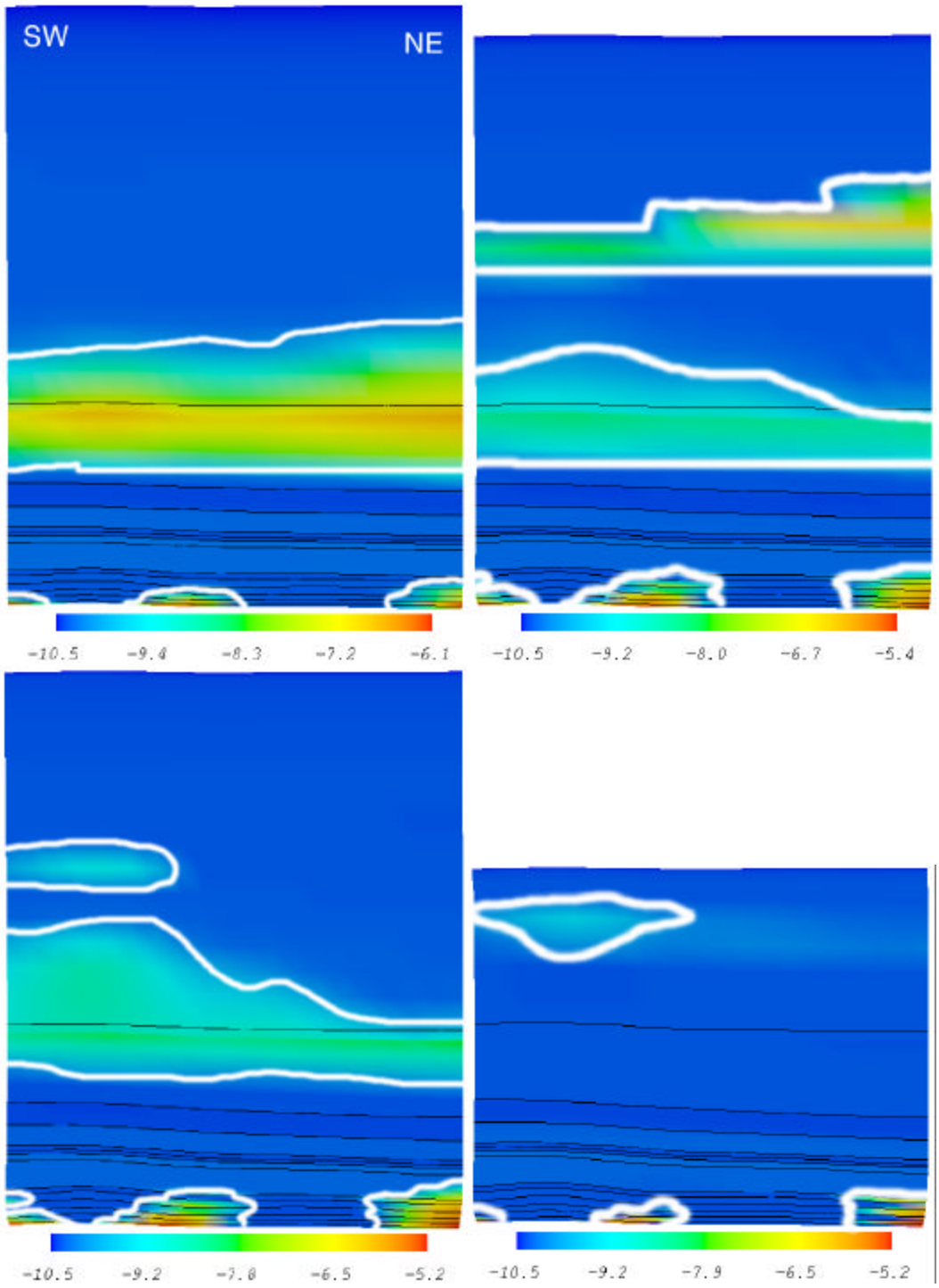

Fig. III-D7 Basin RTM predicted fracture permeability (log Darcy) at a) 30 Ma, b) 20 Ma, c) 10 Ma and d) present day for cross-section L2 of Fig. III-D1. Single phase flow (water) is assumed.

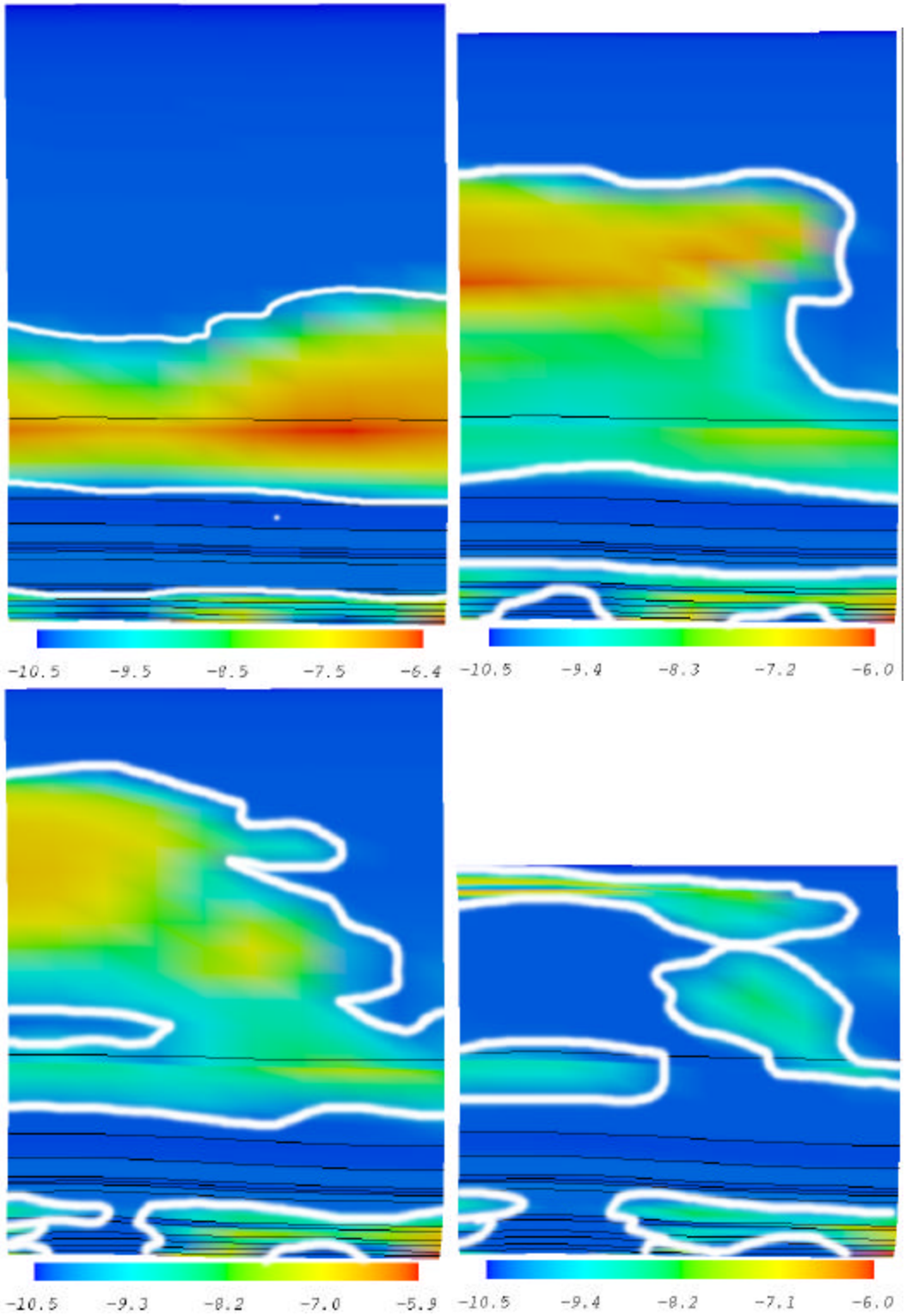

Fig. III-D8 Basin RTM predicted fracture permeability (log Darcy) at a) 30 Ma, b) 20 Ma, c) 10 Ma and d) present day for cross-section L2 when multi-phase flow and methanogenesis are considered.

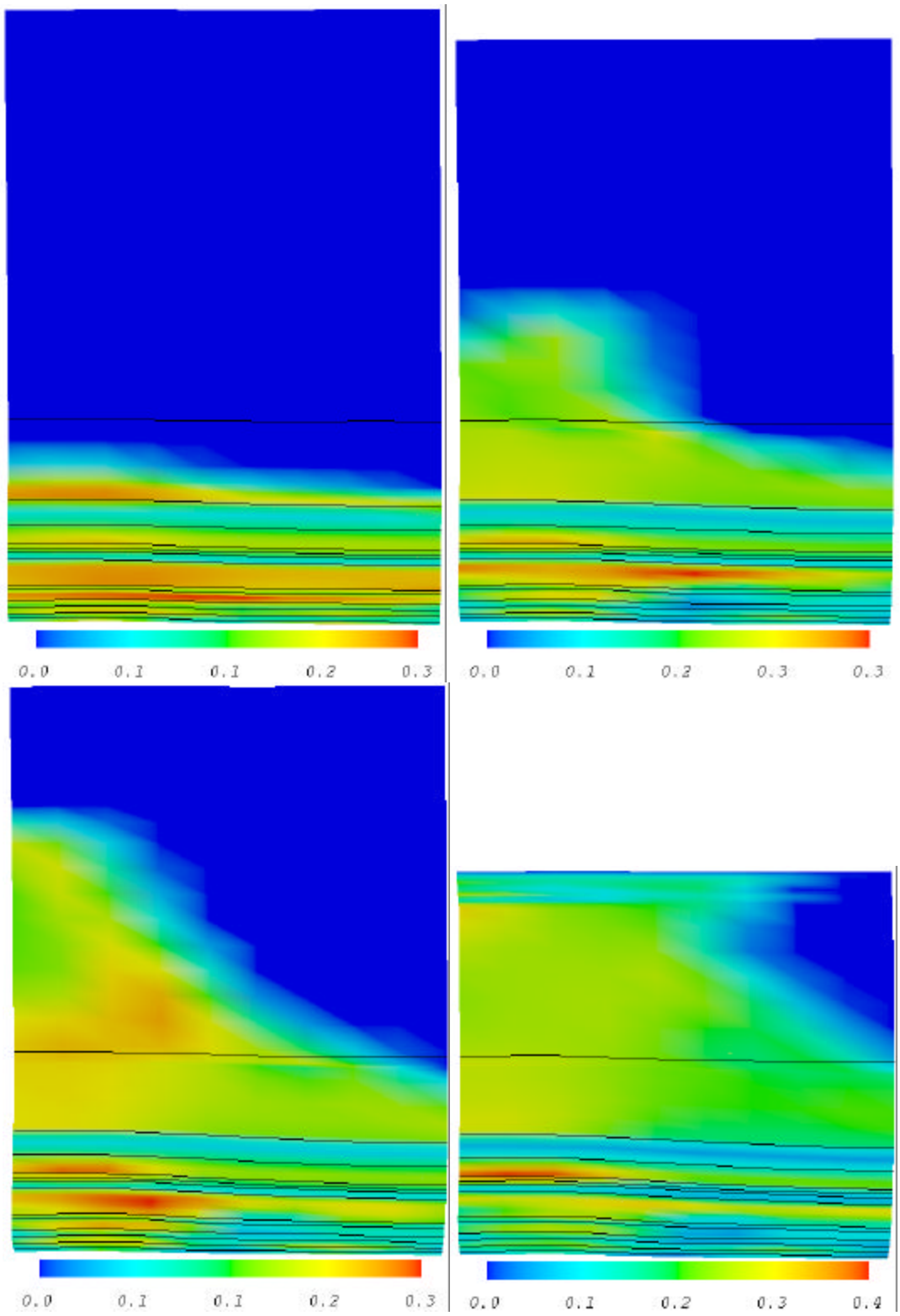

Fig. III-D9 Basin RTM predicted gas saturation at a) 30 Ma, b) 20 Ma, c) 10 Ma and d) present day for cross section L2.

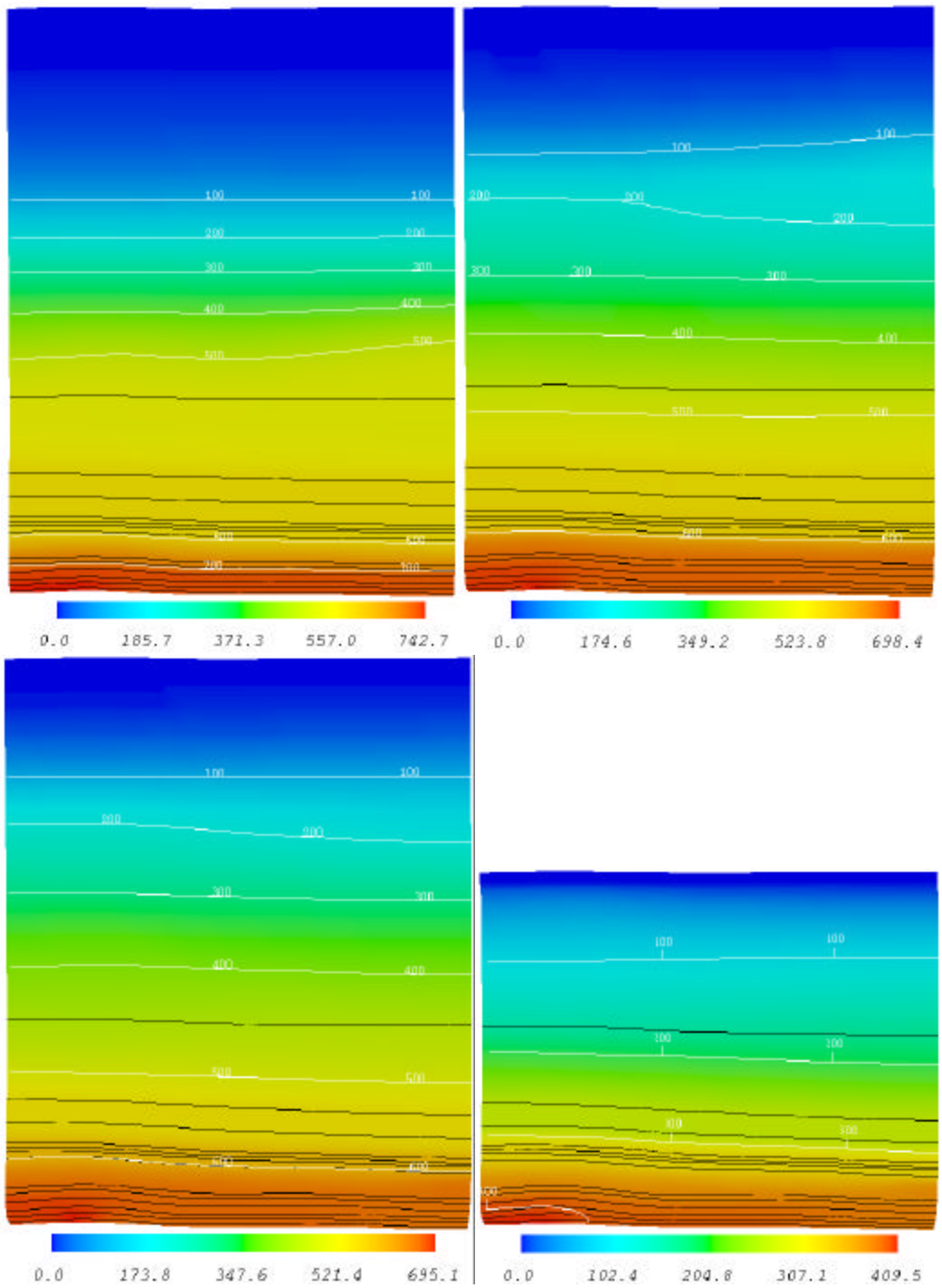

Fig. III-D10 Basin RTM predicted overpressure (bars) at a) 30 Ma, b) 20 Ma, c) 10 Ma and d) present day (cross-section L2) for the same case as in Fig. III-D7.

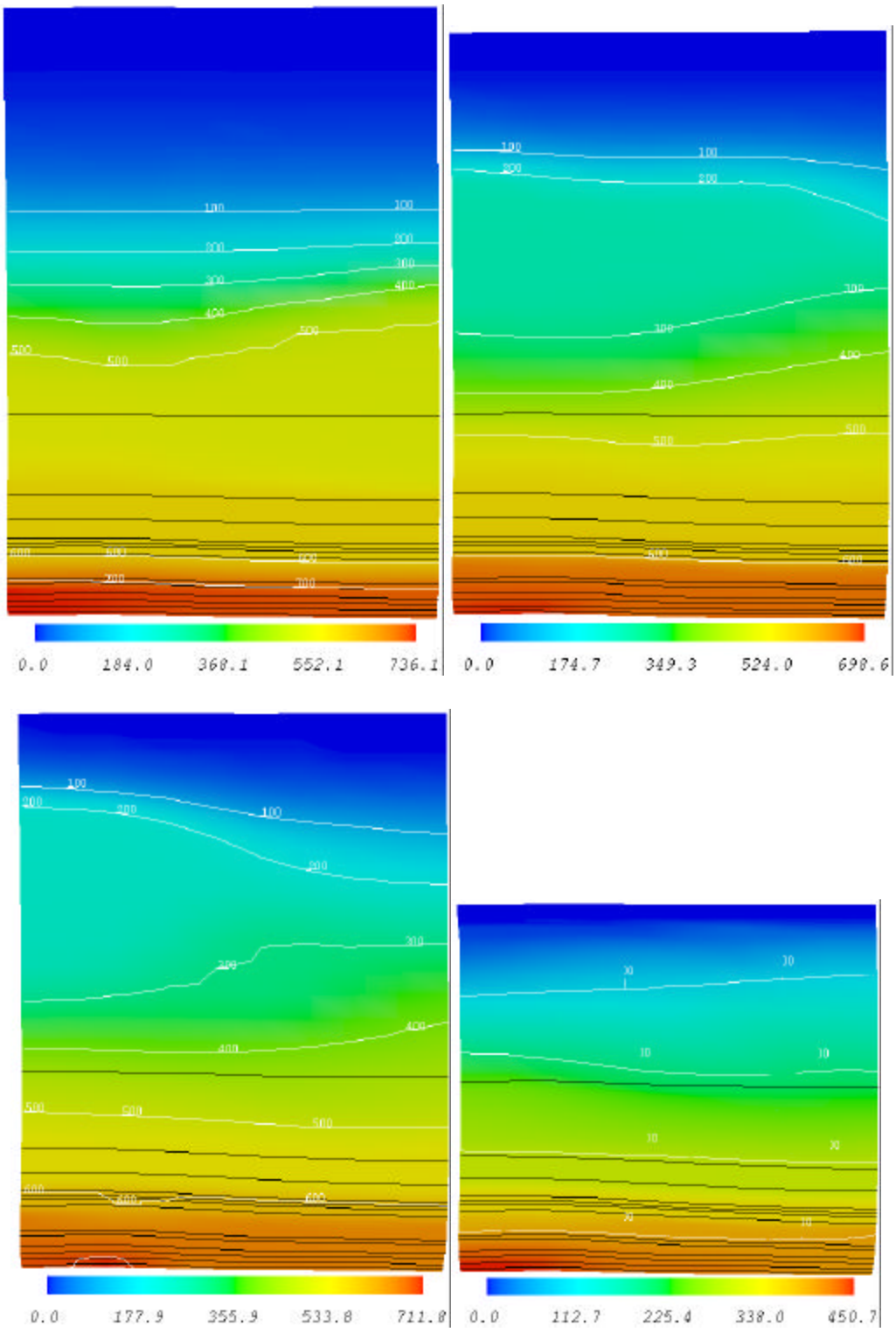

Fig. III-D11 Basin RTM predicted overpressure (bars) at a) 30 Ma, b) 20 Ma, c) 10 Ma and d) present day (cross-section L2) for the same case as in Fig. III-D8.

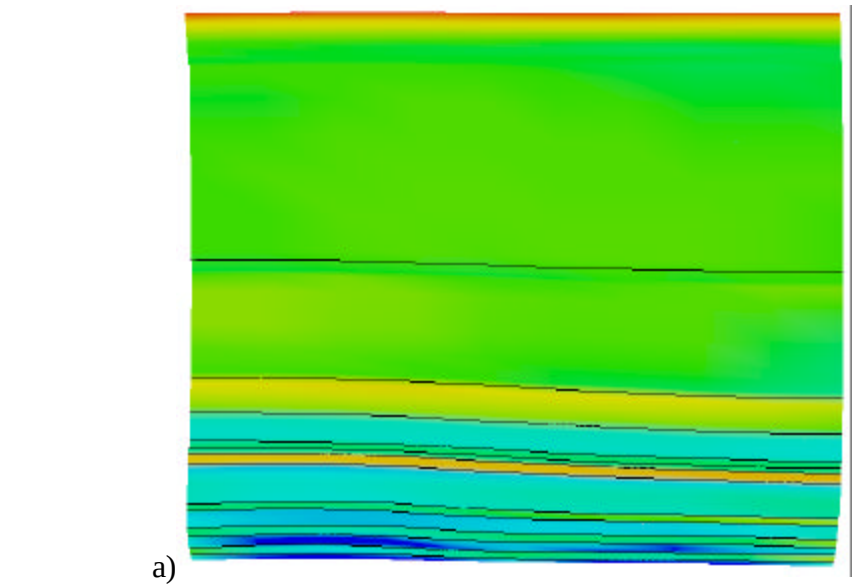

a)

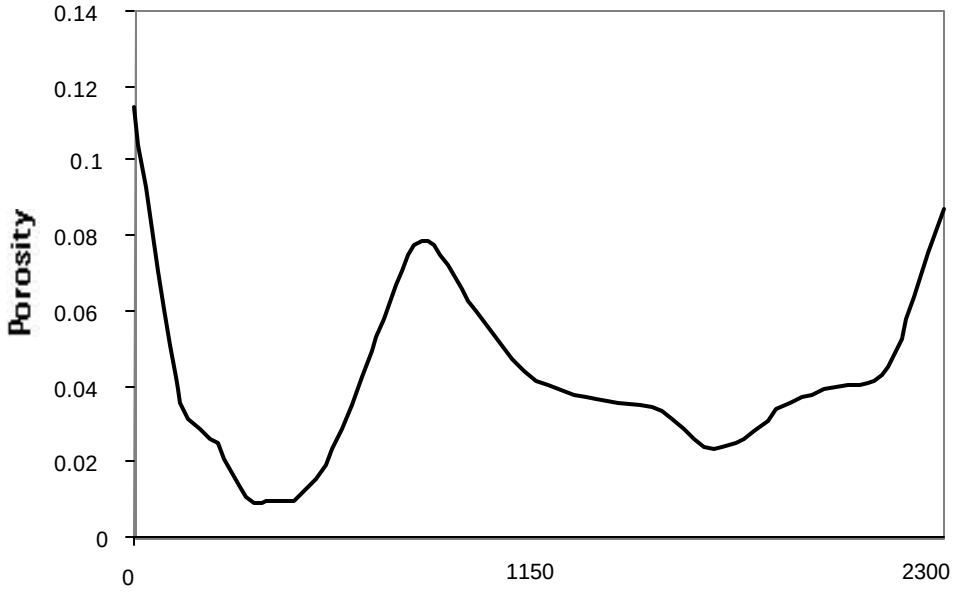

b)

Fig. III-D12 a) Basin RTM predicted porosity at present day (cross section L2). A small curvature results in a significant variation of porosity across a given lithology. b) Porosity varies between 0.01 and 0.10 within the same lithologic layer.

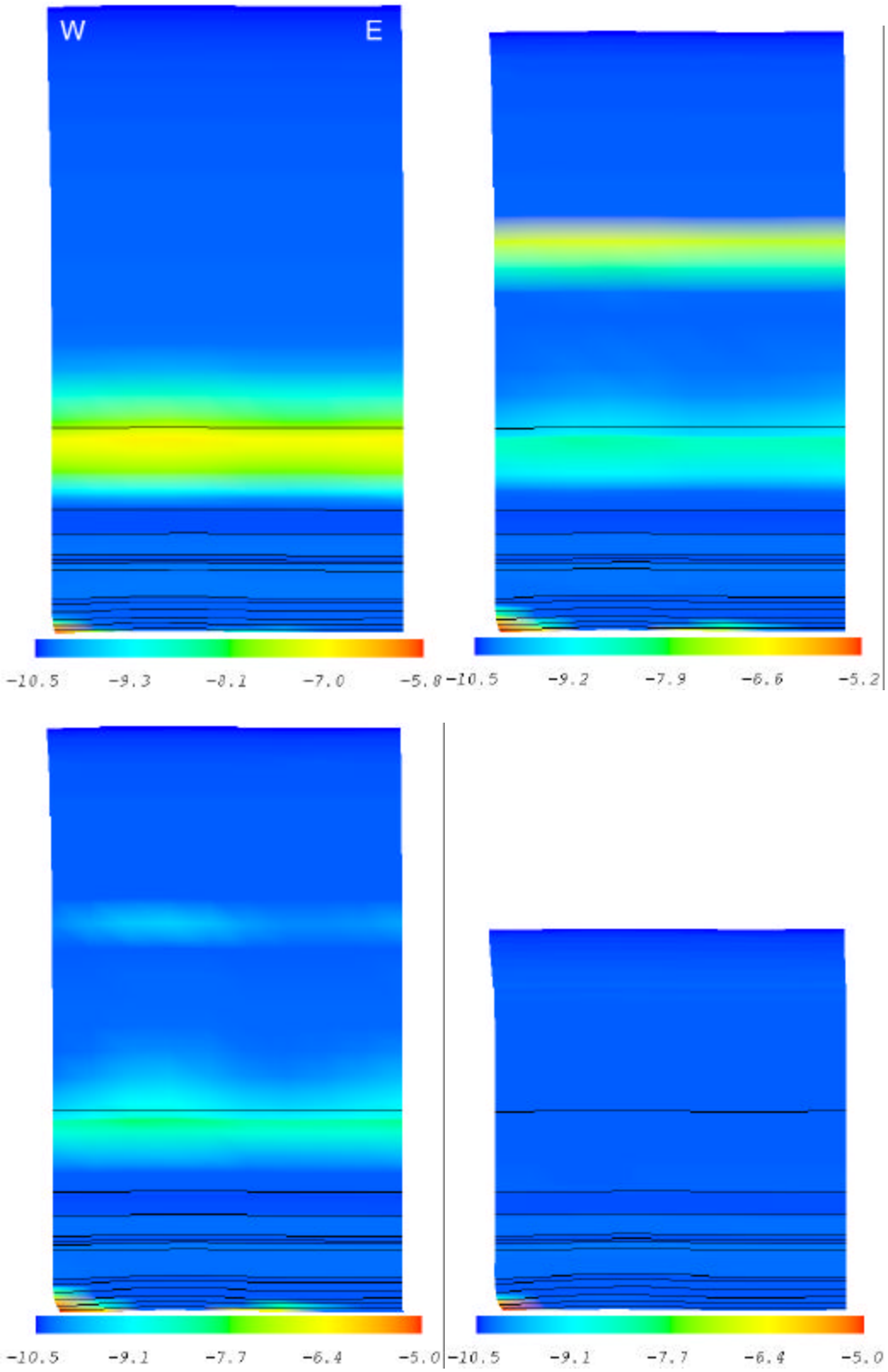

Fig. III-D13 Basin RTM predicted fracture permeability (log Darcy) at a) 30 Ma, b) 20 Ma, c) 10 Ma and d) present day for cross-section L3 of Fig. III-D1. Only single phase (water) flow is considered. W on left, E on right—repeat for 13 and 14.

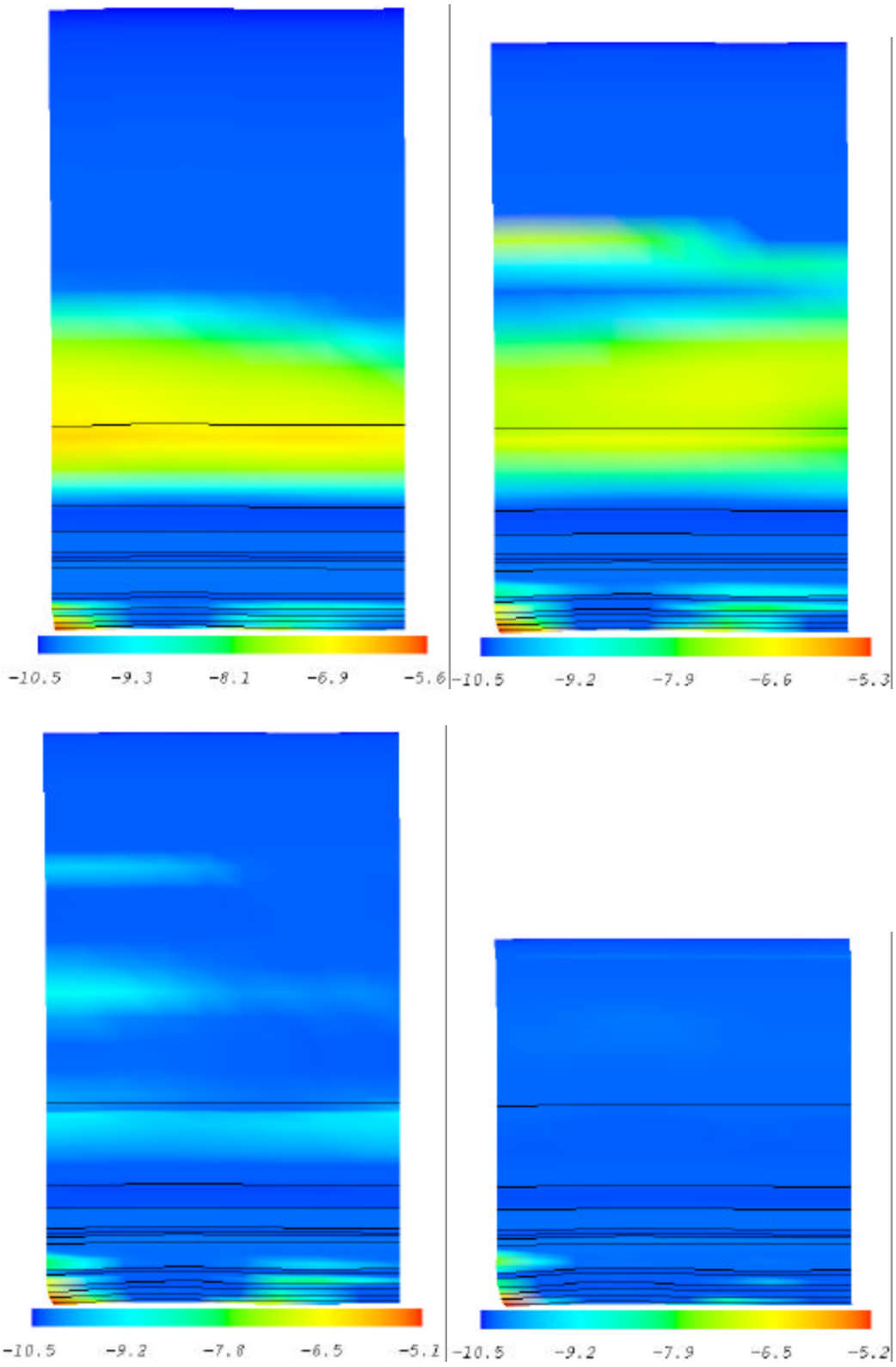

Fig. III-D14 Predicted fracture permeability (log Darcy) at a) 30 Ma, b) 20 Ma, c) 10 Ma and d) present day (cross section L3) when multi-phase (gas/water) flow and methanogenesis are considered.

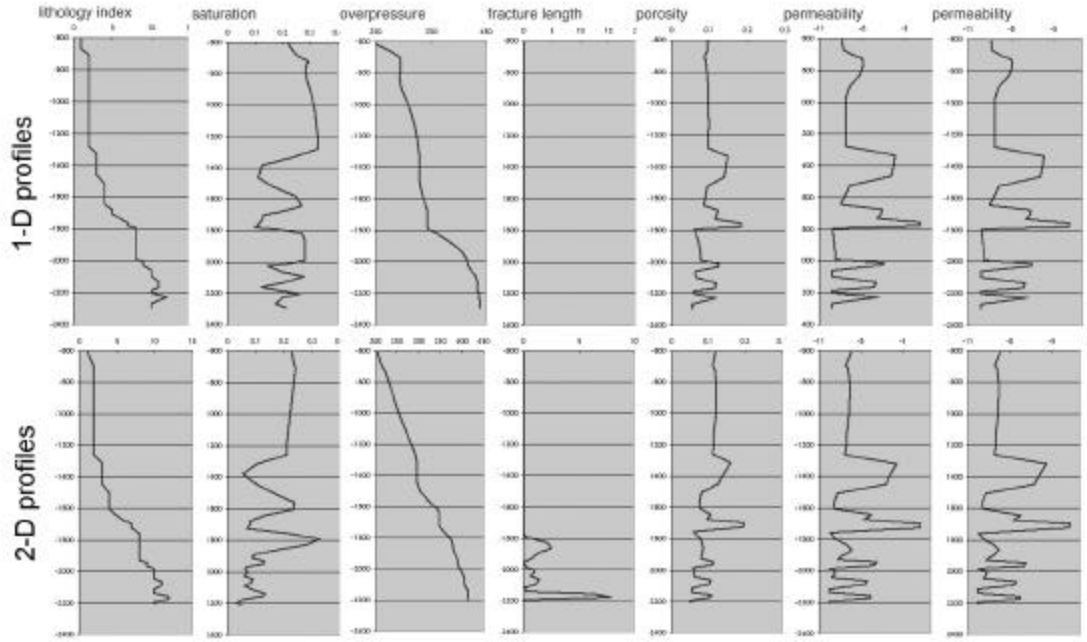

Fig. III-D15 Comparison of 2-D and 1-D simulation results for Well 09 (see Fig. III-C1). 1-D simulation results are presented in the first row. A fairly good match is observed between the results except for the fracture length.

and III-D11 show that overpressure is almost constant within fractured compartments (shown with white bordered zones in Figs. III-D7 and III-D8). The maximum overpressure decreases as a result of cooling. Note the significant drop in overpressure from 695 bars to 409 bars in the last 10 million years in Fig. III-D10. The relatively higher pressures in Fig. III-D11 compared to Fig. III-D10 is due to multi-phase flow (e.g., the high compressibility of gas relative to water as well as capillary effects and methanogenesis). Fig. III-D12 shows the porosity distribution at present day. The small structural curvature results in a significant variation of porosity across a given lithology.

3. Cross Section L3

Similar conclusions can be drawn from 2-D simulations for cross section L3 (Fig. III-D1). Figs. III-D13 and III-D14 show the significant difference between single phase and multi-phase simulations for fracture permeability. However, the results from L3 appear to have less variation in the lateral (E-W) direction, associated with lateral variation of uplift-subsidence.

4. Comparison of 1-D and 2-D Simulations

Fig. III-D15 compares the present day predictions of 1-D and 2-D simulations for MWX site. As anticipated, overpressure from 1-D simulation is higher. Porosity and permeability profiles are in fair agreement. However, significant differences exist in the fracture length attained which may be attributed to the lack of structural tilt and curvature effects in 1-D simulations. The difference in fracturing history is closely related to the difference in lateral stress history.

E. 3-D Rulison Field Simulations and Comparisons with 2-D Results

When 2-D simulations are integrated visually, they give a qualitative view of the 3-D complexity of the fracture zones. Fig. III-E1 shows a comparison of the present day fracture permeability distributions for cross sections L1 and L2.. However, the 3-D nature of the stress tensor makes the true picture, as determined from 3-D simulation, more complex. For example, the fractures may extend in preferred directions that can direct flows out of the plane of either cross section.

The 3-D field scale simulation was done for the domain shown in Fig. III-D1. Fig III-E2 shows the isosurface of fracture permeability (100 Nano Darcy) for five different times. The lithologies are shown in the back panels and labeled in Fig. III-E2a. The simulation predicts a number of fractured layers in the north section of the field at 45 Ma. A fractured compartment is formed in the south at 35 Ma. Fractures in the north section persists during erosion whereas fractures in the south seems to close in the same period.

Fig. III-E3 demonstrates the complexity of porosity variations at 8 Ma. The stress-fluid flow-fracturing feedback and the external influences, mainly variations in subsidence and erosion, results in significant variation of porosity in the field. Isosurface of overpressure (475 bars) shows that extensive fracturing in the north section results in lower pressure there (Fig. III-E4). Therefore, the persistence of fractures in the north is likely to be associated with tectonic effects.

The variation of fracture permeability, porosity and overburden stress in the Coastal Sandstone are shown in Fig. III-E5. Fractures are present only in the northern section of the field. This prediction qualitatively agrees with the widening production trend in the north (Fig. III-C1). The fracture pore volume contributes to the higher porosity as seen in Fig. III-E5b. Fig. III-E6 shows that deeper-lying Mancos shale has fracture zones in the north as well as along the depth contour of 3300 m.

By comparing 1- and 2-D results, we observe a significant difference in fracture distribution and timing. Thus, we expect a similar difference in comparing 2- and 3-D results. Correlation diagrams were used to evaluate the agreement between 2- and 3-D simulations. Fig. III-E7 shows overpressure (bars) correlation diagrams for the transect L1 with data from a 3-D simulation. Note the correlation improves and degrades depending on the time in the basin history at which the correlation is made (here 35, 25, 15, 8 Ma). This shows that good correlation between 2- and 3-D simulations may only be an accidental relationship arising from a fortunate time in the basin's history. This finding strongly suggests that full 3-D simulations are required for prediction of fractured reservoir location and characteristics. Fig. III-E8 shows comparisons of porosity, fracture permeability, and overpressure profiles from the 2-D and 3-D simulations for the green point indicated Fig. III-D1. Neither fracture intensity nor the fracture zones appear to correlate well between 2- and 3-D simulations (see Figs. III-E8 – E9). This is suggested in Fig. III-E9 by the horizontal and vertical sets of points (trends) which indicate that there is appreciable fracturing in the 3-D simulation while there are no fractures in the 1-D simulation for that set of points.

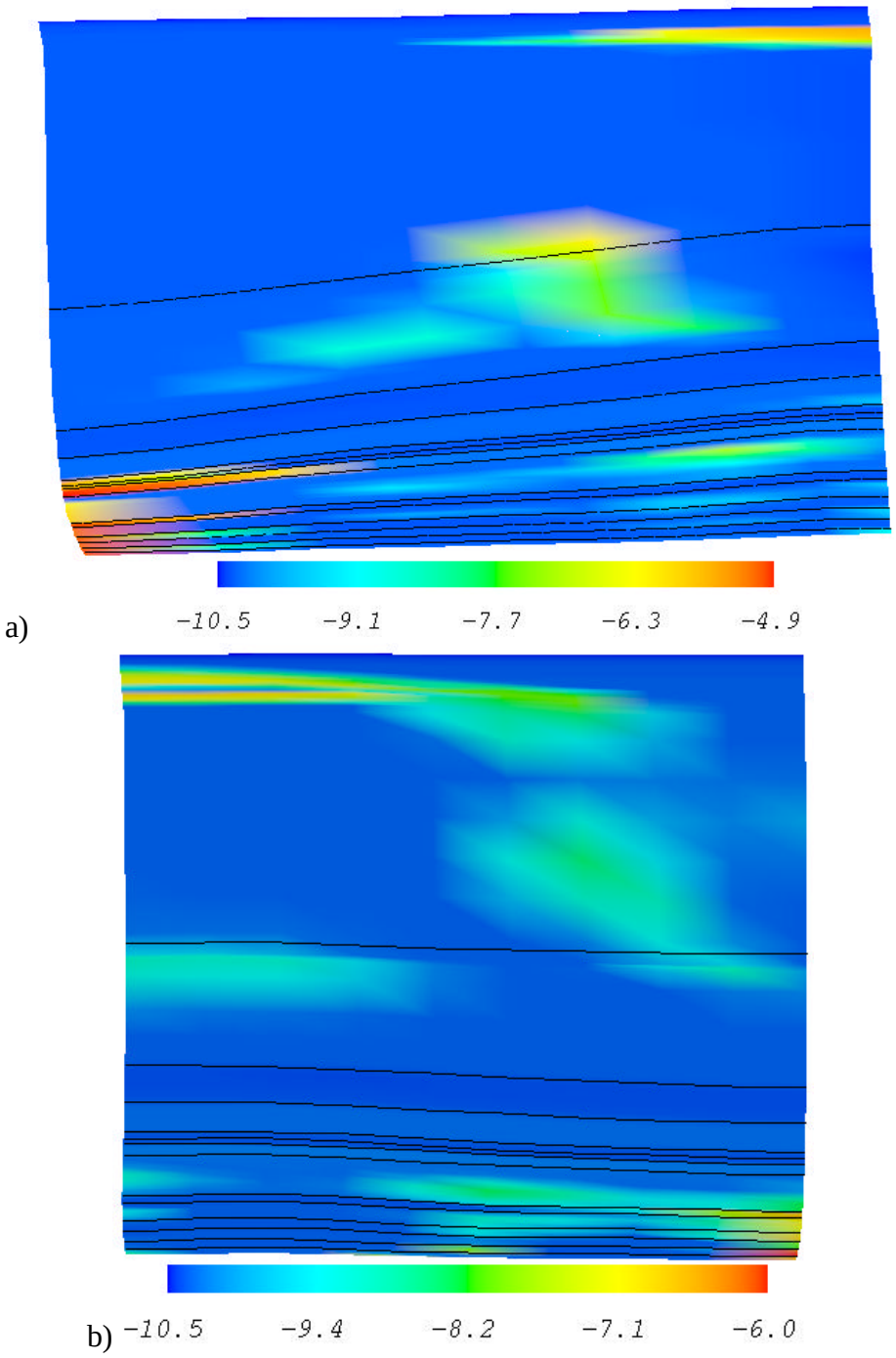

Fig. III-E1 Comparison of Basin RTM-predicted present day fracture permeability (log Darcy) for cross-sections L1 and L2 (see Fig. III-D1). for. When these two cases are integrated visually, they give a qualitative view of the 3-D complexity of the fracture zones. However, the 3-D nature of the stress tensor makes the true picture, as determined from 3-D simulation, more complex. For example, the fractures are not expected to be confined exclusively to the planes arbitrarily defined for 2-D simulations, and thus fluid flow may be directed away from either cross-section L1 or L2.

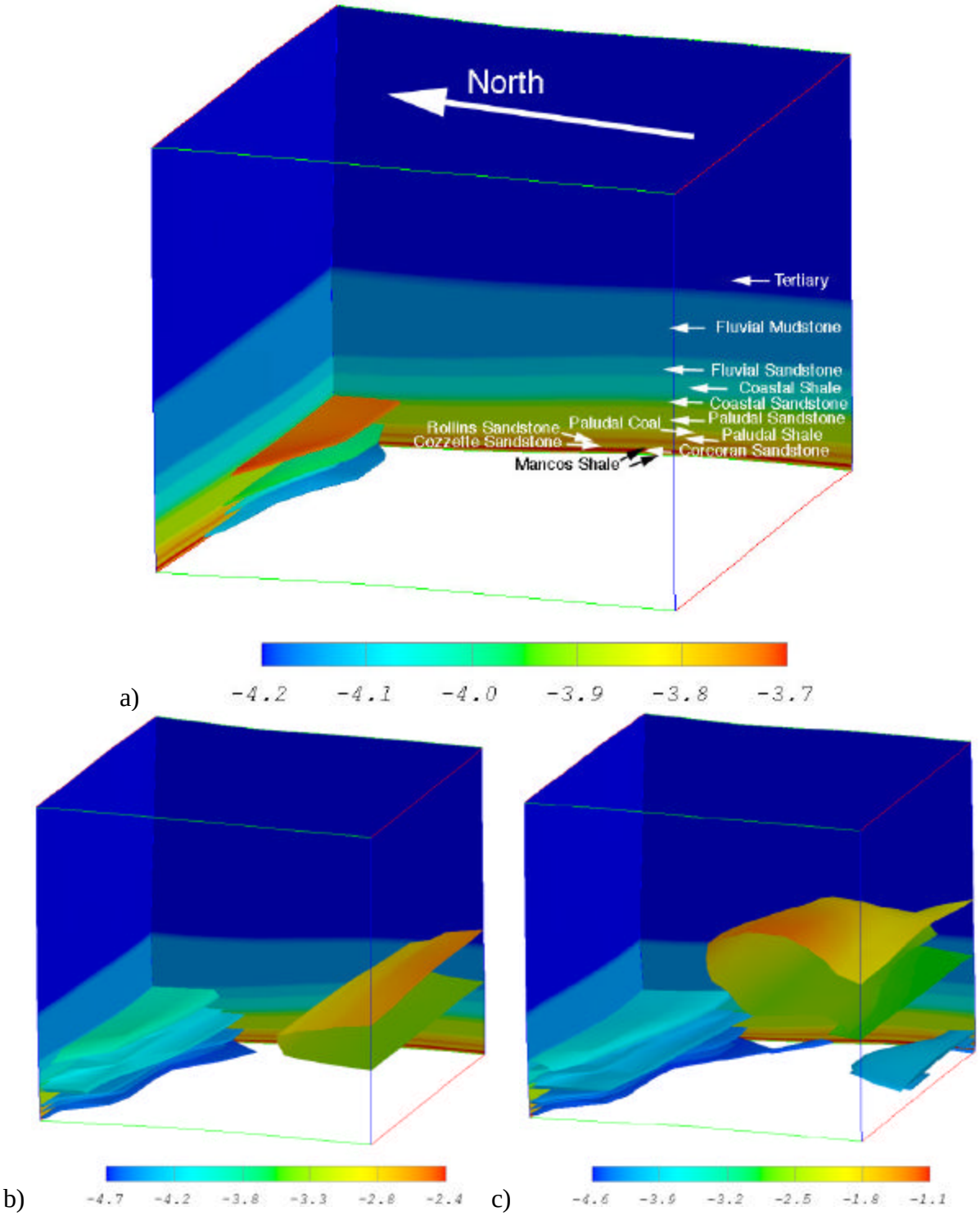
North
Tertiary
Fluvial Mudstone
Fluvial Sandstone
Coastal Shale
Coastal Sandstone
Paludal Sandstone
Paludal Shale
Corcoran Sandstone
Paludal Coal
Rollins Sandstone
Cozzette Sandstone
Mancos Shale
-4.2 -4.1 -4.0 -3.9 -3.8 -3.7
a)
b)
-4.7 -4.2 -3.8 -3.3 -2.8 -2.4
c)
-4.6 -3.9 -3.2 -2.5 -1.8 -1.1

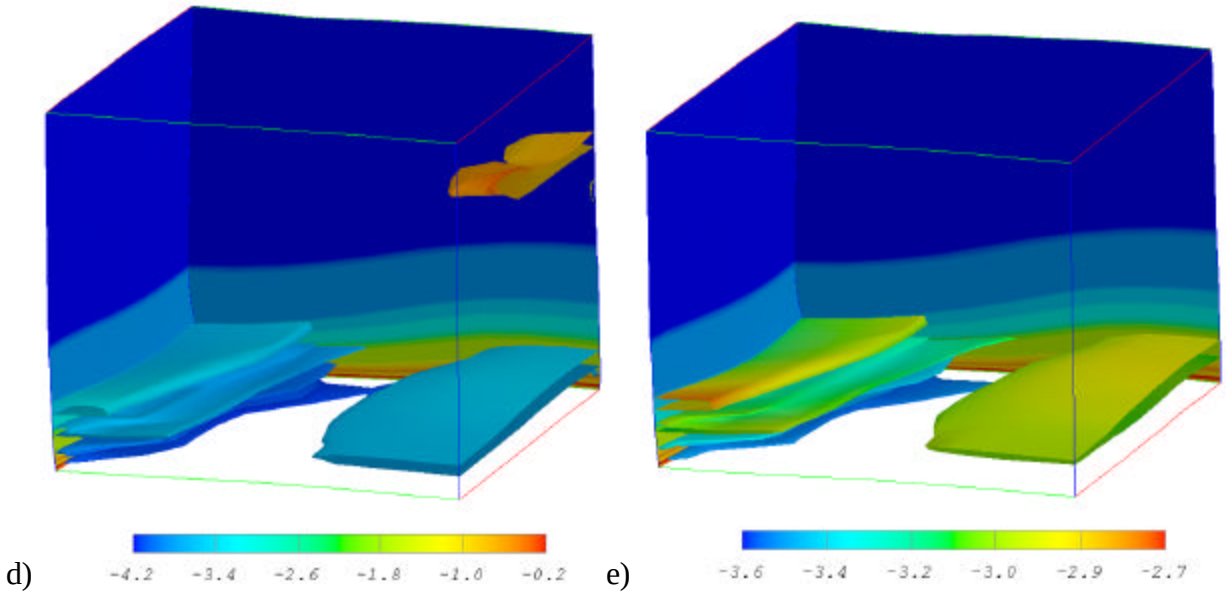

Fig. III-E2 Predicted isosurface of fracture permeability colored with depth (100 nano darcy) at 45, 35, 25, 15, 8 Ma (Rulison Field). The back panels indicate lithology index. Fractures started opening around 45 Ma on the north of the field. A fractured compartment formed in the south around 35 Ma which moved upwards and eventually disappeared around 15 Ma.

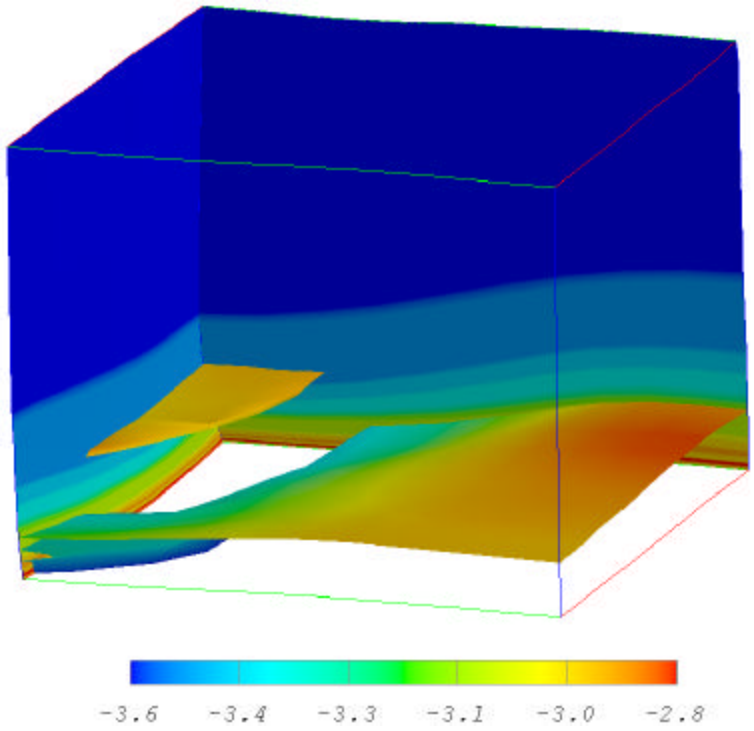

III-E3 Predicted isosurface of overpressure (475 bars) colored with depth at 8 Ma (Rulison Field). Complex topography of the isosurface is a result of significant variation of fracture permeability. Fractures in the north resulted in relatively lower fluid pressure there.

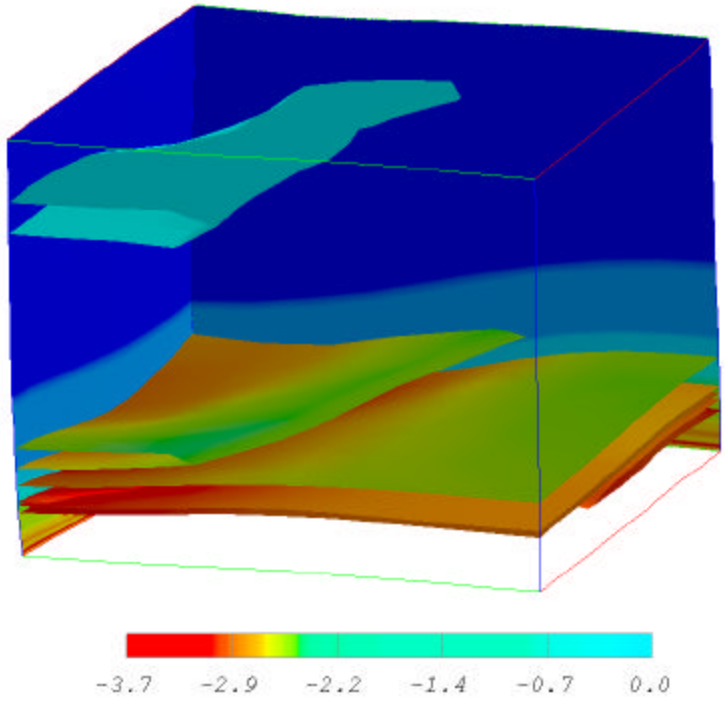

Fig. III-E4 Predicted isosurface of porosity (0.10) colored with depth at 8 Ma (Rulison Field). The variation of porosity in the same lithology is a combined result of fracturing, curvature, and fluid flow.

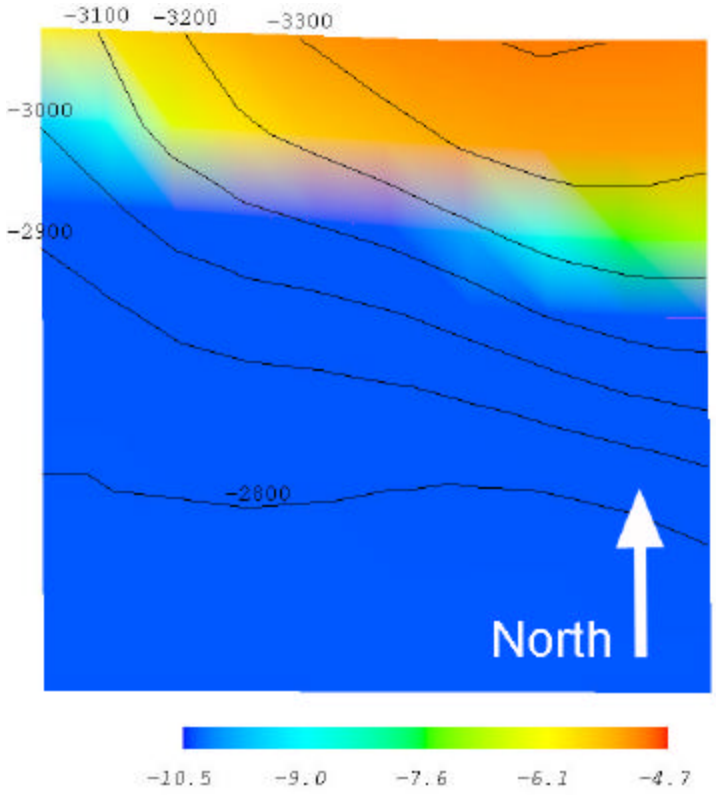
-3100
-3200
-3300
-3000
-2900
-2800
North
-10.5
-9.0
-7.6
-6.1
-4.7

a)

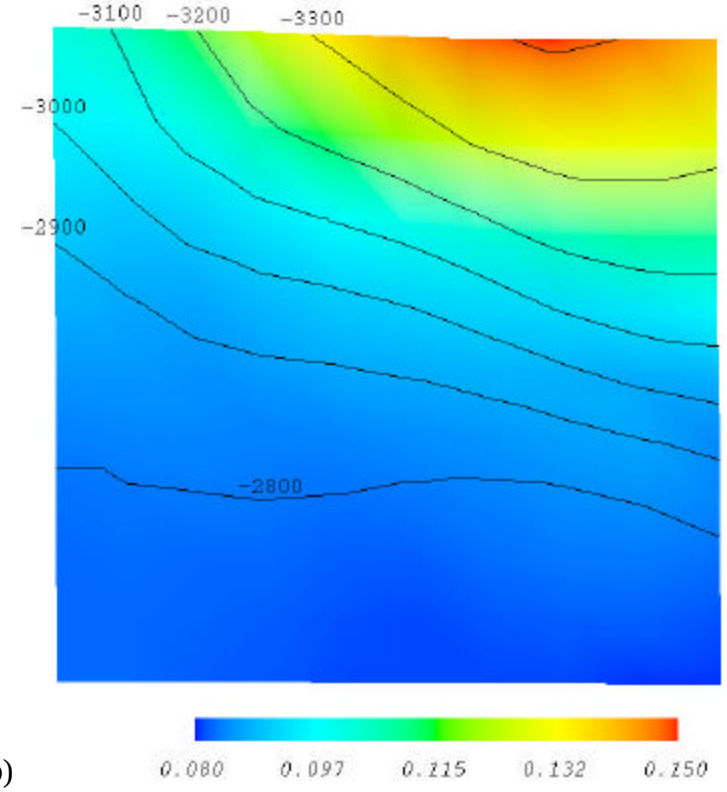
-3100
-3200
-3300
-3000
-2900
-2800
0.080
0.097
0.115
0.132
0.150

b)

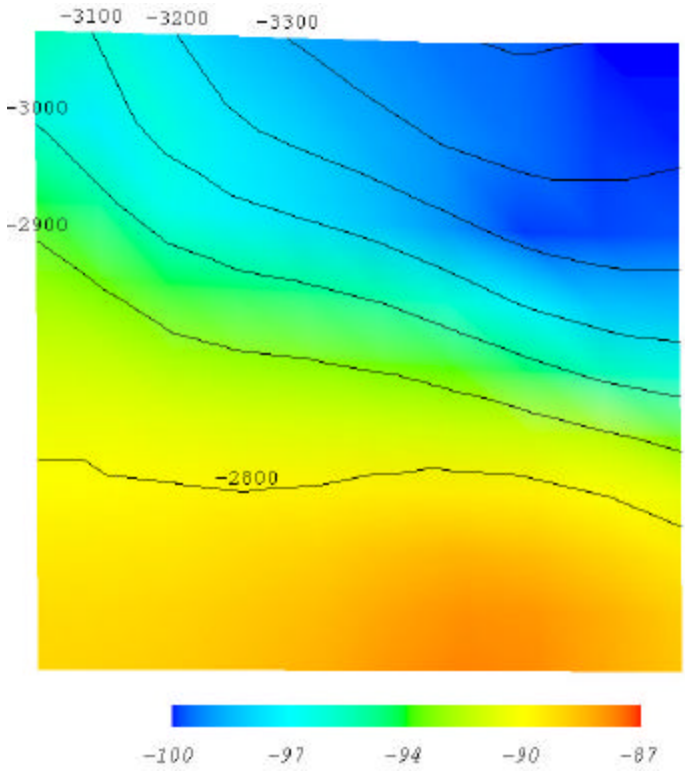

c)

Fig. III-E5 Predicted a) fracture permeability (log Darcy) b) porosity c) overburden stress (Mpa) in the Coastal Sandstone contoured with depth (m) at 8 Ma. The simulation domain is shown in Fig. III-D1.

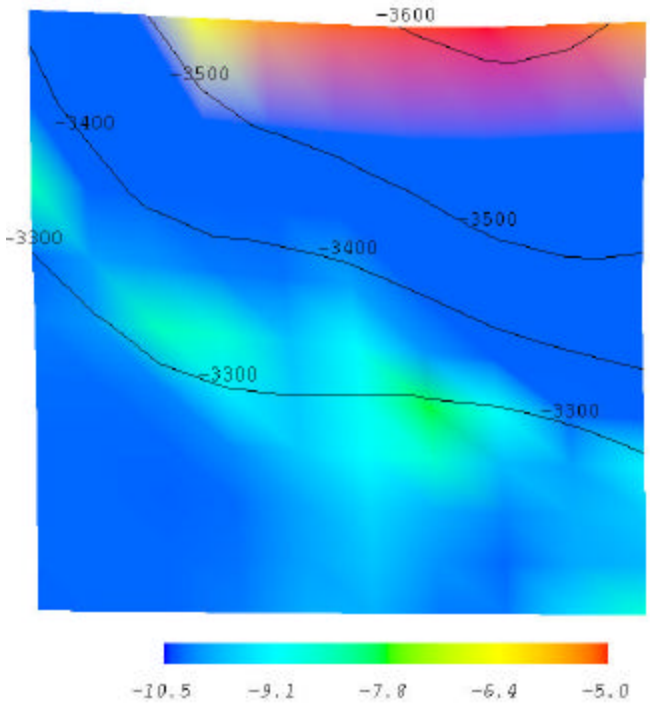

Fig. III-E6 Predicted fracture permeability (log Darcy) in the Mancos Shale contoured with depth (m) at 8 Ma. The simulation domain is shown in Fig. III-D1.

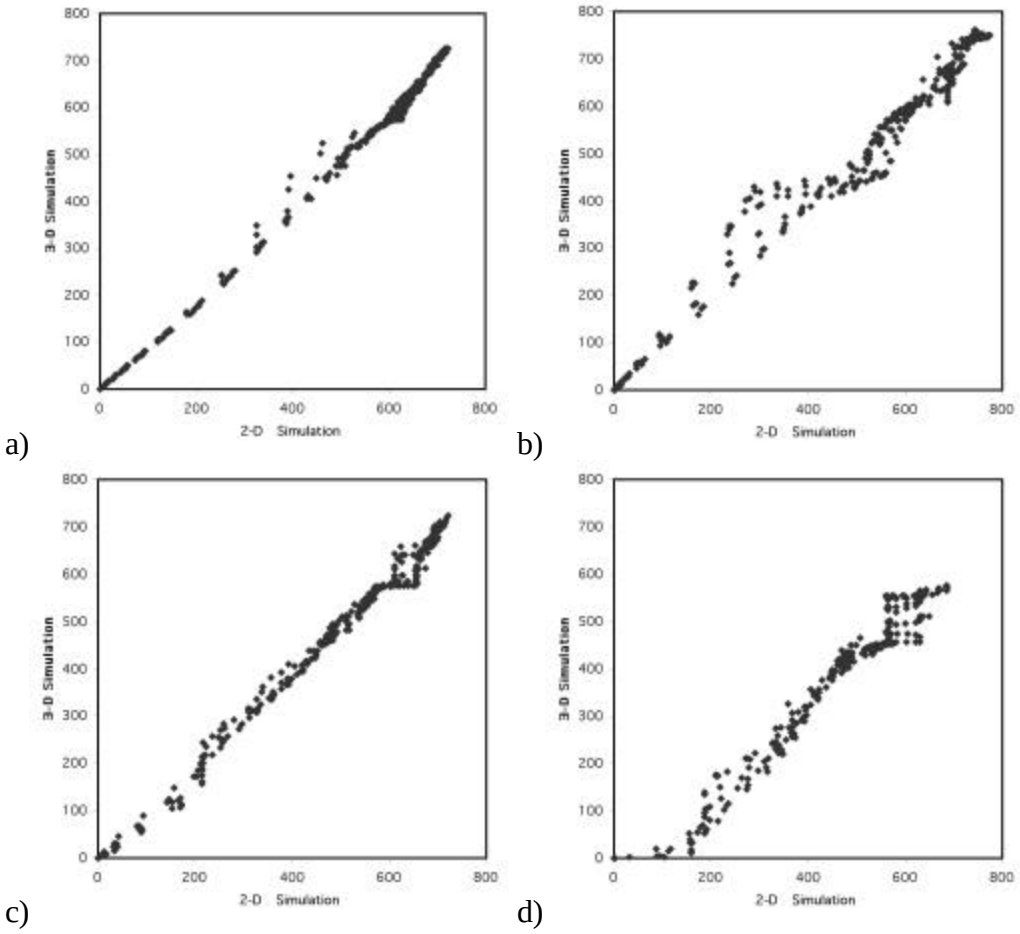

Fig. III-E7 Overpressure (bar) correlation diagrams showing the relation between 2- and 3-D simulations for the transect L1 of Fig. III-E1 at 35, 25, 15 and 8 Ma.

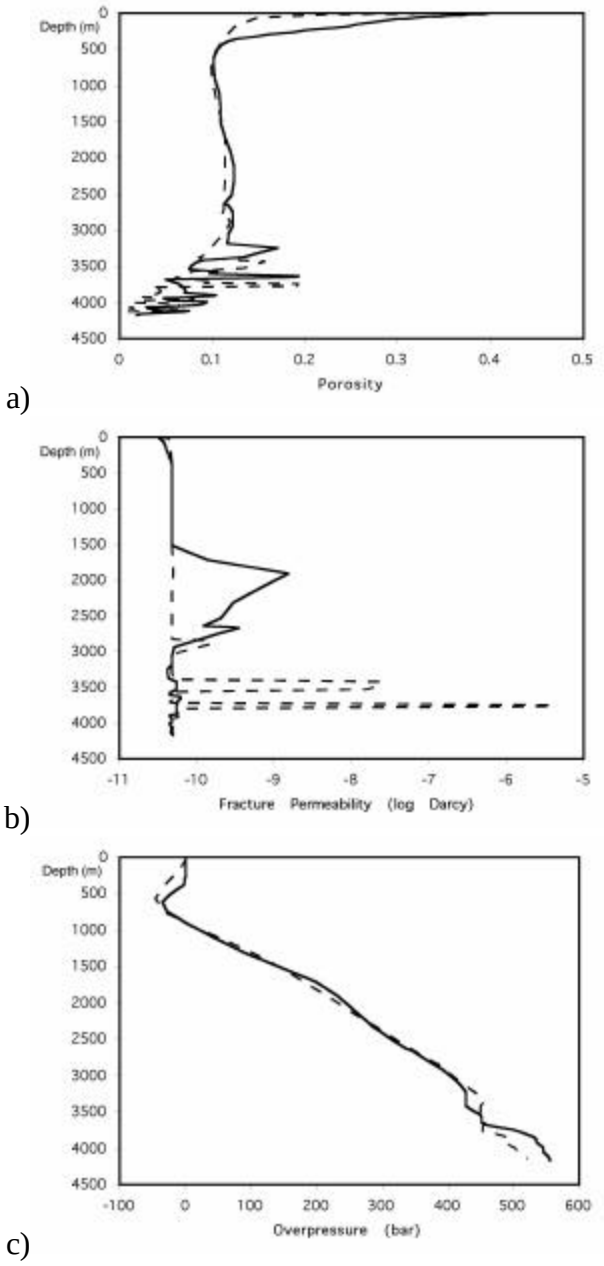

Fig. III-E8 Comparison of porosity, fracture permeability, and overpressure profiles from 2-D and 3-D results for the green point shown in Fig. III-D1 (solid lines represent 2-D simulation results). Although overpressure and porosity profiles seem to be similar, significant differences exist in the fracture permeability profiles. The fracture zones from 2-D and 3-D simulations do not overlap. This behavior results in the vertical and horizontal trends in Fig. III-E9.

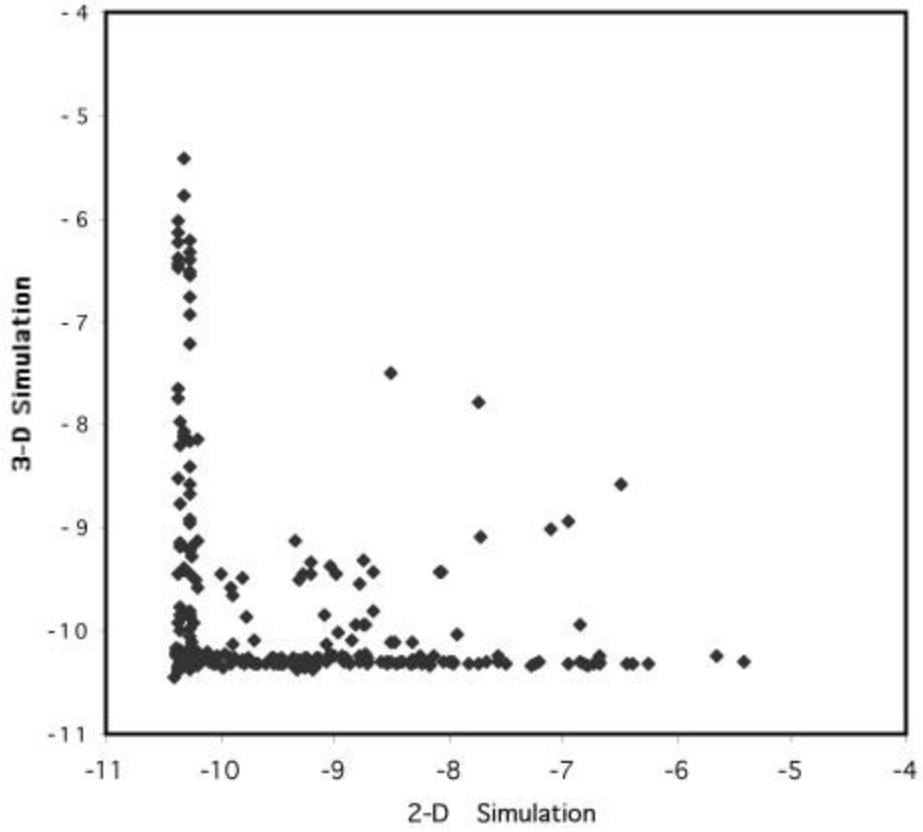

Fig. III-E9 Correlation diagram for fracture permeability between 2-D (L1 transect) and 3-D results at 8 Ma. Horizontal and vertical trends show that fracture zones do not overlap in 2-D and 3-D results.

IV. ORGANIC REACTIONS: MECHANISMS AND COUPLING TO MECHANICS

A. Overview

Much of the natural gas in Rocky Mountain basins is coal derived. As the kerogen evolves through thermal or bacterial processes, it tends to compact and expel volatiles. The devolatization can lead to a shrinkage that causes cleating. As cleating and compaction are key aspects of natural gas geological timescale expulsion, it was recognized that for more accurate predictions, we had to develop a model of coupled organic chemical/mechanical dynamics. The formalism we developed in this project is presented in the following sections.

As organic reactions transform kerogen, the organic solids tend to shrink due to loss of volatiles such as H_2O, CO_2 and CH_4 created by these reactions. The related loss of kerogen volume has two effects—a type of devolatilization compaction and an enhancement of the rate of transport due to cleating that follows from the mutually enhancing effects of kerogen matrix shrinkage and elevation of the fluid pressure within the pores of that matrix. In the following, a formulation is presented that captures these phenomena.

An important factor in the mechanics of the source material and the transport of natural gas is the rate and timing of natural gas generation and more generally, in the context of thermally derived gas from coal, is the organic chemical kinetics of lignin breakdown. We have developed a new lignin kinetics model to address this key issue. The model, summarized in Appendix D, is a breakthrough in kerogen kinetics, as all steps in our detailed multi-step model are based on well-established organic chemical principles and are calibrated with a variety of sources from the chemical and geochemical literature.

B. Formulation

Consider an amount of kerogen initially containing one mole of total organic carbon in the solid phase (TOCS). Let n_α ($\alpha = 1,2,\cdots N_{org}$) be the number of moles of organic constituting the solid molecules that are of type α in this mass of kerogen at any time *t*. The total number of moles of TOCS at any time, *n*, is given by

$$n = \sum_{\alpha=1}^{N_{org}} w_\alpha n_\alpha \le 1. \qquad \text{(IV.1)}$$

Here w_α is the number of carbon atoms in an α molecule. Although *n* is *1* initially, organic reactions decrease *n* in time as CH_4 and other volatile or, more generally, mobile species are produced and escape the organic solid (kerogen) mass. Let $\bar{V}_{ker}(\underline{x}, p, T)$ be the pressure and temperature-dependent volume of one mole of TOCS distributed among the various organic species in mole fractions $\underline{x}$ $(=\{x_1, x_2, \cdots x_{N_{org}}\})$ with $x_\alpha = n_\alpha / (n_1 + n_2 + \cdots n_{N_{org}})$. Thus,

$$V = n\bar{V}_{ker} \qquad \text{(IV.2)}$$

is the volume of the solid organic mass. Note that even if *n* remains constant, loss of, for example, adsorbed H_2O can cause decrease in *V* due to the $\underline{x}$-dependence of V_{ker}.

A first order reaction of the form

$$\text{species } \alpha \rightarrow \text{products} \qquad \text{(IV.3)}$$

decreases n_α at a rate proportional to n_α, i.e.,

$$\left(\frac{dn_a}{dt}\right)_{Rxn(VI.3)} = -k_{(VI.3)} n_a \,. \tag{IV.4}$$

However, a binary reaction of the cross-linking or other type, i.e.,

$$species\ \boldsymbol{a} + species\ \boldsymbol{a'} \rightarrow products \tag{IV.5}$$

contributes a rate of change of n_a that is proportional to both n_a and the probability that an $\boldsymbol{a}$ molecule is near an $\boldsymbol{a'}$ molecule. Let the latter be denoted $P_{aa'}$. Then

$$\left(\frac{dn_a}{dt}\right)_{Rxn(VI.5)} = -q n_a P_{aa'}. \tag{IV.6}$$

The probability $P_{aa'}$ is conditional, i.e., it measures the likelihood that, if there is an $\boldsymbol{a}$ molecule at a given point in space, then there is an $\boldsymbol{a'}$ unit within an interaction distance of that $\boldsymbol{a}$ molecule. One expects that for the rate to be symmetrical in $\boldsymbol{a}$ and $\boldsymbol{a'}$, we must have $n_a P_{aa'} = n_{a'} P_{a'a}$.

The simplest model for $P_{aa'}$ comes from a neglect of correlation. In that case, we assume that $P_{aa'}$ is proportional to the concentration $c_{a'}$ of $\boldsymbol{a'}$ in the organic solid:

$$P_{aa'} \propto c_{a'} \equiv \frac{n_{a'}}{n\bar{V}_{ker}} \,. \tag{IV.7}$$

Implicit in this ansatz is the assumption that either there are sufficient $\boldsymbol{a'}$ units near any $\boldsymbol{a}$ unit or that the $\boldsymbol{a'}$ units are free to migrate around the organic solid on a time scale shorter than that for reaction. On the contrary, if the organic solid immobilizes the $\boldsymbol{a'}$ units, then a given $\boldsymbol{a}$ can become stranded with no $\boldsymbol{a'}$ nearby and Rxn (IV.5) must halt even though there are still $\boldsymbol{a}$ and $\boldsymbol{a'}$ units left in the kerogen. Hence, $P_{aa'}$ should decay faster than linearly as $c_{a'}$ decreases. In fact, one expects there could be a threshold c^* for which $P_{aa'}$ vanishes when $c_{a'}$ decreases below c^*. However, in the present formulation, assumption (IV.7) is adopted for simplicity. With this, (IV.6) becomes

$$\left(\frac{dn_a}{dt}\right)_{Rxn(VI.5)} = \frac{-q n_a n_{a'}}{n\bar{V}_{ker}} \text{ (second order process).} \tag{IV.8}$$

As shrinkage occurs (i.e., as $n\bar{V}_{ker}$ decreases), the rate of reaction is enhanced by the $n\bar{V}_{ker}$ term (i.e., shrinkage brings reactants together) although the rate decreases quadratically with the *n*'s.

The above rate formulae can be used to generate the dynamics of the $\{n_1, n_2, \cdots n_{N_{org}}\}$. Let W_j be the rate of the *j*-th reaction (first or second order). Let v_{aj} be the stoichiometric coefficient for $\boldsymbol{a}$ in the *j*-th reaction (so that $v_{aj} > 0$ for products and <0 for reactants). With this,

$$\frac{dn_a}{dt} = \sum_{j=1}^{N_{Rxn}} v_{aj} W_j \tag{IV.9}$$

for the system with N_{Rxn} kerogen transformation reactions. The form of the W_j are taken here to be as in (IV.4) or (IV.6) for first or second order processes, respectively.

C. Fluid Mass Conservation

The above formalism can be used to generate the evolution of the organic solid material in a sediment and to thereby compute the rate of production of volatile and other mobile components due to organic diagenesis. Let ρ_c be the moles of TOCS per rock volume. If V_m is a macrovolume element, then there are $\tilde{n} = \rho_c V_m$ moles of TOCS in V_m. Each unit type $\alpha = 1, 2, \cdots N_{org}$ has $\tilde{n}_\alpha$ moles in V_m where $\tilde{n}$ is related to the $\tilde{n}_\alpha$ via a formula like (IV.1). With this, the number of moles of α units in V_m is $\tilde{n}$ $(= V_m \rho_c)$ times the fraction of the TOCS that is α (i.e., $\omega_\alpha n_\alpha / n$). If G_α is the number of moles of component α per rock volume, then

$$G_\alpha = \omega_\alpha \rho_c n_\alpha / n . \tag{IV.10}$$

These descriptive variables can be used to formulate an organic reaction-transport theory for the interacting pore fluid/organic solid system.

Let the rate of reaction of the *j*-th organic reaction per rock volume be denoted F_j. Let $\lambda_{\ell j}$ be the stoichiometric coefficient for mobile species ℓ in the *j*-th of the N_{org} reactions and C_ℓ be the concentration of ℓ per pore volume in all fluid phases. Then conservation of mass implies

$$\left(\frac{D\phi C_\ell}{Dt}\right)_{org} = \sum_{j=1}^{N_{org}} \lambda_{\ell j} F_j + \phi H_\ell - \vec{\nabla} \cdot \vec{J}_\ell - \phi C_\ell \vec{\nabla} \cdot \vec{u} \tag{IV.11}$$

where ϕ is porosity and *D/Dt* is the time derivative in a reference frame moving with a material (rock-fixed) point (i.e., at rock deformation velocity $\vec{u}$). The total concentration C_ℓ and flux $\vec{J}_\ell$ (relative to the rock-fixed frame) can be expressed in terms of the single phase quantities. If $m (= 1,2,\cdots N_{ph})$ identifies the *m*-th fluid phase, then

$$C_\ell = \sum_{m=1}^{N_{ph}} c_{\ell m} s_m \tag{IV.12}$$

$$\vec{J}_\ell = \sum_{m=1}^{N_{ph}} \vec{J}_{\ell m} \tag{IV.13}$$

where s_m is the saturation of phase *m* and $c_{\ell m}$ and $\vec{J}_{\ell m}$ are the concentration (moles/fluid volume) and the flux in the *m*-th phase for species ℓ.

The term H_ℓ represents the net rate of fluid reactions affecting fluid component ℓ. If U_{km} is the rate (moles/volume-time) of the *k*-th reaction in the *m*-th fluid phase, then

$$H_\ell = \sum_{m=1}^{N_{ph}} \sum_{k=1}^{N_{hm}} s_m \nu_{\ell mk} U_{km} \tag{IV.14}$$

where N_{hm} is the number of homogeneous reactions in the *m*-th fluid phase while the $\nu_{\ell mk}$ are stoichiometric coefficients. Expressions for the U_{km} and $\vec{J}_{\ell m}$ are those commonly used in the theory of homogeneous chemical kinetics and multi-phase flow, respectively. When some of the U_{km} are fast, (IV.11) can be transformed and equilibrium relations introduced using the multiple timescale methods of Ortoleva (1992, 1994a).

To compute the production rate of mobile species and keep track of the evolving TOCS density, it is useful to introduce a formal quantity $\mathbf{c}$ that keep track of the effect of compaction and other volume loss processes in the sediment. This quantity is, by definition, unity at deposition and evolves via the conservation law

$$\frac{D\mathbf{c}}{Dt} = -\mathbf{c}\vec{\nabla}\cdot\vec{u}\,. \tag{IV.15}$$

If $\mathbf{r}_c^0$ is the TOCS deposited initially for a given material point then, in the absence of any reactions $\mathbf{r}_c^0\mathbf{c}$ will be $\mathbf{r}_c$, the TOCS per rock volume at that point if no reactions affected TOCS. Thus, $\mathbf{r}_c^0\mathbf{c}$ represents $\mathbf{r}_c$ if no reactions took place. Then, the following are implied:

$$\begin{aligned}&\mathbf{r}_c^0\mathbf{c}n = \textit{evolving TOCS/rock volume}\\ &\mathbf{r}_c^0\mathbf{c}n_a = \textit{evolving moles of solid component } \mathbf{a}\textit{/rock volume}\end{aligned} \tag{IV.16}$$

From this it is seen that

$$F_j = \mathbf{r}_c^0\mathbf{c}W_j\,. \tag{IV.17}$$

for each of the N_{org} kerogen reactions $(\,j = 1, 2, \cdots N_{org}\,)$.

To illustrate the above formalism, consider a single reaction wherein a solid constituent *B* reacts via

$$B \rightarrow B' + \mathbf{l}CH_4 \tag{IV.18}$$

for product solid component B' and resulting $\mathbf{l}$ mobile CH_4 molecules. The rate of change W of the number of moles of B, n_B, in a sample initially with 1 mole of TOCS given by -W, $W = kn_B$. This produces $\mathbf{l}W$ moles of CH_4 per second for each initial mole of TOCS. Thus, the rate of mobile CH_4 production/rock volume-time is given by

$$\left(\frac{D(\mathbf{f}C_{CH_4})}{Dt}\right)_{Rxn(VI.18)} = \mathbf{l}\mathbf{r}_c^0\mathbf{c}W\,. \tag{IV.19}$$

This yields the rate of CH_4 production from the solid organic material in a macrovolume element of rock.

D. Rate of Strain from Kerogen Shrinkage

Reactions can lead to a decrease in organic solid volume. If the organic solids are stress-supporting, these reactions are thus a mechanism of shrinkage or other strain. Such shrinkage underlies cleating in coals. Here, a formalism for capturing this phenomenon within the present kerogen kinetic theory is presented.

Assume that the organic solids are stress supporting, i.e., a change in the volume of the organic solids is directly reflected in the rate of strain. Let V_m be the volume of a macrovolume element. At a time *t* it contains $V_m\mathbf{r}_c^0\mathbf{c}(t)n(t)$ moles of TOCS and thereby a volume $V_m\mathbf{r}_c^0\mathbf{c}(t)n(t)\bar{V}(t)$ is occupied by the organic solids within it. At a short time $\mathbf{d}t$ later, the $V_m\mathbf{r}_c^0\mathbf{c}(t)n(t)$ moles of TOCS are changed to $V_m\mathbf{r}_c^0\mathbf{c}(t)n(t+\mathbf{d}t)/n(t)$ moles. This occupies a

volume $V_m \rho_c^0 c(t) n(t+\delta t) \bar{V}(t+\delta t)/n(t)$. The change of volume $(\delta V)_{ker}$ due to kerogen reactions thus becomes

$$(\delta V)_{ker} = V_m \rho_c^0 c(t) \left[\frac{n(t+\delta t)\bar{V}(t+\delta t)}{n(t)} - \bar{V}(t) \right]_{ker} . \qquad \text{(IV.20)}$$

As δt is small, this implies that

$$(\delta V)_{ker} = \frac{V_m \rho_c^0 c}{n} \left(\frac{D(n\bar{V})}{Dt} \right)_{ker} \delta t . \qquad \text{(IV.21)}$$

Let $\underline{\dot{\varepsilon}}^{(ker)}$ be the rate of strain due to kerogen reactions. Assuming $\underline{\dot{\varepsilon}}^{(ker)}$ is diagonal ($\underline{\dot{\varepsilon}}^{(ker)} = \Omega \underline{1}$), the above results imply

$$3\Omega = \frac{\rho_c^0 c}{n} \left(\frac{D(n\bar{V})}{Dt} \right)_{ker} . \qquad \text{(IV.22)}$$

Using (IV.22), this may be expressed in terms of the kerogen reaction rates W_j via

$$3\Omega = \frac{\rho_c^0 c}{n} \sum_{a=1}^{N} \sum_{j=1}^{N_{ker}} \left[\bar{V} + n \frac{\partial \bar{V}}{\partial n_a} \right] \omega_a \nu_{aj} W_j . \qquad \text{(IV.23)}$$

This provides the explicit linkage between organic kinetics and mechanics.

The above formulation has assumed that the kerogen is all stress-supporting. However, as the kerogen content drops and, more notably, as the minerals take all the stress-supporting role, then Ω must drop to zero. Thus, if the organic solids are in the pores of a mineral matrix, then their change in volume makes no contribution to $\underline{\dot{\varepsilon}}$. Noting that $\rho_c^0 c\bar{V}$ is the volume fraction of the rock occupied by the organic solids, then a formula such as

$$\Omega = \frac{(\rho_c^0 c\bar{V})^g}{A^g + (\rho_c^0 c\bar{V})^g} \Omega_{(VI\,23)} \qquad \text{(IV.24)}$$

with coefficients g, A and with $\Omega_{(VI\,23)}$ given in (IV.23) has the qualitative features one might expect as the mode of TOCS passes below a critical value A.

V. AUTOMATED DATA/MODEL INTEGRATION

A. Formulation

A limitation to the use of Basin RTM or other basin simulators is the labor-intensive and often subjective nature of the process for generating the input data. The latter data includes the overall tectonic history (upheaval/subsidence and compression / extension / wrenching), basement heat flux and rates and character of sediment input. One of the conclusions of the present study is that Basin RTM is uniquely suited to serve as a basis for a new generation of basin modeling technology wherein the input data is generated automatically from observed seismic and other data. The general formulation of this approach is presented below. Setting forth this strategy is one of the main accomplishments of this project and will be implemented in a follow-on project, DOE contract #DE-AC26-00NT40689.

There are several challenges to practical basin modeling that the approach proposed here will address:

- the labor-intensive and subjective nature of the task of constructing the input data;
- the incompleteness of the model;
- that there are many textural variables that seismic or well-log attributes depend on so that there is no unambiguous way to invert this data (e.g., predict fractures from seismic data) unless greatly oversimplified assumptions are imposed; and
- an objective procedure is needed to estimate uncertainty/risk in any prediction.

The method we propose to solve these problems is based on information theory, and novel computational techniques for implementing it. The simultaneous use of multiple data types and our information theory algorithm are presented in Figs. V-1 and V-2.

The key to our automation approach is the use of the rich suite of Basin RTM output variables to generate synthetic well logs, seismic data, core analysis, downhole pressure measurements, etc. Denote any one of these data sets or subset of the data $W^{(k)}$; $W^{(k)}$ represents a set $\{W_1^{(k)}, W_2^{(k)}, \ldots W_{N^{(k)}}^{(k)}\}$ of $N^{(k)}$ data values of the k-th type. As $W^{(k)}$ is generated by Basin RTM, it depends on the set, denoted G, of Basin RTM input parameters. Let $O^{(k)}$ denote the set of observed values corresponding to the Basin RTM-predicted values $W^{(k)}$ (e.g., $O^{(1)}$ could be a observed suite of well logs and $W^{(1)}$ are those constructed from Basin RTM output). With this we can construct an error $E^{(k)}$ via

$$E^{(k)}(G) = \sum_{i=1}^{N^{(k)}} \left(W_j^{(k)}(G) - O_j^{(k)} \right)^2 . \qquad \text{(V.1)}$$

Then our scheme is to automatically determine the set G of input variables by constructing the probability $r(G)$ and, in particular, obtaining the most probable value of G, its expected uncertainty and, through r, the uncertainty in the predictions of interest (e.g., reservoir location and characteristics). Basin RTM can predict the variety of textured, fluid, stress and thermal properties needed to make this feasible.

Our methodology takes into account the fact that there are three distinct types of model input parameters:

- discrete variables taking on integer values (e.g., stoichiometric coefficients for chemical reactions);

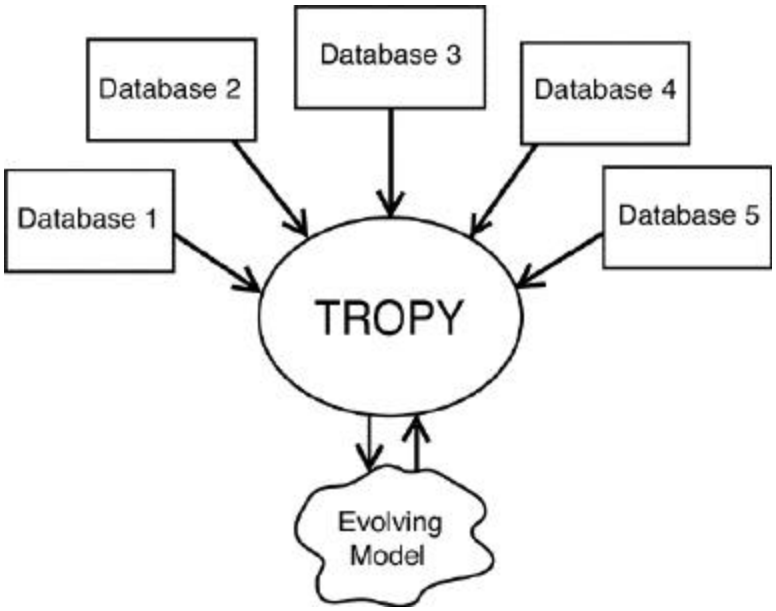

Fig. V-1 Multiple types of data of a range of quality are used to automatically calibrate and evolve a model through information theory as implemented in a shell program TROPY.

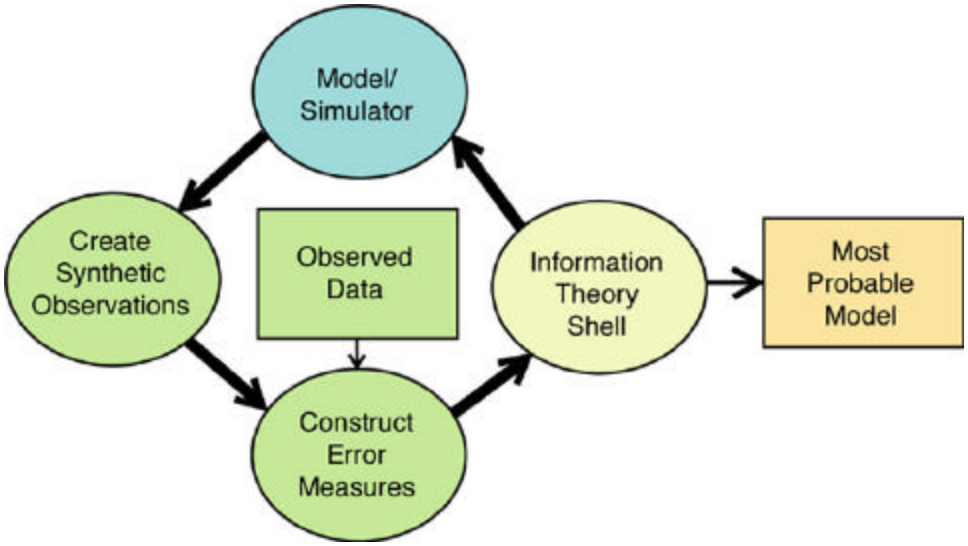

Fig. V-2 Algorithm used to integrate a mathematical/computational model with observed data to calibrate and develop a model in an automated and computationally parallel fashion. The thick arrows outline a fully parallel set of model runs which, when complete, yield information that our algorithm uses to construct the most probable model and associated risk/uncertainty. Our probability functional formulation also allows for the computation of the most probable spatial or temporal distribution or time course of variables not predicted by an incomplete model.

- continuous parameters (e.g., rheologic parameters, reaction rate coefficients, multi-phase flow parameters);
- functions of space/time (the history of overall tectonics, basement heat flux or sediment input rate/character at all points on the basin boundary.

The last type of data is not simply a set of numbers; rather, it is an uncountable set of values at each point on the boundary at each time over the basin history. To address these space/time variables, we have introduced a probability functional method (Tuncay and Ortoleva 2001b,c).

To illustrate our advanced method, consider only one data set O and correspondingly $W(G)$ and error E. Let G represent the history of the spatial distribution of heat flux from the basement to the sediment pile. Thus $G(x,y,t)$ is the heat flux into the bottom of the basin at point x,y at map-view point x,y at time t. The time t varies from the inception of the basin ($t=0$) to the present (t_p). In determining the x,y,t-dependence of G, one faces many uncertainties. Thus we introduce a probability $r(G)$ that depends on G at all x,y,t. As r depends on G at all x,y,t, it changes with the profile of G in space-time; as such it is not just a function of G but is termed a functional--i.e. depends on the functional form of $G(x,y,t)$. To address these problems, we introduced a probability functional formalism (Tuncay and Ortoleva 2001b,c). We then construct the entropy S and determine r as the probability functional that maximizes S subject to normalization of r, a constraint on the average expected error (E) and a regularization constraint (see Tuncay and Ortoleva 2001b,c). The result is that $G(x,y,t)$ satisfies

$$\frac{dE}{dG(x,y,t)} + L\left(\frac{\partial^2 G}{\partial x^2} + \frac{\partial^2 G}{\partial y^2} + l\frac{\partial^2 G}{\partial t^2}\right). \qquad \text{(V.2)}$$

The first term is the functional derivative of E with respect to $G(x,y,t)$. The x,y-derivative terms determine the length scale on which the simulations of interest can be expected to resolve the x,y-dependence of G given the spatial sparseness of the data set O and physical considerations. As the L parameter increases, the crudeness of the determination of G (i.e., the smoothness of the dependence of G on x,y) increases. Similarly, l is the square of the ratio of the spatial to the time resolution; as l increases, the solution of (V.2) becomes increasingly smoother.

What is remarkable about our approach is that it determines the most probable distribution of G and other boundary influences with the direct solution of a functional differential equation (e.g., (V.2)). This is much more efficient than an approach based on a Monte Carlo search for the minimum error E of (V.1). Also our method automatically builds into the computation the practical consideration of the most realistic, yet optimal, spatial resolution consistent with the available observed data coverage.

Our methodology can be generalized to include other Basin RTM input data (texture, mineralogic and rate of sediment input, erosion, overall tectonics, etc.) and sets of observations (seismic, core analysis, thermal, fluid, etc.). We believe that this method is the future of basin modeling--automatically integrating the data basin analysis/modeling activities.

B. Optimal Observed Data Basin RTM Input

The above information theory approach must be used with care and via a strategy that depends on the type of data that is available. Because of their importance for a Basin RTM simulation and their acknowledged uncertainty, we have concluded that the following factors are the most important input variables for determination by information theory:

- rock rheological parameters characterizing the very long time, continuous deformation—parameters not accessible to laboratory rock mechanics experiments;
- in particular, we need the universal parameters characterizing this rheology as it depends on mineralogy, mode, grain size and porosity, as well as meso-fracturing;
- the history of the distribution (latitude, longitude) of the heat flux into the basin from the basement, when intrusions are present, the time dependence of the spatial distribution of heat sources within the sediment pile is also created; and
- the time-course of the upheaval/subsidence of the basin/basement interface, as well as the history of compression, extension and wrenching at the basin lateral boundaries;

These conclusions follow from our Basin RTM numerical experiments described in Chapter III.

The observed data to be used by our information theory methodology depends on availability and quality of the data and the ease and computer speed with which it can be used. Benefits and drawbacks of several data types we have considered are as follows:

- downhole pre-production in fluid pressure is directly compatible with Basin RTM output; however, in tight formations it is fraught with measurement errors due to inadequate shut-in times as well as the fact that the measurements are often sensing the pressure response of a package of layers and not a single layer;
- seismic data has a great deal of information; however, Basin RTM output must be transformed to a synthetic seismic signal, for comparison with the observed data; this transformation introduces errors due to the completeness/accuracy of the synthetic seismic program and the formalism used to compute seismic wave velocities and attenuations from Basin RTM-predicted rock texture and mineralogy, fractures and fluid pressure, composition and phase pore volume (saturations);
- well logs have similar benefits and shortcomings as seismic data;
- core data is very directly comparable to Basin RTM output, but has very sparse spatial coverage;
- pore fluid composition is similar in benefits and shortcomings to core data.

In our follow-on study (DOE contract #DE-AC26-00NT40689) we are further evaluating these factors.

VI. DELIVERABLES FROM THIS GRANT

A. Final Report

- *Fractured Reservoirs E&P in Rocky Mountain Basins* (this report)

B. Piceance Basin Relational Database CD-ROM

- Technology Transfer

C. Papers in Refereed Journals

1. Payne, D.F., K. Tuncay, A. Park, J. Comer, and P. Ortoleva. 2000. A reaction-transport-mechanical approach to modeling the interrelationships between gas generation, overpressuring, and fracturing - Implications for the Upper Cretaceous natural gas reservoirs of the Piceance Basin, Colorado. *AAPG Bulletin* Vol. 84, 545-565.
2. Payne, D. F., and P. Ortoleva. 2001b. Methanogenesis.
3. Tuncay, K., A. Park, and P. Ortoleva. 2000d. Fractures, faults, and the nonlinear RTM dynamics of sedimentary basins. *Institute of Mathematics and its Applications (IMA) publication on Resource Recovery* (in press)

D. Lectures at National Meetings

1. Ortoleva, P., K. Tuncay, and A. Park. 1999. Basin evolution and salt tectonics: A 3-D multi-process crustal deformation model. AGU Fall Meeting, San Francisco, CA.
2. Tuncay, K., and P. Ortoleva. 2000. Three dimensional modeling of salt tectonics and rock deformation: E&P Implications. GEO2000, Bahrain.
3. Park, A., K. Tuncay, and P. Ortoleva. 2000. High-permeability vertical fracture network in carbonate platforms associated with basin-scale reaction-transport-mechanical processes. GEO2000, Bahrain.
4. Comer, J., A. Park, D. Payne, K. Tuncay, and P. Ortoleva. 2000. Fracture Prediction with a 3-D Finite Element Diagenetic, Hydrologic, Mechanical Model. *AAPG Annual Convention*, New Orleans, LA.
5. Ortoleva, P., A. Park, K. Tuncay. 2000. Basin simulation using reaction-transport-mechanical methodology with comprehensive compositional and textural composite-media approach. *GSA Meeting*, Reno, Nevada.
6. Comer, J.B., A. Park, K. Tuncay, and P. Ortoleva. 2000. Predicting fractures with a unique 3-D finite element mechanical, hydrologic, diagenetic model. *GSA Meeting*, Reno, Nevada.

E. Presentations at Petroleum Companies

1. Chevron, July 1997
2. Shell, December 1999
3. Chevron, July 2000
4. Exxon, March 2001

F. Invited Lectures at Academic Institutions

1. Ortoleva, P. Reaction-Transport-Mechanical Modeling of Sedimentary Basin Dynamics. *Texas A&M, Geological Sciences Dept*.

2. Probability Functionals, Homogenization and Comprehensive Reservoir Simulators" (with K. Tuncay) presented at "Resource Recovery" Conference, *Institute for Mathematics and Its Applications*, February 9-13 2000.

G. Technology Transfer

1. Booth, *AAPG Annual Convention*, New Orleans, LA.
2. Website (www.indiana.edu/~lcg).

REFERENCES

AAPG. 2000. Petroleum geology: Is there a future? *Explorer* (May), 3-9.

Advanced Resources International. 1995. *Naturally fractured tight gas reservoir detection optimization*. Annual status report to the U.S. Department of Energy. Contract DE-AC21-93MC30086.

Azzena, U., Denurra T., and Melloni G. 1996. Electron-transfer-induced reductive dealkoxylation of alkyl aryl ethers. II. Reductive cleavage of isomeric dimethoxybenzenes. *Gazzetta Chimica Italiana*, **126**, 141-145.

Bathe, K.-J., E. Ramm, and E. L. Wilson. 1975. Finite element formulations for large deformation dynamic analysis. *Int. J. Num. Meth. in Eng.* 9:353-386.

Behar, F., and Hatcher P.G. 1995. Artificial coalification of a fossil wood from brown coal by confined system pyrolysis. *Energy and Fuels*, **9**, 984-994.

Bell, J.L.S., and Palmer D.A. 1994. Experimental studies of organic acid decomposition. In *Organic Acids in Geological Processes* (Edited by Pittman E.D. and Lewan M.D.) Springer Verlag, Berlin, 226-269.

Berkowitz, B. 1995. Analysis of fracture network connectivity using percolation theory. *Mathematical Geology* 27:467-483.

Berryman, J. G. 1980. Long-wavelength propagation in composite elastic media I. Spherical inclusions, *J. Acoust. Soc. Am.* 68, 1809-1819.

Berryman, J. G. 1986. Effective medium approximation for elastic constants of porous solids with microscopic heterogeneity," J. Appl. Phys. 59, 1136-1140.

Bour, O., P. Davy. 1998. On the connectivity of three-dimensional fault networks. *Water Resource Research* 34: 2611-2622.

Bouska, V. 1981. *Geochemistry of Coal*. Elsevier Scientific Publishing, New York, 284 p.

Britt P.F., Buchanan A.C. III, Thomas K.B., and Lee S-K. 1995. Pyrolysis mechanisms of lignin: surface-immobilized model compound investigation of acid-catalyzed and free-radical reaction pathways. *Journal of Analytical and Applied Pyrolysis*, **33**, 1-19.

Buchanan, A.C. III, Britt P.F., and Struss J.A. 1997. Investigation of reaction pathways involved in lignin maturation. *Energy and Fuels*, **11**, 247-248.

Burnham, A.K., Oh M.S., and Crawford R.W. 1989. Pyrolysis of Argonne Premium Coals: Activation energy distributions and related chemistry. *Energy and Fuels*, **3**, 42-45.

Burnham, A.K, and Sweeney J.J. 1989. A chemical kinetic model of vitrinite maturation and reflectance. *Geochimicia et Cosmochimica Acta*, **53**, 2649-2657.

CRC Handbook of Chemistry and Physics 66th edition (Edited by Weast R.C.). 1986. CRC Press Inc., Boca Raton.

Charpenay, S., Serio M.A., Bassilakis R., and Solomon P.R. 1996. Influence of maturation on the pyrolysis products from coals and kerogens. 2. Modeling. *Energy and Fuels*, **10**, 26-38.

Chen, M. M. Bai, and J.-C. Roegiers. 1999. Permeability tensors of anisotropic fracture networks. *Mathematical Geology* 31:355-373.

del Rio, J.C., Gonzalez-Vila F.J., Martin F., and Verdejo T. 1994. Characterization of humic acids from low-rank coals by ^{13}C-NMR and pyrolysis-methylation; formation of benzenecarboxyl acid moieties during the coalification process. *Organic Geochemistry*, 22, 885-891.

Dewers, T. and P. Ortoleva. 1994a. Nonlinear dynamical aspects of basin hydrology: Fluid compartment formation and episodic fluid release. *American Journal of Science* 294: 713-755.

Dewers, T.A., and P. Ortoleva. 1994b. Formation of stylolites, marl/limestone alternations, and clay seams accompanying chemical compaction of argillaceous carbonates in (G.V. Chilingarian and K.H. Wolf, eds.) *Diagenesis IV: Developments in Sedimentology*, Elsevier, 155-216.

Finley, S.J. and J.C.Lorenz. 1988. Characterization of natural fractures in Mesaverde core from the multiwell experiment. *Sandia Report* SAND88-1800: 90 p.

Gilbert, K.E., and Gajewski J.J. 1982. Coal liquefaction model studies: free radical chain decomposition of diphenylpropane, dibenzyl ether, and phenyl ether via β-scission reactions. *Journal of Organic Chemistry*, **47**, 4899-4902.

Grant, D.M., and Pugmire R.J. 1989. Chemical model of coal devolatilization using percolation lattice statistics. *Energy and Fuels*, **3**, 175-186.

Grout, M.A. G.A. Abrams, R.L. Tang, T.J. hainsworth, and E.R. Verbeek. 1991. Late laramide thrust-related and evaporite domed anticlines in the southern piceance basin, northeastern colordo plateau. *AAPG Bulletin* 75: 205-218.

Gunneson, B.G., M.S. Wilson, and J.A. Labo. 1994. A structural history of the divide creek anticline, piceance basin, northwest colorado. *AAPG Annual Meeting program and Abstracts*, 160.

Gunneson, B.G., M.S. Wilson, and J.A. Labo. 1995. Divide creek anticline: a decapitated pop-up structre with two detacchment zones. In *High-Definition Seismic 2-D, 2-D Swath and 3-D Case Histories* ed by R.R. Ray: 31-45. Rocky Mountain Association of Geologists.

Hartgers, W.A., Sinninghe Damste J.S., and deLeeuw J.W. 1995. Curie-point pyrolysis of sodium salts of functionalized fatty acids. *Journal of Analytical and Applied Pyrolysis*, **34**, 191-217.

Hatcher, P.G. 1990. Chemical structural models for coalified wood (vitrinite) in low rank coal. in Advances in Organic Geochemistry 1989, Organic Geochemistry, **16**, 959-968.

Hatcher, P.G., Faulon J-L., Wenzel K.A., and Cody G.D. 1992. A structural model for lignin-derived vitrinite from high-volatile bituminous coal (coalified wood). Energy and Fuels, **6**, 813-820.

Hoak, T.E., A.L. Klawitler, and A.D. Decker. 1995. Delineation of Piceance Basin Basement structures using multiple source data: Implications for fractured reservoir exploration. *Intergas* 9515: 23 p.

Hoak, T.E. and Klawitter, A.L., 1999, Identifying Zones of Enhanced Permeability in the Piceance Basin, Northwest, Colorado, Extended Abstract in volume produced for Rocky Mountain Association of Geologists Symposium on Coalbed Methane, June 1999.

Hoak, T.E., Klawitter, A.L., and Witherbee, K.G., 1999, Naval oil shale lands may hold large Piceance gas potential, Oil and Gas Journal, March 8, 1999, 83-86.Hoering, T.C. 1984. Thermal reactions of kerogen with added water, heavy water and pure organic substances. *Organic Geochemistry*, 5, 267-278.

Johnson, R.C., and Nuccio V.F. 1986. Structural and thermal history of the Piceance Creek Basin, Western Colorado, in relation to hydrocarbon occurrence in the Mesaverde Group. In *Geology of tight Gas Reservoirs* (Edited by Spencer C.W. and Mast R.F.), AAPG Studies in Geology **24**, 165-205.

Kharaka, Y.K., Carothers W.W., and Rosenbauer R.J. 1983. Thermal decarboxylation of acetic acid: implications for origin of natural gas. *Geochimica et Cosmochimica Acta*, **47**, 397-402.

Kuroda, K-I. 1995. Contribution of an oxirane intermediate in the pyrolytic cleavage of the β-aryl ether substructure in lignin: pyrolysis of 3,4-dimethoxyphenyloxirane. *Journal of Analytical and Applied Pyrolysis*, **35**, 53-60.

Larson, K. W., D. W. Waples, H. Fu, and K. Kodama. 1993. Predicting tectonic fractures and fluid flow through fractures in basin modeling. In *Basin Modeling: Advances and Applications*, edited by A. G. Dore, NPF Special Publications 3, 373-383. Elsevier, Amsterdam: Norwegian Petroleum Society.

Lazana, M.C.R.L.R., Franco M.L.T.M.B., and Herold B.J. 1989. Electron-spin distribution in radical anions of aryl methyl ethers vs. reactivity and regioselectivity of their unimolecular fragmentation. *Journal of the American Chemical Society*, **111**, 8640-8646.

Levine, J.R. 1993. Coalification: the evolution of coal as source rock and reservoir rock for oil and gas. In *Hydrocarbons from Coal* (Edited by Law B.E. and Rice D.D.), AAPG Studies in Geology **38**, 39-77.

Lewan, M.D. 1999. Experiments on the role of water in petroleum formation. *Geochimica et Cosmochimica Acta*, in press.

Lorenz, J.C., and Finley, S.J. 1991. Regional fractures II: Fracturing of Mesaverde reservoirs in the Piceance Basin, Colorado. *AAPG Bulletin* 75, no. 11: 1738-1757.

Luo, X., and G. Vasseur. 1996. Geopressuring mechanism of organic matter cracking: numerical modeling. *AAPG Bulletin* 80: 856-873.

Luo, X., G. Vasseur, A. Pouya, V. Lamoureux-Var, and A. Poliakov. 1998. Elastoplastic deformation of porous medium applied to the modeling of compaction at basin scale. *Marine and Petroleum Geology* 15:145-162.

Luo, Y-R and Holmes J.L. 1993. The prediction of bond dissociation energies for common organic compounds. *Journal of Molecular Structure*, **281**, 123-129.

Manion, J.A., McMillen, D.F. and Malhotra R. 1996. Decarboxylation and coupling reactions of aromatic acids under coal-liquefaction conditions. *Energy and Fuels*, **10**, 776-788.

Mansuy, L. and Landais P. 1995. Importance of the reacting medium in artificial maturation of a coal by confined pyrolysis. 2. Water and polar compounds. *Energy and Fuels*, 9, 809-821.

Maubeuge, F., and I. Lerche. 1993. A north Indonesian basin: geo, thermal and hydrocarbon generation histories. *Marine and Petroleum Geology* 10:231-245.

Maubeuge, F., and I. Lerche. 1994. Geopressure evolution and hydrocarbon generation in a north Indonesian basin: two-dimensional quantitative modeling. *Marine and Petroleum Geology* 104:104-115.

Maxwell, J. M. 1997. The physical chemistry and nonlinear dynamics of compartment formation in sedimentary basins. Ph.D. diss., Indiana University.

McFall, K.S., Wicks D.E., Kuuskraa V.A., and Sedwick K.B. 1986. *A geologic assessment of natural gas from coal seams in the Piceance Basin, Colorado*. Gas Research Institute Topical Report, GRI 87/0060.

McMurry, R. G., and R. Tyler. 1996. Genetic stratigraphy and coal deposition of progradational sequences in the Upper Cretaceous Williams Fork Formation, Mesaverde Group, Piceance Basin, Colorado. In *Geologic and hydrologic controls critical to coalbed methane producibility and resource assessment: Williams Fork Formation, Piceance Basin, Northwest Colorado*, 112-148. Gas Research Institute Topical Report GRI-95/0532.

Meshri, I., and P. Ortoleva, eds. 1990. *Prediction of reservoir quality through chemical modeling*, AAPG Memoir 49. Tulsa, OK: AAPG.

Michels, R., Landais P., Philp R.P, and Torkelson B.E. 1995a. Influence of pressure and the presence of water on the evolution of the residual kerogen during confined, hydrous, and high-pressure hydrous pyrolysis of Woodford Shale. *Energy and Fuels*, **9**, 204-215.

Michels, R., Landais P., Torkelson B.E., and Philp R.P. 1995b. Effects of effluents and water pressure on oil generation during confined pyrolysis and high-pressure hydrous pyrolysis. *Geochimica et Cosmochimica Acta*, **59**, 1589-1604.

Michels, R., Langlois E., Ruau O., Mansuy L., Elie M., and Landais P. 1996. Evolution of Asphaltenes during artificial maturation: A record of the chemical processes. *Energy and Fuels*, **10**, 39-48.

Monthioux, M., Landais P., and Monin J-C. 1985. Comparison between natural and artificial maturation series of humic coals from the Mahakam delta, Indonesia. *Organic Geochemistry*, **8**, 275-292.

Murray, F.N., 1966, Stratigraphy and Structural Geology of the Grand Hogback Monocline, Colorado, Unpub. Ph.D. Dissertation, Univ. of Colorado-Boulder, 218 p.

NPC. 1999. Natural gas-meeting the challenges of the nations growing natural gas demand. A report of the National Petroleum Council. www. fe.doe.gov/oil_gas/npc/index.html.

Navid, A. and P. Ortoleva. 2001a. Simulation of Metabolism in Pig Liver Cells, submitted for publication.

Navid, A. and P. Ortoleva. 2001b. Multi-Compartmentalized Metabolic Model of Glycolysis in *Trypanosoma Brucei,* submitted for publication.

Obeng, M. and Stock L.M. 1996. Distribution of pendant alkyl groups in the Argonne premium coals. *Energy and Fuels*, **10**, 988-995.

Oda, M. 1982. Fabric tensor for discontinous geological materials. *Soils and Foundations* 22: 96-108.

Oda, M. 1985. Permeability tensor for discontinous rock masses. Geotechnique 35: 483-495.

Oda, M. 1986. An equivalent continuum model for coupled stress and fluid flow analysis in jointed rock masses. Water Resources Research 22:1845-1856.

Odling, N.E. 1992. Network properties of a two-dimensional natural fracture pattern. Pure and Applied Geophysics 138:95-114.

Ortoleva, P., ed. 1990. *Self-organization in geological systems: Proceedings of a Workshop held 26-30 June 1988, University of California at Santa Barbara. Earth Science Reviews* 29(1-4) (special issue).

Ortoleva, P. 1992. *Nonlinear chemical waves*. New York: John Wiley and Sons.

Ortoleva, P. 1994a. *Geochemical self-organization*. New York: Oxford University Press.

Ortoleva, P. 1994b. *Basin compartments and seals*, AAPG Memoir 61. Tulsa, OK: American Association of Petroleum Geologists.

Ortoleva, P. 1998. *Basin compartment fundamentals*. Topical report submitted to Gas Research Institute (GRI Project No. 5092-260-2443).

Ortoleva, P. 1999. *Basin compartments.* New York: Oxford University Press. In press.

Ortoleva, P. 2001. *Mesoscopic chemical physics*. In preparation.

Ozkan, G., and P. Ortoleva. 2000. Evolution of gouge grain size distribution: A Markov model. Submitted for publication.

Ozkan, G., K. Tuncay, and P. Ortoleva. 1998. Process-based fault seal/conduit prediction. In *1998 AAPG Annual Convention Abstracts* (CD-ROM format), Salt Lake City, UT, May 17-28, 1998. Forthcoming.

Patel, K.M., Baltisberger R.J., Stenberg V.I., and Woolsey N.F. 1982. Reductive cleavage mechanism of diphenyl ether and apparent ipso trapping of an intermediate radical anion with a silyl ether. *Journal of Organic Chemistry*, **47**, 4250-4254.

Payne, D.F., and Comer J.B. 1997. Geological overview of the Piceance Basin: In Naturally Fractured Tight Gas Reservoir Detection Optimization. A Three-dimensional, Basin Diagenesis, Hydrologic, Mechanical Modeling Approach. Laboratory for Computational Geodynamics internal report, 121-143.

Payne, D. F. 1998. A new, fully coupled reaction-transport-mechanical approach to modeling the evolution of methane reservoirs in the Piceance Basin. Ph.D. Dissertation, Department of Geological Sciences, Indiana University, Bloomington, Indiana.

Payne, D. F., and P. J. Ortoleva. 2001a. Lignin maturation – A chemical structural kinetics model. In preparation.

Payne, D.F., and P.J. Ortoleva. 2001b. Methanogenesis.

Payne, D. F., K. Tuncay, A. Park, J. B. Comer, and P. Ortoleva. 2000. A reaction-transport-mechanical approach to modeling the interrelationships among gas generation, overpressuring, and fracturing: Implications for the Upper Cretaceous. Natural gas reservoirs of the Piceance Basin, Colorado. *AAPG Bulletin* 84:545-565.

Petit, J.C. 1991. A comprehensive study of the water vapour/coal system: application to the role of water in the weathering of coal. *Fuel*, **70**, 1051-1058.

Qin, C., and P. Ortoleva. 1994. Banded diagenetic pressure seals: Types, mechanisms, and homogenized basin dynamics. In *Basin compartments and seals*, AAPG Memoir 61, edited by P. Ortoleva, 385-400. Tulsa, OK: AAPG.

Rice, J. R. 1975. Continuum mechanics and thermodynamics of plasticity in relation to microscale deformation mechanisms. In *Constitutive equations in plasticity,* edited by A. S. Argon, 23-79. Cambridge, Massachusetts: MIT Press.

Rice, J. R. 1992. Fault stress states, pore pressure distributions, and the weakness of the San Andreas Fault. In *Fault mechanics and transport properties of rocks,* edited by B. Evans and T.-F. Wong, 475-503. New York: Academic Press.

Rightmire, C.T., and Choate R. 1986. Coal-bed methane and tight gas sands interrelationships. In *Geology of Tight Gas Reservoirs* (Edited by Spencer C.W. and Mast R.F.) AAPG Studies in Geology **24**, 87-110.

Roberts, S. J., and J. A. Nunn. 1995. Episodic fluid expulsion from geopressured sediments. *Marine and Petroleum Geology* 12:195-204.

Sakrani, K. 1996. A unified texture and mineralogy dependent model for rock deformation. Ph.D. diss., Indiana University, Bloomington.

Sattler, A.R. 1988. Core Analysis, in Multiwell Experiment Final Report: II. The Paludal Interval of the Mesaverde Formation. Sandia National Laboratories report SAND88-1008, UC-92, 5.1-5.50.

Schneider, F.,

J. L. Potdevin, S. Wolf, and I. Faille. 1996. Mechanical and chemical compaction model for sedimentary basin simulators. *Tectonophysics* 263:307-317.

Scott, A. R. 1996. Coalification, cleat development, coal gas composition and origins, and gas content of Williams Fork coals in the Piceance Basin, Colorado. In *Geologic and hydrologic*

controls critical to coalbed methane producibility and resource assessment: Williams Fork Formation, Piceance Basin, Northwest Colorado, 220-251. Gas Research Institute Topical Report GRI-95/0532.

Scott, A.R., Tyler R., Kaiser W.R., McMurry R.G., Nance H.S., and Tremain C.M. 1996. Coal and coalbed methane resources and production in the Piceance Basin, Colorado: In *Geologic and Hydrologic Controls Critical to Coalbed Methane Producibility and Resource Assessment: Williams Fork Formation, Piceance Basin, Northwest Colorado*, GRI Topical Report, GRI-95/0532, 269-285.

Sibo, W., D. F. Payne, and P. Ortoleva. 1998. Automated three-dimensional sediment geometry and history reconstruction. Forthcoming.

Solomon, P.R., Serio M.A., Carangelo R.M., Bassilakis R., Gravel D., Baillargeon M., Baudais F., and Vail G. 1990. Analysis of the Argonne premium coal samples by thermogravimetric fourier transform infrared spectroscopy. *Energy and Fuels*, **4**, 319-333.

Solum, M.S., Pugmire R.J., and Grant D.M. 1989. ^{13}C Solid-state NMR of Argonne premium coals. *Energy and Fuels*, **3**, 187-193.

Snyder, M. D., and K.J. Bathe. 1981. A solution procedure for thermo-elastic-plastic and creep problems. *Nuclear Engineering and Design* 64:49-80.

Song, C., Saini A.K. and Schobert H.H. 1994. Effects of drying and oxidation of Wyodak subbituminous coal on its thermal and catalytic liquefaction. Spectroscopic characterization and products distribution. *Energy and Fuels*, **8**, 301-312.

Sonnenthal, E., and P. Ortoleva. 1994. Numerical simulations of overpressured compartments in sedimentary basins. In *Basin compartments and seals*, AAPG Memoir no. 61, edited by P. Ortoleva, 403-416. Tulsa, Oklahoma: AAPG.

Stach, E., Mackowsky M-Th., Teichmuller M., Taylor G.H., Chandra D., and Teichmuller R. 1982. Stach's Textbook of Coal Petrology. Gebruder Borntraeger, Berlin, 535 p.

Stalker, L., Farrimond P., and Larter S.R. 1994. Water as an oxygen source for the production of oxygenated compounds (including CO_2 precursors) during kerogen maturation. in *Advances in Organic Geochemistry 1993, Organic Geochemistry*, **22**, 477-486.

Suuberg, E.M., Lee D., and Larsen J.W. 1985. Temperature dependence of crosslinking processes in pyrolysing coals. *Fuel*, **64**, 1668-1671.

Tegelaar, E.W., deLeeuw J.W., Derenne S., and Largeau C. 1989. A reappraisal of kerogen formation. *Geochimica et Cosmochimica Acta*, **53**, 3103-3106.

Thomson, M.E., and S.R. Brown. 1991. The effect of anisotropic surface roughness on flow and transport in fractures. *Journal of Geophysical Research* 96: 21923-21932.

Tuncay, K., S. Romer, T. Hoak, K. Sundberg, and P. Ortoleva. 1998. Predicting the natural state of fractured carbonate reservoirs: An Andector Field, West Texas test of a 3-D RTM simulator. In the Final Report submitted to DOE (Contract No. DE-AC22-94PC91008), September 1998.

Tuncay, K., A. Park, and P. Ortoleva. 2000a Sedimentary basin deformation: An incremental stress rheology approach. *Tectonophysics*, Vol. 323, 77-104.

Tuncay, K., A. Park, and P. Ortoleva. 2000b. A forward model of three dimensional fracture orientation and characteristics. *Journal of Geophysical Research* Vol. 105, 16719-16735.

Tuncay, K., and P. Ortoleva. 2001a. Salt tectonics as a self-organizing process: a three dimensional reaction, transport and mechanics model. *Journal of Geophysical Research*, **106**, 803-818.

Tuncay, K., and P. Ortoleva. 2001b. Probability functionals, homogenization and comprehensive reservoir simulators. *IMA Monograph on Resource Recovery* (in press).

Tuncay, K., and P. Ortoleva. 2001c. A probability functional and homogenization approach for imaging hydrologic systems. Water Resources Research.

Tuncay, K., A. Park, and P. Ortoleva. 2000d. Fractures, faults, and the nonlinear RTM dynamics of sedimentary basins. *Institute of Mathematics and its Applications (IMA) publication on Resource Recovery* (in press).

Tyler, R. 1996. Tectonic evolution and stratigraphic setting of the Piceance Basin, Colorado: A review. In *Geologic and hydrologic controls critical to coalbed methane producibility and resource assessment: Williams Fork Formation, Piceance Basin, Northwest Colorado*, 1-32. Gas Research Institute Topical Report GRI-95/0532.

Tyler, R., and R. McMurry. 1995. Genetic stratigraphy, coal occurrence, and regional cross section of the Williams Fork Formation, Mesaverde Group, Piceance Basin, northwestern Colorado. Colorado Geological Society open file report 95-2, Department of Natural Resources, Denver, Colorado.

Ungerer, P., J. Burrus, B. Doligez, P. Y. Chenet, and F. Bessis. 1990. Basin evaluation by integrated two-dimensional modeling of heat transfer, fluid flow, hydrocarbon generation, and migration. *AAPG Bulletin* 74:309-335.

Waite, M.E., S. Ge., H. Spetzler, and D.B. Bahr. 1998. The effect of surface geometry on fracture permeability: A case study using a sinusoidal fracture. *Geophysical Research Letters* 25: 813-816.

Wang, C., and X. Xie. 1998. Hydrofracturing and episodic fluid flow in shale-rich basins - A numerical study. *AAPG Bulletin* 82:1857-1869.

Weitzke, E. and P. Ortoleva. 2001. Cyber-Cell: A Compartmentalized Cell Model With Genomic/Proteomic and Metabolic Kinetics, submitted for publication.

Zhang, E., Tang Y., Hill R., Liu J., Foss D.C., and Chung E.Y. 1997. Kinetic and basin modeling of gas generation form the Cameo Coal, Piceance Basin, Northwest Colorado. Chevron internal report.

Zienkiewicz, O. C., and I. C. Cormeau. 1974. Visco-plasticity–plasticity and creep in elastic solids—A unified numerical solution approach. *International Journal for Numerical Methods for Engineering*, 8:821-845.

APPENDIX A: THE PICEANCE BASIN DATA SET

A. Introduction

In this section, we review the Piceance Basin data set to illustrate its richness and comment on some of its limitations.

Many reservoirs in Rocky Mountain basins are plagued by low matrix permeability so that economic production is only achieved in fractured zones. Therefore, many important aspects of reservoir location and characteristics are expected to be related to fractures, which in turn, are related to excess fluid pressure. An important case is the tight gas reservoirs in the Upper Cretaceous Mesaverde Group of the Piceance Basin (Colorado). The gas-rich Piceance Basin holds many lessons for neighboring Rocky Mountain gas-producing basins because it shares many of the same formations and the timing and intensity of tectonics are similar. Furthermore, the Piceance Basin has been the subject of extensive U.S. DOE and GRI supported research.

B. Basin Context

The Piceance Basin, located in northwestern Colorado, formed during the Late Cretaceous through Eocene Laramide Orogeny. It is an asymmetric basin with a northwest-southeast oriented axis and its steeper flank on the northeast side (Fig. A-1). The Piceance Basin is bounded by the White River Uplift to the east, the Sawatch Uplift to the southeast, the San Juan volcanics to the south, the Uncompaghre Uplift to the southwest, the Douglas Creek Arch to the west, the Uinta Uplift to the northwest, and the Axial Arch Anticline to the north.

The Upper Cretaceous Mesaverde Group constitutes the most important source and reservoir rock for natural gas in the Piceance Basin. It was deposited during the Late Cretaceous, before and coincident with incipient uplift surrounding the basin. The Mesaverde Group is mostly Campanian in age and includes the marine shales and sandstones of the Iles Formation and the coal-bearing paludal, coastal, and fluvial sandstone and shale sequences of the Williams Fork Formation (Fig. A-2). The Mesaverde Group is underlain by the marine Mancos Shale, which is mostly Coniacian and Santonian in age (Tyler 1996). The contact between the Mancos and the overlying Iles Formation locally is difficult to identify because it is commonly represented by coarsening-upward regressive marine siliciclastic sequences. The regressive marine sequences are capped by shoreline sandstones, including from oldest to youngest the Sego, Corcoran, Cozzette, and Rollins (Trout Creek) Sandstone Members. The contact between the Iles and the Williams Fork Formations is abrupt and marked by the transition from sandstone to coal or shale of the Paludal Cameo-Wheeler-Fairfield coal zone, the major coal-bearing sequence in the Mesaverde. The Iles-Williams Fork contact lies at the top of the Rollins Sandstone and is the most easily recognized and mappable horizon in the Mesaverde Group.

During deposition of the marine sediments of the Iles Formation, the Piceance Basin was part of the subsiding western margin of the Late Cretaceous epeiric seaway and was bordered by the Sevier Orogenic belt to the west. Stresses from the Sevier Orogeny caused east-west compression during deposition of Upper Cretaceous and lower Tertiary sediments (see Appendix B). Following deposition of the underlying marine Mancos Shale, episodic uplift from the Sevier Orogenic belt produced pulses of clastic sediments that formed a series of progradational sequences. These progradational sequences are interspersed with transgressive marine shales (Mancos tongues) which together comprise the laterally extensive interbedded marine sandstones and shales characteristic of the Iles Formation (Fig. A-3). Each progradation advanced further to the southeast (Fig. A-4), with the progradational limit of the Rollins extending beyond the

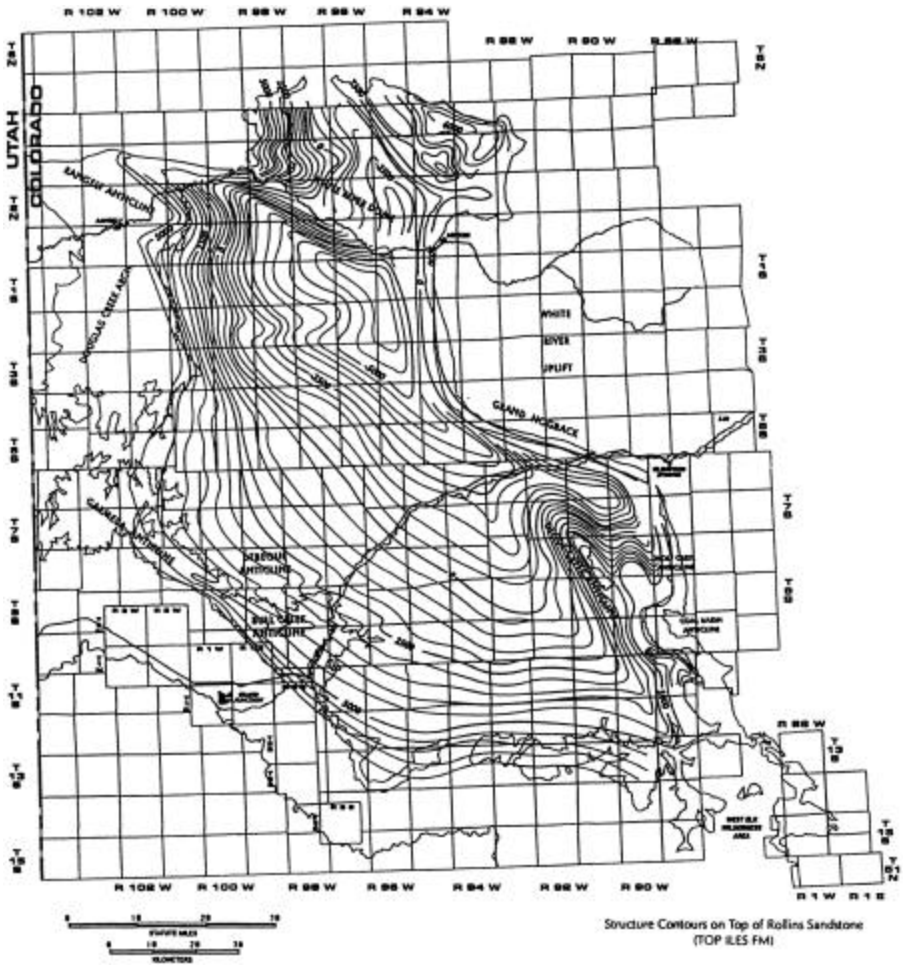

Fig. A-1 Structure map of the Piceance Basin in northwestern Colorado. Contour lines show elevation at the top of Rollins sandstone member of the Iles Formation, Mesaverde Group. This figure shows the asymmetry of the basin, with the steep flank on the northeast side and the basin axis oriented NW-SE (from Advanced Resources International 1995). Such structural maps may indicate regions of expected flexure-induced fractures (and related compartments) or show deeper parts of the basin wherein overpressure (and possible underpressure) could likely have persisted to the present due to poor communication with the distant surface.

southeastern corner of the basin. Following the Rollins progradation, subsequent continental deposition kept pace with the rapid subsidence of the basin giving rise to extensive coastal plains with large coal swamps in the southeast and east (Fig. A-5). Sediment-laden fluvial systems advanced from the northwest, eventually overstepping the older marine, coastal, and swamp deposits, and spreading channel and bar sands and overbank mud across the basin. Agradational sequences of continental shales, siltstones, sandstones and coals comprise these complex, laterally discontinuous coastal plain, swamp, and fluvial deposits characteristic of the Williams Fork Formation.

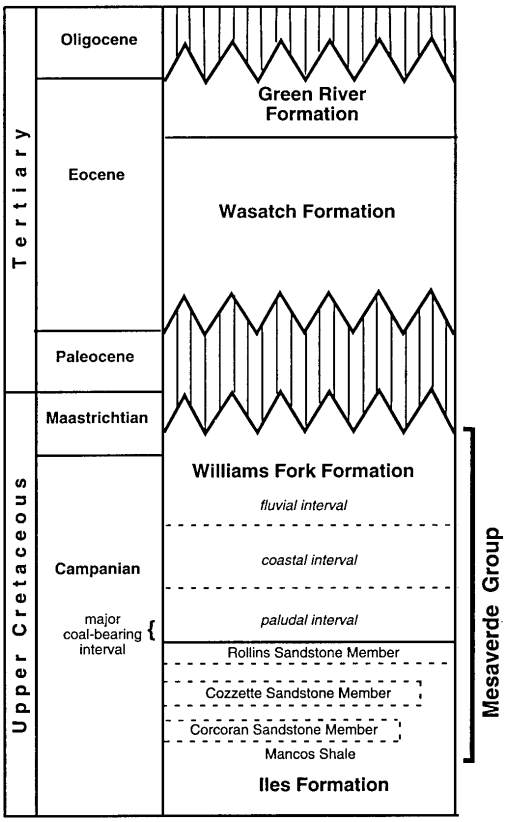

Fig. A-2 Generalized stratigraphic column of the MWX site representing the stratigraphy used in this study as input for the Basin RTM simulator (modified from Payne et al. 2000).

Fig. A-3 Southwest-northeast cross-section across the Piceance Basin, normal to the basin axis, showing the general stratigraphy of the Iles Formation and the Williams Fork Formation of the Mesaverde Group (from Advanced Resources International 1995). These formations contain the major gas reservoirs with production typically from fractures. The laterally discontinuous nature of units above the Rollins should affect the scale and configuration of compartments across the basin. Note that in this illustration the top of the Iles does not coincide with the top of the Rollins but is placed at the maximum flooding surface as defined by Tyler and McMurry (1995).

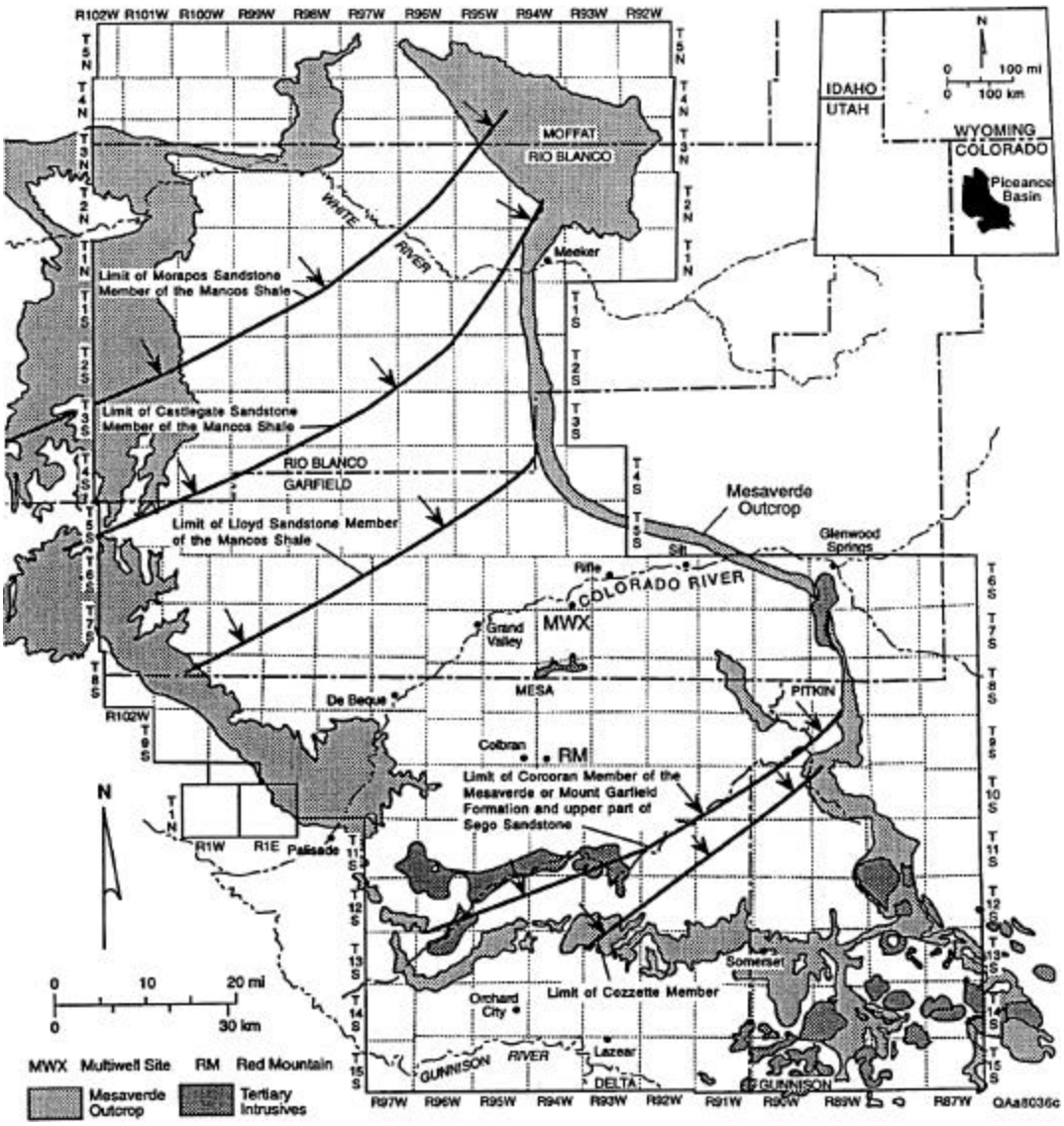

Fig. A-4 Progradational limits of the Upper Cretaceous marine sandstone units. Limits of the Sego sandstone cannot be determined with certainty. Seaward limit of the Rollins-Trout Creek prograda taional sequence is beyond the southeastern corner of the Piceance Basin and the mapped area. Arrows indicate direction of progradation (from Tyler and McMurry 1995).

C. Coal-Derived Natural Gas

Fracturing in the Piceance Basin is believed to be the result of the interplay of methane generation and other overpressuring as well as flexure. The extensive coal deposits in the non-marine coastal plane units of the Mesaverde Group (Fig. A-5) are believed to be the main source for the basin's natural gas reserves. Coals tend to overlie marine sandstones in the progradational sequences (Tyler and McMurry 1995) and represent swamp deposits located landward of a wave-dominated shoreline. The thickest coal units are in the lower (paludal) part of the Williams Fork Formation overlying the Rollins Sandstone. Net thickness of coal beds increases toward the east in the Piceance Basin (Fig. A-5).

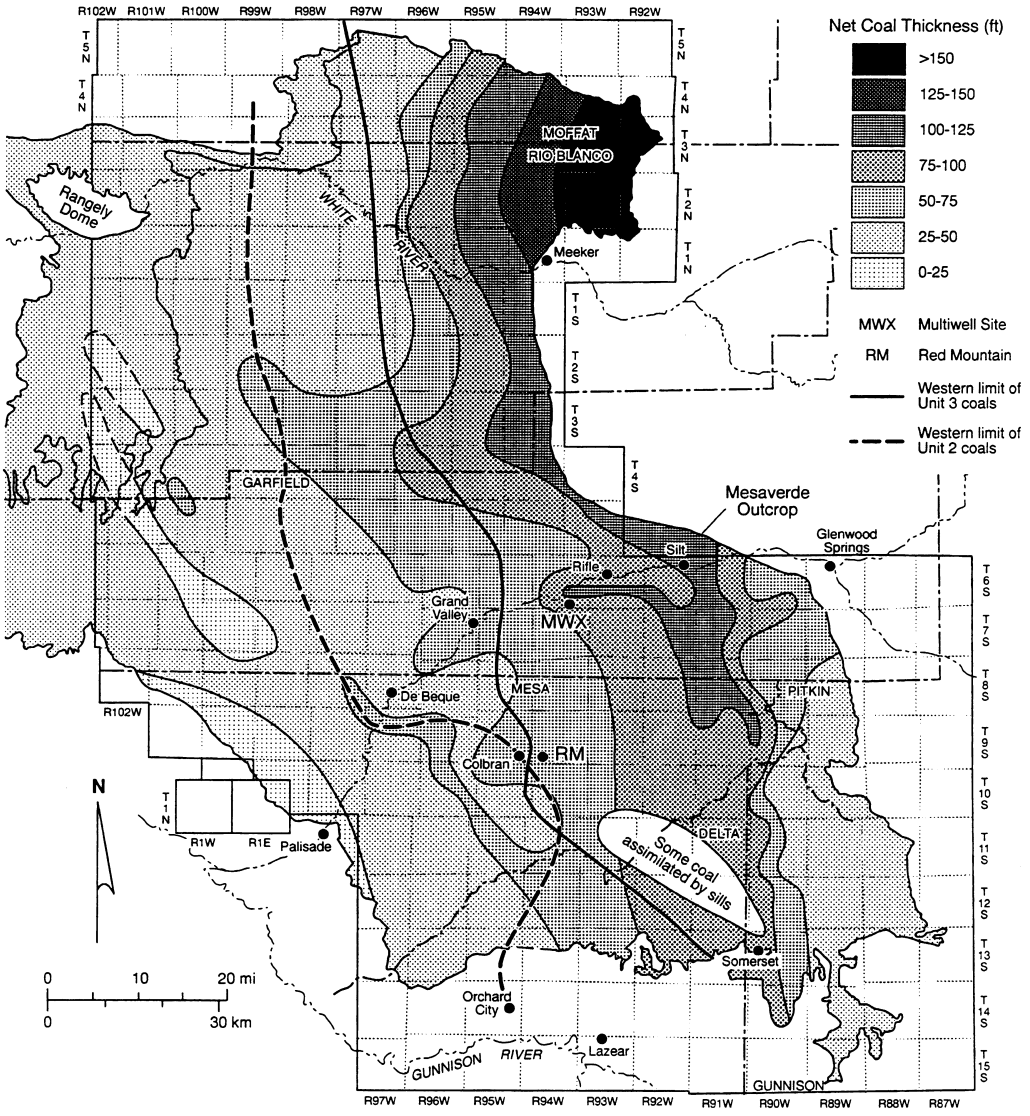

Fig. A-5 Distribution of net coal thickness in the Piceance Basin. Note the increasing net thickness toward the east, due to the repeated transgressive-regressive sequences as the shoreline generally moved toward the east. The distribution of net coal thickness does not correlate with the distribution of major producing gas fields in the Piceance Basin (from McMurry and Tyler 1996).

D. The MWX Site and Rulison Field

The U.S. Department of Energy's Multiwell Experiment (MWX) site located in the Rulison Field was established as a field laboratory in order to characterize low permeability gas reservoirs in the Upper Cretaceous Mesaverde Group and to develop technology for their production. Three vertical wells and one horizontal well have been completed, cored, tested, and stimulated at the site during activities that date back to the mid-1960s. Early work evaluated the use of massive hydraulic pressurization and nuclear explosives for inducing fracturing. Later work amassed detailed core, well log, geophysical *in situ* stress, fracture diagnostics, and well test data in order to define critical factors affecting gas production from Mesaverde reservoirs. The effort has produced volumes of data on the geology and physical characteristics of the reservoirs in the

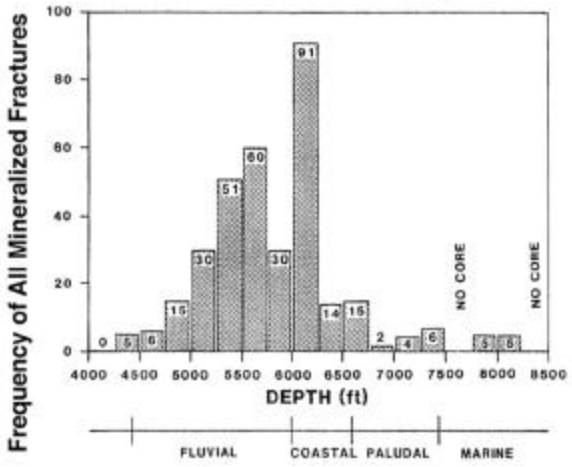

Fig. A-6 Frequency Distribution of all Mineralized Fractures with respect to depth. Core Data from MWX-1 and MWX-2 (from Finley and Lorenz 1988).

Williams Fork and Iles Formations. This extensive data set is key to calibrating our RTM model and testing its predictions.

Among the data is extensive documentation of fractures. Of the 4,200 feet of core recovered from the Mesaverde Group at the MWX site, approximately 1,880 natural fractures were counted and described in detail (Finley and Lorenz 1988). Three quarters, or 1,425 of the fractures are early-formed dewatering or compaction planes and are not important to reservoir productivity. Most the remaining one-quarter are high angle fractures that are mineralized, indicating that they were open during various stages of fluid flow and gas generation, giving them a key role in gas migration, accumulation, and producibility (Lorenz and Finley 1991). Most the mineralized fractures are confined to sandstone and siltstone lithologies and are found in the lower fluvial and upper coastal intervals of the Williams Fork Formation (Fig. A-6). The distribution and characteristics of the fractures predicted by our RTM modeling corresponds closely with distribution and characteristics of the fractures observed at the MWX site, thus validating our RTM simulator and its underlying unique rheological model.

Most of the natural gas (~95%) produced in The Rulison Field comes from reservoirs in the Williams Fork Formation. The remainder comes from the Corcoran and Cozzette Sandstone members of the Iles Formation and the G sandstone (Molina) of the Tertiary Wasatch Formation. Predicting the location and characteristics of these reservoirs was a major test and a significant accomplishment of our RTM simulations.

E. Correlating Reservoirs with Various Factors

Because of the limited conventional permeability (matrix $K < 10^{-6}$ darcy) in the Upper Cretaceous producing units, predicting the locations of naturally fractured zones is the key to predicting the locations of natural gas reservoirs. Presumably, fractured compartments exist where there are productive fields, although lack of production does not necessarily mean lack of fracturing. Fig. A-7 shows that major gas fields that produce from Cretaceous and younger are producing wells in areas outside of these major fields, although individual wells are not shown. The pressure and hydraulic head distributions discussed in the next section suggest areas of compartmentation. These analyses, however, are only reliable where there is significant data density — which is generally where major producing fields are located — and are less reliable in

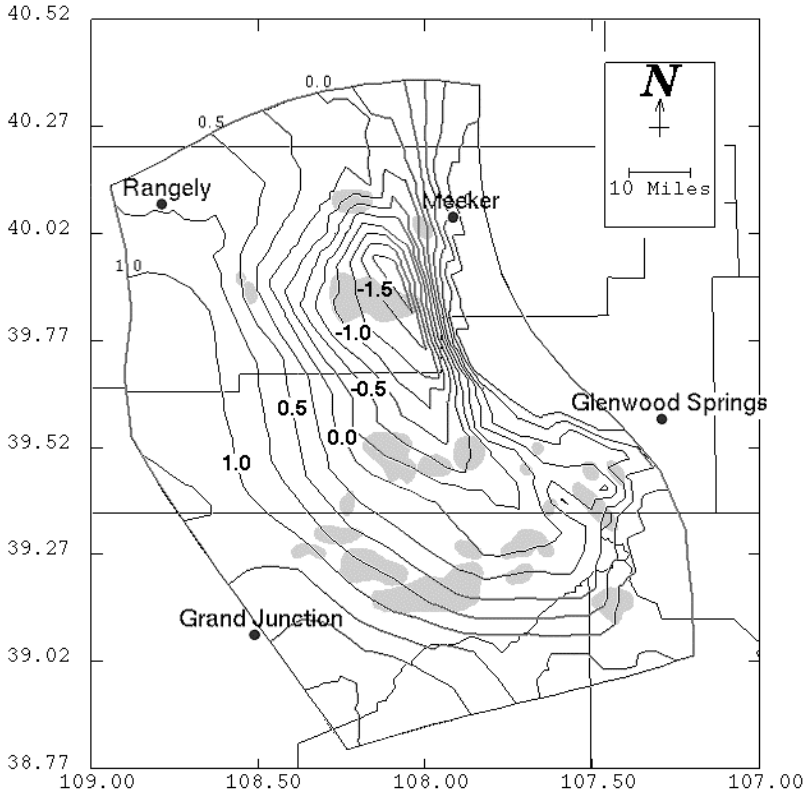

Fig. A-7 Major producing fields (indicated by gray shaded areas) and basin shape (indicated by contour lines in kilometers of elevation for the top of the Rollins Formation).

areas of data paucity. How does one predict fractured reservoirs between productive fields (for example, between the Piceance Creek field and the Grand Valley/Parachute/Rulison fields) or within a field (for example, within the Piceance Creek Field) where data density is low? The following suggests that there are no simple correlations between the location of fractured reservoirs and individual basin characteristics such as structure or natural gas source rocks. Instead, one must consider all of the characteristics simultaneously and understand the timing and coupling of the processes which create those characteristics. This has been achieved with our Basin RTM technology.

Fracturing will occur due to differential rock stress ratios. Factors which contribute to the basin- and field-scale stresses are the time-varying rheological properties of the strata, the development of structures due to the tectonic history of the basin, and the generation of gases due to thermal maturation of organic source material. Fracturing is induced when lateral stresses are sufficiently low, which happens more readily in high viscosity material. Coarser-grained or more well-lithified material have higher viscosity and therefore tend to fracture more readily than fine-grained and unlithified material. Thus, fractured reservoirs are more common in coarser-grained sandstones, with the interlayered mudstones acting as seals to preserve overpressure and thereby decreasing effective stress. In general, this is observed in the Piceance basin where fractured compartments corresponding to good gas reservoirs are found isolated in the lenticular fluvial and the smaller lenticular fluvial and coastal sandstones of the Williams

Fork Formation, and locally in the blanket marine sandstones of the Iles Formation. However, this is not the only key

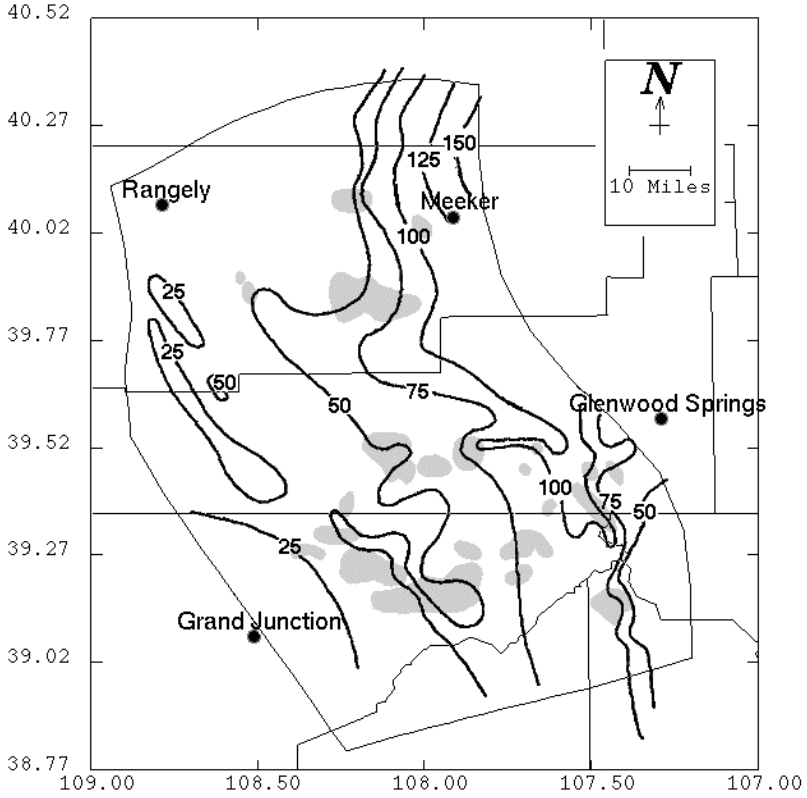

Fig. A-8 Locations of major producing fields and contours showing cumulative thickness of the Williams Fork Formation coals (modified from McMurry and Tyler 1996).

to finding fractured reservoirs because there are parts of these higher viscosity units that do not comprise fractured reservoirs.

The total generation of gases will be affected by the abundance, location, and thermal maturity of the source material. The major sources of natural gas for Upper Cretaceous reservoirs are the coal units of the Mesaverde Group, most of which are in the Williams Fork Formation. Fig. A-10 shows gas fields and contours of cumulative coal thickness in the Williams Fork Formation (Tyler and McMurry 1995). This illustration shows that while source rock abundance increases toward the east and northeast in the Piceance Basin, gas production does not. It is not surprising that there is no correlation between major producing fields and coal thickness because source rock maturity and total thickness are of comparable importance to total gas production. The overall basin shape suggests that coals in the northern half of the basin are likely to be the most mature as they have experienced the deepest burial. However, inferred and observed thermal gradients are higher in the southern part of the basin, presumably due to Oligocene igneous activity. Indeed, the highest coal ranks for the Cameo coal group of the lower Williams Fork Formation are found along synclinal axes south of the Colorado River in the southern part of the basin (Fig. A-9) (Scott 1996). Still, considering source rock abundance and maturity indicators together, there is no obvious spatial relationship between the degree of methanogenesis and major producing zones.

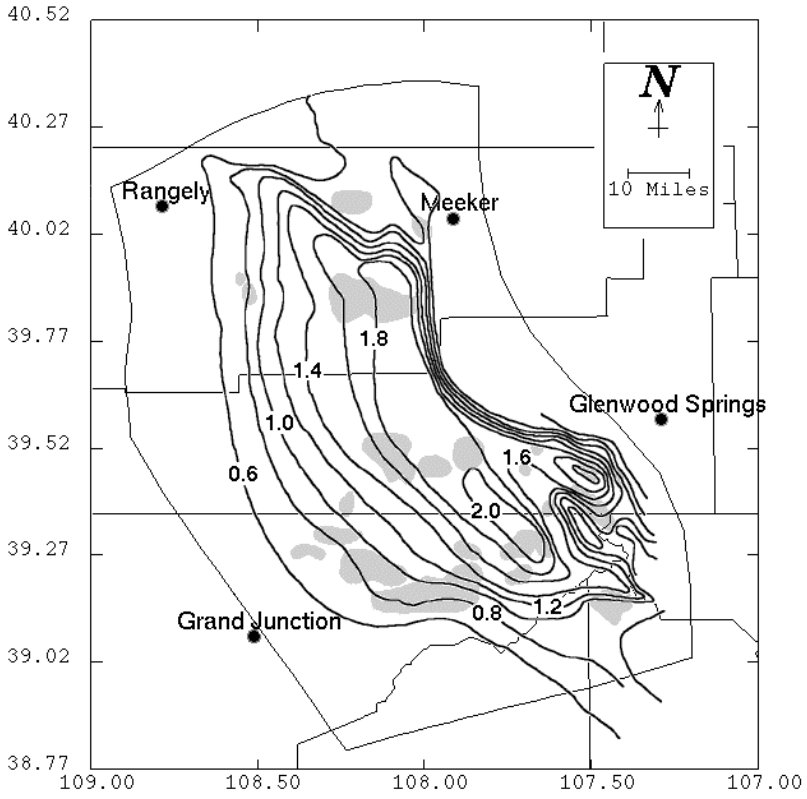

Fig. A-9 Locations of major producing fields with contours showing Cameo Coal vitrinite reflectance (contour intervals in 0.2% Ro).

There is no apparent correlation between the location of major producing fields and the overall basin shape as shown by the contours of the top of the Rollins Formation (Fig. A-7). Fields occur near and far from the basin axis and in no apparent relation to the bend in this axis. Fig. A8 shows locations of other major structural features in the Piceance Basin. These features include major folds, and normal and reverse faults, as well as some shallow Oligocene igneous intrusions in the southeastern part of the basin. Most of the structures trend northwest-southeast. Major structural features indicate zones of extensional stresses with which fractures may be associated. There appears to be some correlation between the locations of basin-scale structures and major producing fields, although not all structures are associated with producing fields and not all fields have a distinct relationship to a structure. Hence, the location of major basin structures cannot be used as a single indicator of likely areas for fractured reservoirs.

F. Observed Pressure Distribution

1. The Data Set

The low permeability of Upper Cretaceous Strata in the deeper Piceance Basin makes reservoir delineation by fluid pressure data particularly difficult. Reliable pre-production data in such a basin can only be obtained using very long shut-in times. Measurements over short times are likely not accurately extrapolatable to native pressure because of the very long transient time for equilibration within the formation being tested. In a recent study, data has been collected by

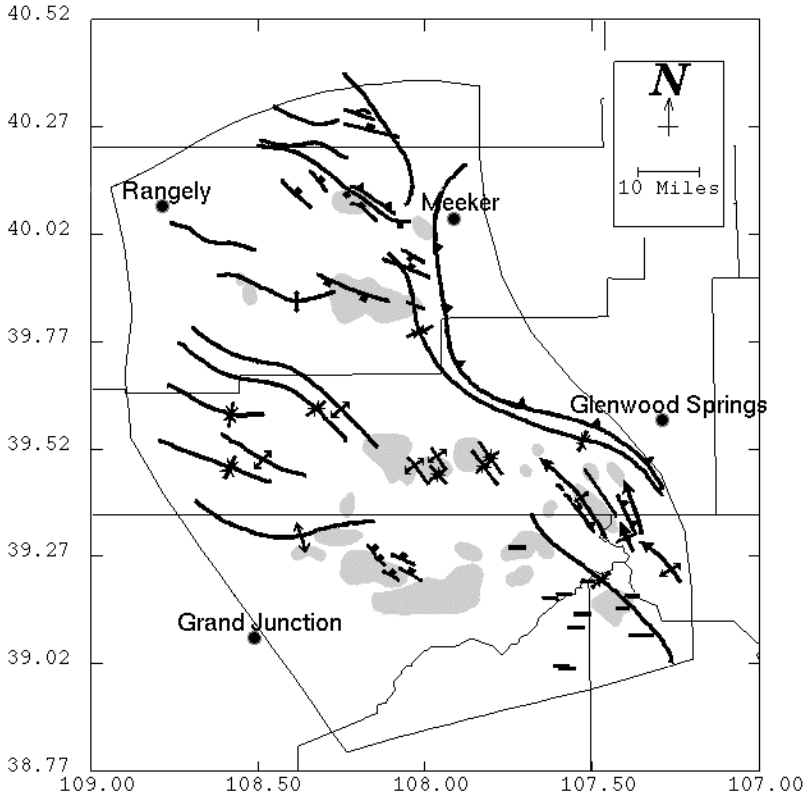

Fig. A-10 Location of major producing fields and basin-scale structural features (information provided by Advanced Resources International).

LCG from its industry and institutional partners (Amoco, Barrett Resources International, Chevron, Koch Exploration, Texas Bureau of Economic Geology, Tom Brown Inc., Unocal and U.S. Naval Oil Shale Reserve). This well-screened data represents weeks, monthsand even years of shut-in time (Payne et al. 2000). Present-day compartmentation in the Piceance Basin was delineated using this unique data set.

The dataset consists of 127 pressure data points taken primarily from intervals in the Mesaverde Group (Fig. A-11). Most of the data were taken after long shut-in times (on the order of weeks) and before production, and are from specific packed-off intervals or from recorded depths. Data were collected from many fields in the basin, although data density across the basin was not uniform due to availability.

2. Data Interpolation

The selected pressure data were examined in one and three dimensions. The three-dimensional interpolation used a modified Gaussian formula which allowed smooth vertical and lateral transitions of pressure within a formation and respected lithologic contacts such that a fluid pressure regime favored continuity along rather than across formations. The interpolation assumed a no-flux bottom boundary and inferred that the unit underlying the Mesaverde Group (the Mancos Shale) is impermeable. The top boundary was taken to be one bar atmospheric pressure. The side boundaries were not constrained. The hydraulic head was calculated using the following relation:

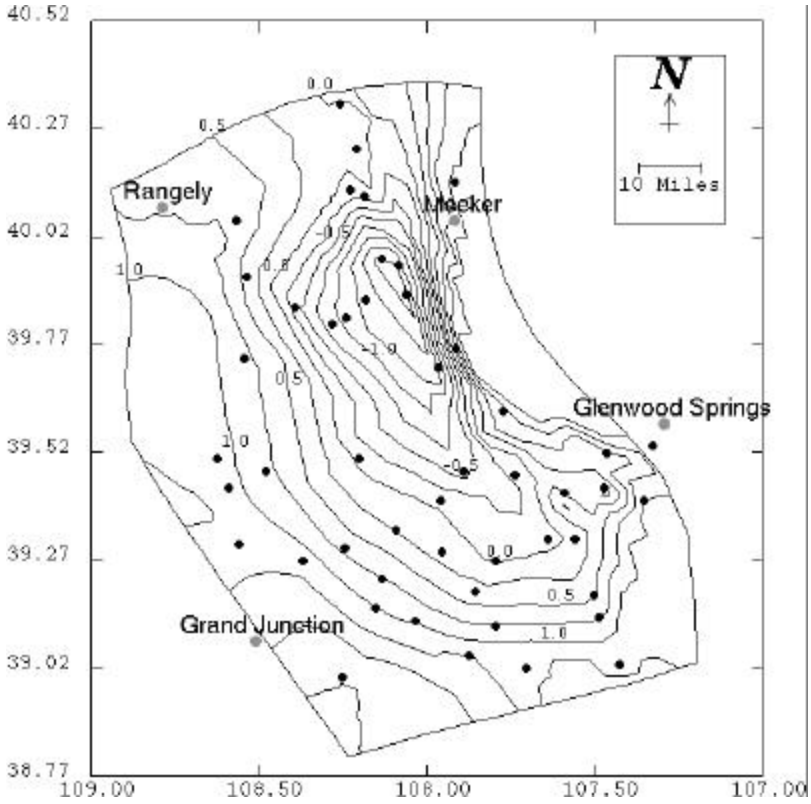

Fig. A-11 Location of wells and outcrops used to interpolate stratigraphy in three dimensions across the basin. Contours indicate elevation in kilometers of the top of the Iles Formation (Rollins Sandstone).

$$h = \frac{P - 1.0\ bar}{\rho g} + z$$

where h is hydraulic head (elevation of a water column supported by the pressure at the measuring point), P is the measured fluid pressure, ρ is water density (assumed to be 1.0 g/ml), g is the gravitational constant, and z is the elevation of the pressure measurement relative to sea level.

The interpolation used here assumed laterally consistent hydraulic flow properties along a lithologic unit. If flow is primarily along fractures, these fractures may not necessarily be evenly distributed nor well connected within a lithology, and they may cross lithologic units depending on the rheological properties of the units. It is likely in the case of predominantly fracture controlled permeability that pressure communication will be more locally confined. Thus, the interpolation may overestimate the fluid communication, pressure regime, and compartment scale within a lithology. This interpolation, however, may be justified if it is assumed that rheological properties and, thereby, susceptibility to fracturing are more continuous within lithologies rather than across their contacts.

In order to account for the extent of a lithology and the locations of lithologic contacts, the pressure data and the hydraulic head were superimposed on a three-dimensional, stratigraphically adapted grid. The stratigraphy was interpolated across the whole basin using stratigraphic data

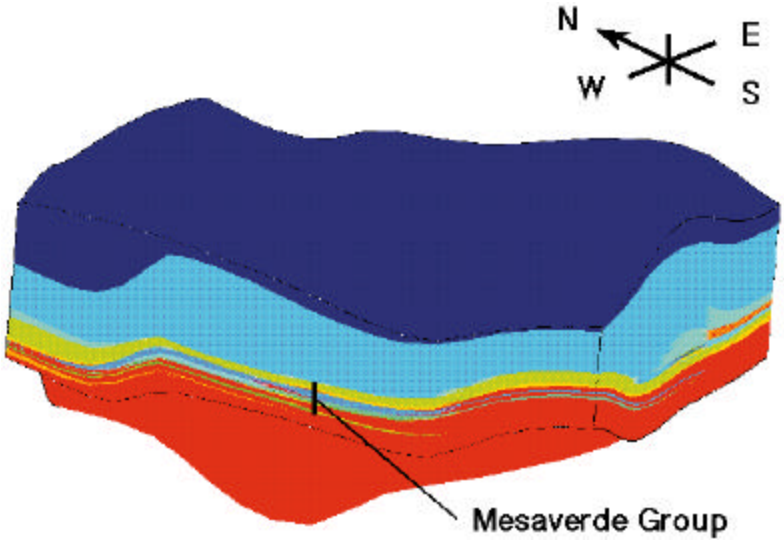

Fig. A-12 Three-dimensional depiction of the interpolated distribution of stratigraphy across the basin.

from more than forty wells and outcrops distributed as evenly as possible across the basin (Fig. A-11). The lithology and contact data were interpolated between the wells using an automated three-dimensional triangulation technique as described in Sibo, et al. (1998). Contour lines in Fig. A-11 show the interpolated depth to the top of the Rollins sandstone which is the contact between the Iles and Williams Fork Formations, and Fig. A-12 shows a three-dimensional depiction of the interpolated distribution of stratigraphy in the Piceance Basin as used in this study.

3. Pressure Distribution

A basin-wide analysis of abnormally pressured zones was attempted. The density of available pressure data (both vertical and horizontal) put limits on the conclusions drawn from such a data interpolation. Nonetheless, the cross-sections and maps presented here served as a good test of Basin RTM when agreement was weighted with the local degree of data density. Fig. A-13 may be viewed as the simplest illustration of the basin-scale complexity of compartmentation. Pressure may be strongly heterogeneous on a sub-field scale. Thus, an increase in data density might be expected to reveal a myriad of small compartments not seen in this analysis. Overpressure is a measure of the driving force for fluid flow and is useful in delineating compartments and their surrounding seals. As lithologic factors strongly influence the spatial geometry of seals, an attempt was made to use the lithologic patterns as in Fig. A-13 in combination with overpressure data to delineate the 3-D structure of compartments in the Piceance Basin (Payne 1998; Ortoleva 1998). Using an overpressure interpolation scheme that assumes correlation along a given lithology, the pressure data was plotted in 3-D. Fig. A-14 shows map views of 3-D isosurfaces of abnormal pressures in the Piceance Basin colored with depth. At every point along a given isosurface, the abnormal pressure is a constant value (as stated in the figure). The color indicates the elevation of the isosurface, with the blue end of the spectrum indicating lower elevation (greater depth) and the red end of the spectrum indicating higher elevation (shallower depth). These isosurfaces are nested such that, for example, the 500 psi overpressure isosurface is contained within the 250 psi overpressure isosurface.

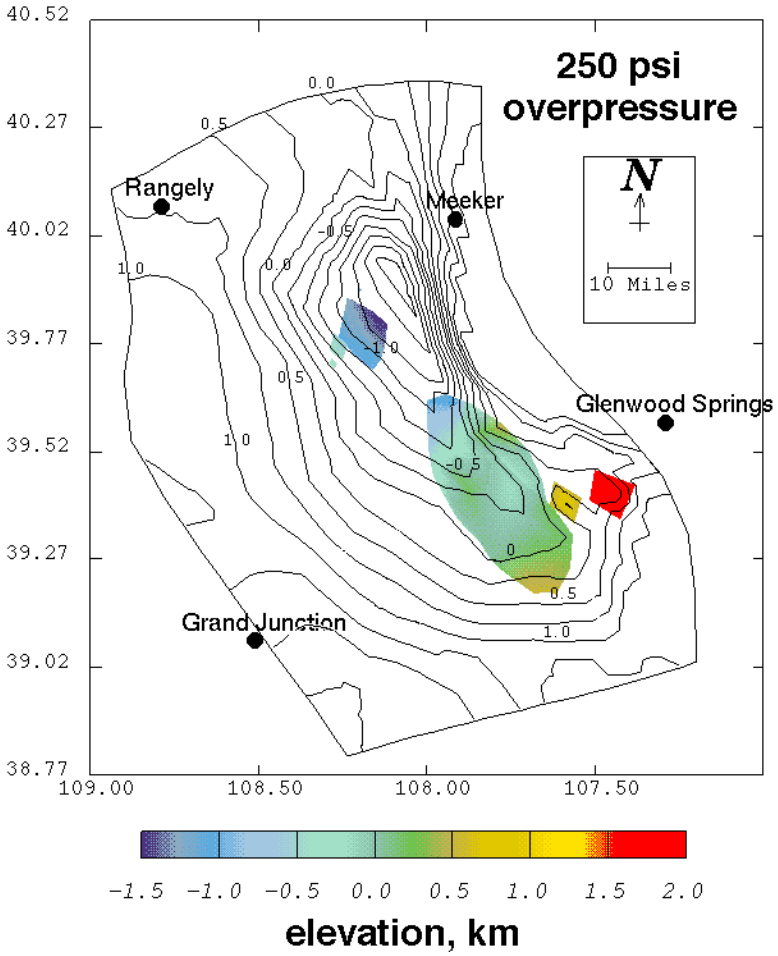

Fig. A-13 Observed overpressure (colored areas) in the Piceance Basin superimposed on a map showing the elevation (km) of the Rollins Sandstone. The colors indicate the elevation of the 250 psi overpressure isosurface. Comparison of overpressure and structure suggest that poor observational data coverage causes a likely connection of high overpressure from the shallower to the deeper part of the basin to be missed (from Payne et al. 2000; Ortoleva 1999).

Fig. A-14 shows the lateral extent of overpressuring in the Piceance Basin. In general, overpressure occurs more widely in the southern part of the basin, including the areas comprising the Grand Valley, Parachute, Rulison, Buzzard Creek, Divide Creek, and Wolf Creek Fields. The observed overpressure distribution may be the consequence of the lower data density in the northern part of the basin, with lower data density associated with the unfavorable economics due to the greater depth to likely producing formations in the north. The zone of overpressure becomes generally shallower toward the south, apparently conforming to the shape of the basin as it slopes upward toward the southern margin. Separated from this region is another region of overpressuring in the north central part of the basin. This smaller, deeper zone in the Piceance Creek Field area is close to the basin depocenter. Except for the apparent gap in overpressuring between the northern and southern overpressured regions, it appears that the zones of overpressuring in general extend from the basin depocenter to the south along the basin axis. The area separating the northern and southern overpressured zones is marked by data paucity, so it is

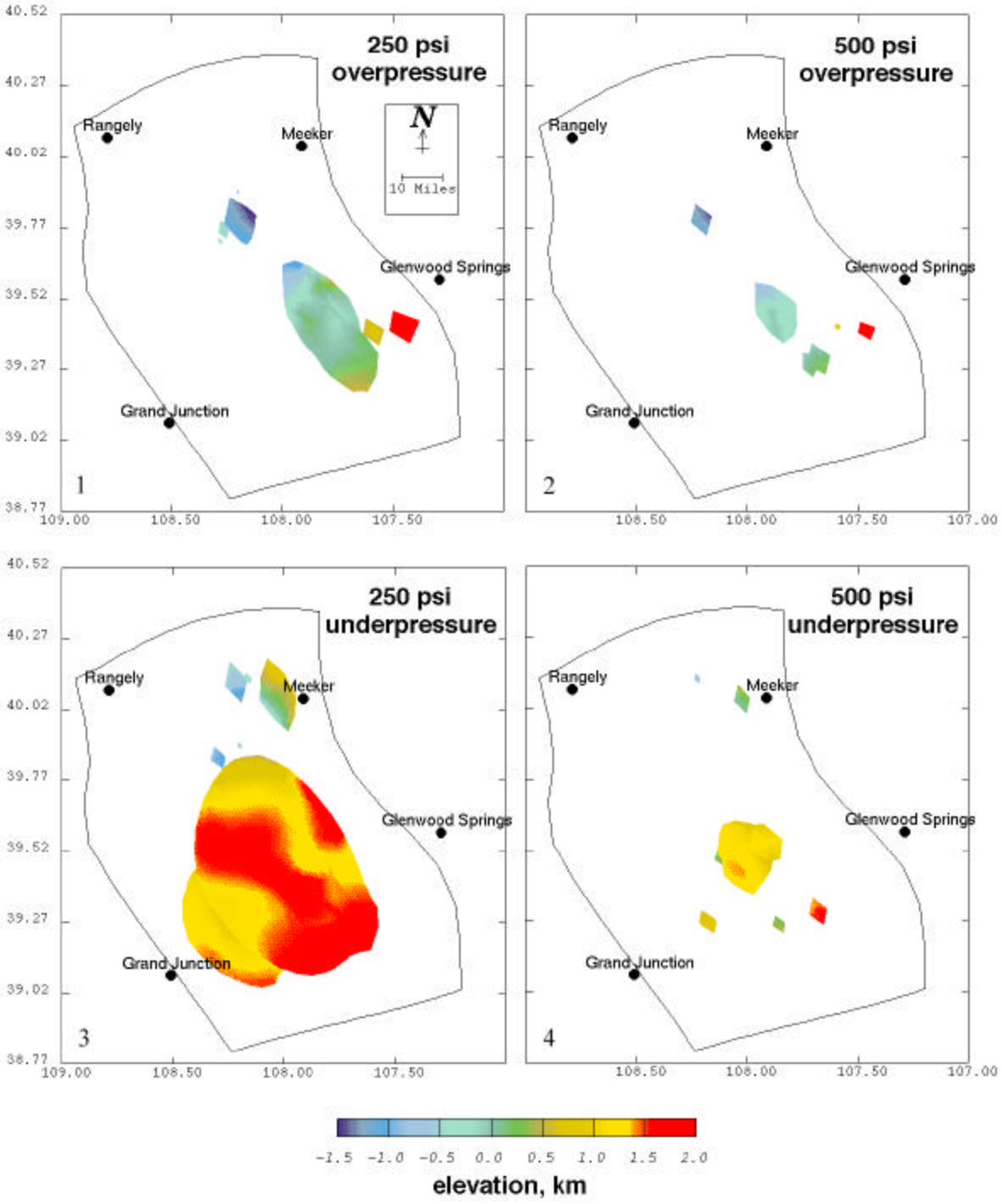

Fig. A-14 Over- and underpressure isosurfaces in the Piceance Basin from three-dimensional interpolation of pressure data. Elevation is relative to mean sea level. See also Fig. A17 (from Payne et al. 2000).

unclear if the overpressuring gap truly exists or if the interpolation is influenced by the lack of data.

Underpressuring is observed generally at shallow depth in the south-central to south-western part of the basin, and at greater depth in the northeastern part of the basin (Fig. A-14). Fig. A-14 indicates that a large portion of the Piceance Basin may be moderately underpressured, presumably the result of unloading and dilation due to recent uplift of the basin. In general, underpressuring exists at shallower depths than overpressuring, and in the southern part of the basin, moderate underpressuring is laterally more extensive than overpressuring. Similar to the overpressuring patterns, the underpressuring is found at greater depths in the northern part of the basin and becomes shallower toward the south, suggesting that underpressuring also conforms to the general basin shape. As with the overpressuring patterns, a gap in the interpolated distribution of underpressures exists in an area of data paucity.

One might suspect that there is a correlation between basin depth and overpressuring. Indeed, Fig. A-14 shows that overpressure isosurfaces in the northern half of the basin exist at a greater depth than do those in the southern part of the basin. In Fig. A-13, contours indicating the elevation in kilometers of the top of the Iles Formation are overlain on the 250 psi overpressure isosurface. These contour lines show the NW trending basin axis near the eastern margin of the basin, and the basin depocenter in the northeastern part of the basin. The overpressure isosurfaces in the southern part of the basin generally lie along the basin axis, but in the northern part of the basin, the overpressure is to the west of the depocenter. From Fig. A-13, it is clear that the overpressure isosurface is interpreted to exist where there is data and to be absent in the depocenter where there is no data. Although no data exists at the depocenter, it is likely that this is a zone of significant overpressure which is slowly leaking up dip toward the western flank of the basin.

Cross-sections constructed for A-A', B-B' (east-west), and C-C' (north-south), as shown in Fig. A-15, depict the vertical distribution and the scale of overpressuring across the Piceance Basin (Fig. A-16). The colors indicate ranges of abnormal pressuring: red and yellow represent overpressuring, green represents approximately normal pressuring, and light and dark blue represent underpressuring. The cross-sections show layered, lenticular patches of overpressuring primarily in the deeper part of the basin, and a large, basin-scale zone of moderate underpressuring in the shallow part. The vertical layering of over- and normal pressuring at depth seen in all three cross-sections is indicative of stacked fluid pressure compartments as described in our study (Maxwell 1997). The greatest overpressuring is observed at shallow depth near the Wolf Creek Field area and along the Divide Creek anticline (C-C'). Significant underpressuring is observed at shallow depth in the Grand Valley Field area within the basin-scale zone of moderate underpressuring (B-B') as indicated by the large area of dark blue. In cross-section C-C', the layered lenticular overpressured zones are discontinuous between the deepest part of the basin and the Grand Valley Field area to the southeast; the discontinuity is seen in the map view of overpressure isosurfaces (Fig. A-15). The gap in overpressure is an area of data paucity, so it is unclear if these overpressured zones are truly discontinuous in this area.

4. Hydraulic Head

Hydraulic head may be a more useful indicator of compartments and their surrounding seals. The determination of overpressure is dependent upon the land surface elevation for a given data point. In regions with significant relief such elevation variability as the Piceance Basin, comparing data and thus interpreting fluid pressure compartmentation in terms of overpressure may be difficult. By looking at hydraulic head values, one expects that all of the data can be more easily

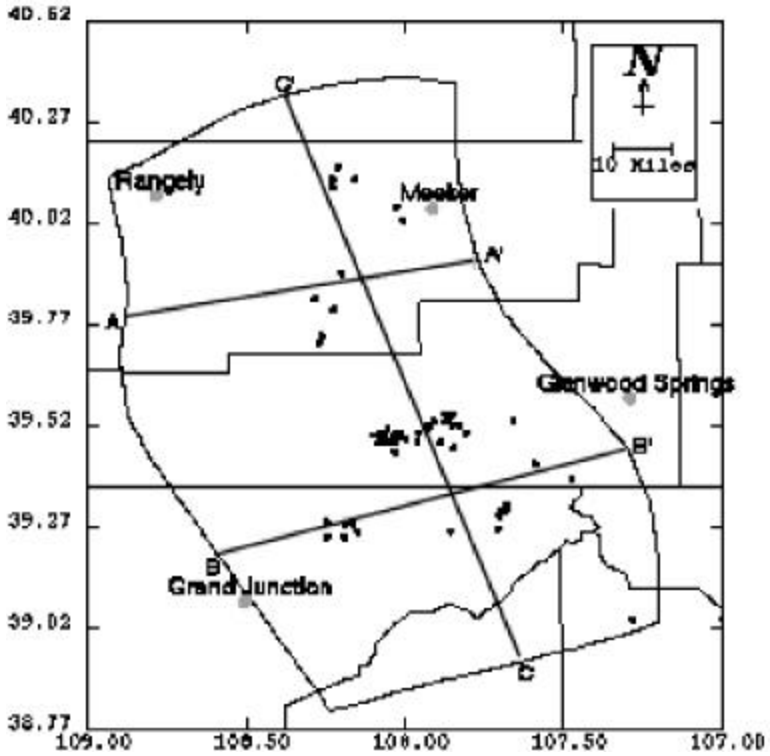

Fig. A-15 Location of wells in the Piceance Basin from which 127 fluid pressure data points were used to identify pressure compartments (Payne et al. 2000). Data were provided by Amoco, Barrett Resources International, Chevron, Koch Exploration, Texas Bureau of Economic Geology, Tom Brown Inc., the U.S. Navy, and Unocal.

interpolated and correlated. Such an analysis of the data has been undertaken for the Piceance Basin (Payne 1998; Payne et al. 2000; Ortoleva 1998) and was used to test Basin RTM.

Fig. A-17 shows hydraulic head along the same cross-section lines as in Fig. A-15. These cross-sections show a stacked compartmentation structure. The abnormally highly pressured compartments are characterized by high hydraulic head values surrounded by zones with lower head values; the reverse is true for underpressured compartments. Seals appear to be located within the relatively lower hydraulic head regions between zones of higher head (and the complement for underpressured compartments). The stacked compartments are most noticeable at depth, lying parallel to stratigraphy (see cross-sections A-A' and C-C'). Compartments on a range of scales are seen in the C-C' cross-section. A basin-scale compartment is suggested by the greenish-yellow shaded area in the deeper part of the basin. It is separated by a thin deep green band from the light turquoise color of the upper part of the basin; within the larger basin-scale compartments, small lenticular-shaped compartments of higher and lower hydraulic head exist.

Fig. A-17 suggests that the compartmentation is strongly controlled by stratigraphy (this may be somewhat prejudiced by the pressure interpolation scheme). Within a given formation, however, there appears to be some degree of lateral variability. Figs. A-18a and b show map views of hydraulic head within the Rollins sandstone of the Iles Formation and the Paludal Interval of the lower Williams Fork Formation, respectively. These are important potential reservoir intervals in the Mesaverde Group. The color indicates the magnitude of the hydraulic

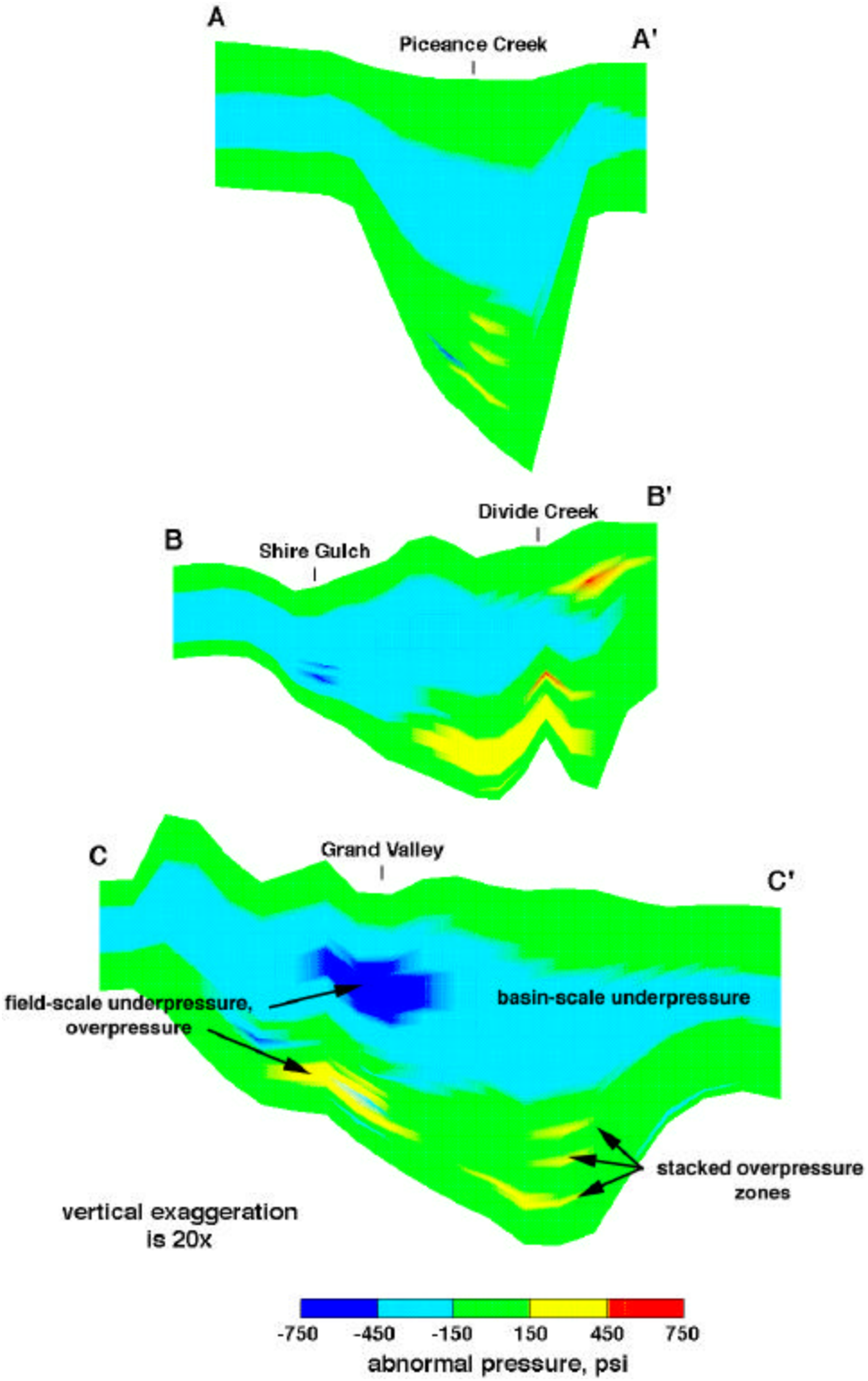

Fig. A-16 Cross-sections of fluid pressure from interpolated pressure distribution; locations of cross-sections are indicated in Fig. A20. Both overpressured and underpressured zones exist. Note different scales and configurations of zones of abnormal fluid pressure.

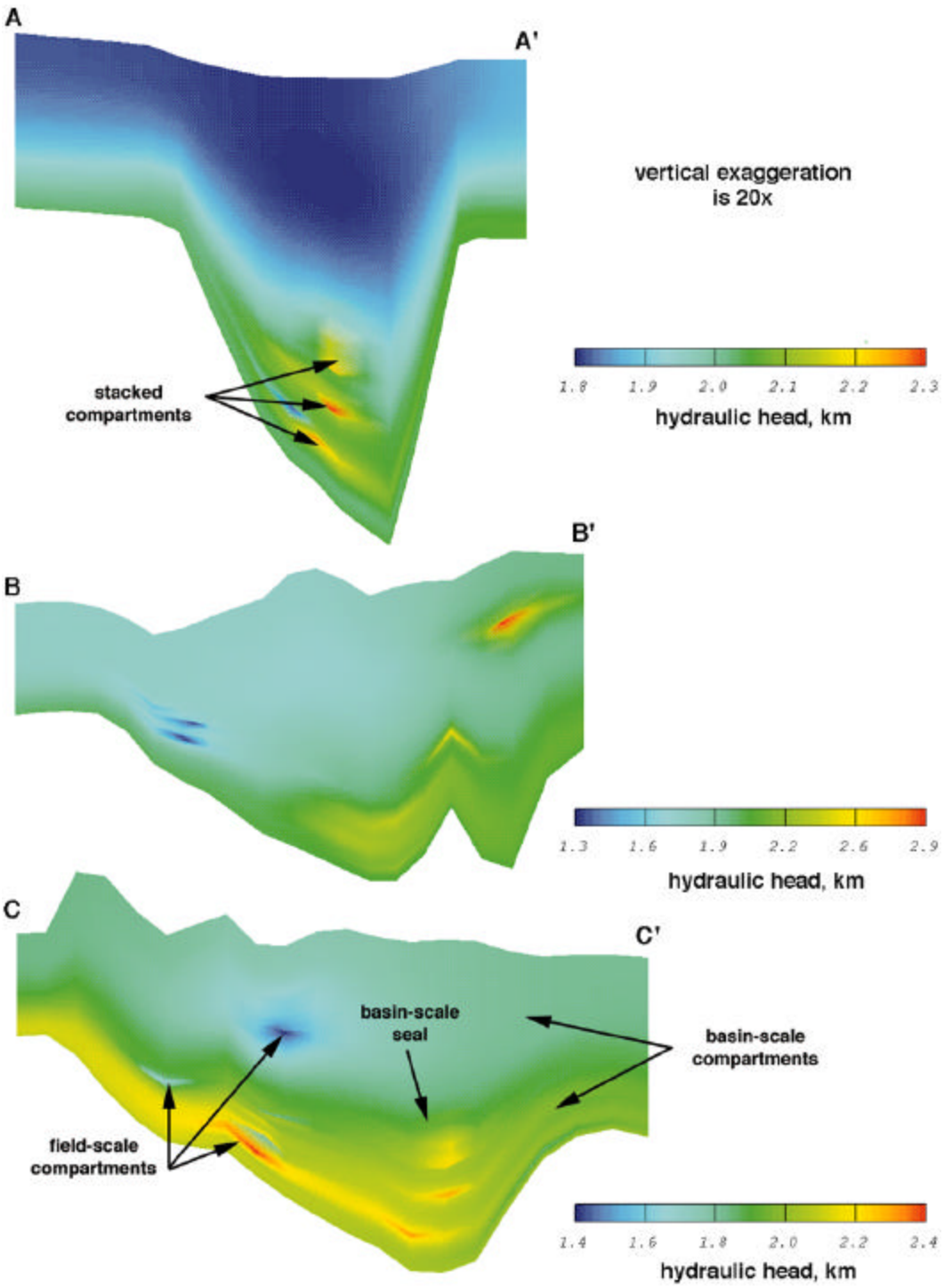

Fig. A-17 Cross-sections of hydraulic head showing stacking and different scales of compartments; cross-sections are located in Fig. A11.

head, and the contour intervals show the elevation in kilometers relative to sea level of the top of the formation represented. Fig. A-18a shows that there is no simple correlation between depth of the Rollins Formation and the hydraulic head. Highest head values are seen in the Rulison Field area and extend southward to the Buzzard Creek Field area. The distribution of green shows that the relatively higher hydraulic head region extends into the southeastern part of the basin. Some of the higher head (green) is found north along the basin axis into the basin depocenter. A small area of higher head is shown by a patch of yellow in the north-central part of the basin, in the Piceance Creek Field area. A region of lower hydraulic head, indicated by dark blue, is found in the southwestern corner of the basin where the Rollins Formation is at its highest elevation. A smaller area of lower head surrounded by higher head (indicated by a separate dark blue patch) is seen in the Shire Gulch area and is suggestive of an underpressured compartment there. Hydraulic head in the Rollins Formation correlates to some degree with the overall basin structure, as higher head values exist along the basin axis and lower ones exist where the Rollins has its highest elevation. However, the locations of small regions of higher head values, indicative of compartmentation, do not correlate with the basin-scale geometry of the Rollins Formation. Factors other than basin structure must be contributing to the hydraulic head distribution within this formation.

Fig. A-18b shows the hydraulic head distribution in the Paludal interval of the Williams Fork Formation. Similarly to the Rollins Formation, there is no simple correlation between the elevation of the formation and the hydraulic head. In the Paludal interval, however, a larger, more distinct continuous area of higher hydraulic head follows the basin axis. Like the Rollins Formation, the highest head areas are in the southeastern part of the basin, particularly around the Buzzard Creek area. In the Paludal interval, the hydraulic head distribution is less patchy, suggesting that the scale of compartmentation is broader in that unit than in the Rollins Formation.

It is contrary to expectation that the extensively continuous Rollins sandstone would have a more discontinuous hydraulic regime than the Paludal interval characterized by thinner, laterally more limited sandstones. This may be the result of differences in bulk rheologic properties which control the fracturing response to stresses, or because the shallower Paludal interval may be subject to lower compressive stresses, enhancing fracturing.

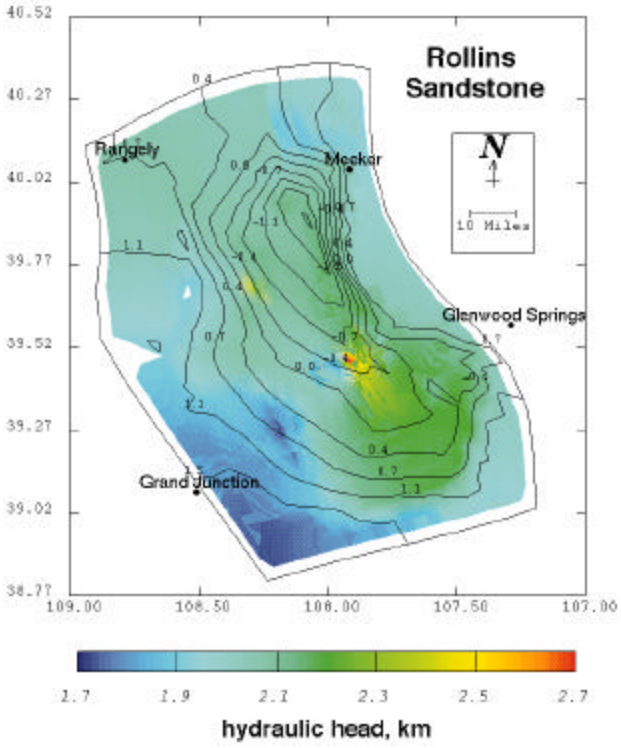

Fig. A-18(a) Hydraulic head distribution indicated by color within the Rollins sandstone; contour lines indicate the elevation in kilometers of the top of the formation relative to sea level.

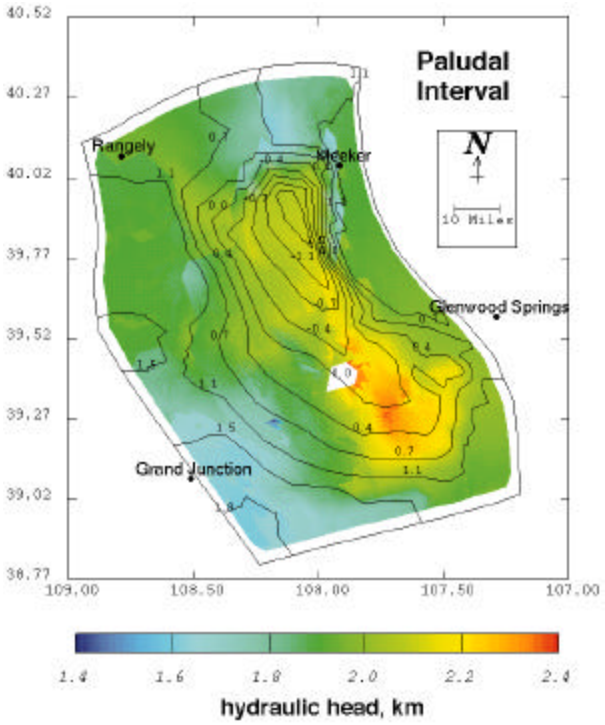

Fig. A-18 (b) Hydraulic head distribution indicated by color within the Paludal Interval of the Mesaverde Group; contour lines indicate the elevation in kilometers of the top of the formation relative to sea level.

APPENDIX B: LATERAL COMPRESSION HISTORY OF PICEANCE BASIN

T. Hoak, Kestrel Geoscience, LLC

A. Structural Style

The Piceance Basin is most intensely deformed near its eastern margin and much less deformed in the west. Along the eastern margin of the basin, the Mesaverde Group is exposed in the Grand Hogback monocline, which is the surface expression of a late Laramide basement involved thrust block. Seismic, gravity, drilling, and outcrop data indicate that décollements developed in front of the thrust block in the southern part of the basin within mechanically weak Pennsylvanian (Desmoinesian) evaporites and in the Upper Cretaceous (Coniacian and Santonian) Mancos Shale (Fig. B-1) died out in the southeastern Piceance Basin as small-scale imbricate thrusts and kinked, complexly contorted strata in the Mancos Shale (Grout et al. 1991; Gunneson et al. 1995). Overthickened Mancos underlies the Divide Creek anticline and some nearby Mancos Shale exposures are highly contorted (Grout et al. 1991; Gunneson et al. 1994). The sandstone- and siltstone-rich Mesaverde units overlying the thrust faulted contorted Mancos Shale are relatively little deformed.

B. Calculation of Regional Shortening

One of the required inputs for Basin RTM is the boundary conditions of the basin through time. This includes the magnitude, direction, and timing of shortening. In the Piceance Basin the greatest amount of shortening occurred in **t**he Grand Hogback fold structure that forms the eastern boundary of the basin. The Grand Hogback is composed of vertically and steeply dipping beds that were folded during reverse (thrust) faulting on a basement-involved system beneath the Grand Hogback monocline (Fig. B-1). Coincidentally, the approximate location of the thrust in the subsurface is beneath the lower boundary of the Mesaverde Group where it is exposed in the Grand Hogback.

A series of cross-sections across the northeastern and eastern boundary of the Piceance Basin (Murray 1966) were used to calculate the magnitude of shortening (Fig. B-2a). Shortening was calculated in two methods. The first method calculated the amount of shortening caused by folding of the stratigraphic units overlying the basement. This was done by measuring the line length of an appropriate contact (usually the top Dakota Group) in the deformed section and comparing that length to the current length of the cross-section. An attempt was made to use points in “no-slip” or “undeformed” areas of the section (e.g. the synclinal axis behind the Hogback and the basin depocenter). The second method assumed that the basement surface prior to faulting was continuous. By examination of seismic data across the Grand Hogback structure, the thrust dips approximately 45 degrees to the east. Shortening was then calculated as the a mount of fault displacement required to uplift basement under the Grand Hogback to the level in the hangingwall (e.g., Fig. B-1) cross-section. Interestingly, this number is generally larger than the amount of shortening accommodated by folding alone. This suggests that a significant amount of the shortening caused by thrusting may have propagated out into the basin instead of being accommodated by folding of the Grand Hogback structure alone. The approximate basement boundary points based on the ten cross-sections (Fig. B-2) are given in Table B-1. The “present-day” eastings and northings are the locations where each of the ten cross-sections enter the basin. These present-day locations have then been moved backward in time to their earlier locations, assuming transport orthogonal to the local trend of the Hogback structure (either due east or northeast, see Table B-1). The two methods for calculating magnitude of shortening are

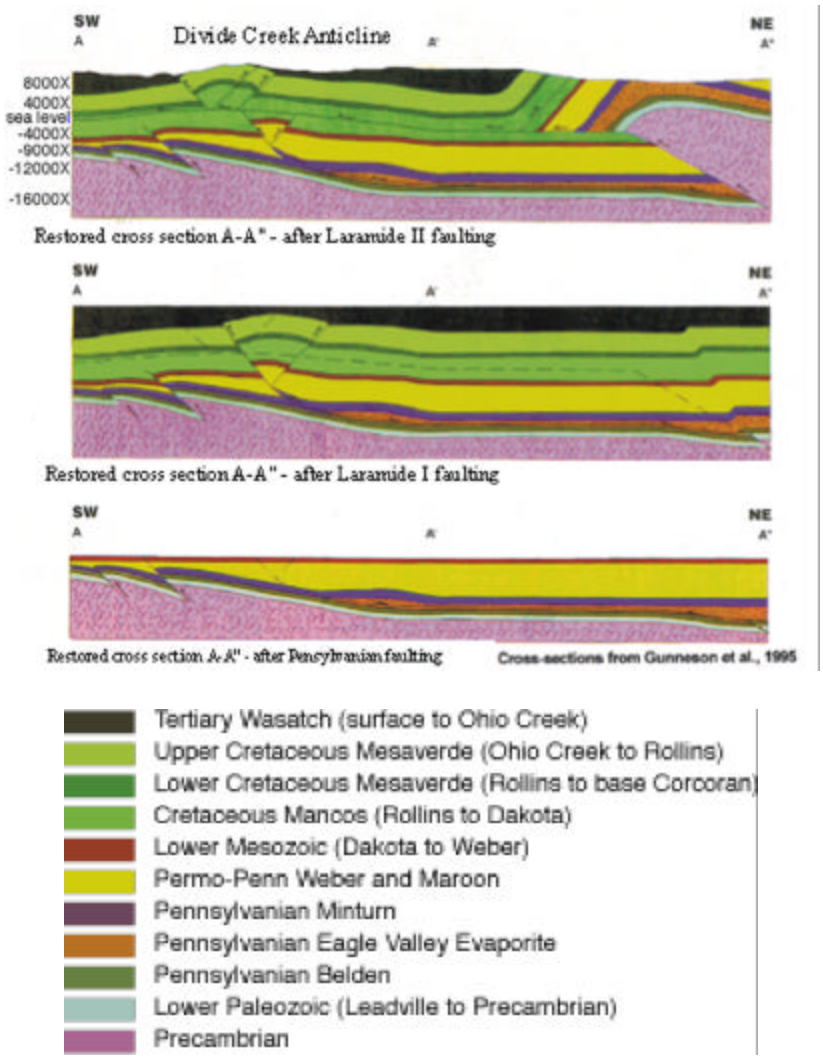

Fig. B-1 Cross-sections showing structural evolution of The Divide Creek anticline and the Grand Hogback monocline. A. Lower Cretaceous. B. Tertiary. C. Recent (modified from Gunneson et al. 1995).

represented as the "folding only" data and the "faulting only" data. The faulting data is probably less rigorous but appears to represent the upper end member for shortening magnitude.

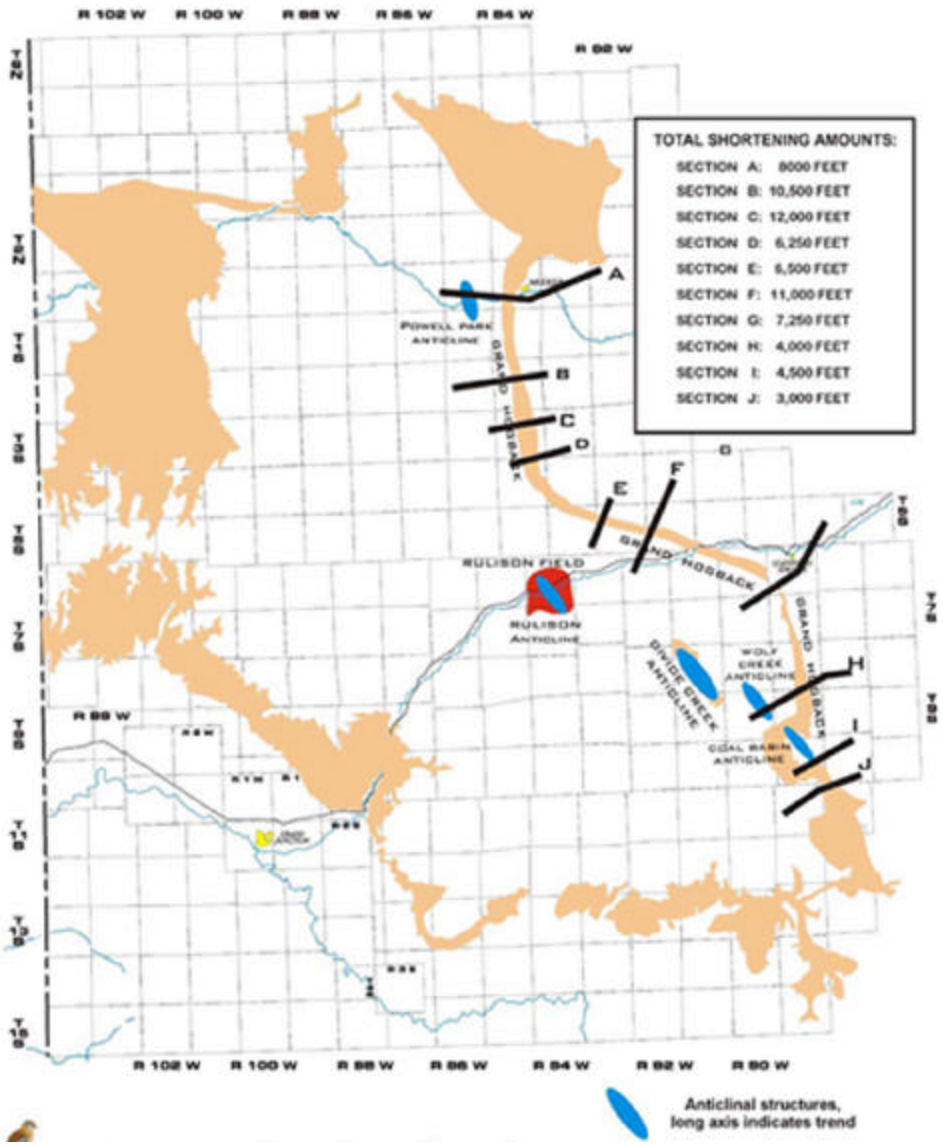

Fig. B-2a Index map showing location of cross-section used to calculate basin shortening (Murray, 1966).

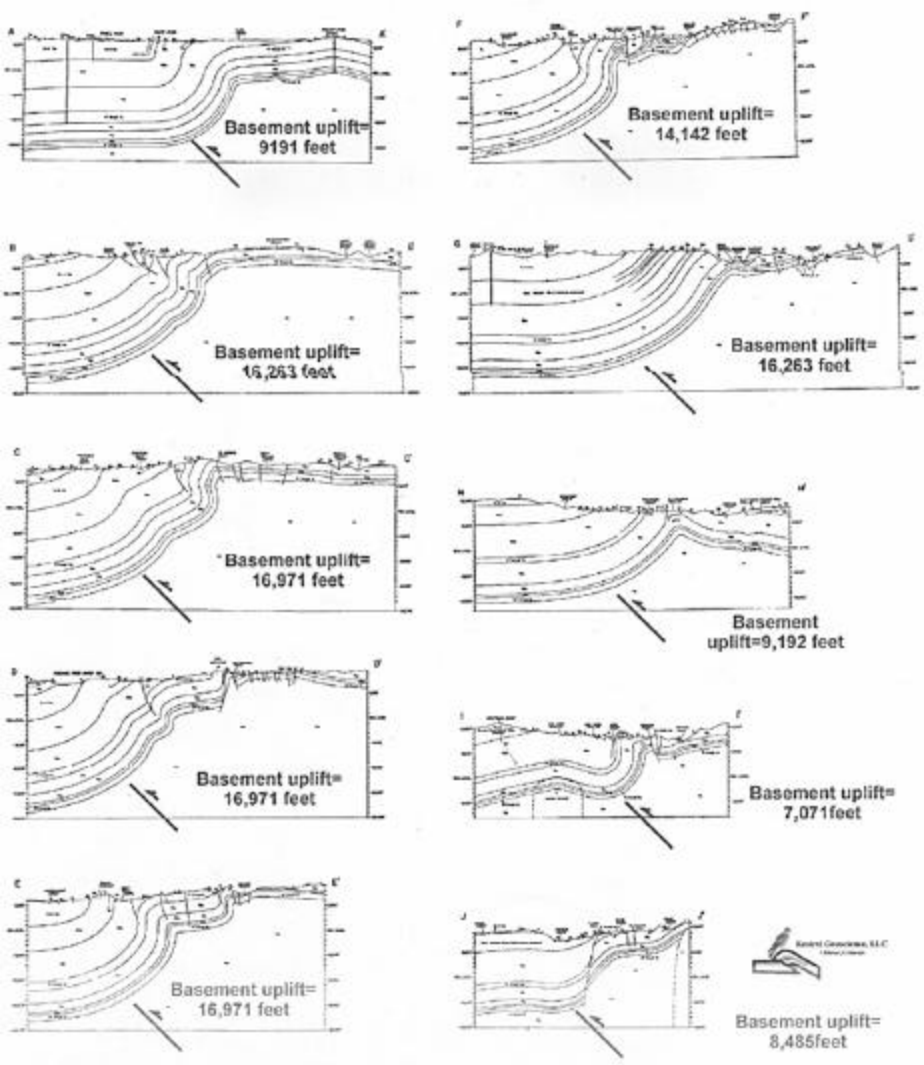

Fig. B-2b Cross sections as indicated in Fig. B-2a (Murray 1966).

		36Ma		46Ma		46Ma	
	Easting	**Northing**	**Easting**	**Northing**	**Easting**	**Northing**	
	present-day	**present-day**	**faulting only**	**faulting only**	**folding only**	**folding only**	
Section A	243500	4434000	245938	4434000	246301	4434000	
due east transport			2438		2801		Meters
Section B	248500	4420000	251700	4420000	253456	4420000	
due east transport			3200		4956		Meters
Section C	248500	4410000	252157	4410000	253672	4410000	
due east transport			3657		5172		Meters
Section D	250000	4402500	251905	4402500	255172	4402500	
due east transport			1905		5172		Meters
Section E	262300	4390000	263701	4391401	267472	4393657	
NE-directed transport			1981		5172		Meters
Section F	270000	4385750	272370	4388120	274310	4388798	
NE-directed transport			3352		4310		Meters
Section G	295300	4375100	296862	4376662	300256	4378604	
NE-directed transport			2209		4956		Meters
Section H	304250	4350000	305112	4350862	307051	4351981	
NE-directed transport			1219		2801		Meters
Section I	303500	4334600	304469	4335569	305655	4336124	
NE-directed transport			1371		2155		Meters
Section J	310000	4320000	310646	4320646	312586	4321829	
NE-directed transport			914		2586		Meters
			646		1828.560		

Table B-1 Piceance Basin boundary conditions including magnitude, direction and timing of shortening. Locations of reference points are in UTM coordinates for zone 13.

APPENDIX C: RELATIONAL DATABASE FOR THE PICEANCE BASIN

A preliminary version of a relational database was created to facilitate access to the massive amounts of data available for the Piceance Basin. Given the short duration of this project and the fact that a relational database was not a contracted deliverable, this work is incomplete. An interim version of the database is included on the compact disk (CD) that accompanies this report in order to provide the contractor access to the digital data sets for the Piceance Basin used to develop input fields for the RTM simulator and to evaluate our modeling results. In its current form, the database contains numerous tables containing much of the data from the MWX site as well as basin-wide well data, coal data, and local gas field data compiled from the published literature and contributed by our industry partners. Some of the tables are linked so that the availability of specific types of data can easily be determined. In its current stage of development, the database contains most of the data used in this report. However, some of the tables have not been proofed for accuracy, much of the well location and identification information is incomplete, and the database has not been normalized to eliminate unnecessary redundancies among the various tables. It is included here because it provides quick access to a large amount of information, it can be continuously expanded as more data is made available, and it can be easily incorporated into geographic information system (GIS) software and the data converted into map coverages. Digital mapping applications are the state-of-the-art for creating and analyzing maps and this database provides a foundation upon which to build a comprehensive Piceance Basin GIS.

Once the CD is loaded and opened, the Relationships page of an Access document is viewed by clicking on the button that looks like  on the toolbar of the Access document. Another way to open relationships is to click “tools” on the menu bar and then click “relationships”. Two types of connections or relationships are possible, one-to-many and one-to-one. The one-to-many relationship is established when one of the fields in Table A contains only unique data and the linked field in Table B has the same data, such as a map location number, repeated many times. In a one-to-one relationship every record in the primary table has no more than one matching record in the related table.

Tables are accessed by using the mouse to click on Tables under Objects in order to view the list of tables in the database. Tables are opened by double clicking on the table name you wish to display. Once the tables are displayed they can be edited or more data can be entered. New tables can be created and linked by dragging a field name from one table to the next. This will make a connection and the computer will ask what type of connection to make and between which tables. When a table is open, a plus sign may appear along the left side of the table inside a box (). By clicking this plus sign, another table will automatically open in a separate window (Fig.C-2). The plus sign will not appear if the table that is being viewed is on the many side of a one-to-many relationship. For any table having a relationship, related tables can be accessed through the plus sign. A different linked table can be accessed by clicking “insert” and then clicking “subdatasheet.” A menu will pop onto the screen and a new table may be chosen from the listed tables. If there is no connection between the tables on the relationships page, when the new table is selected, Access will automatically make a new relationship.

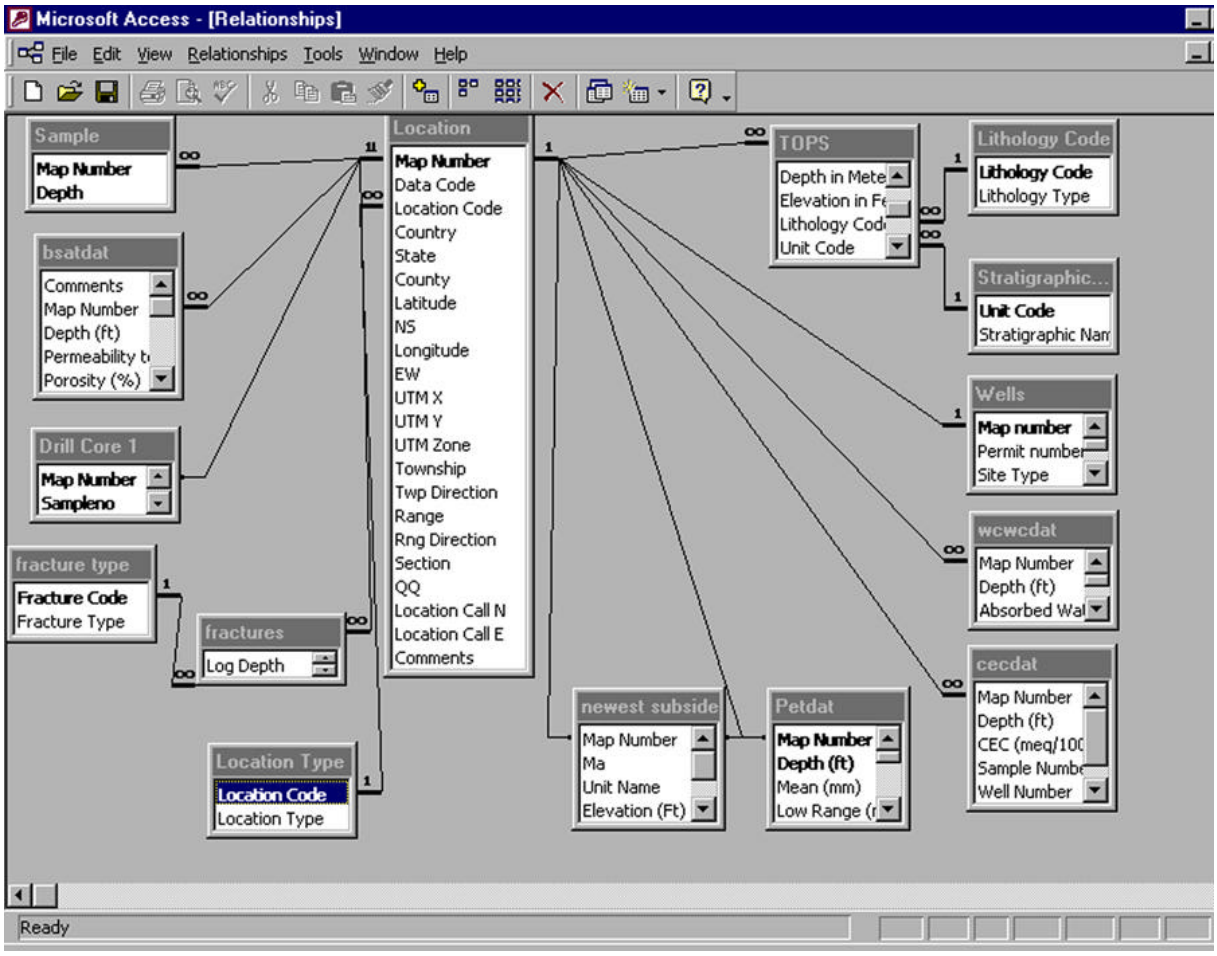

Fig. C-1 Illustration of relationships among tables in Piceance Basin database. Lines between tables indicate key fields that are linked. One-to-many relationships are shown with a "1" next to the primary table having unique entries in the key field and an "∞" next to the table having many data entries from a given location.

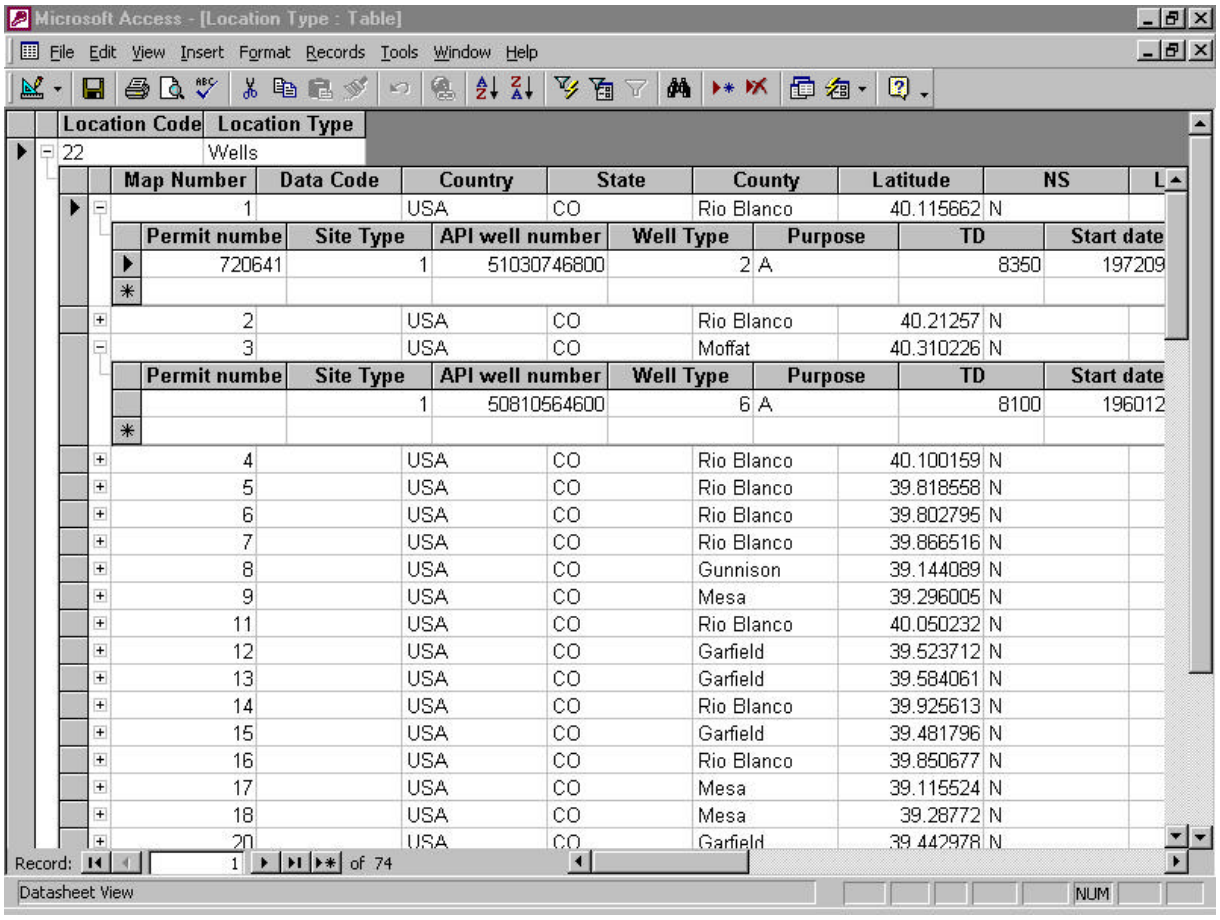

Map Number	Data Code	Country	State	County	Latitude	NS
1		USA	CO	Rio Blanco	40.115662	N
2		USA	CO	Rio Blanco	40.21257	N
3		USA	CO	Moffat	40.310226	N
4		USA	CO	Rio Blanco	40.100159	N
5		USA	CO	Rio Blanco	39.818558	N
6		USA	CO	Rio Blanco	39.802795	N
7		USA	CO	Rio Blanco	39.866516	N
8		USA	CO	Gunnison	39.144089	N
9		USA	CO	Mesa	39.296005	N
11		USA	CO	Rio Blanco	40.050232	N
12		USA	CO	Garfield	39.523712	N
13		USA	CO	Garfield	39.584061	N
14		USA	CO	Rio Blanco	39.925613	N
15		USA	CO	Garfield	39.481796	N
16		USA	CO	Rio Blanco	39.850677	N
17		USA	CO	Mesa	39.115524	N
18		USA	CO	Mesa	39.28772	N
20		USA	CO	Garfield	39.442978	N

Permit numbe	Site Type	API well number	Well Type	Purpose	TD	Start date
720641	1	51030746800	2	A	8350	197209

Permit numbe	Site Type	API well number	Well Type	Purpose	TD	Start date
	1	50810564600	6	A	8100	196012

Fig. C-2 Illustration of how multiple linked tables in the Piceance Basin database open as separate windows. This feature allows the database to be rapidly searched for specific data without having to construct a query program.

APPENDIX D: LIGNIN MATURATION — A CHEMICAL STRUCTURAL KINETIC MODEL

A. Overview

This appendix presents a chemical kinetics model of the transformation of lignin in the geologic environment. The purpose of this model is to simulate organic speciation under natural burial conditions, assuming a terrigenous, primarily lignin-bearing source material. The approach is based on organic and physical chemical principles. The major structural transformations that the lignin molecule experiences during progressive burial are accounted for, as are the geologically relevant kinetics. At the heart of the model is the understanding of the specific bond breaking and linking processes which take place during maturation. While the present treatment is limited to lignin, this novel approach is not, but rather applies to the diverse classes of kerogen precursory molecules.

In the present study we focus on the transformation of lignin to illustrate this approach. The relative abundance of lignin and its resistance to early microbial degradation indicate that it is selectively preserved and concentrated in some sedimentary deposits. Thus, it is a large component of many coals, Type III kerogens, and other hydrocarbon precursors. A significant body of analytical work integrating NMR and pyrolysis analyses has allowed characterization of the lignin structure and chemistry at various stages of thermal transformation, both in the laboratory and natural settings.

The novelty of the model is its chemical kinetic formulation, which allows it to be extended to molecules other than lignin, and thus to the full range of depositional environments. Sedimentary organic matter (SOM) may be thought of as a suite of selectively preserved molecular hydrocarbon precursors (Tegelaar et al., 1989). The exact composition will be largely a function of the characteristics of the depositional environment. In this approach depositional environments are characterized by specific precursor molecules, the maturation of which follows similar pathways to that developed for lignin. There is generally a limited number of fundamental substituent groups and linkages in such molecules, and thus a limited number of processes or reactions that will occur during thermal transformation. Because the kinetics of these processes are intrinsic to the molecular structures (and not the specific molecule), only limited kinetic data are required to describe a complicated network of reactions, involving a variety of hydrocarbon precursor molecules.

In order to be consistent with an emphasis on fundamental chemical and physical laws, the ideal approach would be to model each structural transformation in terms of its elementary processes using appropriate reaction rates. In some cases, specific transformations of the lignin molecule have been studied by examining the mechanisms of reactions of representative compounds. For other transformations, the mechanisms have not been addressed specifically. In this case, similar representative reactions for which mechanisms and rates are well understood could be used to describe observed transformations. For more speculative mechanisms, determining appropriate reaction kinetics would be difficult. Bond dissociation energies are probably inappropriate for these reaction activation energies as they represent homolytic cleavage processes, which require higher temperatures than generally exist in sedimentary basins. Because of the uncertainties and inconsistencies in determining reaction mechanisms and rates for elementary processes in the structural transformation of lignin, the model relies to some degree on empirical correlations. Hence, the model is constructed as follows: each

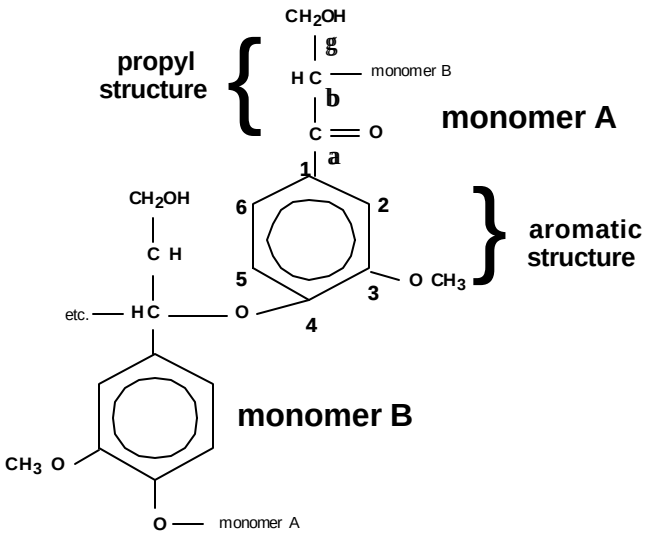

Fig. D-1 Simplified model of lignin structure used in this study; one molecular unit of lignin comprises one monomer each of A and B, except as noted in the lignin composition sensitivity tests.

transformation of a functional group or molecular structure is described as a single process (many of the transformations require that the representative reaction is non-first order); then, a relative order of reaction rates is determined based on the observed relative order of the timing of functional group transformations; finally, the reaction rates were calibrated against observed molecular structures and elemental chemistry for samples of known thermal history.

In the following, we first present a simplified lignin structure, based on the most commonly observed structural features. Observations of the transformations that occur in lignin during thermal maturation are discussed in relation to the adopted lignin structure and are described in terms of reactions. The general mathematical formulations to solve the concentrations of species through time are presented. The reaction network is constructed based on observed correlations of structural changes with increasing coal rank, and the kinetics are calibrated for the MWX site in the Piceance Basin in western Colorado. Finally, the results of simulations using the reaction network and the kinetics are presented and compared with observed data.

B. Modeling Approach

1. Lignin structure

The lignin structure adopted here (Fig. D-1) has been modified from Hatcher (1990) to include only the most basic features for the purpose of simplifying of the reaction network. It is a polymer of guaiacyl units linked by the most common types of linkage in lignin, the -O-4 linkage as well as the –O-4 linkage, (Fig. D-1). Guaiacyl, the monomethoxylated lignin monomer, was chosen because there is an average of one aryl-methoxyl group per aromatic ring (Hatcher, 1990). According to Hatcher's structure, most of the -carbons of the propyl side chains have a hydroxyl substituent. Also, most of the propyl -carbons that are not part of ether linkages have hydroxyl or carbonyl substituent groups. The model is based on the progressive decomposition

I. Isomerization
   β-O-4 cleavage
II. Modification of the Propyl Structure
   a. oxidation of α-carbonyl to carboxyl
   b. oxidation of γ-OH to aldehyde
   c. oxidation of γ-aldehyde to carboxyl
   d. reduction of γ-OH to methyl
III. Defunctionalization
   a. demethoxylation
   b. decarboxylation
   c. dehydration
   d. demethylation of pendant aryl-ethyl
   e. demethylation of pendant aryl-methyl
IV. Cross-linking
   a. with loss of H_2O to from ether linkage
   b. with demethylation
   c. with loss of hydrogen

Table D-1 Reaction classes and descriptions of specific types

of these guaiacyl units into a host of intermediate and mobile species by a network of sequential and parallel reaction pathways.

2. Representative Structural Transformations

The types of reactions, their relative rates, and the general order of the reaction network are determined by the observed structural transformations that occur to the lignin structure with increasing rank up to the high volatile bituminous rank (Hatcher, 1990; Hatcher et al, 1992; del Rio et al. 1994). At higher maturities, observed and inferred transformations in pyrolysis experiments determine the types and relative rates of reaction occurring later in the reaction network (Behar and Hatcher, 1995; Charpenay et al, 1996; Grant and Pugmire, 1989; Hatcher et al, 1992; Levine, 1993; Manion et al, 1996; Mansuy and Landais 1995; Obeng and Stock, 1996; Solomon et al, 1990; Solum et al, 1989; Suuberg et al. 1985). The kinetics of the reactions in the reaction network were then calibrated on the geochemistry and thermal indicators of Mesaverde Group coals of the MWX site and other sites in the Piceance Basin, under the assumption that these coals are derived primarily from lignin.

The general processes observed with increasing maturation of lignin are cleavage of the main polymer linkage, modification and loss of various functional groups including methyl, carboxyl, and hydroxyl groups, and cross-linking. Some of the major expected mobile products of lignin transformation are methane, carbon dioxide, and water. In order to describe the transformations that occur to the lignin structure, eleven reactions have been formulated that we divide into four classes: isomerization; modification of the propyl structure; defunctionalization; and cross-linking (Table D-1).

The isomerization reaction class comprises the -O-4 cleavage, which is nearly completed by the time lignin-bearing material has matured to the brown coal rank, and results in the

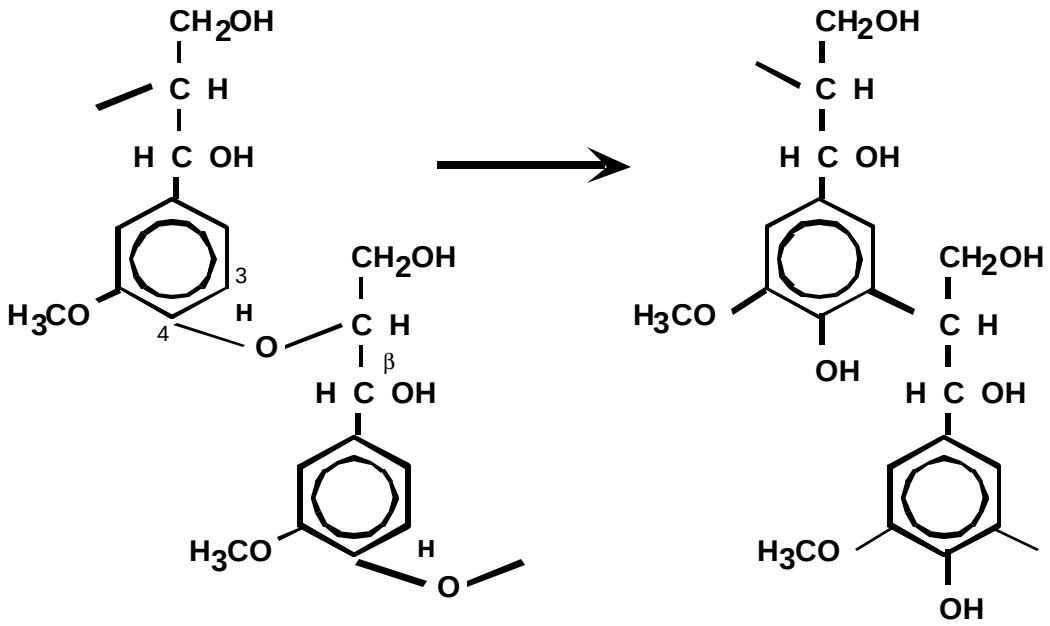

Fig. D-2 Isomerization: cleavage of the β-O-4 linkage. This reaction results in no change in the elemental composition of the lignin.

creation of a phenol group and the reattachment of the propyl structure to the C3 of the aromatic group (Hatcher 1990) (Fig. D-2). The mechanism of this transformation is still open to debate, whether it is purely a free radical chain mechanism as addressed in thermolytic cleavage experiments (Britt et al., 1995; Gilbert and Gajewski, 1982; Hartgers et al., 1995; Kuroda, 1995) or whether under geologic conditions catalysts such as clays are required for the reaction to occur (Buchanan et al., 1997). As the reaction is nearly complete by the brown coal rank, purely thermolytic reactions probably cannot describe the geologic processes. The choice of mechanism will ultimately have bearing on the way the reaction is modeled in terms of the reaction order and the requirement of other components as reactants or catalysts.

Modification of the propyl structure includes oxidation of the propyl- alcohol functional group to a carbonyl functional group, and a subsequent oxidation at that site to form a carboxyl functional group (Fig. D-3). Progressive oxidation of hydroxylated alkyl side chain carbons is observed in a natural series, eventually leading to decarboxylation (Hatcher, 1990; del Rio et al., 1994): carbonyl functional groups increase as the brown coal rank is approached, and decrease steadily thereafter; carboxyl functional groups increase as the lignite rank is approached, then decrease dramatically between the lignite and the sub-bituminous stages. The carboxyl functional groups are believed to be decreasing from decarboxylation reactions. However, the total CO2 is more accurately balanced if it has been sourced by both the carboxyl and carbonyl functional groups (Behar and Hatcher, 1995). Thus, a reaction that transforms carbonyl groups into carboxyl groups is invoked. Although a specific mechanism is not documented, an analogy is made to the anhydride hydrolysis reaction, in which anhydride reacts with water to form carbon dioxide by way of a dicarboxyl acid (Petit, 1991; Song et al., 1994). Indeed, water has been suggested as a reactant in the production of CO2 in pyrolytic experiments (Stalker et al., 1994). Perhaps these reactions can be seen as the progressive oxidation of a hydroxylated alkyl site first to a carbonyl functional group, then to a carboxyl functional group, followed by

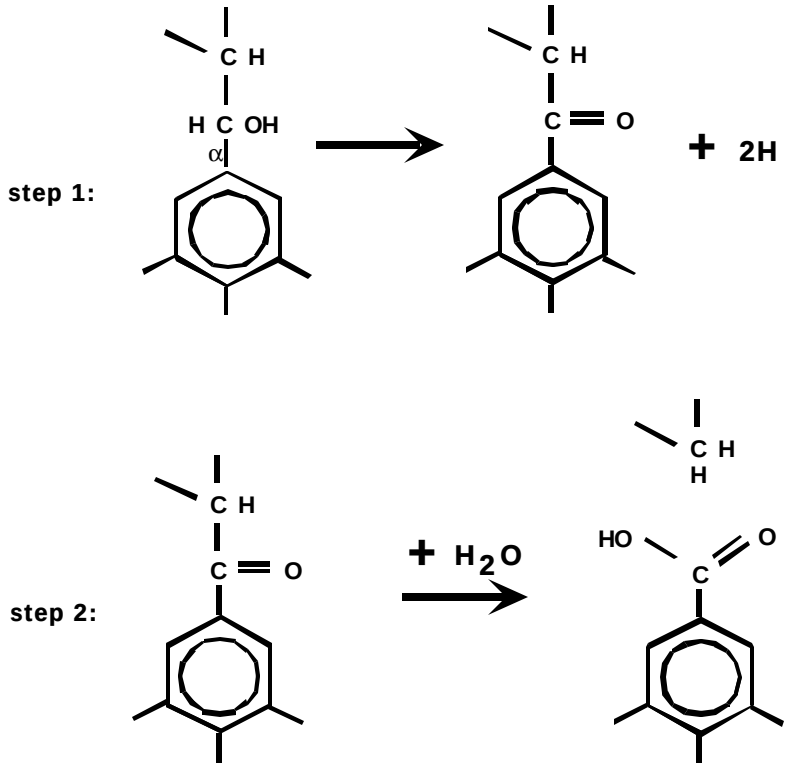

Fig. D-3 Progressive oxidation at the propyl α-site. This sequence is suggested by an increase in carbonyl groups with increasing thermal maturity up to the brown coal rank, followed by a decrease, and a concomitant increase in carboxyl functional groups.

decarboxylation. Although not specific to the lignin structure, evidence for this may also be seen in the generation of excess CO2 related to the relative oxidation of asphaltenes during hydrous pyrolysis (Michels et al., 1996). Pyrolysis-methylation data suggest that a likely, though not exclusive location for the formation of ketones and carboxyl functional groups is the α-carbon (del Rio et al., 1994).

The modifications at the propyl γ-site include reduction of the alcohol to a methyl group, oxidation of the alcohol to an aldehyde group, and transformation of the aldehyde to a carboxyl group (Fig. D-4). On the alkyl structure, reduction is suggested to occur as thermal maturity approaches the lignite rank because an increase in carboxyl functional groups is accompanied by a lack of change in total alkyl carbon-oxygen bonds. In terms of the adopted lignin structure, for every oxygen atom gained in transformation of a carbonyl to a carboxyl group, an oxygen atom must be lost by alkyl dehydration. The oxidation reactions at the γ-site also are not specifically indicated by the structural data, but there is uncertainty in the structural transformations of this site, as well as with the location of the aliphatic carbonyl and carboxyl functional groups, so it is possible these reactions occur at this site. As these reactions are written in this paper, the electron transfer processes can be considered as occurring within the lignin structure, and do not require external sources or sinks for electrons, which is an important consideration in non-aqueous reactions, where contact with electron sources or sinks may be limited.

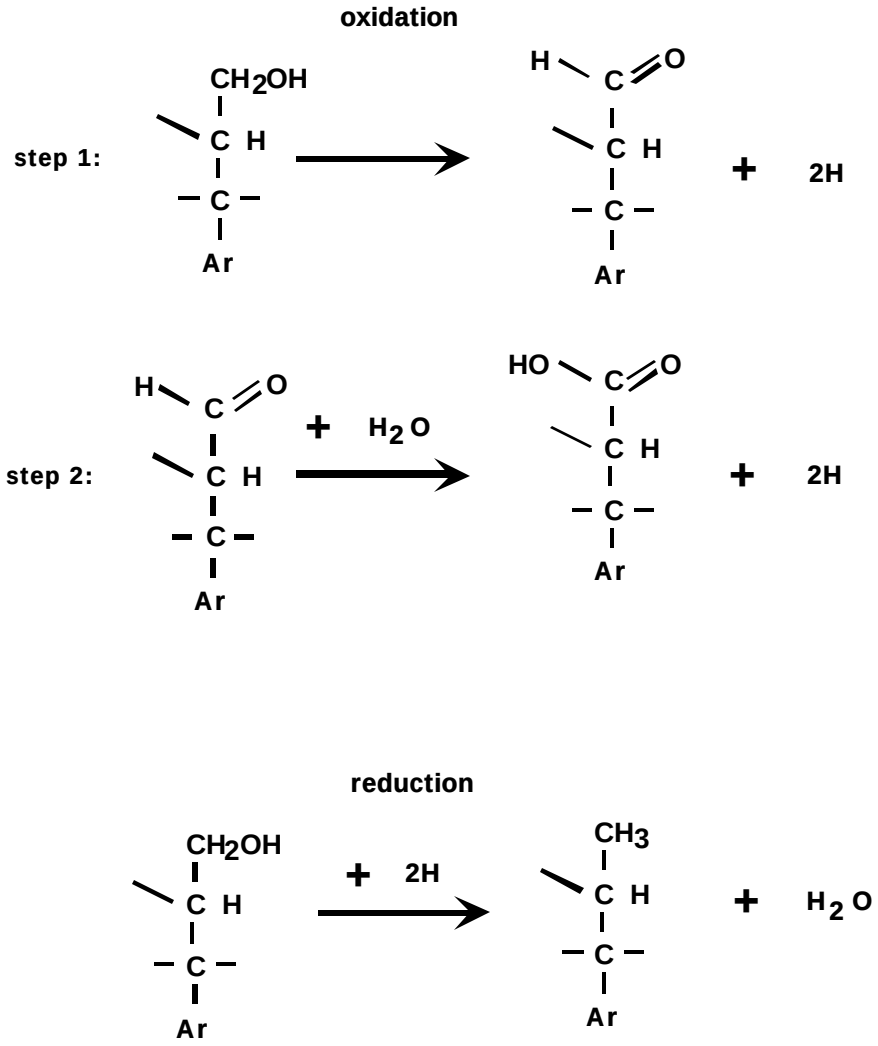

Fig. D-4 Transformation of the propyl γ-site from alcohol to carboxyl and methyl functional groups. This series illustrates hydrogen and water sources and sinks within the lignin structure.

Defunctionalization class reactions include demethoxylation of the aromatic methoxyl functionality, decarboxylation, loss of OH groups on the aromatic structures, and higher temperature loss of methyl groups attached to the aromatic structure. The loss of the aromatic methoxyl functionality is indicated by NMR data which show that between the unaltered lignin and brown coal ranks of a natural series of coals, aromatic methoxyls decrease by about 50%, and by another 50% through the lignite rank, until essentially none is left by the sub-bituminous rank (Hatcher, 1990). Because there is little change in the quantity of aromatic oxygen substituents, the cleavage is believed to occur between the methyl and the oxygen, and the methyl group is replaced with a hydrogen atom to become an OH group (Fig. D-5). Although this reaction mechanism has not been approached from a geochemical standpoint, some experimental data on the reductive demethoxylation of simple methoxylated phenyls (anisoles) in the presence of strong reducing agents (alkali metals) show that in the presence of a hydrogen donor and an electron donor, demethoxylation occurs by cleavage of the methyl-oxygen bond,

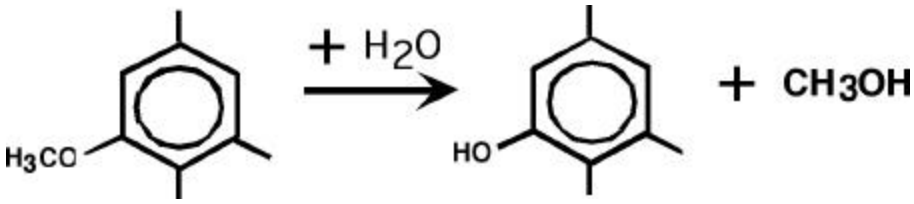

Fig. D-5 Transformation of an aromatic methoxyl to an aromatic hydroxyl functionality. This transformation is invoked by an inverse relationship between aromatic methoxyl and hydroxyl functional group content between unaltered lignin and sub-bituminous rank coal.

producing a phenol (Azzena et al., 1996; Lazana et al, 1989; Patel et al., 1982). Although such strong reducing agents are not found in the geochemical environment of lignin transformation, there are other reducing species available in the diagenetic system, most notably Fe and S species, or the organic species themselves. Given geological time scales, it is possible that such reductive reactions occur under natural coalification conditions. However, a suggested mobile product is methanol (P.G. Hatcher, personal communication), indicating that the reaction is not a reduction, but more likely an addition of water.

Decarboxylation is documented by a decreasing concentration of carboxyl functional groups with progressive maturation in the geologic environment after the lignite rank and through the high volatile bituminous rank (Hatcher 1990; Hatcher et al., 1992), and by pyrolysis experiments as mentioned earlier. Thermal decarboxylation of simple aliphatic acids is observed to follow first-order rate laws (Kharaka et al, 1983). A suggested mechanism is by means of a catalyst, which causes cleavage between the aliphatic and carboxyl carbon atoms, and subsequent combination of the carboxyl proton and the aliphatic carbon (Bell and Palmer, 1994). However, in the case of lignin, which is a more complex molecule and has more aromatic carboxyl functional groups, the mechanisms of decarboxylation may differ. In coal pyrolysis experiments, cross-linking of aromatic groups associated with decarboxylation suggests that the decarboxylation mechanism may indeed be a non-first order process (Solomon et al, 1990; Charpenay, 1996; Suuberg et al, 1985). However, in the model presented here, simple first-order decarboxylation reactions are assumed, occurring primarily at the propyl -carbon and secondarily at the propyl –carbon where carboxyl functional groups are formed (Fig. D-6).

Loss of OH groups is likely to cause production of H2O, and two elimination reactions may be responsible for the loss of hydroxyl substituent groups from the lignin structure. These dehydration reactions are inferred by NMR data which show a general reduction of oxygen functionalities with progressive coalification (Hatcher, 1990), and are suggested by structural H2O produced during pyrolysis (Behar and Hatcher, 1995). The OH groups may be lost from either of the hydroxylated alkyl sites (discussed above) or the aromatic sites (phenol groups are produced in the demethoxylation reaction and during -O-4 cleavage). For maturities greater than the lignite rank and through the sub-bituminous rank, dehydration of aromatic sites is inferred from NMR evidence of the transformation of the aromatic structure from a catechol-like (two hydroxyl) to a phenol-like (one hydroxyl) structure. This is suggested to be the main cause of loss of oxygen from the lignin structure occurring at the sub-bituminous rank and later. In an environment with sufficient activated hydrogen, this transformation may occur as indicated in Fig. D-7. Loss of oxygen through cross-linking is discussed below.

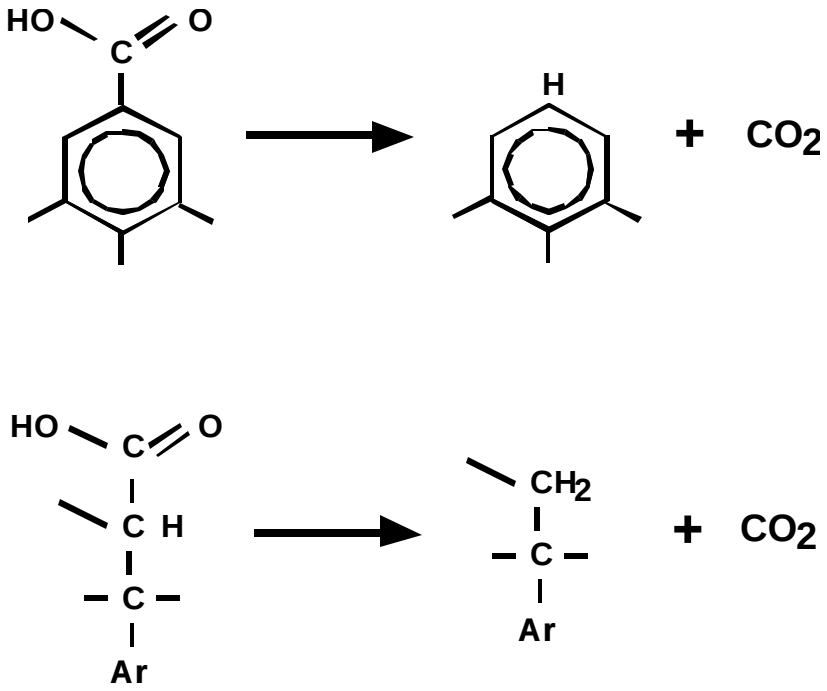

Fig. D-6 Decarboxylation for both aromatic and aliphatic carboxyl groups is assumed to be a first order process.

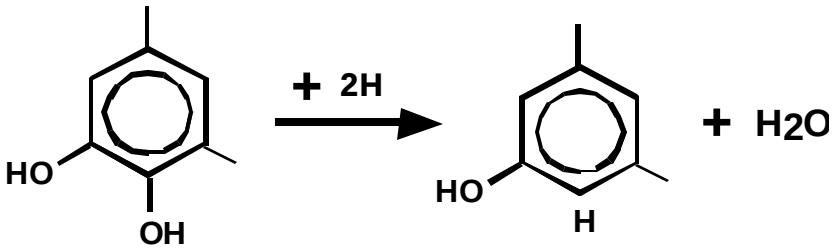

Fig. D-7 Dehydration of the aromatic structure is suggested to describe observed loss of aromatic hydroxyl functional groups between the lignite and sub-bituminous coal ranks.

It has been suggested that methane generated at greater maturities than the sub-bituminous rank and at higher pyrolysis temperatures are probably from functional groups attached directly to the aromatic structure (Behar and Hatcher, 1995; Charpenay et al., 1996). The likely candidates in this model are ethyl and methyl groups that remain attached to the aromatic structure after the propyl chain has been cleaved by oxidation at the -site. An increase in CH4 generation with increasing rank (Charpenay et al., 1996) and an increase in pendant methyl groups (those attached directly to the aromatic structure) from the lignin through the low volatile bituminous rank (Obeng and Stock, 1996) suggest that aryl methyl groups probably do not play an important role in methane generation until after the low-volatile bituminous rank. In this model, it is considered that if demethylation occurs earlier from demethylation of a pendant ethyl group, this will effectively increase the number of pendant methyl groups. Indeed, the

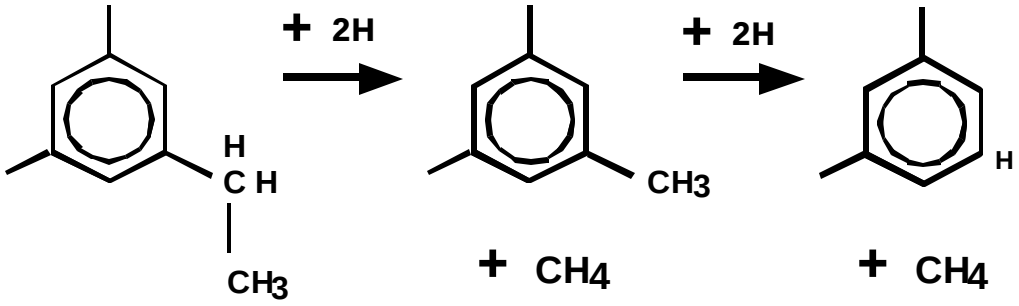

Fig. D-8 Progressive demethylation first from a pendant aryl-ethyl, and subsequently from a pendant aryl-methyl are suggested to account for methane generated primarily from aromatic functional groups.

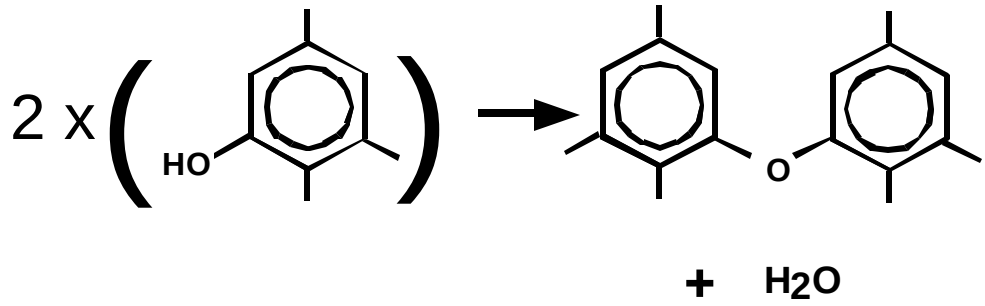

Fig. D-9 Cross-linking reaction associated with dehydration and formation of an aryl-ether linkage accounts for a relatively unchanged aromatic oxygen content associated with a total oxygen loss of about 50% by the high volatile bituminous coal rank.

activation energy for homolytic cleavage of aryl methyl is about 26 kcal/mole greater than that for the ethyl bond on an aromatic pendant ethyl (Luo and Holmes, 1993). Thus, two methane-producing reactions incorporated in this model include demethylation of an aromatic pendant ethyl, and later demethylation of the resultant pendant methyl (Fig. D-8). In addition, coal pyrolysis experiments suggest that demethylation may result in cross-linking (Solomon et al., 1990), so a demethylation reaction resulting in cross-linking is also included and discussed later.

It is widely accepted that during the coalification process the aromatic structures condense, or combine with each other, producing an increasingly graphitic molecular structure (Behar and Hatcher, 1995; Grant and Pugmire, 1989; Levine, 1993; Manion et al., 1996; and Solum et al., 1989). This kind of reaction might occur when two carbon sites are made available for bonding, for example when a functional group has been removed. Pyrolysis experiments indicate that cross-linking may be associated with the generation of CO2, CH4, and H2O (Solomon et al., 1990; Charpenay et al., 1996; Suuberg et al., 1985; Hatcher et al., 1992). This model does not attempt to fully characterize the graphitization process, but it does incorporate cross-linking associated with dehydration, demethylation and loss of hydrogen. Cross-linking associated with decarboxylation is also discussed.

Cross-linking associated with loss of H2O is observed in pyrolysis experiments (Charpenay et al., 1996; Solomon et al., 1990). Moreover, kerogen depleted in oxygen-bearing functional groups during natural maturation is less likely to exhibit cross-linking in pyrolysis experiments (Burnham et al., 1989), suggesting that oxygen-bearing sites may be favorable for

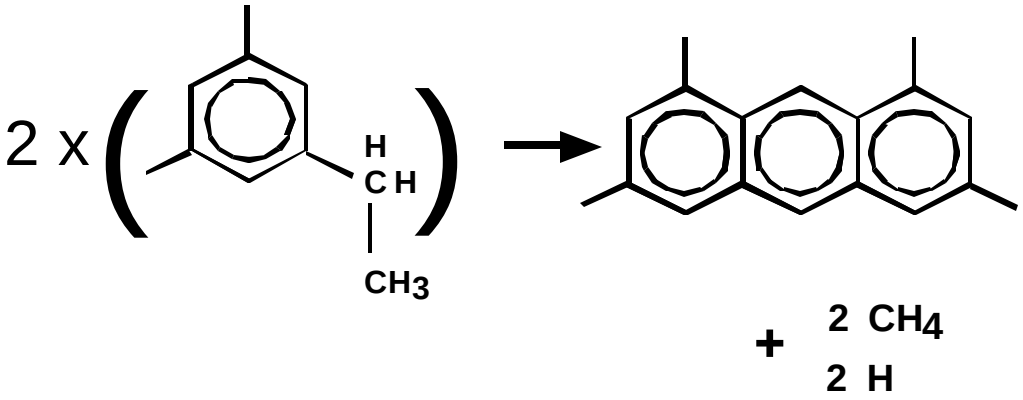

Fig. D-10 Cross-linking reaction associated with demethylation, which accounts for increasing condensation with thermal maturity.

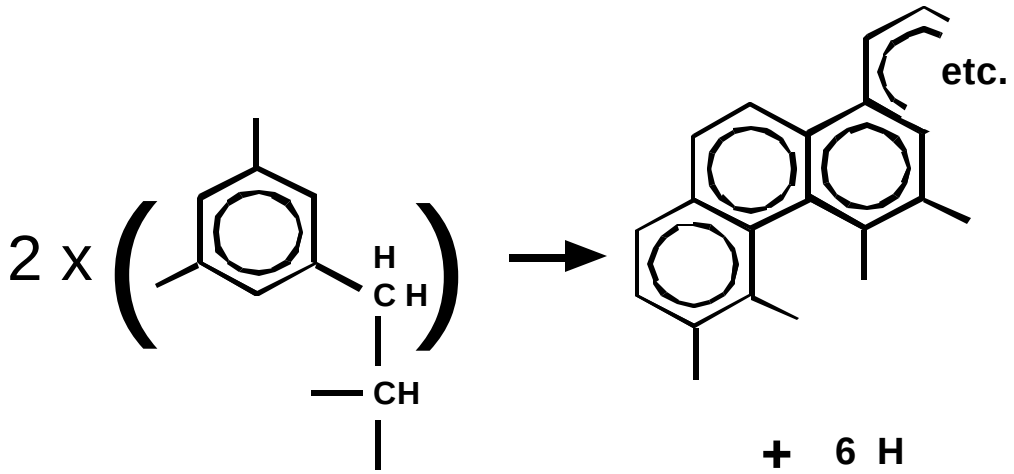

Fig. D-11 Cross-linking associated with loss of hydrogen, illustrating another means of condensation and creation of polyaromatic structures.

cross-linking processes. More importantly, studies of naturally matured lignin structures at the high volatile bituminous rank show that the aromatic-oxygen content has decreased little, but that total oxygen content has decreased by about 50%. This suggests that many of the remaining aromatic oxygen atoms are transformed into aromatic ethers, sharing one oxygen between two aromatic rings (Hatcher et al., 1992). A suggested reaction is represented in Fig. D-9.

Methane formation associated with cross-linking during pyrolysis experiments is observed at higher temperatures than cross-linking reactions associated with CO2 or H2O generation (Solomon et al, 1990). A suggested demethylation reaction involves cross-linking with loss of a methyl group from a pendant ethyl and recombination with an aromatic carbon to produce an anthracene-like structure (Fig. D-10). Additional methane may be generated during further condensation of anthracene- or naphthene-like structures, but this would require loss of carbons from the aryl-structures and probably significantly higher activation energies.

During the coalification process hydrogen is gradually lost. This loss can be attributed to some of the processes described earlier, for example loss of hydroxyl functional groups, or

demethylation. As the condensation continues, the aromatic content increases, suggesting that carbon sites become increasingly unsaturated. Although this may occur due to loss of saturated carbons, for example through demethylation of pendant aliphatic methyl groups, it is conceivable that cross-linking of aromatic structures with loss of hydrogen from saturated carbons may occur (Fig. D-11). Although this reaction is speculative, it suggests another source of hydrogen atoms within the organic material, which allows hydrogen-consuming reactions to occur (for example demethylation of pendant methyl groups) (Fig. D-8).

C. Mathematical Formulation

The chemical kinetic model representing a network of these reactions can be formulated using standard reaction-transport equations in the form of *n* th-order processes. The model focuses on the dynamics of the immobile species, because these are the natural choice for calibration. As all reactions of these species are considered irreversible, the transformation of lignin is separable as follows. Let C_i be the moles of immobile kerogen species *i* per rock volume and k_a^{eff} be an effective rate coefficient for the process α that consumes one or more *i'* reactant molecules and generates ν_{ia} product molecules. Kerogen generation and consumption rates for all species can be described by

$$\frac{dC_i}{dt} = \sum_a \nu_{ia} k_a^{eff} \left(\prod_{i'} C_{i'(a)} \right). \qquad \text{(D.1)}$$

By convention, ν_{ia} is -1 when *i* is being consumed by the reaction, or ν_{ia} is the number of *i* molecules produced by the reaction. Because the reactions are *n*th order where *n* is an integer, the solution is strongly non-linear and must be solved iteratively. Computations are facilitated by using a time step that dynamically changes to minimize errors, to allow faster convergence, and to proceed with sufficient computational speed. Thus, the speciation is solved by a network of reactions, as described by these equations, which occur simultaneously and sequentially.

1. Preliminary Calibration

Because the model is based on observed and inferred structural transformations, kinetics for the processes were derived not from laboratory derived pyrolysis experiments, but rather were estimated in such a way as to better capture the kinetics of the processes under geological conditions. To derive the kinetic parameters, first the reaction network was constructed based on the relative order of structural transformations that occur. For example, because CH4 generation is observed with cross-linking at higher temperatures than CO2 generated with cross-linking, the former processes would be modeled to follow the latter. Secondly, estimates of rates were made based on the timing of specific structural transformations relative to coal rank. For example, approximately 50% of the aromatic-methoxyl groups are lost between the lignin and brown coal stage (Hatcher, 1990); it can be roughly estimated that this occurs over a temperature range from 10 C to 45 C (Bouska, 1981). Solving the differential equation for rate

$$dc/dt = k \qquad \text{(D.2)}$$

(*c* is concentration, *t* is time, *k* is the rate coefficient),

$$\ln c0/c = kt, \qquad \text{(D.3)}$$

(*c0* is the initial concentration of reactant) the rate coefficient of demethoxylation (hence methanol production) can be estimated for this temperature range.

These processes are observed to be temperature dependent and thus, by convention, follow the Arrhenius law

$$k = A \exp(-Eact/RT), \qquad \text{(D.4)}$$

where *k* is the rate coefficient, *A* is the Arrhenius pre-exponential, *Eact* is the activation energy, *R* is the universal gas constant, and *T* is temperature. Because not enough information exists to solve for both *A* and *Eact* for geological reactions with available data, *A* is assumed to be constant for all reactions and is calculated independently from statistical mechanics:

$$AKbT/h\ exp(Sact/R), \quad \text{(D.5)}$$

where *Kb* is Boltzman's constant, *h* is Planck's constant, and *Sact* is the activation entropy. Determining *Sac* requires knowledge of elementary mechanisms and transition state geometries of the molecules, which is beyond the scope of this model. Thus *Sact* is assumed to equal zero, which is appropriate for first order reactions. When a constant is used for *T* (298 C), *A* equals a constant value of 6.18x1012 sec-1 for all reactions. From the estimated rate of each process, an estimated *Eact* is calculated from the Arrhenius law. Sensitivity testing indicates that changing values of *A* may shift the timing of the reaction, but does not significantly affect the shape of the reaction slope, unless it is changed by many orders of magnitude.

Using the estimated activation energies and independently derived thermal and burial histories (Payne and Comer, 1997), the model is run iteratively to calibrate the kinetics against observed C, H, and O weight percents at the MWX site in the Piceance Basin. The model is further refined by calibrating predicted vitrinite reflectance values as calculated from the H/C and O/C ratios (Burnham and Sweeney, 1989) against observed values for a range of maturities. The calibration was constrained to preserve the relative order of observed structural transformations. Table D-2 shows the activation energies determined for and used in the model. With the availability of more well constrained molecular structural data, this kind of model can be calibrated more specifically and directly.

2. Model Reaction Network

The reaction types are formulated into a reaction network comprising twenty-six species and twenty-two reactions (Fig. D-12). Currently this network incorporates the fifteen types of reactions listed in Table D-1 as sequential and parallel pathways. Each species has a chemical formula and a unique set of reactions for which it is a product and for which it is a reactant. Most of these species are immobile intermediate species, defunctionalized or fragmented parts of the lignin structure; the mobile species include CH3OH, H2O, CO2, CH4 and H*. The set of unique parameters for each reaction includes stoichiometric coefficients and an activation energy (the Arrhenius pre-exponential coefficient is assumed constant). The network of reactions is tabulated, then used to construct a matrix of reactions used in the speciation computations, along with an array of initial concentrations of each species (it is assumed that the initial concentration of each species, except the unmodified lignin molecular species and H2O, is zero).

D. Simulation Results

1. MWX Site

The model was tested using the MWX site in the Piceance Basin of western Colorado (Fig. D-13). This site was chosen because of on-going RTM modeling work being done there, and because it is a well-studied site. The MWX site is one of the few with published kerogen elemental weight percent data and vitrinite reflectance data, and well understood burial and thermal histories with which to calibrate the model (Johnson and Nuccio, 1986; Sattler, 1988; Zhang et al, 1997). In the Piceance Basin, much of the methane resources are believed to be sourced by Upper Cretaceous Williams Fork Formation coals, which are vitrinite-rich (Zhang et

Reaction	Activation	Figure

number	Energy, KJ/mol	number
I 1	152.7	D2
I 2	152.7	D2
II a 1	163	D3
II a 2	163	D3
II b	161	D4
II c 1	163	D4
II c 2	163	D4
II d	160	D4
III a 1	163	D5
III a 2	163	D5
III a 3	163	D5
III a 4	163	D5
III b 1	165	D6
III b 2	165	D6
III c 1	167	D7
III c 2	172	D7
III d	173	D8
III e	205	D8
IV a	166	D9
IV b	199	D10
IV c 1	213	D11
IV c 2	216	D11

Table D-2 Reaction Information (refer to Table D-1 and Fig. D-12 for reaction numbers)

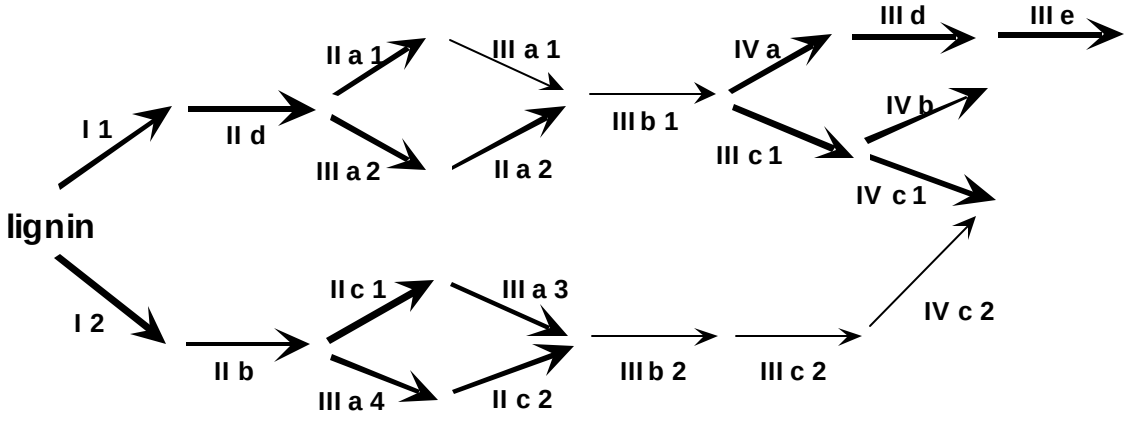

Fig. D-12 The model reaction network comprises twenty-six species and twenty-two reactions, incorporating the fifteen types of reactions listed in Table D1. Other reaction information is listed in Table D-2.

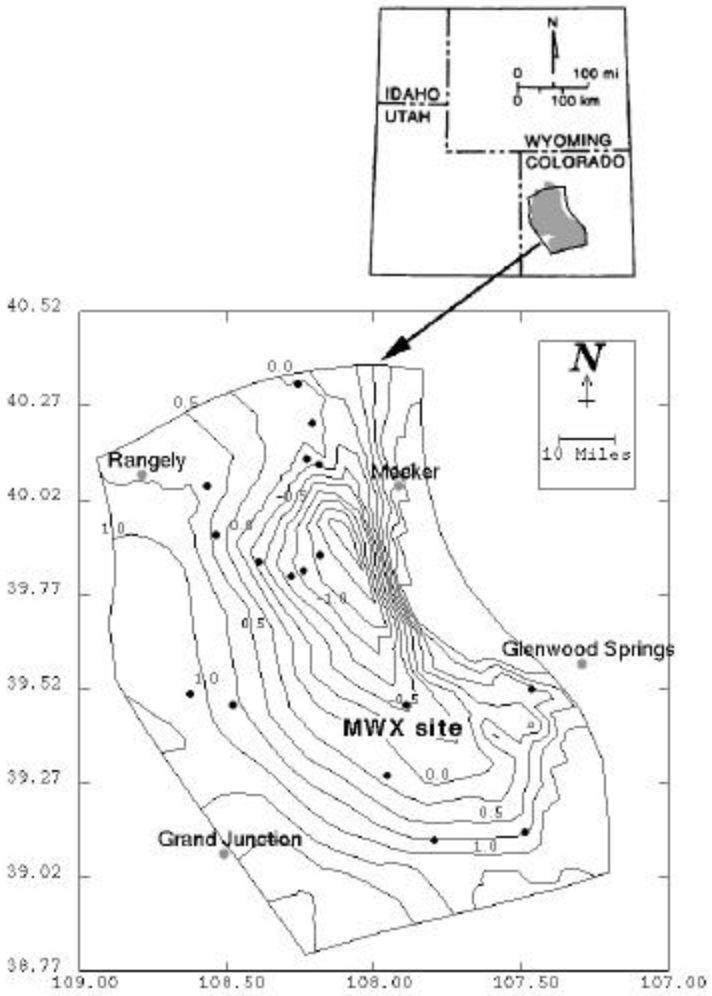

Fig. D-13 Location of the Piceance Basin, and the multi-well experiment (MWX) site. The dots indicate locations of sites for which there is vitrinite reflectance data and burial and thermal histories; the contours indicate present day elevation (in km relative to sealevel) to the top of the Rollins sandstone marker unit of the Mesaverde Group. Many of the coal source rock units are in the interval above this marker.

al, 1997) and thus are probably derived largely from lignin. A simple first assumption to test this kind of kinetic structural modeling is that the starting material is all lignin, although proto-kerogen compositional differences will undoubtedly affect the reaction network, maturity indices, and evolved product timing and abundance.

Input for the model includes thermal and burial histories, the lignin composition (relative abundance of monomers A and B, Fig. D-1), and initial H2O content (a reactant in several of the reactions). The thermal and burial history used were constructed using available published data and thermal modeling (Fig. D-14) (Payne and Comer, 1997). The starting lignin composition

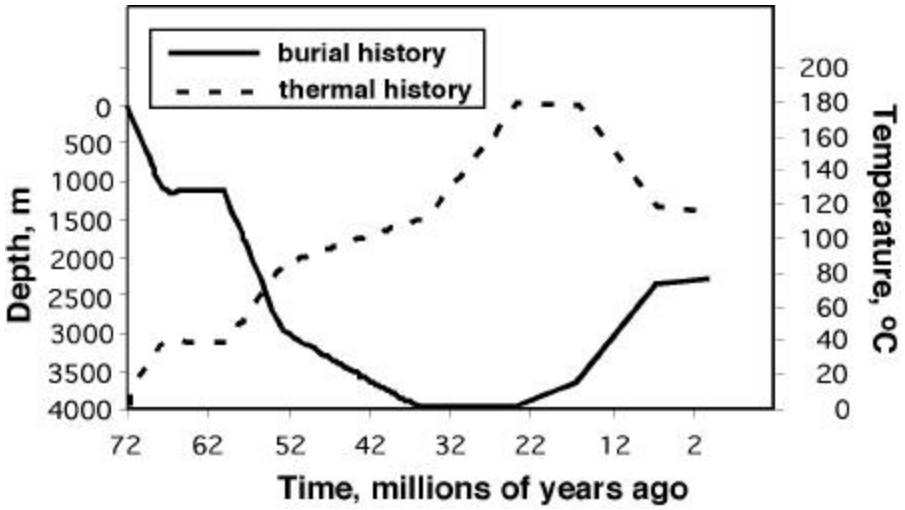

Fig. D-14 Burial and thermal histories at the MWX site in the Piceance Basin, used as input for the simulations. The curves follow the depth and temperature of a source rock-bearing interval at the bottom of the William's Fork Formation over the last 72 millions years.

was assumed to be a two-monomer unit, 50% each of monomers A and B (this has an elemental weight percent of C: 64.3; H: 5.67; O: 30.0, compared with unaltered lignin C: 62.7; H: 5.5; O: 30.4; Hatcher, 1990). Thus one mole of the lignin comprises one mole of monomer A and one mole of monomer B. Initial H2O content was taken to be 0.55 moles of H2O for every mole of lignin. This was the minimum required for all the reactions to go to completion (see Sensitivity Testing section), yet there is not so much as to simulate a situation in which lignin molecules were dissolved in H2O (probably not a likely scenario).

The output includes the following: content of functional groups (aromatic methoxyl, α-carbonyl, carboxyl, aromatic and aliphatic hydroxyl groups, and aromaticity); elemental weight percents (C, H and O) of immobile species; atomic O/C and H/C ratios; vitrinite reflectance (calculated from elemental atomic ratios by the method of Burnham and Sweeney, 1989); and moles of all species, mobile and immobile, through time.

Figures 15 a-f show how the structures of the immobile species change with time by showing the abundance of specific functional groups. Fig. D-15a shows the fraction of C3 aromatic sites with a methoxy functional group over the course of the simulation. The initial value represents lignin with one aromatic carbon site occupied by a methoxy functional group per lignin monomer, in accordance with the observed estimated average (Hatcher, 1990). The complete loss of this functional group is attained by about 37 Ma in the simulation, which corresponds to a predicted vitrinite reflectance of about 0.45 (Fig. D-15b). This roughly corresponds to the sub-bituminous coal rank (Stach et al., 1982), in agreement with the observation that this functionality is lost by the sub-bituminous rank (Hatcher, 1990).

Fig. D-15c shows the fraction of carbon sites occupied by a carbonyl substituent group, which occurs in this network only at the propyl-α site. The initial value is higher than observed (Hatcher, 1990), because in lignin, some of these propyl-α sites are probably initially occupied by hydroxyl functionalities, which may subsequently become oxidized to carbonyl groups. The loss of these substituent groups corresponds to an increase in carboxyl functional groups, as these sites are oxidized (Fig. D-15d). The carboxyl functional groups are eventually lost by

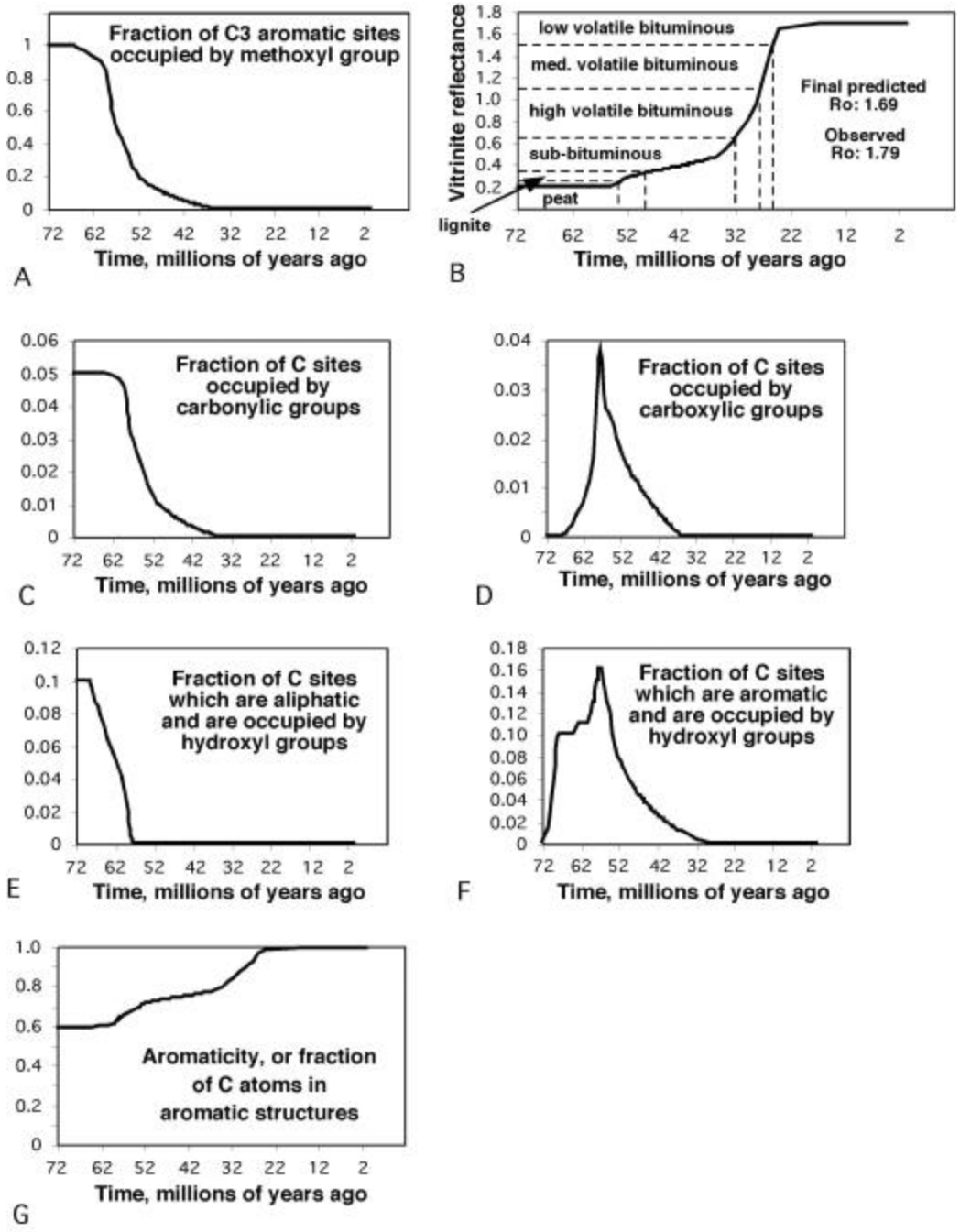

Fig. D-15 Simulated structural changes of lignin at the MWX site through time: a) fraction of C3 aromatic sites with a methoxyl functional group, assuming all C3 aromatic sites are initially occupied by a methoxyl functional group; b) predicted vitrinite reflectance and approximate rank classification, and final predicted and observed present-day values; c) fraction of total carbon sites occupied by carbonyl functional groups; d) fraction of total carbon sites occupied by carboxyl functional groups; e) fraction of carbons which are aliphatic and have attached hydroxyl groups; f) fraction of carbons which are aromatic and have attached hydroxyl groups; g) aromaticity, or fraction of carbons in aromatic structures.

decarboxylation reactions, as indicated by the subsequent decrease in carboxyl groups. These changes also occur as the predicted vitrinite reflectance approaches a value of 0.45 indicative of the sub-bituminous coal rank. This differs from observed data because small amounts of carboxyl and even carbonyl functional groups remain by the sub-bituminous coal rank (Hatcher, 1990). This suggests that the first-order decarboxylation reaction rates may be too fast, and that other non-first order processes are operating during decarboxylation. Fig. D-15e shows the fraction of carbons atoms that are aliphatic and occupied by hydroxyl functional groups. In the adopted initial lignin structure, these hydroxyl sites are all located at the propyl-γ site, although observations suggest that many of these may be located on the propyl-α site. This shows that these sites are dehydroxylated early in the simulation, by about 57 Ma, which corresponds to a coal rank of below lignite. This change corresponds to observations of early loss of hydroxyl groups from the γ-site (Hatcher, 1990). Fig. D-15f shows that as aliphatic hydroxyl groups are decreasing, aromatic hydroxyl content increases, then subsequently decreases. This corresponds to observations according to Hatcher (1990) mentioned earlier here. The initial increase in aromatic hydroxyl functional groups corresponds to the cleavage of the β-O-4 bond (Fig. D-2) resulting in an aromatic hydroxyl functional group. Subsequent increases in aromatic hydroxyl are the result of the demethoxylation reaction (Fig. D-5), which also results in substitution with an aromatic hydroxyl functional group. Loss of aromatic hydroxyl groups after about 55 Ma result from dewatering reactions, both with and without associated cross-linking. Aromatic hydroxyl functional groups are entirely lost from the kerogen by about 29 Ma, corresponding to a predicted vitrinite reflectance of about 0.9 (high-volatile bituminous rank). Fig. D-15g shows the general increase in aromaticity (or fraction of C atoms in aromatic structures) with time. Three periods of aromaticity increase are associated with demethoxylation, subsequent decarboxylation, and finally late stage demethylation. A final aromaticity of 1.0 may be high compared with observed aromaticity of higher coal ranks (Hatcher et al, 1992; Solum et al 1989). This is a result of the simplifications involved in the construction of the model lignin structure and the reaction network, as well as in the assumption that the initial molecular composition is 100% lignin.

Fig. D-16a shows the predicted production of mobile species in moles per mole of starting lignin over the simulation history. The mobile species include H2O, CH3OH, CO2, CH4, and H*. The species H* is the cumulative concentration of reactive hydrogen in an unspecified form. When hydrogen is produced from any of the reactions, it may either react with itself to form H2 gas, or it may serve as a reactant. Although the former is certainly possible, the latter may be a pre-requisite for many of the other reactions to take place. For example, if demethylation of pendant aromatic methyl is written as a balanced reaction, a hydrogen source is necessary:

$$ArCH3 + 2H^* \rightarrow ArH + CH4 \qquad (D.6)$$

The importance of determining a hydrogen source is critical and is addressed elsewhere (Hoering 1984; Lewan 1999, in press; Mansuy and Landais, 1995; Michels et al. 1995a,b, 1996; Monthioux et al., 1985), but is not the focus of this paper.

H2O content is initialized as 0.55 moles. Its concentration drops after 62 Ma as it is being consumed in several reactions mentioned previously. Until about 37 Ma, any H2O produced is being immediately consumed, and thus there is no extra H2O in the system (its concentration is negligible). After about 37 Ma, the H2O consuming reactions have ceased, and

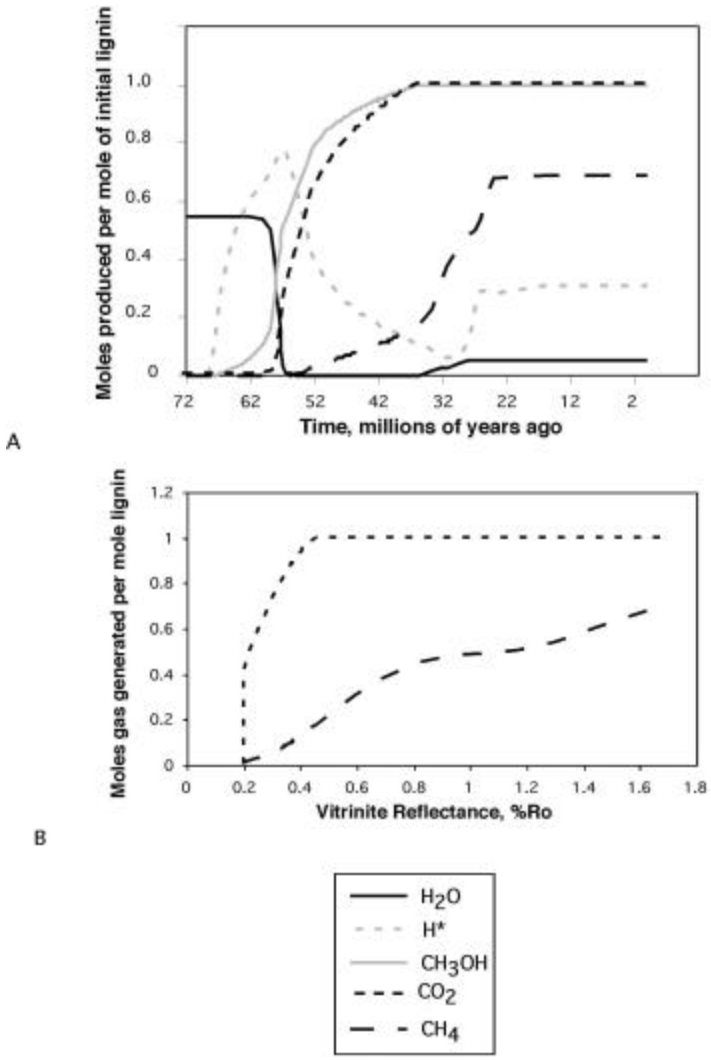

Fig. D-16 a) Total production of mobile species in moles per mole of lignin reacted, over the simulated basin history; b) CO2 and CH4 generated per mole of lignin vs. vitrinite reflectance.

H2O producing reactions are still occurring, allowing a build-up of H2O in the system. Thus there is a net production of H2O in the system over the course of the thermal history.

Similarly, H* production increases over the first 15 my (57 Ma), then experiences a decline as it is consumed in other reactions. From about 57 Ma to about 32 Ma, more H* is consumed than produced by the reaction network. After about 30 Ma, H* consuming reactions cease and H* producing reactions continue, allowing a build-up of H*.

CH3OH, CO2, and CH4 all show increases over the course of the simulation history. None of these species is a reactant in the model reaction network. The different timing of the generation of these species reflects the kinetics of the involved reactions. Demethoxylation occurs at lowest activation energies; decarboxylation occurs at higher activation energy; and demethylation reactions require still higher activation energies. The methane generation slope is complex, indicative of the different types of reactions invoked for demethylation, each with different kinetics (demethylation through reaction with H*, or through cross-linking).

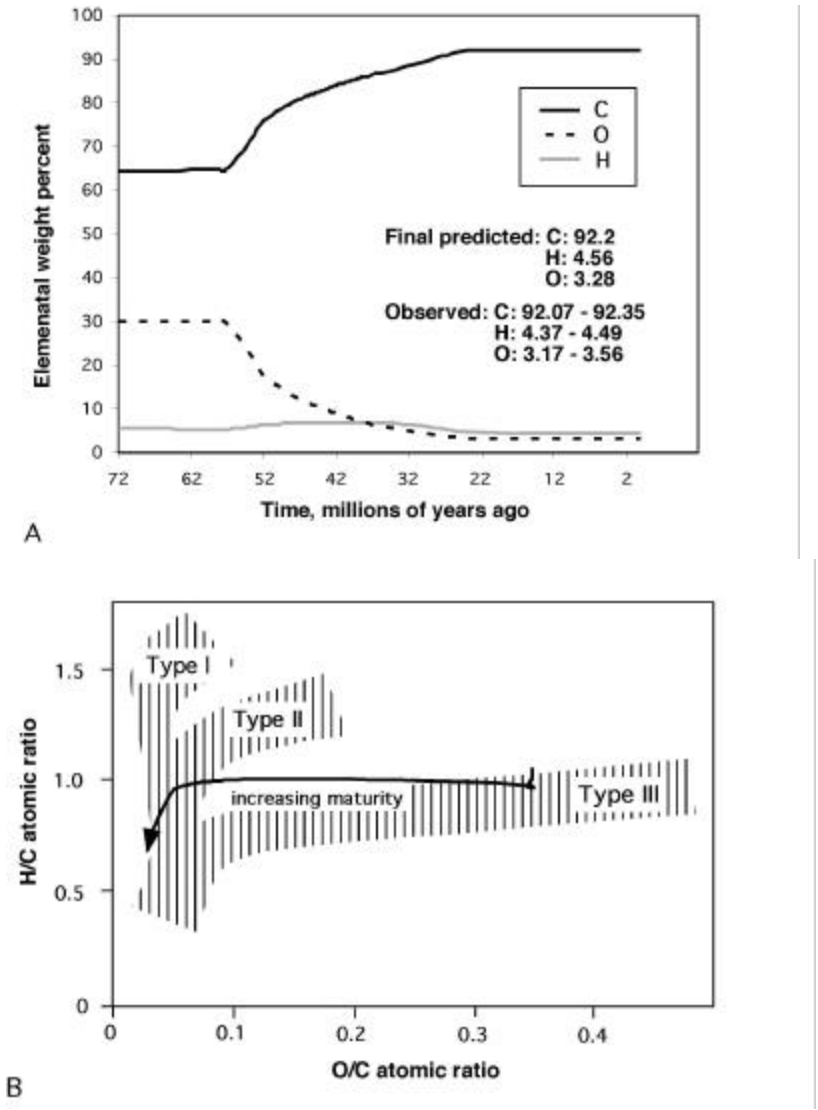

Fig. D-17 Predicted residual chemistry through time: a) carbon, hydrogen, and oxygen elemental weight percents, with final predicted and observed values; b) H/C versus O/C atomic ratios – the trend is similar to that for Type III kerogen; the tail at the high atomic ratio end of the curve is due to earliest loss of hydrogen from oxidation at the propyl-γ site.

The total amount of each of mobile species produced reflects the molecular structural configuration of the reactant immobile species. For example, there is one methoxyl functional group per lignin monomer, thus one mole of lignin will produce a maximum of one mole of methanol by the demethoxylation reaction, assuming this reaction process goes to completion over the simulation history. The total amount of methane produced will vary depending on the kinetics of various reaction pathways. For example, an immobile species may react by demethylation of pendant methyl groups, or by a cross-linking reaction which produces no methane. The relative reaction rates of these two processes will affect the total amount of methane produced. This represents one of the complexities of bifurcating reaction pathways in a reaction network that is composed of neither simple parallel nor sequential reactions.

In this model, the bulk of CO2 generation occurs below 0.4 %Ro (lignite rank) and a significant quantity of CH4 is generated below 0.8 %Ro (sub-bituminous to high volatile bituminous rank) (Fig. D-16b). This implies lower maturity gas generation than is suggested by Scott (1996) (using data from Burnham and Sweeney, 1989), who shows that CO2 generation doesn't start until above 0.35 %Ro and CH4 generation doesn't start until almost 0.8%Ro. Similarly, Zhang et al. (1997) suggest that the CH4 generation doesn't start until after 0.6 %Ro. In the latter two cases, gas generation kinetics are determined from pyrolysis experiments, and thus will have higher activation energies than are determined for the model presented in this paper. If the reaction kinetics used in this model more accurately represent reaction rates under geologic conditions, then more gas may be generated by less mature source rocks. This may have implications for natural gas resource assessments, as will be discussed later.

The compositional change of the remnant immobile species is most easily illustrated by looking at the chemical composition (Fig. D-17a). As expected, carbon content increases significantly over the course of the simulation, and oxygen decreases significantly. Hydrogen content decreases generally, but in smaller amounts. Relative changes in atomic O/C and H/C ratios show the generally expected trend, similar to the trend for Type III kerogen (terrigenously-derived), with relative loss in O/C preceding relative loss of H/C. At high H/C and O/C values, the relationship between the ratios reflects early reactions in which H* (possibly loosely bound) are lost, and reactions in which H2O is consumed and oxygen is added to the structure (Fig. D-17b).

2. Sensitivity Testing

a. Initial Temperature

Because the kinetic transformation of organic matter is temperature dependent, the assumed land surface (or initial) temperature is important in thermal modeling. Over the history of a basin, the mean earth surface temperature may have changed before becoming the present day value of approximately 17 C (CRC Handbook of Chemistry and Physics 1986). Sensitivity testing of this model illustrates the effect of initial temperature over a reasonable range for the Mesozoic to present day history of the earth (Figs. D-18a and b).

Varying initial temperatures from 0 to 25 C, affects the final predicted chemistry very little. Using vitrinite reflectance values as an indicator of final predicted chemistry, Fig. D-18a shows that although the final predicted chemistry may be essentially the same, the maturation paths are offset according to the initial temperatures: at lowest initial temperatures the maturation occurs later, and at higher initial temperatures the maturation occurs earlier. Thus at higher maturities, the initial temperature does not affect the final predicted vitrinite reflectance. At lower maturities, for example vitrinite reflectance less than 0.8 %Ro, predicted reflectance values may be offset by as much as 0.4 %Ro; or, the time to reach a particular vitrinite reflectance may be different by as much as 15 my, as for a reflectance value of 0.5 %Ro. Similarly, by the end of the simulation, total predicted amounts of produced CO2 and CH4 are the same regardless of the initial temperature, but the initial temperature is an important factor in the timing of gas generation over the course of the basin history (Fig. D-18b). For example, at an initial temperature of 25C, by 10 my into the simulation, considerable CO2 has been generated, whereas for lower initial temperatures none has been generated yet. This is critical in such processes as overpressuring, in which the relative timing of compaction and compartment seal development with respect to gas generation is important. Early loss of gas before formation of compartment seal will allow less overpressuring to develop. It must be noted that the higher initial temperatures may also affect diagenetic processes and thus the timing of the formation of

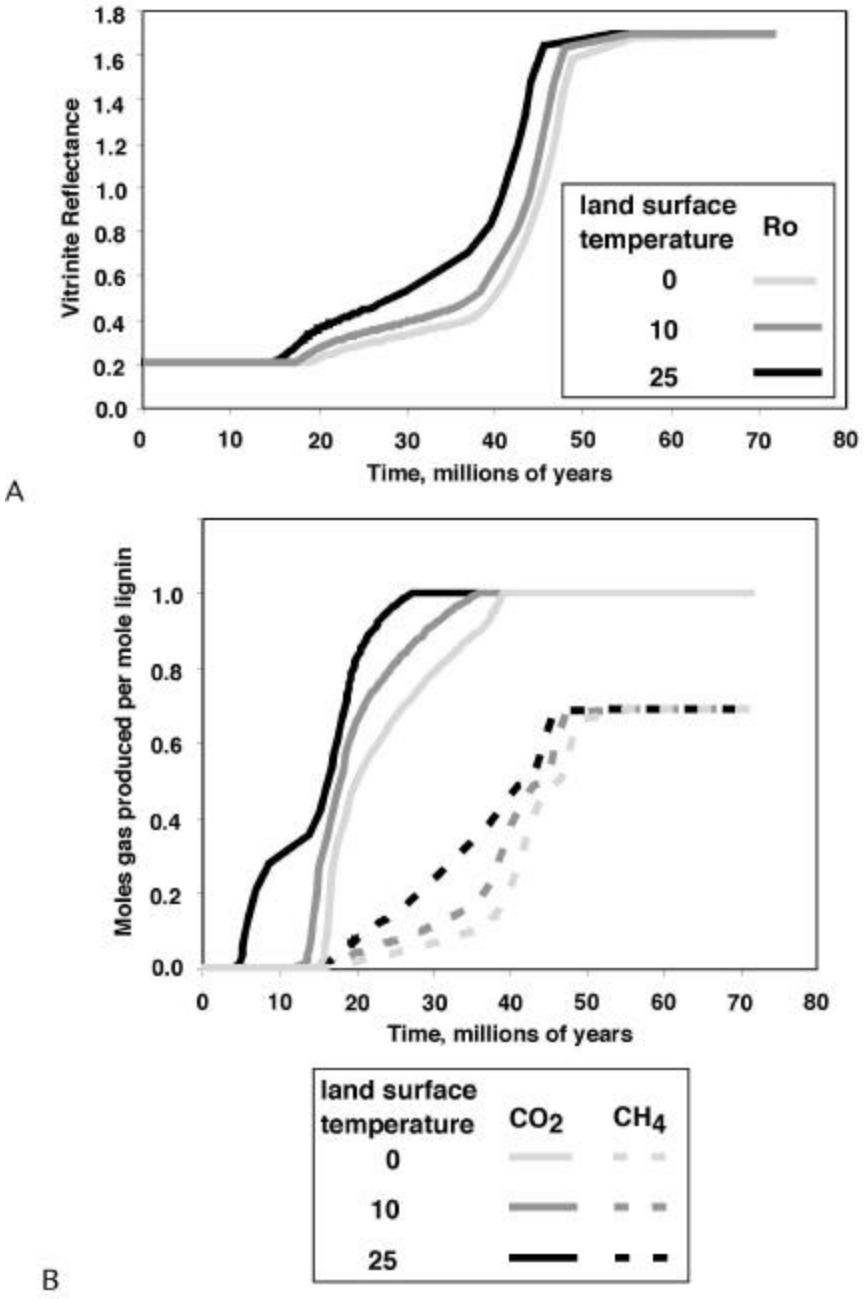

Fig. D-18 Results of sensitivity testing for varying assumptions of land surface temperature: a) predicted vitrinite reflectance; b) predicted total production of CO_2 and CH_4. All three simulations have the same geothermal gradient history. Hence, the fundamental difference in results is the timing of initiation of reactions.

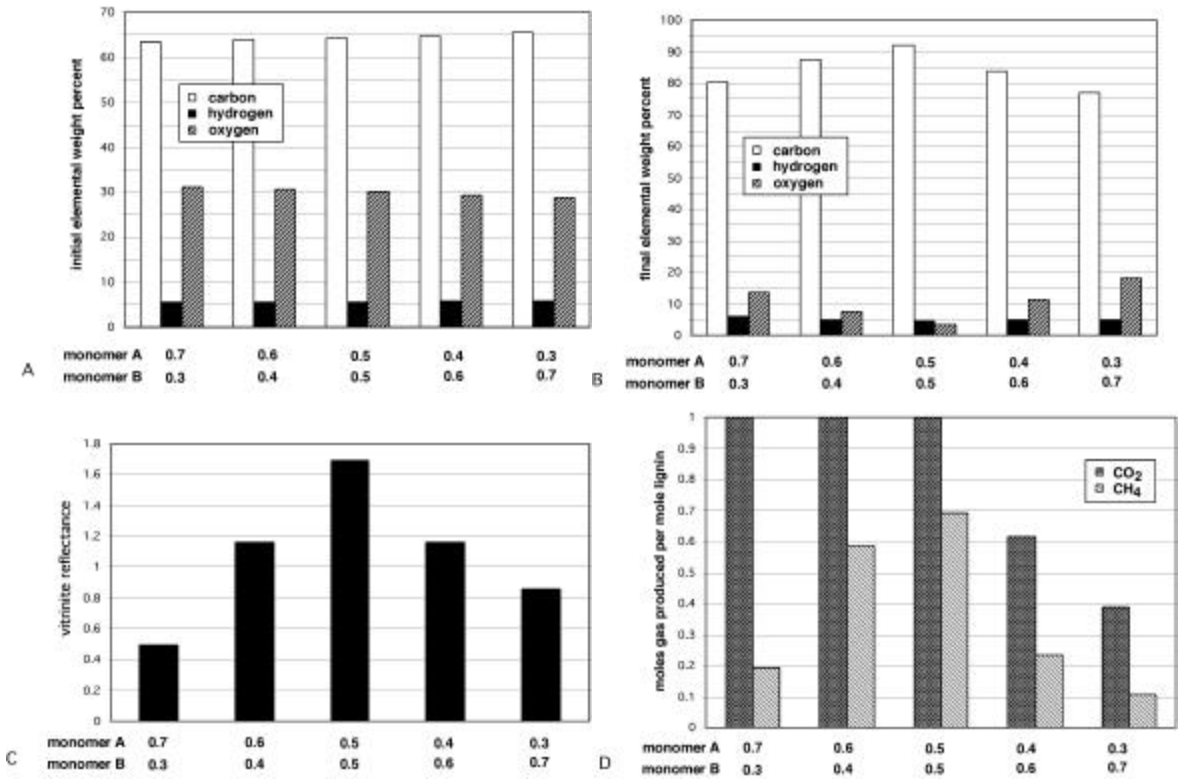

Fig. D-19 Results of sensitivity testing for varying ratios of monomers A and B in the model lignin molecular unit: a) initial elemental weight percents; b) final elemental weight percents of residual species; c) final predicted vitrinite reflectance; d) total CO_2 and CH_4 production.

a compartment seal. Although initial temperature is not important in the final chemistry results for this model, it is potentially important over the course of basin development and in consideration of the timing of other basin processes.

b. Lignin Chemistry

Sensitivity testing of the model shows that predicted results are influenced by the initial lignin structure and chemistry. Lignin is a complex molecule with variable composition, which, for the purpose of modeling, has been simplified to represent a distribution of its major functional groups. Different functional groups will undergo different types of reactions, resulting in different structures and products. This model allows for flexibility in the initial composition and structure of the lignin molecule.

The results of simulations at the MWX site discussed previously are based on a model lignin structure comprising 50% each of monomers A and B (Fig. D-1). This would represent a lignin molecule comprised of 67% β-O-4 linkages, 33% α-linkages, one methoxyl group per aromatic ring, 33% of aliphatic carbons with a hydroxyl functional group, 17% of aliphatic carbons with a carbonyl group, and one propyl structure for every aromatic structure. To test the effect of variations in initial lignin structure on the model, simulations were run for monomer fractions ranging from 0.3 to 0.7. Fig. D-19a shows that over this compositional range, the initial carbon and oxygen weight percents vary by a few percent. By the end of the simulation, the resultant weight percents may vary by almost 15% for carbon and oxygen, and a few percent

for hydrogen (Fig. D-19b). These results show that starting chemical composition is not necessarily an indicator of chemical composition at the end of the simulation. For example, if monomer A comprises 30% and monomer B comprises 70% initially, this starting composition has the highest carbon weight percent of the tested combinations. However, the highest carbon weight percent predicted at the end of the simulation results from a starting composition of 50% monomers A and B. The highest predicted vitrinite reflectance values (calculated from Burnham and Sweeney, 1989) also result from equal amounts of initial monomers A and B (Fig. D-19c). The predicted maturities are vastly different, ranging from 0.5 to 1.7 %Ro. Thus if using the model to predict maturity, the initial chemical composition of proto-kerogen is very important The reason for this discrepancy is that the initial lignin structure, not the chemical composition, controls which reactions occur and therefore the resulting chemistry. This is illustrated by examining variations in predicted CH4 production with starting material composition (Fig. D-19d). CH4 production is maximized with an equal distribution of starting monomers A and B. Monomer A evolves more CH4 in the reaction network, so more of monomer A results in more total CH4 production. However, monomer B generates much of the H* required for the CH4 generating reactions of monomer A' s reaction pathway. With less initial monomer B, less reactant H* is produced, thus less total CH4 can be produced. Thus CH4 production is maximized because equal parts of monomers A and B cancel these effects. This figure also shows that production of CO2 decreases with decreasing initial amounts of monomer A. This is because there are two sites on monomer A which can evolve carboxyl functional groups and subsequently decarboxylate, the propyl-α and the propyl-γ sites. However, on monomer B, the propyl-α site is a polymer linkage and thus only the propyl-γ can evolve a carboxyl functional group. Clearly, the differences in total gas produced show that in this model, different starting compositions affect predictions of gas abundance and chemical composition of residual material.

c. Initial H2O Content

Several of the early, low-maturation reactions require the addition of H2O as a reactant, for example the demethoxylation reaction, and the oxidation of the alpha-carbonyl to carboxyl functional groups. Although H2O is generated by some of the reactions, in order for all reactions to go to completion, H2O is required as an initial input. Availability of H2O will control to some degree the reaction rates, because its concentration is a factor in some non-first-order reaction rates, and by creating a domino effect by limiting the production rate of species that behave as reactants in ensuing reactions.

In order to test the effects of varying amounts of initial H2O in the system, simulations were run with initial input of H2O ranging from 0.0 to 1.0 moles for every mole of input lignin (Figures 20a - d). Fig. D-20a shows the elemental weight percent distributions of the final residual material with varying amounts of initial H2O in the system. The results show that final carbon weight percent decreases and oxygen weight percent increases for initial H2O decreasing below 0.5 moles. This suggests that below this amount, some of the reactions are retarded or inhibited by the lack of H2O available for reaction. At initial values of 0.55 moles and above, the resultant elemental weight percents are very close, suggesting that at least 0.55 moles of H2O per mole of lignin are needed in this reaction network to allow all reactions to go to completion. Similarly, Fig. D-20b shows that vitrinite reflectance values decrease with decreasing initial H2O content below 0.5 moles; above this the maturity is constant. If the assumptions in this model are correct, particularly that H2O is a reactant in some of the transformation reactions, and that

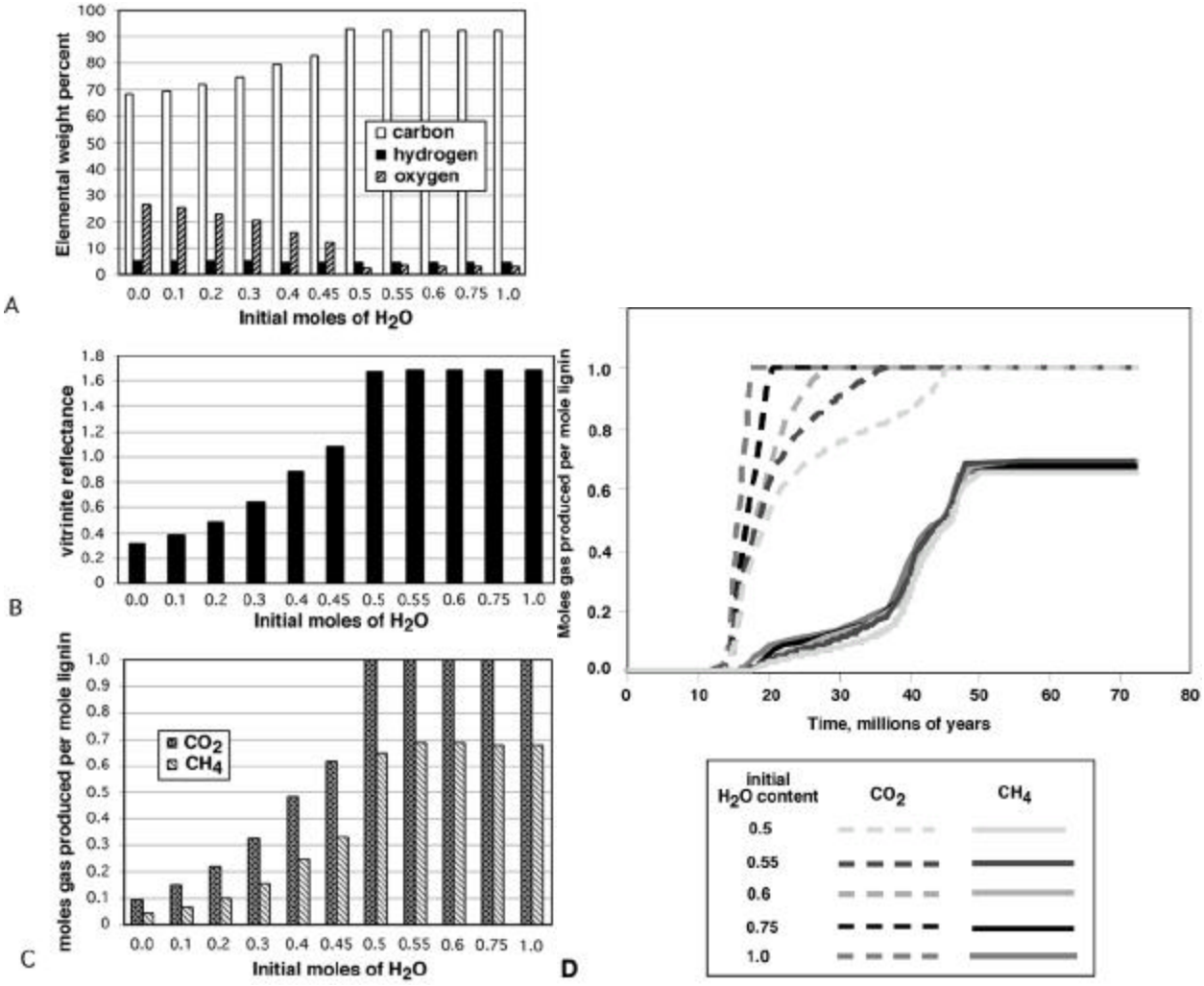

Fig. D-20 Results of sensitivity testing for varying initial moles of H_2O per mole of unaltered lignin: a) final predicted elemental weight percents of residual species; b) predicted final vitrinite reflectance; c) total CO_2 and CH_4 production at the end of the simulation; d) total CO_2 and CH_4 production over time for initial H_2O content of 0.5 to 1.0 moles per mole of lignin.

Ro can be accurately calculated from kerogen elemental composition, then one must consider the importance of H2O to the maturation of organic matter, as well as the thermal history. Naturally, it follows that some of the mobile product distribution will be affected by initial H2O content. Fig. D-20c shows that with increasing initial H2O content up to about 0.5 moles, both CO2 and CH4 total production increase. From 0.55 to 1.0 moles of initial H2O, CO2 production remains constant, but CH4 production decreases slightly. This occurs because as H2O content is increased, the rates of reactions that compete with demethylation reaction pathways increase, limiting CH4 production slightly. Above 0.5 moles of initial H2O, the total gas produced does not change much, however the timing of gas production varies. In Fig. D-20d the total production of CO2 and CH4 for initial H2O contents of 0.5 moles and above are shown through the simulation time. This figure shows the timing of CO2 production is quite sensitive to initial H2O content above 0.5 moles, and that of CH4 production is only slightly sensitive.

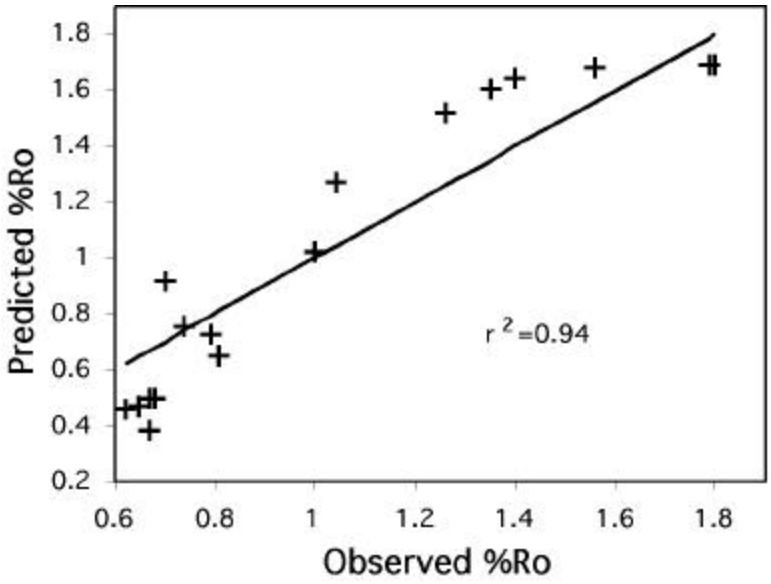

Fig. D-21 Cross-plot of predicted and observed vitrinite reflectance values shows relatively good agreement. Solid line has a slope of 1.0.

3. Piceance Basin

Simulations were run at seventeen sites for which there are independently developed burial and thermal histories (Payne and Comer, 1997) in order to test the model. Fig. D-21 compares the resulting vitrinite reflectance values with observed values at each site. In general, the predicted and observed reflectance values differ by a maximum of 0.29 %Ro, but most are within 0.2 %Ro. The model generally predicts higher reflectance values at lower maturities, lower values at moderate maturities, and slightly lower values at the highest maturities over the range of observed maturities.

In order to evaluate these results several factors need to be considered. First, this model is not designed to account for complete graphitization of the lignin-derived kerogen, but instead is designed to account for maturities into the low volatile bituminous rank, below about 1.7% Ro. Secondly, there is natural error associated with vitrinite reflectance values from the following: natural compositional variation in the vitrinite; vitrinite reflectance anisotropy, which depends on the orientation of the molecular structures within the vitrinite (the randomness of orientation increases at lower maturities); and from sample preparation or instrumentation error (Stach et al. 1982). Stach (1982) shows an example in which the error may be as large as 0.4% for reflectance values ranging from 0.2 to 0.7 %Ro. In addition, this model calculates vitrinite reflectance from predicted atomic ratios using the empirical relationship developed by Burnham and Sweeney (1989), so any error in that relationship will be embedded in predictions by this model. Finally, a fundamental source of error in this analysis is that the development of burial and thermal histories used as input in this model often includes calibration to maturity parameters using a variety of thermal models (for example, Johnson and Nuccio, 1986). Thus any error in the input burial and thermal histories will be embedded in the calculations of this model.

Maturity, %Ro	Coal volume (10^{10} m^3)	Coal density (g/cm^3)	CH_4 generated per mole lignin (moles)	Total CH_4 generated (10^{13} moles)	Total CH_4 generated per ton of coal (scf/ton)
< 0.6	9.31	1.35	0.13	4.38	275
0.6 – 0.8	5.72	1.41	0.39	8.42	826
0.8 – 1.0	1.76	1.44	0.47	3.19	996
1.0 – 1.2	1.75	1.45	0.50	3.39	1059
1.2 – 1.4	1.17	1.47	0.54	2.49	1145
1.4 – 1.6	2.05	1.48	0.63	5.12	1333
> 1.6	4.64	1.49	0.69	12.8	1463

Table D-3 Coal volume, density, and methane produced for several maturity ranges.

E. Application of the Model to Resource Assessment

The natural application of this kind of model is predicting the hydrocarbon generation for a given source rock of known depositional environment and geologic history. With further research and development and integration with calculations of in place reserves, this model may become a useful tool for assessing the quality and quantity of natural gas resources, such as in the Piceance Basin. As an example, an assessment is presented here of the total methane generated for the whole Piceance Basin over its history, assuming that the Williams Fork coals are wholly lignin derived and that they represent the majority of the methane source rock. This assessment is not intended to be a complete and detailed assessment of gas in place, and is only meant as an example of an application of the results of this kind of modeling.

To calculate the total methane generated, first the volume of the Williams Fork coal was estimated for each of several ranges of Cameo Coal vitrinite reflectance using a map of coal thickness (McMurry and Tyler, 1996), and a map of vitrinite reflectance (Scott, 1996) (Table D-3). For each maturity range a total amount of methane generated is calculated as follows:

$$\begin{pmatrix}\text{coal}\\ \text{volume}\\ cm^3\end{pmatrix}\times\begin{pmatrix}\text{coal}\\ \text{density}\\ g/cm^3\end{pmatrix}\times\begin{pmatrix}\text{moles } CH_4\\ \text{per mole}\\ lignin\end{pmatrix}^{-1}=\begin{pmatrix}\text{total } CH_4 \text{ generated}\\ moles\end{pmatrix}. \qquad \text{(D.7)}$$

The coal density is calculated from the carbon weight percent in the lignin maturation model using an empirical function which is derived from data in Levine (1993). This calculation assumes that 100% of the coal volume is comprised of lignin and that one mole of lignin can be described as one mole of the molecular unit described in the lignin maturation model (Fig. D-1). This value was summed for all of the ranges of %Ro to give a total value of CH4 generated in the Piceance Basin: 3.98x1014 moles. This results in an estimated volume of 314 tcf (trillion cubic feet) of methane gas (assuming a gas density of 4.92x10-2 ft3/g), part of which is in place as coal-bed methane, part of which has migrated to other reservoirs such as the local Mesaverde sandstones, some of which has been migrated out of and lost from the basin, and some of which has been produced.

Although this rough estimate calculates the total amount of methane generated and other estimates calculate the total gas in place, the validity of this estimation can be addressed. Scott et al. (1996) estimate a coal gas resource of 99 tcf, using coal gas analysis data from coals of various rank and from coal volume estimates. This value is expected to be smaller than that calculated here because it comprises only part of the total natural gas generated by the coals over the basin history, yet the order of magnitude suggests that the estimate presented in this paper is reasonable. Similarly, earlier assessments by Rightmire and Choate (1986) estimate a value of 60 tcf of coal bed methane for the whole Piceance Basin, and McFall et al (1986) estimate a value of 84 tcf. Hence, if it is assumed that 100-200 tcf of gas migrated away from the source coals or has been produced, then the model presented here may provide insight into the whole basin natural gas resources, both those found within coal beds and those found in associated sandstone reservoirs, as suggested by Rightmire and Choate (1986).

F. Discussion

One of the unique features of this approach to modeling maturation is its versatility and potential applicability to many different kerogen types in a variety of source rocks. A specific depositional environment may be characterized by a distribution of resistant biomolecular components. For example, the precursory chemical composition of a coal derived primarily from woody material, and thus being composed of primarily lignin, will differ from that of a coal with a significant algal contribution. The model reflects these differences by considering that the former comprises 100% lignin, and the latter 75% lignin and 25% algaenan. The algaenan, being of a different structure and composition than lignin, has its own reaction pathways and produces a different set of intermediate and mobile species. Likewise, one could distinguish a shallow marine carbonate source material from that of a delta by considering compositional differences in the amount of terrigenous versus marine biomolecular input. These are important factors that are expected to cause significant variations in timing and yields in gas-bearing versus oil-bearing petroleum systems, which are lost in models which are calibrated on standard kerogen types, or assume a single precursor composition with a highly generalized set of kinetic parameters.

Similarly, this approach allows accounting for the natural variability and complexity of the lignin molecule, or any other proto-kerogen molecule of interest. The structure of unaltered lignin is assumed in this model to be a simplified guaiacyl-like polymer when in reality, its form is more complex. For example, it is suggested that many of the propyl-α sites are occupied by hydroxyl functional groups, and that there may be some hydroxyl groups located on the aromatic structures. In addition, some ether linkages may be between two propyl structures. The design of this model allows straightforward modification of the starting lignin composition to account for the statistical distribution of structures, linkages, and functional groups in order to account for greater complexity in the starting material. Specifically, the model may be modified to include several different types of lignin monomers with different linkages. For example, if 50% of the linkages are of the β-O-4 type, 25% are of the α-O-4 type and 25% link propyl structures, then one would construct a model in which the starting material comprises 50%, 25% and 25% of the molecules with these respective structures, each structural type having its own network of reaction pathways depending upon its initial structure. In the spirit of this modeling approach based on molecular structures, it would be assumed that most of the reaction stoichiometries and kinetics for a given reaction type would be the same. Many such modifications to the original lignin structure could be accounted for in this way, creating a larger and more complex reaction network, but allowing the fundamental processes and their kinetics to remain the same.

Another useful feature of this model is that it includes the formalism to account for *n*th order processes, when *n* is an integer. Observations of certain structural changes indirectly suggest the occurrence of non-first order processes, for example reactions in which hydrogen or oxygen must be added to the structure, or cross-linking. Potential reactants, connate H2O and hydrogen bound to the organic material itself, are probably sufficiently abundant. Naturally, if a reactant is scarce, reaction rates are slowed, and if abundant, rates increase. Direct evidence of the mechanisms involved is lacking, but the *n*th order formalism allows more exact reactions to be modeled when or if specific evidence is available.

This approach to modeling organic maturation is well suited to predictive basin modeling of hydrocarbon potential, specifically for gas generating basins. The essence of this model is the identification of specific and characteristic molecular structures and linkages, and the reactions that transform them. Characterizing specific reactions allows for the bookkeeping of mobile and intermediate species, accounting for a variety of reaction pathways depending on molecular input and thermal history. This model also allows for a complex network of competing or augmenting pathways. By accounting for *n*th order reactions, this model can incorporate cross-linking processes, as well as processes which appear to require reaction with H2O, or addition of hydrogen. Finally, by focusing on physical transformations of specific precursor molecules rather than empirical fitting of bulk chemistry, the model framework accommodates the inclusion of other precursory molecules, and thus a petroleum generation model tailored directly to specific kerogen types and indirectly to depositional environments.

Ongoing and future work on this model include the following:

- increasing the complexity of the model lignin structure to more closely reflect its observed structure and composition;
- expanding the reaction network by including more cross-linking and condensing reactions, in order to account for greater thermal maturation, and reactions which generate ethane and other components of natural gas; and
- developing reaction networks for other kerogen precursor molecules, for example algaenans, cutans, and tannins, in order to model thermal transformation of compositionally more complex assemblages; this will allow modeling of a variety of depositional environments.

G. Summary

The model presented in this paper simulates lignin maturation based primarily on structural transformations of the lignin molecule observed in naturally matured samples. This model adopts a simplified guaiacyl polymer as the assumed starting lignin structure. The structural transformations are described as fifteen processes, which are divided into four classes: isomerization, modification of the propyl structure, defunctionalization, and cross-linking. Assuming that the natural gas generating Upper Cretaceous coals of the Mesaverde Group are primarily lignin-derived, the kinetics of the model are calibrated to the MWX site in the Piceance Basin.

Input for the simulation includes a reaction network containing twenty-six species and twenty-two sequential and parallel reactions, the kinetic parameters and stoichiometries for all reactions, and a burial and thermal history for the MWX site in the Piceance Basin. Output includes mole fractions of all species, intermediate and mobile, functional group fractions, elemental weight percents, and vitrinite reflectance calculated from elemental atomic ratios. The model is sensitive to initial chemistry of the system, both lignin composition and initial H2O in

the system. Results show reasonable prediction of maturities at other sites in the Piceance Basin for maturities up to the low volatile bituminous rank. Because the model predicts the speciation of gases, it can be used to estimate the quality and quantity of natural gas generated over the course of a basin's history, and therefore may be a useful tool in natural gas resource assessments, complementary to in place coal bed methane analyses. The flexible design of the model allows it to be modified to account for a more complex lignin molecule and reaction network, or even compositionally heterogeneous source material.